



Provided by the author(s) and University of Galway in accordance with publisher policies. Please cite the published version when available.

Title	Accurate dielectric characterisation of biological tissues in the microwave range using the open-ended coaxial probe technique
Author(s)	La Gioia, Alessandra
Publication Date	2019-12-19
Publisher	NUI Galway
Item record	http://hdl.handle.net/10379/15660

Downloaded 2024-05-01T21:31:58Z

Some rights reserved. For more information, please see the item record link above.



Accurate Dielectric Characterisation of Biological Tissues in the Microwave Range using the Open-ended Coaxial Probe Technique

Presented by:
Alessandra La Gioia

to:
Electrical and Electronic Engineering,
College of Engineering and Informatics,
National University of Ireland Galway,

in fulfillment of the requirements for the degree of
Doctor of Philosophy.

Supervised by:
Martin O'Halloran and Emily Porter

December 16, 2019

Contents

Contents	i
Abstract	iv
Acknowledgements	vi
List of Figures	vii
List of Tables	xxix
Acronyms	xxxii
1 Introduction	1
1.1 Motivation	2
1.2 Thesis contributions	6
1.2.1 Journal and Conference publications	8
1.3 Thesis structure	11
2 Dielectric properties of biological tissues	13
2.1 Theoretical background	13
2.1.1 Definition of dielectric properties	14
2.1.2 Dielectric dispersions	15
2.1.3 Dielectric models	17
2.2 Measurement techniques	18
2.2.1 Transmission line	19
2.2.2 Cavity	21
2.2.3 Open-ended coaxial probe	22
2.3 Open-ended coaxial probe technique: Electromagnetic theory and design advances	23
2.3.1 Electromagnetic transmission across a coaxial probe	23
2.3.2 Reflection coefficient conversion into permittivity	28
2.3.3 State-of-the-art of coaxial probe designs and fabrica- tion materials	32

CONTENTS

2.4	State-of-the-art of dielectric properties of biological tissues	34
2.4.1	Seminal dielectric studies of biological tissues	35
2.4.2	Dielectric measurement of tissues: Inconsistencies and sources of uncertainty	38
2.5	Summary	46
3	Dielectric measurement protocol	48
3.1	Characterisation of the dielectric measurement system	50
3.1.1	System calibration	50
3.1.2	Measurement validation	55
3.1.3	Measurement uncertainty calculation	58
3.2	Dielectric measurement of biological tissues	61
3.2.1	Probe selection considerations	62
3.2.2	Tissue handling and confounders	64
3.2.3	Acquisition of dielectric properties and confounders	68
3.3	Post-measurement processing	72
3.3.1	Data post-processing	72
3.3.2	Sample post-processing	77
3.4	Summary	84
4	Sensing radius of coaxial probes	87
4.1	Sensing radius of an open-ended coaxial probe	89
4.1.1	Importance of an accurate evaluation of the sensing volume	89
4.1.2	State-of-the-art in sensing volume studies	91
4.1.3	Sensing radius definition	94
4.2	Methodology for the sensing radius investigation	96
4.2.1	Experimental methodology	97
4.2.2	Numerical methodology	112
4.2.3	Mathematical prediction of sensing radius	122
4.3	Results and Discussion of the sensing radius investigation	124
4.3.1	Dependence of sensing radius on probe dimensions	124
4.3.2	Dependence of sensing radius on tissue dielectric properties	135
4.3.3	Mathematical prediction of sensing radius	145
4.4	Summary	151
5	Material dielectric contribution	154
5.1	Dielectric contribution of individual materials within a heterogeneous sample	155
5.2	Methodology	157

CONTENTS

5.2.1	Experimental methodology	158
5.2.2	Numerical validation and modelling	166
5.3	Results and Discussion	173
5.3.1	Dielectric contribution of materials in linear heterogeneity configuration	174
5.3.2	Dielectric contribution of materials in concentric heterogeneity configuration	178
5.3.3	Modelling of the individual tissue dielectric contribution within radially heterogeneous samples	185
5.4	Summary	192
6	Post-measurement histology	194
6.1	Methodology	195
6.1.1	Choice of heterogeneous tissue samples	195
6.1.2	Dielectric measurement protocol	197
6.1.3	Traditional histology protocol	199
6.1.4	MicroCT protocol	202
6.2	Results and Discussion	204
6.2.1	Traditional histology process and challenges	204
6.2.2	Dielectric characterisation of radially heterogeneous samples through traditional histology	208
6.2.3	MicroCT preliminary results	218
6.2.4	Dielectric characterisation of a highly heterogeneous sample through microCT-based and traditional histology	220
6.3	Summary	225
7	Conclusions and future work	227
7.1	Summary and Conclusions	227
7.2	Future Work	232
	Bibliography	236

Abstract

Accurate dielectric measurements of biological tissues are crucial for the development of electromagnetic diagnostic and therapeutic devices, such as microwave breast imaging systems and microwave ablation applicators. In fact, such technologies are designed based on estimates of the dielectric properties of diseased and healthy tissues. Dielectric properties of biological tissues are currently measured in the microwave frequency range using the open-ended coaxial probe technique. Although the dielectric measurement procedure with an open-ended coaxial probe is straightforward, several factors can introduce uncertainties into dielectric data, which can consequently reduce the efficacy of electromagnetic medical technologies. Generally, uncertainties are higher in the dielectric measurement of heterogeneous tissue samples, such as breast tissue samples, due to the fact that the open-ended coaxial probe technique is based on the assumption that the measured sample is homogeneous. Thus, in order to reduce uncertainties related to the measurement of heterogeneous samples, post-measurement histological analysis may be conducted to associate the measured dielectric properties to the different tissue types within heterogeneous samples. Specifically, histological analysis needs to be conducted on the region of sample consisting of the tissues that may have contributed to the measured dielectric properties. To this extent, it is fundamental to define the sensing volume of the measurement probe, which is delineated by the sensing radius and sensing depth. Recent research studies have investigated the impact of the sensing depth definition and calculation on the dielectric characterisation of a number of layered material samples, thus demonstrating how this parameter may be a source of error in the interpretation of dielectric data acquired from heterogeneous samples. However, few studies have investigated the sensing radius, and only for a limited number of probes and material samples. For this reason, in this thesis, the sensing radius is investigated through both dielectric measurements and numerical simulations conducted on radially heterogeneous tissue-mimicking and biological samples, with different dielectric properties and contrasts.

Firstly, the sensing radius is examined as the minimum radius of the

CONTENTS

homogeneous tissue region required to accurately acquire only the dielectric properties of that homogeneous tissue without the influence of the surrounding tissues. The sensing radius values obtained across a number of biological tissues are also modelled in order to support prediction of the sensing radius for a subset of biological samples, with the aim of improving the dielectric characterisation of biological samples presenting radial heterogeneities.

Secondly, the dielectric contribution of single tissues constituting radially heterogeneous samples is examined within the sensing radius. This analysis has the aim of supporting the dielectric characterisation of radially heterogeneous tissue samples within which it is not possible to find a homogeneous tissue region with radius larger than the sensing radius. The outcomes of this analysis suggest that the dielectric properties of radially heterogeneous samples depend on the spatial distribution of each material within the sensing radius, and that the bulk dielectric properties of concentric heterogeneous tissues highly depend on the properties of each constituent material within the sensing radius.

Lastly, the significance of the experimental findings from these two analyses is demonstrated in the dielectric characterisation of radially heterogeneous biological samples by the analysis of the histological content following the dielectric data acquisition. Thus, the importance of the knowledge of the histological content for a rigorous dielectric characterisation is highlighted for biological tissues with simple heterogeneous structures. However, the sample histological information may not be sufficient for an accurate dielectric characterisation of samples with complex heterogeneous structures, due to the challenges in correlating the measured dielectric properties with complex histological features. These challenges suggest the investigation of novel histological techniques, such as micro computed tomography, to combine with the open-ended coaxial probe technique, with the aim of improving dielectric characterisation of highly heterogeneous biological tissues. Thus, a preliminary investigation demonstrating the potential of using micro computed tomography for this application is also presented.

In summary, this thesis provides a basis for consistent identification of the sensing radius and accurate interpretation of the dielectric properties acquired from radially heterogeneous tissue samples, with the aim of supporting the design of microwave medical devices.

Acknowledgements

I would like to thank Martin for giving me the opportunity to work in his lab with friendly people and to supervise my work with the fundamental support of Emily. In particular, I would like to thank Emily for her dedication to my work and her crucial feedback throughout these four years. I would also like to thank Adnan and Declan, who gave me technical support during the thesis writing, and Anna for her vital moral support in the lab. Finally, from the lab, I would like to thank Laura, Adam, Eoghan, Barry, Niko, Hamza, Bilal and Nadia, who made my working hours more pleasant.

Out of the lab, I would like to particularly thank Ryan, who, with his patience and his support, gave me strength in the hardest moments. I would like to thank my mum and my dad for their constant support in my life. I would like to thank also my brother for making me laugh with his surreal experiences in the tired evenings. Finally, I would like to thank my precious friends Federica, Martina, Sabrina, Anna, Beatrice, Claudia, Nunzia and Rosanna.

List of Figures

2.1	Logarithmic plot of the major dielectric dispersion regions, α , β and γ , for bone and muscle tissue. Relative permittivity data is from Gabriel <i>et al.</i> [46]. The α region arises from the ionic diffusion associated with fixed charges on cell membranes and is centred around 10^2 Hz, the β region is caused by the capacitive charging of cell membranes through electrolytes and covers frequencies between 10^4 and 10^7 Hz, and the γ dispersion is caused by the relaxation of water molecules and occurs in the range from 10^8 up to 10^{10} Hz. In the plot, the δ dispersion that is thought to be caused by the dipolar relaxation of bound water is not depicted since it overlaps with the strong γ dispersion . . .	16
2.2	Schematised measurement set-up of the three techniques: (a) transmission line, (b) cavity perturbation and (c) open-ended coaxial probe. Portions of this figure were adapted from [75]. The transmission line technique (a) consists of placing a sample in a coaxial line that is connected to two ports of a Vector Network Analyser (VNA) to acquire the scattering parameters S_{11} and S_{21} , which are then converted into complex permittivity. The cavity perturbation method (b) consists of inserting a sample with width smaller than 1 mm into a resonant cavity, thus altering resonant frequency (f) and quality factor (Q) of the cavity. Then, the dielectric properties are computed using the frequency, the Q-factor, and the volume of the sample. Lastly, the open-ended coaxial probe (c) consists of a truncated section of a transmission line connected to one port of the VNA. The sample is placed in contact with the probe and reflects the transmitted signal back to the VNA, which generally converts the resulting S_{11} parameters into complex permittivity	20

- 2.3 Diagrams illustrating the EM transmission along an open-ended coaxial probe and the electric probe-sample interaction: (a) top cross-section of a coaxial probe with indicated probe dimensions; (b) top cross-section of a coaxial probe with generated EM signals; (c), side cross-section of a coaxial probe placed in contact with a sample. In particular, (a) illustrates the inner and outer conductors, and the insulator characterised by the relative permittivity ϵ_r , of a coaxial probe with dimensions a , b and c , which, specifically, are inner conductor radius, outer conductor inner radius and insulator width, respectively. Due to the Transversal Electro-Magnetic (TEM) propagation mode generated by the application of a voltage signal V between the two conductors, (b) depicts an electric field component E_ρ along the radial direction ρ , and a magnetic field component H_ϕ along the azimuthal direction ϕ . In (b), the resulting generated current I encircling the probe is also labelled. In (c), the side-view cross-section of the interaction between the probe and the sample is illustrated by highlighting the radial electric field within the probe and the fringing electric field across the sample, due to the impedance mismatch between the probe and the sample, which have impedances of Z and Z_S , respectively. When the electric field fringes, part of the signal is transmitted into the sample and the rest of the signal is reflected back to the probe. Note that the diagrams are not to scale . . . 25
- 2.4 Schema of the lumped equivalent circuit models used to convert the reflection coefficient into permittivity: (a) capacitive model, (b) antenna model, and (c) virtual line model (adapted from [107]). In the capacitive model (a), the termination of the coaxial probe is assumed to be purely capacitive, and is then modelled as a lumped admittance Y [S] with a capacitance C_f [F] originating from the fringing field within the probe insulator, and a capacitance $C(\epsilon^*)$ deriving from the sample fringing field. In the antenna model (b), the sample losses are taken into account by adding a resistor with conductance G [S] in parallel to the probe capacitance C_f and the sample capacitance $C(\epsilon^*)$. Lastly, in the virtual line model (c), the dielectric sample is modelled with a virtual transmission line of length L , which has the same dimensions as the physical probe of length D and terminates with an open circuit 30

2.5	Relative permittivity and conductivity plots from adrenal gland and kidney associated with the tissue sample anatomy: (a) diagram illustrating the three anatomical regions, capsule, cortex and medulla, which characterise both adrenal gland and kidney (figure adapted from [134]); (b) relative permittivity plot and (c) conductivity plot summarising adrenal gland data from [132], [134] and kidney data from [46], [133]. In both (b) and (c), it can be noted that, in past studies [46], [132], measurements were performed only on the capsule (that is the external anatomical region of adrenal gland and kidney), while, in more recent studies [133], [134], cortex and medulla (i.e., the other two anatomical regions of adrenal gland and kidney) were also considered for the dielectric characterisation of adrenal gland and kidney	41
2.6	Relative permittivity and conductivity plots from healthy and cancerous liver tissue: (a) figure from [48] illustrating a subset of diseased liver samples; (b) relative permittivity plot and (c) conductivity plot summarising healthy liver data from [31], [46], [53], [54], [57], [61] and diseased liver data from [48], [53]. In both (b) and (c), it can be noted that consistent data was found for healthy liver tissue [31], [46], [54], [57], [61], while a wider range of dielectric properties were acquired for diseased liver tissues [48], [53]	42
2.7	Examples of (a) healthy and (b) cancerous breast samples from [10], [11]	44
2.8	(a) Relative permittivity and (b) conductivity plots summarising healthy and cancerous breast tissue data from [10], [11], [15], [49], [60], [61]. In the legend in (a), the low, medium and high density healthy breast tissue refer to the three categories, Group 3 with 85–100% adipose content, Group 2 with 31–84 % adipose content, and Group 1 with 0–30% adipose content, respectively, in the study by Lazebnik <i>et al.</i> [10], and to the three categories, 80-100% adipose content, 20–80% adipose content and 0-20% adipose content, respectively, in the study by Martellosio <i>et al.</i> [49]. Furthermore, from (a) and (b), it can be noted that the reported dielectric data is inconsistent for both healthy and cancerous breast tissue, mostly due to tissue heterogeneity and differences in sample categorisation across the literature	45
3.1	Flowchart of the main steps of the protocol for measuring the dielectric properties of biological tissues	49

3.2	Schematised set-up for the calibration of the coaxial probe. The calibration procedure involves the measurement of the three standards: (a) open-circuit, (b) short-circuit and (c) broadband load. Portions of this figure were adapted from [75]	53
3.3	Flowchart of the common steps to minimise tissue-related errors in <i>in vivo</i> and <i>ex vivo</i> dielectric measurements	73
3.4	Histology diagrams of a breast sample composed of fat and gland modules (distinguishable by their distinctive colours) highlighting the impact of the sensing volume on the tissue categorisation and thus on the interpretation of the acquired dielectric data. In (a-c), the probe location is denoted with a black oval on the top of the side view of the sample histology, where different values of sensing radius and depth are marked with dotted lines. Specifically, in (a), the sensing volume is expressed by r_1 and d_1 and delineates the histology region occupied by 100% fat, in (b), the sensing volume is expressed by r_2 and d_1 and delineates the histology region occupied by 50% fat and 50% gland, and, in (c), the sensing volume is expressed by r_2 and d_2 and delineates the histology region occupied by 67% fat and 33% gland	82
4.1	Example illustrating the importance of knowledge of the sensing radius of the measurement probe for the dielectric characterisation of single tissue types within heterogeneous samples. Both (a) and (b) illustrate a portion of porcine kidney, where the cortex is separated from the medulla with a black dashed line. In (a) and (b) the transversal sensing areas corresponding to the sensing radii r_1 and r_2 , respectively, are marked with a black solid line. The figure highlights how an inaccurate evaluation of the sensing radius can lead to an inaccurate dielectric characterisation of tissues: if the sensing radius r_1 is erroneously considered (instead of the correct sensing radius r_2), the measured dielectric data is erroneously associated only to the cortex, although the medulla is within the sensing area and is likely to contribute to the dielectric measurement	90

4.2 Diagram schematising the dielectric impact of individual materials within two concentric samples: one sample with saline as inner material (dielectrically contributing 80%) and Teflon as outer material (dielectrically contributing 20%), and the other sample with saline as inner material (dielectrically contributing 80%) and DI water as outer material (dielectrically contributing 20%). The respective values of relative permittivity (corresponding to 0.5 GHz) of the two samples demonstrate how concentric materials with a high contrast in relative permittivity (like that of saline and Teflon) substantially affect the measured dielectric properties, while concentric materials with a low contrast in relative permittivity (like that of saline and DI water) introduce only a small change in the measured dielectric properties, which may be within the uncertainty 96

4.3 (a) Relative permittivity and (b) conductivity plots of the average measured and reference data from the literature for 0.1 M NaCl. In both relative permittivity and conductivity plots, the average measured data at 23.7°C is reported with a blue dotted line, the fitted data with a black solid line, together with the standard deviation (covering 95% of the confidence interval) indicated with black dotted lines, the data at 23.7°C by Peyman *et al.* [146] with a red dash-dotted line, the data at 23.7°C by Gulich *et al.* [73] with a dash-dotted yellow line, and the data at 20°C and 25°C by Buchner *et al.* [143] with green dashed and dash-dotted lines, respectively. The plots show that the measured data is in agreement with the data from the literature 102

4.4 Relative permittivity and conductivity plots of the average measured and reference data from the literature for methanol (a-b) and ethanediol (c-d). In all plots, the average measured data is reported with a blue dotted line, the fitted data with a black solid line, together with the standard deviation (covering 95% of the confidence interval) indicated with black dotted lines, the data at the measurement temperature by Gregory *et al.* [145] with a red dash-dotted line, and the data at 20°C and 25°C by Jordan *et al.* [147] with green dashed and dash-dotted lines, respectively. The plots show that the measured data is in agreement with the data by Gregory *et al.* [145] and gradually diverges from the data by Jordan *et al.* [147] for frequencies above 5 GHz 104

4.5 (a) Relative permittivity and (b) conductivity plots of the average measured and reference data from the literature for 1-butanol. In both plots, the average measured data at 23.8°C is reported with a blue dashed line, together with the standard deviation (covering 95% of the confidence interval) indicated with blue dotted lines, the fitted data with a black solid line (only up to 5 GHz), and the data at 23.8°C by Gregory *et al.* [145] with a red dash-dotted line. Both plots show that the measured data is in agreement with the reference data up to 5 GHz. However, measured data is not reliable for frequencies above 5 GHz, where the loss tangent of 1-butanol is below the minimum recommended value of 0.05 reported in the Keysight probe datasheet [113] . . . 105

4.6 Dimensions of the coaxial probe: a is the radius of the inner conductor, c is the insulator width, b (obtained by summing a and c) is the inner radius of the outer conductor, and r is the total radius of the probe 106

4.7 (a) Photograph and (b) diagram of the measurement scenario for the calculation of the maximum sensing radius. In the photograph (a), the Keysight performance probe is in contact with the Teflon block immersed in the 0.1 M NaCl solution. On the Teflon block, the sizes of the apertures are labelled and, for apertures smaller than the total radius r of the probe, the size of the probe is marked in black around the apertures in order to facilitate probe positioning. In the diagram (b), the measurements of each aperture, with radius ranging from 0.5 mm to 5 mm, are schematised. The red circle outlines the probe position, and the solid and dotted circles concentric to the probe denote the smallest and largest radius of the saline solution, respectively, within Teflon, which is represented by the yellow square 108

4.8 (a) Relative permittivity and (b) conductivity traces obtained from measurements involving the Keysight performance probe and the sample consisting of Teflon apertures filled with saline. In the legend, the radius of the Teflon apertures, ranging from 0.5 mm to 5 mm, is specified. As the radius of the Teflon aperture increases, the relative permittivity tends toward that of the saline solution 110

4.9 Plot of the percent difference in (a) relative permittivity and (b) conductivity between the measurements from each aperture (plotted in Fig. 4.8) and the reference data, for the frequencies of 2 GHz, 4 GHz and 6 GHz. The reference data is the measurement at the 5 mm aperture, which is representative of saline in isolation. In both plots, the 2 GHz data is indicated with a blue solid line, the 4 GHz data with a red dash-dotted line, and the 6 GHz data with a green dashed line. The 2.4% and 4.6% threshold values are indicated with horizontal grey lines in (a) and (b), respectively, for the calculation of the maximum sensing radius. In fact, the maximum sensing radius is calculated as the radius at which the outer material (Teflon) ceases to contribute to the acquired dielectric properties, within the measurement uncertainty of 2.4% for relative permittivity and 4.6% for conductivity. In both plots, the maximum sensing radius values of approximately 1.7 mm are marked with a vertical grey line, where the (a) relative permittivity and (b) conductivity percent difference lines intercept the horizontal threshold trace 111

4.10 (a) Relative permittivity and (b) conductivity of the 15 biological tissues selected for the 38 simulated samples constituting the third simulation set samples. The 15 tissues were selected in order to span a wide range of relative permittivity and conductivity values. The relative permittivity and conductivity of each of the 15 tissues were obtained from the IT'IS database [190] 118

4.11 Determination of the maximum sensing radius for the three Keysight probes through (a) measurements and (b) simulations. In both plots, the percent relative permittivity difference is calculated by considering the relative permittivity of 0.1 M NaCl averaged across frequency as the reference signal. The percent difference was calculated between each Teflon aperture (saline as inner material surrounded by Teflon), and the reference signal. In both plots, the 2.4% threshold value used for the calculation of the sensing radius is indicated with a horizontal line, and the black trace refers to the slim form probe, the red trace to the performance probe, and the blue trace to the high temperature probe. In (b), the sensing radius values are marked where the relative permittivity difference lines intercept the horizontal threshold trace 126

4.12 Regression lines (solid for saline and Teflon samples and dash-dotted for breast fat and gland samples) fitting the sensing radius data (stars) obtained for different radii of inner conductor. The data refers to the scenarios S1, where only a and then b are increased. The lines, with parameters reported in Table 4.12, show the same trend across all samples. Specifically, the sensing radius is found to increase with increasing inner conductor radius; however, the rate of increase is dependent on the sample composition 127

4.13 (a) Relative permittivity, (b) conductivity, (c) S_{11} magnitude and (d) S_{11} phase of the materials constituting the four samples within the second simulation set: Teflon, fat, gland and saline. The relative permittivity (a) and conductivity (b) traces were obtained from the conversion of the S_{11} magnitude (c) and S_{11} phase (d) obtained from the simulations reproducing the interaction of the probe CP1 with each of the four materials, in isolation. As illustrated in (c) and (d), the S_{11} magnitude of Teflon and fat is close to 1, and the S_{11} phase of Teflon and fat is close to 0. Such values reflect the high impedance mismatch between the probe and Teflon, and the probe and fat 129

4.14 Sensing radius vs. inner conductor radius for the scenario S4, where both a and c are increased with b . The regression lines fitting the sensing radius data, with parameters reported in Table 4.13, show the same trend for different samples. Solid and dash-dotted lines are the fitted lines for saline and Teflon samples and for breast fat and gland samples, respectively, while the data is indicated with stars 130

4.15 Regression lines (solid for saline and Teflon samples and dash-dotted for breast fat and gland samples) fitting the sensing radius data (stars) obtained for different insulator widths. The data refers to the scenario S2, where c and thus b are increased. The lines, with parameters reported in Table 4.14, show the same trend across all samples 131

4.16 Sensing radius vs. inner conductor radius for the scenario S3, where b is kept constant while a increases and c decreases. The data is interpolated with second degree polynomials, with parameters reported in Table 4.15. Solid and dash-dotted lines are the fitted polynomials for saline and Teflon samples and for breast fat and gland samples, respectively, while the data is indicated with stars 132

4.17 Contour plot of the electric field magnitude (V/m) at 4 GHz of the simulated probes (a) CP8 and (b) CP4 in contact with Teflon surrounded by saline. In the simulations, a simplified 2D axis-symmetric model was used and, in both plots, radial and axial distances are shown in mm horizontally and vertically, respectively. In both plots, to the right of the symmetry axis ($x = 0$), is the half cross-section of the probe tip and the interrogated sample (Teflon). The electric field isolines are marked, with the last isoline referring to the location where the electric field decays 40 dB. The two probes CP8 and CP4 both have the inner radius of the outer conductor equal to 1.5 mm, but different inner conductor radii and insulator widths, which affect the electric field magnitude such that it is higher in (b) than (a) at the radial distance of 1.5 mm. Also, in (a), the last isoline includes a smaller geometrical region than the region delineated by the last isoline in (b), thus suggesting that the inner conductor radius has higher impact than the insulator width on the sensing radius 133

4.18 3D plot of the average sensing radii (i.e., sensing radii averaged across frequency) from all simulation scenarios vs. the average relative permittivities (i.e., relative permittivities averaged across frequency) of the inner and outer tissues constituting each concentric sample. Two different clusters were identified: the cluster including samples composed of an inner tissue with relative permittivity lower than that of the outer tissue is indicated in blue, and the cluster of samples composed of an inner tissue with relative permittivity higher than that of the outer tissue is indicated in red 136

4.19 Sensing radius vs. contrast in relative permittivity for the two clusters identified in Fig. 4.18: the blue cluster consisting of the samples with an inner tissue having lower relative permittivity, and the red cluster consisting of the samples with an inner tissue having higher relative permittivity. The plot also shows the linear polynomials interpolating the two data subsets (with solid lines). Specifically, the blue line is defined by Eq. (4.8), with an RMSE of 0.0764 between data and polynomial, and the red line is defined by Eq. (4.9), with an RMSE of 0.0918 138

4.20 Plot of the average sensing radius vs. average relative permittivity of the inner tissue for scenarios consisting of samples having the same outer tissue, i.e., muscle, but different inner tissues (included within the category C1). The average relative permittivity of muscle (50.8) is marked with a grey vertical line in the plot and separates the data into two clusters: on the left, in blue, the cluster including samples composed of an inner tissue with relative permittivity lower than that of muscle, and, on the right, in red, the cluster of samples composed of an inner tissue with relative permittivity higher than that of muscle. The data from the two clusters show different trends. To better define the trends, the two data subsets are interpolated with second degree polynomials, which are defined by Eq. (4.10) and Eq. (4.11) for the blue and red curves, respectively. The RMSE calculated between the data and the fitted polynomials is 0.0248 for the blue cluster and 0.0339 for the red cluster. From both trends, it is clear that the sensing radius is lower when the average relative permittivity of the inner tissue is closer to that of muscle 140

4.21 Sensing radius vs. outer tissue relative permittivity for two clusters corresponding to the category C2 of samples having the same inner tissue, but different outer tissues. The data in blue refers to samples having fat as inner tissue with a range of other tissues as outer tissue, and the data in red refers to samples having lymph node as inner tissue with a range of other outer tissues. The two clusters have different trends, since in one case, fat has an average relative permittivity lower than that of all the outer tissues, and in the other case, lymph node has an average relative permittivity higher than that of all the outer tissues. The blue and red data clusters are interpolated with linear polynomials defined by Eq. (4.12) and Eq. (4.13), respectively. Furthermore, the RMSE is 0.0105 and 0.0868 for the clusters from samples with fat as inner tissue and lymph node as inner tissue, respectively 141

4.22 Sensing radius vs. relative permittivity contrast for the two clusters illustrated in Fig. 4.21. For both clusters, the sensing radius increases with the contrast in relative permittivity. The blue and red data clusters are interpolated with linear polynomials defined by Eq. (4.14) and Eq. (4.15), respectively. Furthermore, the RMSE is 0.0161 and 0.0942 for the clusters from samples with fat as inner tissue and lymph node as inner tissue, respectively 143

4.23 Sensing radius vs. inner tissue relative permittivity for three couplets of datasets corresponding to the category of samples C3, having same tissues but with the locations swapped. The two tissues from each couplet have different percent contrasts in relative permittivity, which are reported in the legend. The data in blue is from the sample composed of fat and lymph node, the data in red is from the sample composed of pancreas and muscle, and the data in green is from the sample composed of brain and lymph node. In each couplet, the lowest sensing radius corresponds to the case of the lower permittivity tissue occupying the inner region of the concentric sample 144

4.24 Plot comparing the sensing radius data predicted by the first set of linear regression and neural network (estimates) with the sensing radius data obtained numerically from the second simulation set (targets). The testing data obtained from the linear regression is indicated in blue and the testing data from the neural network is indicated in red. The dashed black line, which is obtained by matching the estimates with the targets, facilitates the data comparison and illustrates that the neural network is more accurate than the linear regression at predicting the sensing radius 147

4.25 Plot comparing the sensing radius data predicted, for the Keysight slim form probe, by the second set of linear regression and neural network (estimates) with the sensing radius data obtained numerically from the third simulation set (targets). The testing data obtained from the linear regression is indicated in green and the testing data from the neural network is indicated in yellow. The dashed black line, which indicates the ideal match between the estimates and the targets, facilitates data comparison and illustrates that the neural network is more accurate than the linear regression at predicting the sensing radius 150

5.1 Set-up for the measurement scenario used to evaluate how radial heterogeneities in linear configuration impact the measured dielectric properties. In the picture, the probe is positioned on sample L2 at the interface between Phantom A and saline. Phantom A is the low permittivity rubber-based phantom and was attached to the bottom of the plastic box using double-sided tape. The probe position on the sample was controlled, radially, by the calliper attached to the right extremity of the box and, longitudinally, by the lift table 160

5.2 (a) Side view picture and (b) top view diagram of the measurement scenario used to evaluate how radial heterogeneities in linear configuration impact the measured dielectric properties. In the photograph, the probe is positioned on sample L1 at the interface between Phantom A and Phantom B. In the diagram, the red bordered circles represent the probe and the two sample materials are represented with the colours yellow and blue. Measurements were performed at the material interface and at different distances from the interface (from -10 mm to +10 mm) 161

5.3 Example of measurement sample used to estimate the contribution of side-by-side tissues to the measured permittivity. The picture illustrates Sample L4, a porcine sample consisting of side-by-side fat and muscle tissues. In the figure, the probe is positioned on the fat-muscle interface, where both fat and muscle tissues occupy approximately 50% of the sensing volume 162

5.4 Example of measurement sample used to estimate the contribution of concentric tissues to the measured permittivity. The picture illustrates Sample C5, a concentrically heterogeneous porcine sample having muscle as the inner tissue and fat as the outer tissue. The size of the inner muscle tissue is highlighted in the picture with reference to the diameter of the slim form probe (2.2 mm) 165

5.5 (a) Side view picture and (b) top view diagram of the measurement scenario used to evaluate how radial heterogeneities in concentric configuration impact the measured dielectric properties. In the photograph, the probe is positioned on Sample C3, consisting of the 0.75 mm radius PLA cylinder immersed in saline. In the diagram, the red bordered circle represents the probe and the two sample materials are represented with the colours yellow and blue. The inner material (in blue) has a radius ranging from 0.25 to 1 mm, and the outer material (in yellow) extends outside of this extent 165

5.6 2D axially symmetric model designed to evaluate the dielectric contribution of concentric materials to the acquired signal. Different values were used for the radius of the inner material and dielectric properties were assigned to the inner and outer materials of each simulated concentrically heterogeneous sample 168

5.7 3D simulation model designed to evaluate the dielectric contribution of side-by-side materials from the simulated Samples L1 and L4. In the diagram, the probe is positioned at the material interface (exactly in the middle of the sample). However, for each sample, different probe positions with distances between 0-10 mm from the interface were considered in order to estimate the radial distance at which only the dielectric properties of one material are detected (i.e., the radial distance at which the effect of the other material ceases) 169

5.8 Flowchart summarising the experimental and numerical steps taken to estimate the material/tissue contribution within radially heterogeneous samples (consisting of two side-by-side or concentric materials/tissues). In case of mismatch between simulated and measured data, the measurements were repeated by monitoring all the confounders and by minimising the sources of error 171

5.9 Relative permittivity traces from (a) measurements and (b) simulations performed over the range of 2-6 GHz on Sample L1, composed of a linear configuration of Phantom A (left material) and Phantom B (right material). Both measurements and simulations were performed with the probe positioned over small increments in distance from the low permittivity (Phantom A) to the high permittivity phantom (Phantom B). The distances, reported in the legend, are negative if the probe is positioned on the left material (Phantom A), and positive if the probe is positioned on the right material (Phantom B). The traces from acquisitions performed at distances ± 1.1 mm between the probe centre and the interface are dashed. The thick yellow solid trace is from the measurement/simulation performed with the probe centre lined up with the phantom interface, and is overlapped by the relative permittivity trace obtained by averaging the relative permittivity values of Phantom A and Phantom B (indicated with a green dash-dotted line). While in (a) all the measurement traces are reported, in (b), the simulation data obtained at the intermediate distances between 1.1 mm and 10 mm are not illustrated, since this data overlaps with the 1.1 mm and 10 mm distance data, and thus does not provide additional information 175

5.10 Relative permittivity and conductivity plots from the measurements (a-b) and simulations (c-d) performed on Sample L4. In all plots, the average data from muscle is reported with a blue solid line, the average data from fat with a red solid line, and the average data from the fat-muscle interface with a thick yellow line. Furthermore, across all the plots, the data acquired at the interface is compared with the data estimated by averaging the fat and muscle data (indicated with a green dash-dotted line). The permittivity values from the fat-muscle interface are halfway between the permittivity values of fat and muscle tissues and within 10% of the permittivity values calculated by averaging the fat and muscle permittivity 177

5.11 Plot of the relative permittivity mean, minimum and maximum values calculated across three measurements, each on 100% Teflon, 100% saline, and the concentrically heterogeneous sample consisting of 29% saline and 71% Teflon (Sample C1). The relative permittivity from Sample C1 is between that of Teflon and saline and overlaps with the permittivity estimated based on the material composition within the sensing radius 179

5.12 Plot of the relative permittivity mean, minimum and maximum values calculated across three measurements, each on 100% Teflon, 100% saline, and the concentrically heterogeneous sample consisting of 46% PLA and 54% saline (Sample C3). The relative permittivity from Sample C3 is close to that of PLA but 63% different from the relative permittivity estimated based on the material composition within the sensing radius 180

5.13 Plot of the relative permittivity values obtained from simulations performed with the following samples: 100% Teflon, 100% saline, 29% saline 71% Teflon (Sample C1), 46% Teflon 54% saline (Sample C3, with Teflon replacing PLA). The relative permittivity traces from Samples C1 and C3 (plotted with yellow solid and dashed lines, respectively) are compared with the relative permittivity traces estimated based on the material composition within the sensing radius of Sample C1 and C3 (plotted with green solid and dashed lines, respectively). While, for Sample C1, the estimated relative permittivity trace is about 40% different from the simulated relative permittivity, for Sample C3, the estimated relative permittivity trace is about 50% different from the simulated relative permittivity, which is approximately equal to the relative permittivity of Teflon 181

5.14 Average relative permittivity calculated across five measurements on muscle, fat, Samples C5, which consist of inner muscle tissue having radii ranging from 0.5 to 0.9 mm surrounded by fat tissue (indicated with a violet dashed line), and Samples C6, which consist of inner fat tissue having radii ranging from 0.5 to 0.9 mm surrounded by muscle tissue (indicated with a yellow dashed line). The permittivity values obtained from Samples C5 are within 15% of the permittivity values obtained from muscle tissue. On the other hand, the permittivity values obtained from Samples C6 are within 10% of the permittivity values obtained from fat tissue 183

5.15 Relative permittivity obtained from 2D simulations of muscle, fat, and two 50% muscle and 50% fat tissue concentric samples, one with muscle as the inner tissue and fat as the outer tissue (indicated with an orange dashed line), and the other one with fat as the inner tissue and muscle as the outer tissue (indicated with a light blue dashed line). The relative permittivity from the simulated 50% fat and 50% muscle tissue concentric samples are significantly different from the relative permittivity values obtained by averaging the simulated fat and muscle permittivity 184

5.16 Relative permittivity traces obtained from simulations conducted on Sample S2 in linear configuration. Each trace corresponds to a specific location of the centre of the probe with respect to the tissue interface, which is indicated in the legend. Specifically, the distances are negative when the probe was mostly in contact with the left tissue (fat), and positive when the probe was mostly in contact with the right tissue (muscle). The reported traces are symmetric with respect to the trace of the fat-muscle interface, thus indicating that the two tissues have equal contribution to the dielectric signal 186

5.17 Dielectric weights of muscle (Tissue 2, on the right) for Sample S2 in linear configuration obtained at the single frequencies of 2 GHz and 6 GHz as a function of the probe distance from the tissue interface. The dielectric weights obtained at 2 GHz (indicated in blue) are approximately equivalent to the dielectric weights obtained at 6 GHz (indicated in red). Due to the fact that the two Richards functions fitting the two sets of data, at 2 GHz and 6 GHz, overlap, the dielectric weight can be generally represented by the function expressed in Eq. (5.10) 187

5.18 Relative permittivity traces obtained from simulations conducted on (a) Sample S1 and (b) Sample S2 in concentric configuration. Both samples consists of the same tissues, fat and muscle, but with swapped location. Specifically, Sample S1 has muscle as the inner tissue and fat as the outer tissue and Sample S2 has fat as the inner tissue and muscle as the outer tissue. In both plots, each trace corresponds to a specific radius of the inner tissue. By comparing the relative permittivity traces from (a) and (b), it can be observed that the traces of (b) tend to the trace of the inner tissue (fat, in this case) considerably faster than how the traces of (a) tend to the trace of the inner tissue (muscle, in this case). In fact, the dielectric trace corresponding to the inner tissue radius of 0.40 mm (reported with a dark red solid line) is half way between muscle and fat in (a) and closer to fat in (b) . 189

5.19 Dielectric weights of muscle (in blue) and fat (in red) for Sample S1 and Sample S2 in concentric configuration, respectively. The dielectric weights and the corresponding fitted Richards curves (parameters of which are reported in Table 5.5) are valid for any single frequency between 2-6 GHz. The two Richards curves fitted to the two sets of data from Sample S1 and Sample S2 highlight that the dielectric weights of fat increases faster than the weights of muscle, thus confirming that tissues with a lower permittivity has a greater dielectric impact than tissues with a higher permittivity 190

5.20 Model weights for the inner tissue obtained for all concentric samples, for frequencies between 2 and 6 GHz. The dielectric weights of the inner tissues are modelled with Richards curves, with corresponding parameters provided in Table 5.5 191

6.1 Example of ovine kidney sample, where the medulla region is easily distinguishable from the cortex region 196

6.2 Example of porcine muscle sample, where the fat tissue is easily distinguishable from the muscle tissue 196

6.3 Mammary fat pad sample, where the fat tissue region is easily distinguishable from the cancerous region 197

6.4 Post-measurement marking on an ovine kidney sample for identifying the measurement sites during the histological analysis . . 199

List of Figures

6.5 Sample illustrated in Fig. 6.4 after undergoing fixation in 10% w/v formalin solution. Two green stitches can be observed beside the measurement sites across the heterogeneous regions of the sample. The stitches were not inserted over the measurement sites in order to avoid tissue damage in the region of interest. Furthermore, the sample is placed into a cassette to be inserted into the tissue processor. The cassette was labelled with the unique identifier, i.e. LK7M 26-11, written in the pencil since graphite is resistant to all chemicals used by the tissue processor 200

6.6 Summary of the haematoxylin and eosin (H&E) staining protocol, consisting of different steps, from the slice re-hydration to the staining and dehydration 202

6.7 Photographs depicting the change in the size of a side of a porcine muscle sample (Sample PM1 in Table 6.2) through the traditional histology process, from (a) pre-fixation to (c) post-processing . . 206

6.8 Ovine muscle sample that was excluded from histology after being damaged in the tissue processor 207

6.9 Porcine muscle sample that was excluded from histology, since the tissues constituting the sample were too fibrous and crumbled during slicing with the microtome 207

6.10 (a) Post-fixation picture, (b) post-processing picture and (c) 5 μm thick histological slice of Sample PM1 (reported in Table 6.2) used to support the dielectric data acquired to validate the sensing radius findings of Chapter 4. The five marked measurement sites in (a) are faded in (b). Among the five measurement sites, one is from muscle, two from fat (from smaller and larger regions), and two from concentrically heterogeneous regions. The slice in (c) was obtained at the depth of 0.3 mm and is representative of the whole sample consisting of muscle tissue (which appears in pink due to the eosin staining) and fat tissue (which appears in white since the H&E staining cannot perfuse through hydrophobic tissues) 209

6.11 5 μm thick histological slice of Sample PM1 used to support the dielectric data acquired to validate the sensing radius findings of Chapter 4. On the histological slice, the change in size of the small fat region is highlighted. Specifically, before fixation, the small fat region had a diameter of approximately 2.2 mm (which is the diameter of the probe). After processing, the diameter of the same region was 1 mm. This change in size suggests a fat tissue shrinkage of approximately 50% 210

- 6.12 (a) Relative permittivity and (b) conductivity traces from three measurements performed on Sample PM1 to validate the sensing radius findings of Chapter 4. Among the three measurements, one measurement was performed on muscle, one measurement on a larger fat region (approximately two-three times larger than the probe) and one measurement on a smaller fat region (approximately as large as the probe). A difference of less than 5% was found between the measurements performed on the two fat regions, thus suggesting that the sensing radius for fat is within the size of the probe. In addition, in both (a) and (b), the bovine muscle and fat data by Gabriel *et al.* [46] is reported. Consistent differences of approximately 20% were found between measurement and reference relative permittivity data, which can be attributed to biological variability between and within animals, different tissue handling procedures and temperature variations 211
- 6.13 (a) Post-fixation picture and (b) 5 μm thick histological slice of a kidney sample used to support the dielectric data acquired to validate the sensing radius findings of Chapter 4. Four measurement sites are marked in (a): one faded on the medulla and three on the cortex. Among the three measurement sites on the cortex, the point that is less than 1 mm distant from the medulla was further marked with a green stitch, which is highlighted in (a). The extremities of the green stitch can be observed in (b) on the 5 μm histology slice that was obtained at the depth of 0.1 mm. This slice is representative of the whole sample, which was confirmed to have only radial heterogeneities. In (b), the medulla (which appears in the top right portion of the image) is not easily distinguishable from the cortex 212
- 6.14 5 μm histological slice of the kidney sample in Fig. 6.13 used to support the dielectric data acquired to validate the sensing radius findings of Chapter 4. On the histological slice, the medulla and the measurement point marked with the stitch are highlighted, in order to facilitate the correspondence between dielectric data and histological information. The measurement point was identified by considering the location of the probe (which has a diameter of 2.2 mm) and the distance of the measurement point from the stitch 213

- 6.15 (a) Relative permittivity and (b) conductivity traces from three measurements performed on the kidney sample in Fig. 6.13 to validate the sensing radius findings of Chapter 4. Among the three measurements, one measurement was performed on the medulla, one measurement on the cortex far from the medulla and one measurement on the cortex close to the medulla. A difference of less than 1% was found between the measurements performed on the two cortex regions, thus suggesting that the sensing radius for cortex is within 2.1 mm (i.e., the radius of the probe which is 1.1 mm + the distance of the measurement point from the medulla which was 1 mm). In addition, in both (a) and (b), the porcine cortex and medulla data from Salahuddin *et al.* [133] is reported. The measurement data is in agreement with the reference data, since only differences within the tissue measurement uncertainty (less than 5%) were found between measurement and reference data 214
- 6.16 (a) Post-fixation picture, (b) post-processing picture and (c) 10 μm histological slice of Sample LK2 (reported in Table 6.2) used to support the dielectric data acquired to validate the dielectric contribution findings of Chapter 5. Among the four marked measurement sites in (a), two are from the medulla, two from the cortex (with one point closer to the medulla than the other) and one is at the cortex-medulla interface. The two measurement sites at/closer to the interface were further marked with green stitches, since the marks faded away during sample processing, as is clear in (b). In (c), the extremities of the green stitch marking the measurement point at the interface between the cortex and medulla are highlighted, since this point is used to validate the dielectric contribution findings of two side-by-side tissues. The slice in (c) is representative of the whole sample, which was found to have only radial heterogeneities. In (c), the 10 μm slice allows for the distinction of the medulla (which appears more blue than pink) from the cortex (which appears mostly pink) 215

- 6.17 10 μm histological slice of Sample LK2 used to support the dielectric data acquired to validate the dielectric contribution findings of Chapter 5. On the histological slice, the medulla and the measurement point at the cortex-medulla interface (marked with the stitch) are highlighted, in order to facilitate the correspondence between dielectric data and histological information. The measurement point was identified by considering the location of the probe (which has a diameter of 2.2 mm) and the distance of the measurement point from the stitch 216
- 6.18 (a) Relative permittivity and (b) conductivity traces from three measurements performed on Sample LK2 to validate the findings (in Chapter 5) regarding the dielectric contribution of side-by-side tissues. Among the three measurements, one measurement was performed on the medulla, one measurement on the cortex (far from the medulla) and one measurement at the cortex-medulla interface. The data from the cortex-medulla interface is comparable with the estimated data obtained by averaging the data from the cortex and medulla, thus suggesting that the cortex and medulla had equal dielectric contribution to the dielectric signal acquired at the interface. In addition, in both (a) and (b), the porcine cortex and medulla data from Salahuddin *et al.* [133] is reported. The measured cortex and medulla data was consistently different from the reference data due to tissue dehydration, different tissue handling procedures and temperature variations 217
- 6.19 5 μm histological slice of Sample PM1, where the two concentrically heterogeneous measurement points are highlighted with the aim of validating the findings (in Chapter 5) regarding the dielectric contribution of concentric tissues. However, the morphology of the two concentrically heterogeneous measurement sites changed during the traditional histology procedure, making the interpretation of the dielectric data in Fig. 6.20 difficult . . . 218

6.20	(a) Relative permittivity and (b) conductivity traces from four measurements performed on Sample PM1 to validate the findings (in Chapter 5) regarding the dielectric contribution of concentric tissues. Among the four measurements, one measurement was performed on muscle, one measurement on fat and two measurements on concentrically heterogeneous tissue consisting of muscle surrounded by concentric fat. Due to the morphology change of Sample PM1 during traditional histology, it was not possible to associate the dielectric traces from the concentrically heterogeneous points with the histological information reported in Fig. 6.19	219
6.21	MicroCT scan obtained at 0.5 μm depth from the surface of an ovine muscle sample. From the image, it is easy to distinguish the muscle tissue, visualised in white, from the fat tissue, visualised in black, since the contrast agent (Lugol's iodine) is able to perfuse through muscle but not through fat	220
6.22	MicroCT scan obtained at 0.5 mm depth from the surface of a rodent kidney sample. From the image, it is easy to distinguish the cortex region from the medulla region, since the cortex region is brighter than the medulla region. For ease of visualisation, the medulla region is contoured by a red solid line	221
6.23	Relative permittivity and (b) conductivity traces from three measurement regions of the mammary fat pad, to validate the applicability of the findings of Chapter 4 and Chapter 5 to highly heterogeneous biological samples. The three measurement regions include a mostly cancerous breast region, a mostly fatty region and two points at the interface between the two regions. In addition, in both (a) and (b), the human breast cancerous and fat tissue data from Lazebnik <i>et al.</i> [11] is reported as reference. While the average measured cancerous tissue data is close to the reference data, the average measured fatty tissue data is notably different. The considerable differences (above 80%) between measurement and reference data for the fatty tissue region suggest that the mostly fatty tissue may have presented inclusions of cancerous tissue	222

6.24 MicroCT scan obtained at 0.3 mm depth from the surface of the mammary fat pad. The heterogeneity visible in the image is representative of that of the whole sample, and illustrates the tissue structure of the mammary fat pad, which includes a heterogeneous mixture of tumour, fat and blood vessels (bright spots). The microCT scan supports the interpretation of the dielectric traces in Fig. 6.23 223

6.25 5 μm histological slice obtained at 0.3 mm depth from the surface from the mammary fat pad. Together with the microCT scan in Fig. 6.24, the histological slice including a heterogeneous mixture of tumour, fat and blood vessels (bright spots), supports the interpretation of the dielectric traces in Fig. 6.23. The contours of the histological slice appear slightly different from the contours of the sample imaged by microCT. These changes are due to the orientation of the sample immersed in Lugol's iodine that was not parallel to the bottom of the sample holder during the microCT scan 223

6.26 3D reconstruction of the mammary fat pad from the microCT scans (a 2D slice of which is reported in Fig. 6.24). The reconstruction shows that the sample immersed in Lugol's iodine during the scan was not parallel to the bottom of the sample holder. This suggest that the orientation of the scanned sample needs to be taken into account when associating the measured dielectric data with the tissue structure reconstructed from the microCT scans 224

List of Tables

2.1	Use of the commercial probes in recent works. Studies involving breast tissues are shaded in grey. The others involve liver tissues, apart from the porcine skin study conducted by Karacolak <i>et al.</i> [114]	34
3.1	The standard calibration process with confounders and compensation techniques listed for each step, with open-circuit, short-circuit, and a liquid load material shown as the three calibration standards	51
3.2	Reference liquid properties, available models, and storage and handling procedures (where f =frequency, T =temperature) . . .	59
3.4	Example of the calculation of standard individual, combined and extended uncertainties for relative permittivity measured on 0.1 M NaCl in the frequency range 300 MHz–10 GHz in the study conducted by Peyman <i>et al.</i> [47]. The nomenclature and methodology follow the guidelines defined by the National Institute of Standards and Technology (NIST) [131]. The calculation was performed at each measurement frequency and averaged across the frequency range	61
4.1	Summary of sensing depth investigations in the literature	92
4.2	Summary of sensing radius investigations in the literature . . .	93
4.3	Calculation of standard uncertainty for relative permittivity measured on 0.1 M NaCl in the frequency range 0.5–10 GHz. The nomenclature and methodology follow the guidelines defined by the NIST [131], as reported in Section 3.1.3. The calculation was performed at each measurement frequency and averaged across the frequency range. The uncertainty in accuracy is calculated by considering the model by Peyman <i>et al.</i> [146] as reference data	100

4.4	Standard uncertainty for 0.1 M NaCl in terms of both relative permittivity and conductivity across the entire measurement frequency range, divided in two frequency subranges, 0.5-10 GHz and 10-20 GHz	100
4.5	Standard uncertainty in accuracy for the three alcohols, methanol, ethanediol and 1-butanol across the frequency range of 0.5-5 GHz. The uncertainty values are reported for the subrange of frequencies 0.5-5 GHz, since such values were obtained by comparing the measured average data with the models reported in Gregory <i>et al.</i> [145], which are from traceable data but only available up to 5 GHz	102
4.6	Dimensions of the three Keysight probes: a , b , c and r refer to the probe dimensions illustrated in Fig. 4.6	106
4.7	Summary of the three simulation sets	113
4.8	One-pole Cole-Cole parameters for simulated saline and Teflon .	114
4.9	List of probe dimension combinations (CP1,..,CP12) grouped in four subsets (S1,..,S4). a , b and c refer to probe features in Fig. 4.6. Each probe has an outer conductor of 1 mm width . .	115
4.10	Modelled concentric materials with their contrast in relative permittivity. The average relative permittivity values of the materials across the range 2–6 GHz are specified in brackets . .	116
4.11	Schematic information regarding the three categories of samples included within the third simulation set (indicated in Table 4.7)	121
4.12	Parameters, R^2 value and RMSE of the regression lines in Fig. 4.12	126
4.13	Parameters, R^2 value and RMSE of the regression lines in Fig. 4.14	129
4.14	Parameters, R^2 value and RMSE of the regression lines in Fig. 4.15	130
4.15	Parameters and RMSE of the second degree polynomial curves in Fig. 4.16	133
5.1	Summary of heterogeneous samples measured in linear configuration. The average relative permittivity values of the materials/tissues across the range 2-6 GHz are specified in brackets . .	159
5.2	Summary of heterogeneous samples measured in linear configuration. The average relative permittivity values of the materials/tissues across the range 2-6 GHz are specified in brackets . .	164
5.3	Debye parameters to simulate radially heterogeneous samples, each consisting of two of the following materials: Phantom A, Phantom B, porcine muscle and fat	170
5.4	Summary of simulated samples in linear and concentric heterogeneity configurations. The average relative permittivity values of the tissues across the range 2-6 GHz are specified in brackets	173

List of Tables

5.5 Best fit parameters and root mean square error for the dielectric weights of the inner tissue for all six concentric samples S1-S6 . 190

6.1 Summary of the tissue samples analysed in three different studies, each having a different aim 198

6.2 Change in size for a subset of radially heterogeneous samples during traditional histology, from pre-fixation to post-processing. All samples were fixed for 3 days, except for Sample PM3 which was fixed for 2 days 205

Acronyms

CT	Computed Tomography. 5, 7
DI	deionised. 52, 54, 57, 58, 95
DMSO	dimethyl sulphoxide. 57, 58
EIT	Electrical Impedance Tomography. 1
EM	Electromagnetic. 1, 2, 3, 14, 18, 23, 24, 94
FEM	finite element method. 112
GA	genetic algorithm. 74
H&E	haematoxylin and eosin. xxiii, 201, 208, 209
HT	Hyperthermia. 1
I₂	iodine. 203
IFBW	intermediate frequency bandwidth. 98
KI	potassium iodide. 203
MRI	Magnetic Resonance Imaging. 1
MSE	mean squared error. 123
MUMPS	multifrontal massively parallel sparse direct solver. 119
MW	Microwave. 2, 3, 8, 9, 13, 15, 18, 19, 21, 36, 38, 46, 48, 56, 57, 58, 64, 65, 68, 70, 71, 74, 78, 81, 94, 154
MWA	Microwave Ablation. 1
MWI	Microwave Imaging. 1, 35, 37
NIST	National Institute of Standards and Technology. xxix, 19, 38, 58, 61, 60, 100
NRW	Nicolson-Ross-Weir. 19
OsO₄	osmium tetroxide. 203
PLA	polylactic acid. 163

ACRONYMS

PMA	phosphomolybdic acid. 203
PSO	particle swarm optimisation. 74
PTA	phosphotungstic acid. 203
RFA	Radio Frequency Ablation. 1
RMSE	root mean square error. 75, 126
SAR	Specific Absorption Rate. 1, 2
TEM	Transversal Electro-Magnetic. vii, 24, 23
VNA	Vector Network Analyser. vii, 19, 21, 22, 23, 24

Introduction

The interaction of Electromagnetic (EM) fields with the human body is dependent on the inherent dielectric properties of each tissue. Based on these properties, EM waves are transmitted, absorbed, and reflected by biological tissues in different ratios. Accurate knowledge of these properties is crucial for dosimetry (safety) calculations and for medical diagnostic, monitoring, and therapeutic technologies.

The dielectric properties of tissues can be incorporated into highly accurate computational and physical models, and the generated preliminary data can be used to assess the technical risk, efficacy, and safety of the medical device or treatment. For instance, numerical models based on tissue dielectric parameters are used to calculate the Specific Absorption Rate (SAR) in biological tissues. SAR levels are regularly calculated to validate the safety of many medical technologies, including Magnetic Resonance Imaging (MRI) and implantable devices. Since SAR is a complex function of the dielectric properties of tissue, accurate knowledge of these properties are the foundation upon which SAR safety analysis is built [1], [2]. Furthermore, accurate knowledge of the dielectric properties of biological tissue have prompted the development of a wide range of novel EM diagnostic and therapeutic technologies.

EM diagnostic systems range from the low-frequency Electrical Impedance Tomography (EIT) to higher-frequency Microwave Imaging (MWI). Both of these techniques rely on dielectric contrasts between organs, or contrasts between healthy and diseased tissue. These imaging methods have gained significant academic and commercial interest, since both EIT and MWI are non-invasive and potentially low-cost techniques [3]–[7]. While EIT is now established commercially for lung-function monitoring applications [8], [9], MWI similarly has made considerable progress toward clinical usage in the past two decades, as tissue dielectric properties enable the differentiation of benign and malignant tissues in breast cancer imaging [10]–[15], the monitoring of bladder volume in the treatment of enuresis and urinary incontinence [16], [17], and the detection of stroke in intracranial imaging [18]–[21].

From a therapeutic perspective, knowledge of the relevant dielectric properties are used in the design and optimisation of Hyperthermia (HT) applicators [22]–[24], Radio Frequency Ablation (RFA) [25]–[27] and Microwave Ablation (MWA) systems [28]–[32]. Hyperthermia consists of elevating the temperature of a diseased tissue to just above a normal physiological level in order to sensitise tumour cells, making the cancerous tissue more susceptible to chemotherapy and radiotherapy [33]. Targeted HT has been demonstrated to be particularly effective in the treatment of cervical cancer, breast cancer, cancers of the head and neck and sarcoma in adults [22] and germ cell tumours in young children [24]. In EM-based HT systems, heating is achieved by coherently adding signals at the tumour location. In order to achieve coherent summing of the waves at the appropriate location, knowledge of the wave propagation speed is required, which depends on the dielectric properties of the tissues in the region. Similarly, RFA and MWA are two treatments for liver, kidney, and lung cancer [34], [35]. Both methods cause the direct necrosis of disease, and the relative high frequencies allow for good selectivity in terms of targeting the cancerous tissue while protecting the surrounding healthy tissue [36]. Knowledge of the dielectric properties of tissues in the ablation region are factored into the design of ablation probes, where they are used to optimise the probe antenna efficiency and directivity, along with the size and shape of the ablation zone [37].

Thus, an accurate knowledge of the tissue dielectric properties not only has the potential to improve SAR estimates and reduce undesired tissue heating, but also enhances the detection and localisation of specific tissue types in novel EM-based imaging systems and the targeting of diseased tissues (while preserving surrounding healthy tissues) in therapeutic technologies.

1.1 Motivation

Dielectric properties of biological tissues have been a topic of interest since the 1940s [38]–[41]. In the last decades, due to the increase of emerging Microwave (MW) medical devices, a number of *in vivo* and *ex vivo* studies have been conducted on animal and human tissues [11], [15], [42]–[49]. Several methods have been adopted to measure the dielectric properties of biological tissues in the MW range, including the transmission line, cavity, and open-ended coaxial probe techniques [50]. Among these methods, the coaxial probe technique is the most commonly used in the MW frequency range for tissue characterisation, since it is non-destructive, and allows for *ex vivo* and *in vivo* broadband measurements [11], [30], [31], [42], [46], [47], [51]–[54].

CHAPTER 1. INTRODUCTION

The open-ended coaxial probe measurement technique comprises of a coaxial probe connected to one port of the VNA (Vector Network Analyser) through a cable or an L-shaped connector. Measurements with the open-ended coaxial probe technique consist of placing a coaxial probe in contact with the sample to interrogate dielectrically so that a portion of the EM signal generated from the VNA propagates into the sample and the remaining signal is reflected back to the VNA, based on the characteristics and properties of the sample. From the reflected EM signal, the dielectric properties of the interrogated sample are then obtained.

Although the dielectric measurement process with the open-ended coaxial probe appears straightforward, a number of different factors, or confounders, can affect the dielectric measurement increasing the uncertainty of the acquired data and compromising the data interpretation. Throughout this thesis, the term “confounders” refers to factors that affect the outcome (i.e., the measured dielectric properties) other than the cause (the actual tissue properties). These confounders can be separated into two types: equipment-related and tissue-related confounders. Equipment-related (or system) confounders can be intrinsic to the instrumentation or depend on the calibration procedure and the methods used to verify the quality of the calibration. On the other side, tissue-related confounders depend on the characteristics of the examined sample and the interaction of the sample with the coaxial probe. Examples of tissue-related confounders are: differences between *in vivo* and *ex vivo* samples, tissue handling, tissue dehydration (and then water content differences), tissue temperature change, unsteady probe-tissue contact and tissue heterogeneity.

Due to the high number of confounders involved in the dielectric measurement with a coaxial probe, inconsistent dielectric data has been reported in the literature for several biological tissues, such as fat and lung [55]. For this reason, in the last two decades, a comprehensive uncertainty analysis has been completed and standard techniques have been developed to reduce the effect of equipment-related confounders to the measured data [47], [55]. Also tissue-related confounders, such as tissue temperature change [46], [47], differences between *in vivo* and *ex vivo* measurements [46], [56], characteristics of the animal/individual from which the tissue is excised [47], [56]–[59], moisture content [46], [47], [58], and probe-sample contact [47] have been examined and good benchmarks have been defined to compensate for a subset of these tissue-related confounders. However, inconsistencies in dielectric data can still be found across more recent studies involving the dielectric characterisation of healthy and cancerous breast tissue [10]–[12], [15], [49], [60], [61], thus complicating the design of breast imaging devices, which rely on the dielectric properties of breast tissue [62].

CHAPTER 1. INTRODUCTION

Due to the importance of accurate knowledge of dielectric properties for the design of EM medical technologies and to the increase of emerging MW devices, nowadays, it is vital to reduce uncertainty in dielectric data and particularly over the MW range. To this extent, in this dissertation, a number of dielectric studies are reviewed and compared with the aim of highlighting the main confounders causing uncertainty in dielectric data, and the most effective techniques adopted to compensate for these confounders and reduce data uncertainty. As previously stated by Peyman *et al.* [47], most of the uncertainty is attributed to poor measurement repeatability. Specifically, measurements are less repeatable for heterogeneous biological samples than for homogeneous ones. The low measurement repeatability for heterogeneous samples may be primarily attributed to the high variability of the tissue content across different measurement regions of each sample. Hence, in order to optimise the dielectric characterisation of heterogeneous biological samples, post-measurement histological analysis can be conducted, so that dielectric data can be accurately correlated with the sample tissue content [63]. However, in the literature, there is no consensus on the procedure to accurately correlate the dielectric data with the histological information [63], [64]. For instance, sample heterogeneities have been reported with inconsistent definition and categorisation [10], [11], [15], and different methodologies have been adopted to correlate the dielectric data to the sample histological content [63].

Besides an accurate histological procedure, a rigorous methodology to associate the acquired dielectric data with the sample histological content involves:

- Accurate knowledge of the sensing volume of the probe;
- Accurate knowledge of the dielectric contribution of each tissue occupying the sensing volume.

In particular, accurate knowledge of the sensing volume, which consists of sensing radius and sensing depth, supports an accurate definition of the radial and longitudinal extents of the sample region to analyse histologically, i.e., the histology region [63]. In fact, by matching the size of the histology region with the sensing volume, it is ensured that the histology region contains all the tissue types contributing to the acquired dielectric data. Once the sensing volume is defined, it is essential to know the dielectric weight of each tissue occupying the sensing volume on the acquired signal for an accurate correlation between dielectric data and histological information.

Although several studies have investigated the sensing volume with the aim of improving the correspondence between acquired dielectric data and sample histological content [63], [65], [66], there are still a number of unanswered research questions regarding the sensing radius and the

CHAPTER 1. INTRODUCTION

procedure to correlate the dielectric data to the histological information. The unanswered research questions can be grouped in the following categories.

1. What are the factors to consider for the calculation of the sensing radius? For instance, how does the sensing radius vary with the dimensions of the probe? Does the sensing radius depend also on the dielectric properties of the investigated tissue?
2. What are the factors to consider for an accurate quantification of the dielectric contribution of a tissue to the acquired data? For instance, how does the tissue structure impact the tissue dielectric contribution? Within the same tissue structures, do tissues have different dielectric contributions according to the dielectric properties of each?
3. If the sensing volume and the dielectric contribution of each tissue within the sensing volume are well defined, what are the challenges involving the correlation between dielectric data and histological information? How can such challenges be addressed?

These unanswered questions motivate the following research objectives of this thesis:

1. Evaluating and modelling the dependence of the sensing radius on the dimensions of the probe and on the dielectric properties of the investigated tissue;
2. Evaluating how the volume occupied by a tissue (within the sensing volume), the tissue location and the tissue dielectric properties impact the tissue dielectric contribution to the acquired data;
3. Evaluating further challenges regarding the correlation between dielectric data and histological information by conducting post-measurement histological analysis and identifying novel techniques to overcome such challenges.

The first two research objectives listed above are achieved by conducting a number of custom dielectric measurements and numerical simulations involving several probes having different geometry and dimensions, and a variety of heterogeneous tissue-mimicking materials and biological tissues. Secondly, the last research objective is achieved by conducting histological analysis of a subset of heterogeneous biological samples previously characterised dielectrically. Finally, due to the numerous challenges involving the correlation between dielectric data and histology images, microComputed Tomography (CT) is proposed as alternative technique to support dielectric characterisation of heterogeneous biological samples.

The specific research contribution of this thesis are summarised in the following sections, including journal and conference publications arising from these contributions.

1.2 Thesis contributions

Significant contributions are presented in the chapters of this thesis addressing the challenges regarding accurate dielectric characterisation of heterogeneous biological tissue samples. The specific novel contributions of this thesis are as follows:

- Open-ended coaxial probe measurement protocol and meta-data analysis;
- Sensing radius analysis and modelling;
- Sample tissue dielectric contribution analysis and modelling;
- Sample tissue dielectric characterisation through histology.

Open-ended coaxial probe measurement protocol and meta-data analysis

The main steps of the open-ended coaxial probe measurement protocol are: calibration, validation, sample handling, sample dielectric measurement and sample post-processing. Each step of the measurement protocol is reviewed in Chapter 3 to investigate common practices, challenges, and techniques for controlling and/or compensating for confounders. This investigation highlights the importance of reporting the meta-data corresponding to each step of the measurement protocol to support the interpretation of the measured dielectric properties. For instance, the meta-data for the calibration and validation steps include calibration settings and calibration and validation materials. The meta-data for the remaining steps include measurement time from excision, sample temperature and sample tissue content. In particular, the meta-data regarding the sample tissue content may come from post-measurement histology, which is required for the interpretation of the dielectric properties from heterogeneous samples. In fact, histology enables identification of the constituent tissue types in the sample that may have contributed to the acquired dielectric properties. The importance of histology for an accurate dielectric characterisation of heterogeneous tissues is highlighted in the last section of Chapter 3.

Furthermore, the minimum information required for an exhaustive interpretation of the acquired data resulted in the design of a database relating tissue dielectric data to the correspondent meta-data.

Sensing radius analysis and modelling

Knowledge of the sensing depth and sensing radius of the measurement probe supports the dielectric characterisation of heterogeneous tissues. In the literature, extensive studies have been conducted to investigate the sensing

depth. On the other hand, the sensing radius has been analysed in selected scenarios with limited number of probes and tissue-mimicking materials. Therefore, in Chapter 4, the sensing radius is examined both numerically and experimentally with a range of probes of different dimensions and a wide variety of materials including biological tissues. In particular, for the quantitative estimation of the sensing radius, concentric samples are used, in the same way as layered samples have been used in the literature for the estimation of the sensing depth. Then, the sensing radius values obtained from a set of probes and interrogated concentric samples are used to develop linear regression and neural network models. These mathematical models enable prediction of the sensing radius from knowledge of the probe dimensions and the dielectric properties of the interrogated sample. Thus, the developed models presented in Chapter 4 support accurate quantitative estimation of the sensing radius, which enhances the interpretation of the dielectric properties measured from heterogeneous samples.

Sample tissue dielectric contribution analysis and modelling

For an accurate dielectric characterisation of highly heterogeneous biological tissues, knowledge of the sensing volume needs to be accompanied by knowledge of the dielectric contribution of each tissue constituting the sensing volume. In past studies, the dielectric contribution of layered materials within the sensing depth has been thoroughly examined. Conversely, there are no quantitative studies in the literature investigating the dielectric contribution of radially heterogeneous materials within the sensing radius. To this extent, Chapter 5 presents both dielectric measurements and numerical simulations performed on several well-controlled radially heterogeneous samples. Across all the measured and simulated sample, the dielectric contribution of the tissues within the sensing volume is quantitatively estimated and modelled. The models described in Chapter 5 enable prediction of the sample dielectric properties from *a priori* information regarding the structure, the location and the dielectric properties of each constituent tissue. Thus, the analysis and modelling of the tissue dielectric contribution within the sensing volume further improves the dielectric characterisation of heterogeneous samples.

Sample tissue dielectric characterisation through histology

Further challenges in the dielectric characterisation of heterogeneous samples are investigated in Chapter 6. These challenges involve the correlation of the measured dielectric data with the sample tissue content obtained from post-measurement histology. For instance during the histology pro-

cess, sample fixation and processing modify the sample tissue morphology and the sample slicing can irreversibly damage the tissues. Due to these limitations, in Chapter 6, a novel histological technique based on microCT images is presented, which enhances the interpretation of dielectric data from heterogeneous samples. MicroCT-based histology is non-destructive, less invasive and less time-consuming than traditional histology. Therefore, MicroCT-based histology has the potential to support accurate dielectric characterisation of heterogeneous biological samples.

The novel contributions above have been published in journal articles and conference publications that are listed in the following section.

1.2.1 Journal and Conference publications

Open-ended coaxial probe measurement protocol and meta-data analysis:

1. **A. La Gioia**, E. Porter, I. Merunka, S. Salahuddin, A. Shahzad, M. Jones, and M. O'Halloran, "Open-ended Coaxial Probe Technique for Dielectric Measurement of Biological Tissues: Challenges and Common Practices," *Diagnostics*, 8, 40, 2018.
2. E. Porter, **A. La Gioia**, S. Salahuddin, S. Decker, A. Shahzad, M. A. Elahi, M. O'Halloran, O. Beyan, "Minimum information for dielectric measurements of biological tissues (MINDER): A framework for repeatable and reusable data," *International Journal of RF and MW Computer-Aided Engineering*, Article ID: e21201, 2017.
3. E. Porter, **A. La Gioia**, S. Salahuddin, A. Shahzad, M. A. Elahi, and M. O'Halloran, "Minimum Reporting Requirements for Dielectric Property Measurements of Biological Tissues," *12th European Conference on Antennas and Propagation (EuCAP)*, London, UK, 2018.
4. M. R. Karim, M. Heinrichs, L. C. Gleim, M. Cochez, E. Porter, **A. La Gioia**, S. Salahuddin, M. O'Halloran, S. Decker, and O. Beyan, "Towards a FAIR Sharing of Scientific Experiments: Improving Discoverability and Reusability of Dielectric Measurements of Biological Tissues," *Proceedings of the 10th International Conference on Semantic Web Applications and Tools for Health Care and Life Sciences (SWAT4LS)*, Rome, Italy, Dec. 4-7, 2017.

Sensing radius and dielectric contribution investigation:

1. **A. La Gioia**, S. Salahuddin, M. A. Elahi, M. O'Halloran, and E. Porter "Investigation of histology radius in dielectric measurements

- of heterogeneous materials,” *IEEE Transactions on Dielectrics and Electrical Insulation*, vol. 25, no. 3, pp. 1065–1080, 2018.
2. **A. La Gioia**, S. Salahuddin, M. O’Halloran, and E. Porter, “Quantification of the Sensing Radius of a Coaxial Probe for Accurate Interpretation of Heterogeneous Tissue Dielectric Data,” *IEEE Journal on Electromagnetics, RF, and MWs in Medicine and Biology*, vol. 2, no. 3, pp. 145–153, 2018.
 3. **A. La Gioia**, M. O’Halloran, and E. Porter, “Modelling the Sensing Radius of a Coaxial Probe for Dielectric Characterisation of Biological Tissues,” *IEEE Access*, vol. 6, pp. 46516–46526, 2018.
 4. **A. La Gioia**, A. Santorelli, M. A. Elahi, M. O’Halloran, and E. Porter, “Predicting the Sensing Radius of a Coaxial Probe based on the Probe Dimensions,” *IEEE Transactions on Antenna and Propagation Systems*. (Under review)
 5. **A. La Gioia**, M. O’Halloran, and E. Porter, “Sensing Radius of an Open-Ended Coaxial Probe for Dielectric Measurement of Tissues: Calculation with Relative Permittivity versus Conductivity,” *URSI AP-RASC 2019*, New Delhi, India, 2019.
 6. **A. La Gioia**, M. O’Halloran, and E. Porter, “Modelling of Tissue Dielectric Contribution Within the Sensing Radius of a Coaxial Probe,” *1st EMF-Med World Conference on Biomedical Applications of Electromagnetic Fields*, Split, Croatia, 2018.
 7. **A. La Gioia**, E. Porter, S. Salahuddin, and M. O’Halloran, “Impact of Radial Heterogeneities of Biological Tissues on Dielectric Measurements,” *2017 19th International Conference on Electromagnetics in Advanced Applications (ICEAA)*, Verona, Italy, 2017, pp. 421-424.
 8. **A. La Gioia**, E. Porter, and M. O’Halloran, “Examination of the Sensing Radius of Open-ended Coaxial Probes in Dielectric Measurements of Biological Tissues,” *2017 IEEE International Symposium on Antennas and Propagation and USNC/URSI National Radio Science Meeting*, San Diego, CA, 2017, pp. 215-216.

Sensing depth and dielectric contribution investigation:

1. E. Porter, **A. La Gioia**, A. Santorelli and M. O’Halloran, “Modelling of the Dielectric Properties of Biological Tissues within the Histology Region,” *IEEE Transactions on Dielectrics and Electrical Insulation*, vol. 24, no. 5, pp. 3290-3301, 2017.
2. E. Porter, **A. La Gioia**, and M. O’Halloran, “Impact of Histology Region Size on Measured Dielectric Properties of Biological Tissues,” *2017 Progress In Electromagnetics Research Symposium - Spring (PIERS)*,

St. Petersburg, 2017, pp. 3406-3411.

3. E. Porter, **A. La Gioia**, M. A. Elahi, and M. O'Halloran, "Significance of Heterogeneities in Accurate Dielectric Measurements of Biological Tissues," *2017 XXXIInd General Assembly and Scientific Symposium of the International Union of Radio Science (URSI GASS)*, Montreal, QC, 2017, pp. 1-4.
4. E. Porter, **A. La Gioia**, A. Bottiglieri, and M. O'Halloran, "Challenges in the Dielectric Measurement of Heterogeneous Tissues: Impact of Uncertainty in Sensing Depth Calculation," *2nd URSI Atlantic Radio Science Meeting (URSI AT-RASC)*, Gran Canaria, Spain, 2018.

Other research contributions:

1. **A. La Gioia**, M. A. Elahi, A. Bottiglieri, N. Ištuk, C. Dowling, F. D'Arcy, M. O'Halloran and E. Porter, "Early-stage Dielectric Characterisation of Renal Cell Carcinoma for Positive Surgical Margin Detection," *13th European Conference on Antennas and Propagation (EuCAP)*, Krakow, Poland, 2019.
2. **A. La Gioia**, M. Ragulskis, M. Kasper, I. Alic, M. O'Halloran, E. Porter, and F. Kienberger, "Effect of Network Analyzer Trace Noise on Dielectric Measurements with an Open-ended Coaxial Probe," *12th European Conference on Antennas and Propagation (EuCAP)*, London, UK, 2018.
3. **A. La Gioia**, S. Salahuddin, A. Shahzad, M. A. Elahi, E. Porter, and M. O'Halloran, "Dielectric Measurement of Porcine Pancreas for Medical Application Design," *24th Annual Conference of the Section of Bioengineering of the Royal Academy of Medicine in Ireland (BINI)*, Dublin, Ireland, 2018
4. S. Salahuddin, **A. La Gioia**, A. Shahzad, M. A. Elahi, A. Kumar, D. Kilroy, E. Porter, and M. O'Halloran, "An anatomically accurate dielectric profile of the porcine kidney," *Biomedical Physics and Engineering Express*, vol. 4, no. 2, Article ID: 025042, 2018.
5. S. Salahuddin, **A. La Gioia**, A. Shahzad, M. A. Elahi, A. Kumar, D. Kilroy, E. Porter, and M. O'Halloran, "Demonstration of dielectric heterogeneity of previously assumed homogeneous tissues: Examination of the Heart," *12th European Conference on Antennas and Propagation (EuCAP)*, London, UK, 2018.
6. E. Porter, S. Salahuddin, **A. La Gioia**, M. A. Elahi, A. Shahzad, and M. O'Halloran, "Characterisation of the Dielectric Properties of the Bladder over the Microwave Range," *IEEE Journal of Electromagnetics, RF and Microwaves in Medicine and Biology*, vol. 2, no. 3, pp.

208-215, Sept. 2018.

7. S. Salahuddin, E. Porter, **A. La Gioia**, and M. O'Halloran, "Comparison of in-vivo and ex-vivo Dielectric Properties of Biological Tissues," *2017 International Conference on Electromagnetics in Advanced Applications (ICEAA)*, Verona, Italy, 2017, pp. 582-585.

1.3 Thesis structure

The remainder of this thesis describes the background, the dielectric measurement technique, and methods and results used to address the research objectives.

Chapter 2 introduces dielectric properties and related measurement techniques, and underscores the motivation of this dissertation by reviewing past and recent dielectric studies together with their reported inconsistencies.

Chapter 3 critically reviews each step of the protocol concerning dielectric measurement of biological tissues with a coaxial probe, from the system settings and calibration to the post-measurement analysis. As part of the post-measurement analysis, this chapter describes and reviews also the histological analysis, which is normally conducted for the dielectric characterisation of heterogeneous tissues. Specifically, at the end of Chapter 3, the challenges in combining dielectric and histological data for an accurate dielectric characterisation of heterogeneous biological tissues are highlighted and the motivation for the studies detailed in Chapter 4, Chapter 5 and Chapter 6 is provided. In the final section of Chapter 3, the sensing volume of the coaxial probe and the dielectric contribution of each tissue constituting the heterogeneous biological sample are identified as main sources of data uncertainty when combining dielectric data with the histological information.

Since the sensing volume consists of the sensing radius and sensing depth, and the sensing depth has been thoroughly examined in several recent dielectric studies, Chapter 4 focuses on the sensing radius. Firstly, the sensing radius is defined as the minimum radius of the homogeneous tissue region required to accurately acquire only the dielectric properties of that homogeneous tissue without the influence of the surrounding tissues. As the sensing depth has been investigated in the literature by conducting dielectric experiments and numerical simulations on layered material samples, in Chapter 4, the sensing radius is investigated both experimentally and numerically by examining concentric tissue-mimicking materials and biological tissues. Then, the sensing radius is calculated in a number of scenarios involving different coaxial probes and concentric samples in order to evaluate the

CHAPTER 1. INTRODUCTION

dependence of the sensing radius on both the physical dimensions of the probe and the dielectric properties of the investigated sample. Lastly, the results are also modelled in order to support prediction of the sensing radius for a subset of biological samples, with the aim of improving the dielectric characterisation of biological samples presenting radial heterogeneities.

As the dielectric contribution of tissues within layered structures has been investigated in the literature in the context of determining the sensing depth, in Chapter 5, the dielectric contribution of tissues constituting different radially heterogeneous biological samples is investigated. This analysis has the aim of supporting the dielectric characterisation of radially heterogeneous tissue samples within which it is not possible to find a homogeneous tissue region with radius larger than the sensing radius. In particular, the dielectric contribution of single tissues is analysed within tissue-mimicking and biological samples that consist of two side-by-side or concentric materials (or tissues). Both the experimental and numerical outcomes of this analysis suggest that the dielectric properties of radially heterogeneous samples depend on the spatial distribution of each material within the sensing radius, and that the bulk dielectric properties of concentric heterogeneous tissues highly depend on the properties of each constituent material within the sensing radius.

In Chapter 6, the significance of the experimental findings summarised in Chapter 4 and Chapter 5 is demonstrated in the dielectric characterisation of radially heterogeneous biological samples. In particular, biological tissue samples are analysed histologically after the acquisition of their dielectric properties. Due to the numerous challenges of conducting post-measurement histological analysis in the traditional way, micro computed tomography (microCT) is investigated as an alternative histological technique to histology for accurately attributing the acquired dielectric data to the tissue content of a heterogeneous sample. Thus, the potential advantages of microCT over traditional histology are discussed with the aim of improving the dielectric characterisation of heterogeneous biological samples.

Lastly, a concise summary and discussion of the experimental findings are provided in Chapter 7. In particular, this final discussion highlights the applicability of the outcomes of this thesis only to biological samples with simple heterogeneous structures, and emphasises the challenges in dielectrically characterising biological samples consisting of more complex heterogeneous structures.

Dielectric properties of biological tissues

In this chapter, fundamental background information regarding the dielectric properties of biological tissues is provided, ranging from the physical principles of the dielectric properties of biological tissues to the current state-of-the-art in the acquisition of the dielectric properties of biological tissues over the MW frequency range.

Firstly, the theoretical aspects of the dielectric spectrum of biological tissues are introduced, including the definition of the dielectric properties, the dielectric dispersions of biological tissues and the mathematical representation of such data.

Next, the current techniques used to dielectrically characterise biological tissues in the MW frequency range are discussed. For each acquisition technique, the basic operating principle is provided along with the known advantages and drawbacks. Due to key advantages of the open-ended coaxial probe technique over the other measurement techniques, the open-ended coaxial probe technique is then discussed in more detail and is the focus of the following sections and chapters of this thesis. Finally, the main studies in the literature involving characterisation and acquisition of dielectric properties of biological tissues with a coaxial probe are reported chronologically. In particular, gaps and challenges in dielectrically characterising biological tissues with the open-ended technique are identified. Methods to address these challenges are reviewed in Chapter 3 in order to define the measurement protocol used for the dielectric characterisation of tissue-mimicking materials and biological tissues in this thesis.

2.1 Theoretical background

In this section, the theoretical background of the dielectric properties of biological tissues is introduced. Specifically, in Section 2.1.1 the interaction of EM fields with biological tissues is described and the definition of dielectric properties is provided. In Section 2.1.2, the dispersion regions characterising

the dielectric spectrum of biological tissues are reviewed. Lastly, in Section 2.1.3, the mathematical models used to graphically represent the dispersion regions are presented.

2.1.1 Definition of dielectric properties

Biological tissues possess bound charges (polar molecules) that are characterised by a dipole moment and free charges (ions). After the application of an external electric field, polar molecules, or dipoles, change orientation opposing to the applied field and positive ions get separated from negative ions. Specifically, the electric field causes different mechanisms of polarisation, which generate both displacement and conduction currents [41], [45], [67]. As a result, both electric flux density, or electric displacement field, D [$\frac{C}{m^2}$] (that accounts for the effects of free and bound charges) and conduction electric current density J [$\frac{A}{m^2}$] (that accounts for the effect of displacement and ionic currents) vary directly with the strength of the electric field E [$\frac{V}{m}$] and are defined by the following constitutive relations [68]:

$$D(\omega) = \epsilon_0 \epsilon^*(\omega) E(\omega), \quad (2.1)$$

$$J(\omega) = \sigma(\omega) E(\omega), \quad (2.2)$$

where $\omega = 2\pi f$ [$\frac{1}{s}$] is the angular frequency, with f [$\frac{1}{s}$] the frequency of the applied field, ϵ_0 [$\frac{F}{m}$] is the permittivity of the vacuum, ϵ^* is the unitless relative complex permittivity, and σ [$\frac{S}{m}$] is the electric conductivity. The relative complex permittivity, also generically called “complex permittivity” or “permittivity”, is a constitutive parameter, which defines the dielectric properties of biological tissues and is related to the electric conductivity by the following expression:

$$\epsilon^*(\omega) = \epsilon'(\omega) - j\epsilon''(\omega) = \epsilon'(\omega) - j\frac{\sigma(\omega)}{\omega\epsilon_0}, \quad (2.3)$$

where $j = \sqrt{-1}$, ϵ' is the real part of the complex permittivity, also denoted as ϵ_r and called “relative permittivity”, ϵ'' is the imaginary part of complex permittivity. The relative permittivity expresses the ability of the tissue to store energy from an external electric field, and the imaginary part of permittivity is related to the electrical conductivity and is a measure of the dissipative nature of the tissue, which absorbs energy and partially converts it to heat [41], [45], [67]. Furthermore, the dielectric properties are temperature-dependent, and, generally, for small increases of temperature, the relative permittivity decreases and the conductivity increases [31], [41].

CHAPTER 2. DIELECTRIC PROPERTIES OF BIOLOGICAL TISSUES

In other words, the complex permittivity defines the interaction of a biological tissue with an external electric field, determining the spatial extent to which the electric field can penetrate into the tissue and how electric energy propagates through the tissue. Also, dielectric properties are used to derive parameters that define EM wave propagation into biological tissues, such as the propagation constant and wave impedance.

Furthermore, Eq. (2.1), Eq. (2.2) and Eq. (2.3) express the dependence of dielectric properties on the frequency of the applied external electric field. In fact, the tissue response to a time-varying electric field is not instant but time-dependent. Specifically, when a biological tissue is excited by a time-varying electric field, the dipoles in the tissue orient with the direction of the field and then relax back toward the steady orientation with a characteristic time constant τ [s], which is related to the relaxation frequency, f_c , where $f_c = (2\pi\tau)^{-1}$ [45]. In each biological tissue, a number of different polarisation mechanisms and, then, relaxation processes (or dispersion phenomena) occur at different frequency bands. The main dispersion regions of biological tissues are detailed in the following section.

2.1.2 Dielectric dispersions

The dielectric spectrum of a biological tissue is characterised by three main dispersion regions, α , β and γ , and other minor dispersions including the δ dispersion.

The α dispersion arises from the ionic diffusion associated with fixed charges on cell membranes. The relaxation frequency (that is around 100 Hz) is proportional to the mobility of the ions. In the α region, the relative permittivity of tissues has a magnitude of about 10^6 [45], [67].

At intermediate frequencies between 50 kHz and 3 MHz, the β dispersion is caused by the capacitive charging of cell membranes through electrolytes [67], [69]. In this frequency range, the relative permittivity can vary from 10^5 down to 10^2 .

At MW frequencies ranging from 100 MHz up to 50 GHz, the γ dispersion is caused by the relaxation of water molecules, which act as permanent dipoles that follow the alternating electric field [67]. In this MW range, the dielectric properties depend primarily on the tissue water content [67], [69]. In the γ region, the relative permittivity magnitude ranges from 10^2 to 10^0 .

Over a limited frequency range from 0.1 to 3 GHz, the δ dispersion also occurs. The δ dispersion is thought to be caused by the dipolar relaxation of bound water [67], [70]. However, the δ dispersion is relatively poorly defined since it overlaps with the strong γ dispersion.

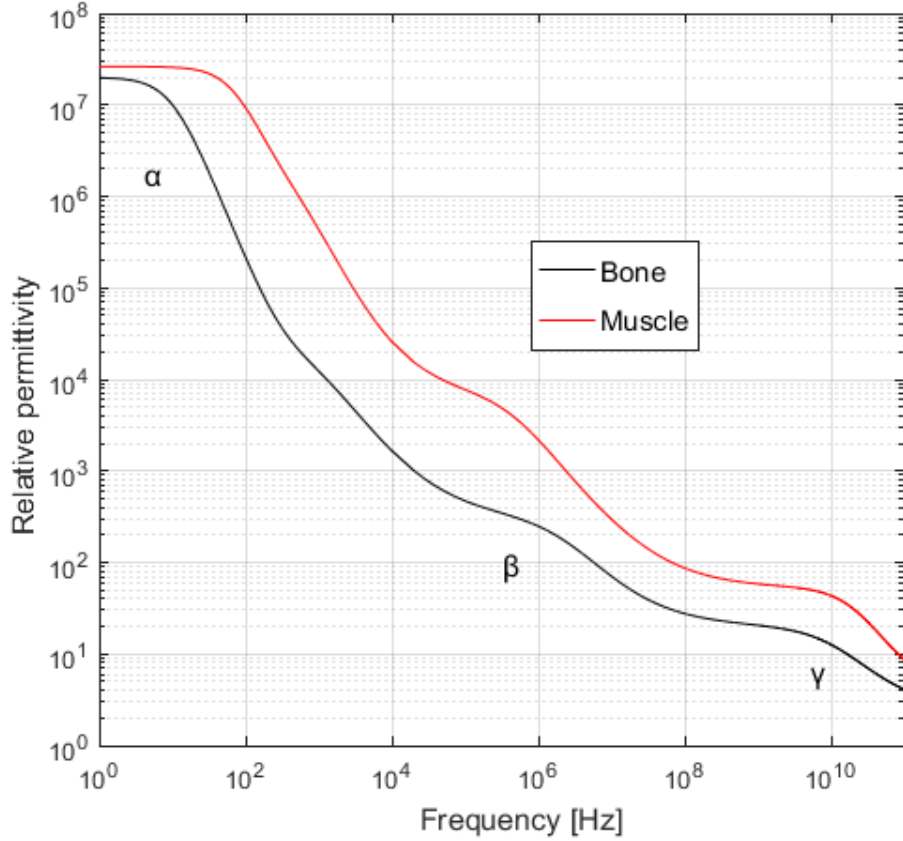


Figure 2.1: Logarithmic plot of the major dielectric dispersion regions, α , β and γ , for bone and muscle tissue. Relative permittivity data is from Gabriel *et al.* [46]. The α region arises from the ionic diffusion associated with fixed charges on cell membranes and is centred around 10^2 Hz, the β region is caused by the capacitive charging of cell membranes through electrolytes and covers frequencies between 10^4 and 10^7 Hz, and the γ dispersion is caused by the relaxation of water molecules and occurs in the range from 10^8 up to 10^{10} Hz. In the plot, the δ dispersion that is thought to be caused by the dipolar relaxation of bound water is not depicted since it overlaps with the strong γ dispersion.

The main dielectric relaxation regions α , β and γ are depicted in Fig. 2.1, for bone and muscle tissue. The relative permittivity values are higher for muscle than for bone, since muscle tissue contain more electrolytes and water than bone tissue. The two curves are obtained from the dielectric models by Gabriel *et al.* [46]. Details regarding dielectric models are provided in the following section.

2.1.3 Dielectric models

Differential equations have been developed to model the dielectric dispersions of biological tissues and other polar materials. A dispersion region is generally described by first order differential equations that lead to single time constant responses [67]. However, since, in biological materials, several relaxation processes may occur in parallel, the total response of a specific tissue may be characterised by several time constants characterising the poles (one per relaxation process) of the differential equations of the dielectric model [71].

Dielectric models are generally used to fit dielectric data, thus reducing measurement data points to closed form equations and convenient graphical representations [10], [71]. These models allow the calculation of the relative permittivity and conductivity (or imaginary part of the complex permittivity) values at any desired frequency within the range for which the relaxation equation is valid [71], [72].

The most common models used to fit the dielectric data of aqueous electrolytic solutions and tissues are: Debye, Cole-Cole and Cole-Davidson models [73].

The Debye relaxation is the dielectric relaxation response of an ideal, non-interacting dielectric material to an alternating external electric field. The dielectric response of a first order system in the frequency domain can be expressed as:

$$\epsilon^*(\omega) = \epsilon_\infty + \frac{\epsilon_s - \epsilon_\infty}{1 + j\omega\tau}, \quad (2.4)$$

where ω and τ were defined in Section 2.1.1, ϵ_∞ refers to the permittivity at infinite frequencies, and ϵ_s is the static (low frequency) permittivity. Eq. (2.4) does not take into account the dissipative effects of the material [45]. Then, Eq. (2.4) can be expanded including a static conductivity term, σ_s , as follows:

$$\epsilon^*(\omega) = \epsilon_\infty + \frac{\epsilon_s - \epsilon_\infty}{1 + j\omega\tau} + \frac{\sigma_s}{j\omega\epsilon_0}. \quad (2.5)$$

Eq. (2.5) does not present a conductivity term at infinite frequencies, since the conductivity at such frequencies tend to zero [74]. As a modification of the Debye model, the Cole-Cole model is commonly used as a physics-based representation of wideband frequency-dependent dielectric properties [71]. In the Cole-Cole first order equation the empirical variable α is introduced to account for the statistical distribution of the relaxation time and Eq. (2.5) becomes:

$$\epsilon^*(\omega) = \epsilon_\infty + \frac{\epsilon_s - \epsilon_\infty}{1 + (j\omega\tau)^{1-\alpha}} + \frac{\sigma_s}{j\omega\epsilon_0}. \quad (2.6)$$

In general, the Debye, Cole-Cole and Cole-Davidson models can be represented collectively by the Havriliak–Negami relaxation [73] (that does not include the static conductivity σ_s), which is an empirical modification of the Debye relaxation model, accounting for the asymmetry and broadness of the dielectric dispersion curve, as follows:

$$\epsilon^*(\omega) = \epsilon_\infty + \frac{\epsilon_s - \epsilon_\infty}{[1 + (j\omega\tau)^{1-\alpha}]^\beta}. \quad (2.7)$$

When $\alpha = 0$ and $\beta = 1$, Eq. (2.7) is equivalent to Eq. (2.4), and corresponds to the Debye model. For $0 < \alpha < 1$ and $\beta = 1$, Eq. (2.7) results in the Cole-Cole equation (Eq. (2.6)). Lastly, for $\alpha = 0$ and $0 < \beta < 1$, Eq. (2.7) corresponds to the Cole-Davidson equation. In Eq. (2.7), the empirical variable β acts to account for the asymmetry of the statistical distribution of the relaxation time [73]. While all of these models are used for fitting polar aqueous solutions, biological tissue data is generally fitted with Debye and Cole-Cole models [10], [71].

The equations described present a single relaxation; however, if the dielectric behaviour of a material is analysed across a wide frequency range, more relaxation processes occur and more poles (corresponding to the different relaxation times of the material) must be introduced to describe the properties of the material [67]. Biological tissues are generally described in terms of multiple Cole-Cole dispersions, which is a physics-based compact representation of wideband frequency-dependent dielectric properties [71]. Importantly, these models allow for the dielectric properties of biological tissues to be easily incorporated into sophisticated computational models.

In the next section, the most common measurement techniques used to acquire dielectric properties of biological tissues in the MW frequency range are summarised and discussed. This thesis focuses on the dielectric properties of biological tissues in the MW range, since a large number of EM-based diagnostic and therapeutic devices operate within this range.

2.2 Measurement techniques

Different techniques have been used to measure the dielectric properties of biological tissues in the MW range, including the transmission line, open-ended coaxial probe, and perturbation cavity methods [50]. The three techniques are illustrated in Fig. 2.2 and are overviewed in the next sections

CHAPTER 2. DIELECTRIC PROPERTIES OF BIOLOGICAL TISSUES

by highlighting the advantages and drawbacks of each. For any given set of dielectric measurement experiments, the selection of the measurement technique depends on specific requirements concerning either the characteristics of the sample or the measurement system, such as:

- *In vivo/Ex vivo* samples;
- Broadband or single frequency measurement;
- Sample size restrictions;
- Required measurement accuracy;
- Measurement complexity.

2.2.1 Transmission line

In transmission line measurement methods, a sample is placed in a coaxial line or, in the case of anisotropic tissue, in a rectangular waveguide so that the field polarisation may be varied [75]. The transmission line is connected to two ports of a Vector Network Analyser (VNA) in order to acquire the scattering parameters S_{11} and S_{21} [76], [77], which are then converted into the complex permittivity (dielectric properties) of the tissue. The two most commonly used conversion methods are the Nicolson-Ross-Weir (NRW) method [78], [79], and the NIST iterative conversion method [80], [81]. The NRW method provides a direct calculation of permittivity from the complex reflection and transmission coefficients obtained from the S-parameters [78], [79], [82], [83]. Other common conversion methods are iterative and receive the initial guess from the NRW method or users' input [82]. The algorithm developed to implement the NIST iterative conversion method is reported in detail in Baker-Jarvis *et al.* [80]. The NIST iterative conversion method is generally more stable than the NRW approach, which fails for low loss samples of arbitrary length [80].

The transmission line method allows accurate measurements (with a typical average accuracy within 5%) at room temperatures over a large frequency range [50], [77], [80]. The measurement accuracy can be smaller for temperatures higher than room temperatures in coaxial lines, due to the difficulty in controlling the temperature of the inner conductors in such conditions [50]. Conversely, waveguides are suitable for accurate measurements of larger samples (i.e., samples with the size of the waveguide) at temperatures higher than room temperatures and at frequencies up to 2.45 GHz, which is the frequency point normally used in MW ablation. However, in case of samples with size smaller than 2 mm, a coplanar waveguide (with a circular aperture with a diameter of approximately 2 mm) can be used to facilitate the sample pre-processing [50], [84]. For instance, coplanar waveguide systems were used to dielectrically characterise white

CHAPTER 2. DIELECTRIC PROPERTIES OF BIOLOGICAL TISSUES

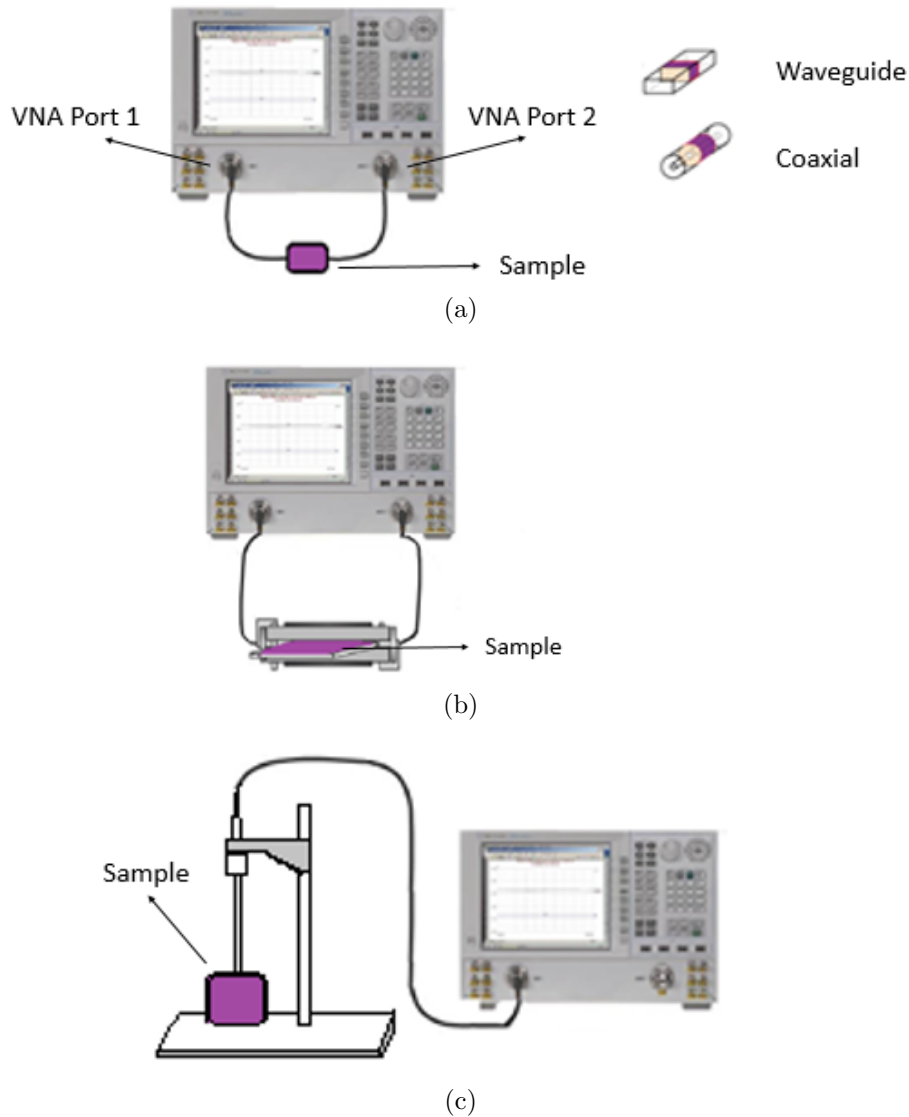


Figure 2.2: Schematised measurement set-up of the three techniques: (a) transmission line, (b) cavity perturbation and (c) open-ended coaxial probe. Portions of this figure were adapted from [75]. The transmission line technique (a) consists of placing a sample in a coaxial line that is connected to two ports of a VNA to acquire the scattering parameters S_{11} and S_{21} , which are then converted into complex permittivity. The cavity perturbation method (b) consists of inserting a sample with width smaller than 1 mm into a resonant cavity, thus altering resonant frequency (f) and quality factor (Q) of the cavity. Then, the dielectric properties are computed using the frequency, the Q-factor, and the volume of the sample. Lastly, the open-ended coaxial probe (c) consists of a truncated section of a transmission line connected to one port of the VNA. The sample is placed in contact with the probe and reflects the transmitted signal back to the VNA, which generally converts the resulting S_{11} parameters into complex permittivity.

CHAPTER 2. DIELECTRIC PROPERTIES OF BIOLOGICAL TISSUES

and grey matter from rat brain tissue samples [85]. Coplanar waveguides were also used in microfluidic devices to acquire the dielectric properties of haemoglobin solutions and *E. coli* populations [86].

Samples up to five centimetres in size can be measured in a coaxial line, although this method also requires careful sample preparation in order to shape the sample to fit the line, and the method generally assumes that there are no air gaps in or around the sample and that the sample has smooth flat faces [75]. Thus, the transmission line method is unsuitable for *in vivo* measurements and is not recommended for *ex vivo* measurements of semisolid or solid biological samples. However, the transmission line technique can be suitable for the measurement of biological fluids. For instance, the transmission line has been used to measure tissue-mimicking liquid phantoms in the study by Shibata *et al.* [87] and to quantify the edema in brain tissue in the study by Reinecke *et al.* [77].

2.2.2 Cavity

The cavity perturbation method consists of a resonant cavity that resonates at specific frequencies. The tissue samples are inserted into the cavity and analysed by measuring the resonant frequency (f) and quality factor (Q), which are altered by inserting the tissue sample [50], [75], [88]–[90]. The tissue dielectric properties are then computed using the frequency, the Q-factor, and the sample volume. Details regarding the mathematical formulation to obtain the permittivity of the sample are reported by Campbell *et al.* [70]. However, the resonant frequency and quality factor are generally computed automatically with a VNA. Since the maximum change in resonant frequency is achieved when a small perturbation occurs at the maximum intensity of the cavity mode, the cavity perturbation method requires a sample with thickness smaller than 1 mm [50], [89].

Dielectric measurements performed using the cavity perturbation method can be highly accurate (with an accuracy to within 4%), but only provide dielectric data at a single frequency (in the upper MW frequency range of 1-50 GHz) [89]. While the equipment needed for cavity perturbation measurements is readily available, the sample preparation is relatively complicated, requiring an excised tissue sample to be cut and moulded to a precise size and shape to fit into the cavity [75], [89]. This process may introduce air pockets within the sample or between the sample and the cavity, loss of fluid in the tissue (which would affect the tissue properties), and an increase in density from pushing the tissue into the cavity (which could also affect tissue properties) [89]. Due to the required sample size and

thus sample preparation, achieving accurate biological tissue measurements with the cavity perturbation method is highly challenging.

To date, there are only a few studies in the literature that have used cavity perturbation techniques to characterise biological tissues [88], [89]. For instance, the cavity perturbation technique has been used to detect the dielectric properties of healthy, benign and malignant breast tissue at 3.2 GHz by Campbell and Land [89]. In particular, in this study, Campbell and Land demonstrated the capability of the cavity perturbation technique of dielectrically differentiating healthy breast tissue from cancerous breast tissue [89].

2.2.3 Open-ended coaxial probe

The open-ended coaxial probe consists of a truncated section of a transmission line that is connected to one port of a VNA. The electromagnetic field propagates along the coaxial line and reflection occurs when the electromagnetic field encounters an impedance mismatch between the probe and the tissue sample. The reflected signals at different frequencies are measured, and then the resulting S_{11} parameters are converted into complex permittivity values, which can be calculated using different mathematical models [91]–[95].

The open-ended coaxial probe has become the most commonly used method to measure the dielectric properties of tissues for several reasons: the method allows measurements at different temperatures; sample handling is minimal and non-destructive; and both *ex vivo* and *in vivo* measurements over a broad frequency range are possible [42], [46], [47], [50], [96]. However, the open-ended coaxial method is based on the assumption that a homogeneous sample is in good contact with the probe; therefore, air bubbles and uneven sample surfaces can result in inaccurate measurements [75], and heterogeneous samples present a particular challenge. There are also limits to the magnitudes of material properties that can be measured reliably [75]. The limits of what can be measured depend on a number of factors, including the probe design and materials (and therefore the probe impedance), precision of probe fabrication procedure, calibration procedure (standards used) and the capabilities of the measurement device (i.e., the VNA). Furthermore, the accuracy of the measurement conducted with the open-ended coaxial probe technique can be estimated in different ranges of complex permittivity, and the error in accuracy generally ranges from 1 up to 10% [47].

Overall, many challenges associated with tissue dielectric property measurements may arise in each of the above measurement techniques, e.g.,

issues related to temperature change, and tissue heterogeneity. Since the coaxial probe technique is by far the most commonly used method for tissue measurements [10], [12], [15], [42]–[44], [46], [51], [52], [54], [58], [76], [97], it is examined in more detail in the subsequent sections.

2.3 Open-ended coaxial probe technique: Electromagnetic theory and design advances

The open-ended coaxial probe technique consists of placing a tissue sample in contact with the probe, after calibrating the measurement system, which consists of the probe connected to one port of the VNA through a specialised cable or L-shaped connector. Details regarding the calibration and the measurement process is described in Chapter 3. Instead, in this section, the state-of-the-art of coaxial probes in the literature is reported after providing the theoretical background involving the EM interaction between a coaxial probe and a tissue sample. In particular, in Section 2.3.1, the theoretical basis of EM transmission across a coaxial probe and the interaction between the coaxial probe and the biological sample are presented. In Section 2.3.2, the empirical models used to convert the EM reflected signal into complex permittivity are described in detail. Lastly, in Section 2.3.3, the evolution of the open-ended coaxial probe through past and more recent dielectric studies is discussed.

2.3.1 Electromagnetic transmission across a coaxial probe

The design of a coaxial probe is based on the theoretical assumption that the sample interrogated by the probe occupies a semi-infinite volume so that the acquired signal is due only to the impedance mismatch between the system and the sample [91], [98]. A coaxial probe, generally, consists of an inner conductor of radius a , an insulator of width c having low relative permittivity ϵ_r (i.e., relative permittivity close to that of air), and an outer conductor having an inner radius b . Ideally, in order to minimise EM signal attenuation, the probe insulator is lossless and the conductors are perfect conductors (i.e., the conductors have infinite conductivity). An illustration of the top view of a coaxial probe, with its dimension a , b and c , is shown in the top left picture of Fig. 2.3. In the other pictures of Fig. 2.3, illustrations

CHAPTER 2. DIELECTRIC PROPERTIES OF BIOLOGICAL TISSUES

of the EM propagation across the probe and the sample are provided; this information is further explained in the following paragraphs.

In a dielectric measurement, from the VNA, an input voltage signal of magnitude V [V] is applied between the two conductors at the entrance of the coaxial line so that $V(a) = V$ and $V(b) = 0$. The input signal propagates along the coaxial line in TEM mode. Thus, within the coaxial line, the generated electric and magnetic fields are perpendicular to the direction of propagation of the signal, which is along the symmetry axis z of the coaxial line. Specifically, the incident TEM mode has an electric field component E_ρ along the radial direction ρ , and a magnetic field component H_ϕ [T] along the azimuthal direction ϕ . Both electric and magnetic fields are illustrated on a coaxial probe top cross-section in cylindrical coordinates in the top right picture of Fig. 2.3. The fields generated by the incident TEM wave exhibit no variations in the angular direction. As illustrated in the side cross-section of a coaxial probe in contact with a sample in the bottom picture of Fig. 2.3, at the probe-sample interface, part of the incident signal is reflected back, and the rest is transmitted into the sample due to the difference between the probe impedance Z [Ω] and the sample impedance Z_S . The reflection from the interface is considered as a series of reflected, but evanescent, TM_{0n} modes [92]. A detailed mathematical formulation of the relationship between the incident and reflected EM waves as a function of the impedance (or dielectric properties) of the sample is provided by Levine and Papas [99].

For simplicity, in this section, the equivalent electrostatic formulation of the incident TEM mode is reported, conveniently in cylindrical coordinates, ρ , ϕ and z .

Considering V as the input voltage signal applied to the probe, the radial component of the electric field is obtained from the gradient of the electric potential field and can be expressed as follows [68]:

$$E_\rho = \frac{V}{\ln \frac{b}{a}} \frac{1}{\rho}, \quad (2.8)$$

where ρ can be any point across the radial extent of the coaxial probe between the points delineated by a and b , which are the dimensions of the probe previously defined and illustrated in Fig. 2.3.

Furthermore, considering the characteristic impedance η [Ω] of the insulator between the two conductors:

$$\eta = \sqrt{\frac{\mu}{\epsilon_0 \epsilon_r}}, \quad (2.9)$$

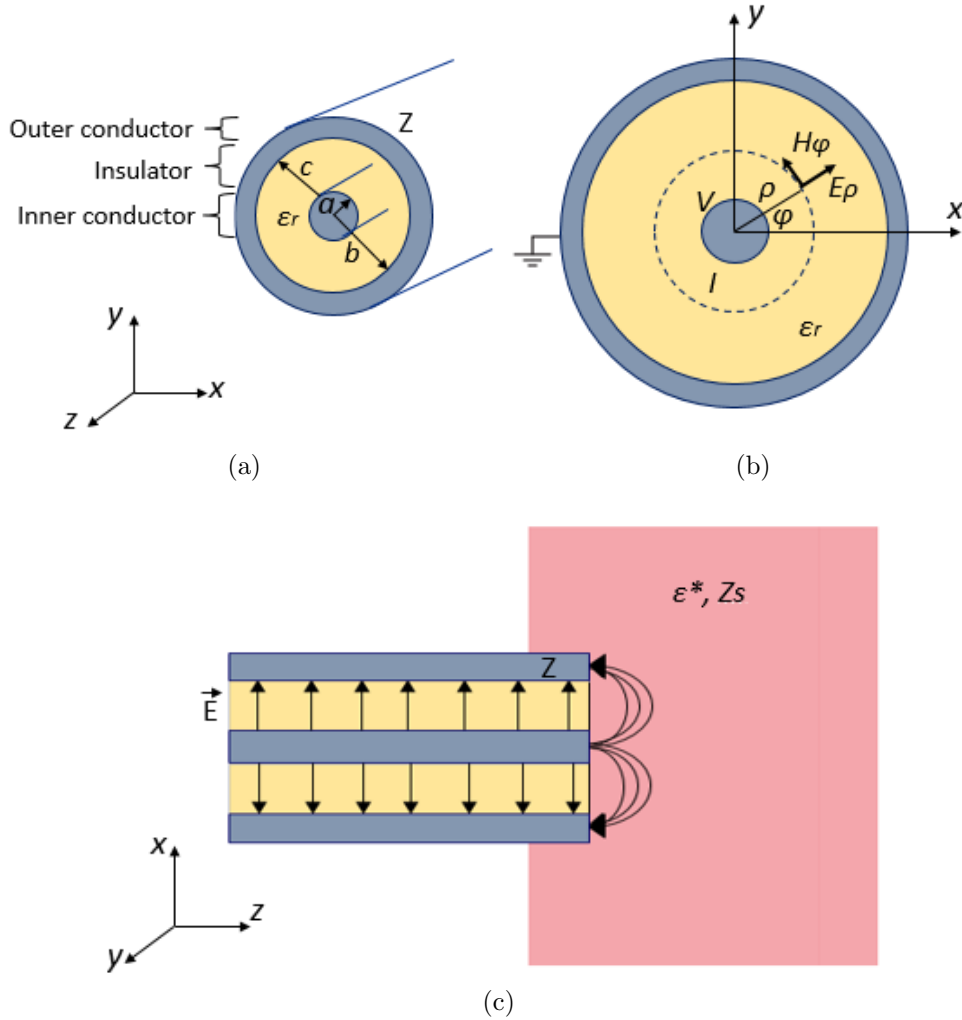


Figure 2.3: Diagrams illustrating the EM transmission along an open-ended coaxial probe and the electric probe-sample interaction: (a) top cross-section of a coaxial probe with indicated probe dimensions; (b) top cross-section of a coaxial probe with generated EM signals; (c), side cross-section of a coaxial probe placed in contact with a sample. In particular, (a) illustrates the inner and outer conductors, and the insulator characterised by the relative permittivity ϵ_r , of a coaxial probe with dimensions a , b and c , which, specifically, are inner conductor radius, outer conductor inner radius and insulator width, respectively. Due to the TEM propagation mode generated by the application of a voltage signal V between the two conductors, (b) depicts an electric field component E_ρ along the radial direction ρ , and a magnetic field component H_ϕ along the azimuthal direction ϕ . In (b), the resulting generated current I encircling the probe is also labelled. In (c), the side-view cross-section of the interaction between the probe and the sample is illustrated by highlighting the radial electric field within the probe and the fringing electric field across the sample, due to the impedance mismatch between the probe and the sample, which have impedances of Z and Z_s , respectively. When the electric field fringes, part of the signal is transmitted into the sample and the rest of the signal is reflected back to the probe. Note that the diagrams are not to scale.

CHAPTER 2. DIELECTRIC PROPERTIES OF BIOLOGICAL TISSUES

with μ [$\frac{H}{m}$] and ϵ_r defining the magnetic permeability and the relative permittivity of the insulator, respectively, the linear relationship between the radial component of the electric field E_ρ and the azimuthal component of the magnetic field H_ϕ can be expressed as follows:

$$H_\phi = \frac{E_\rho}{\eta}. \quad (2.10)$$

By taking into account Eq. (2.10), the azimuthal component of the magnetic field can be defined as in Eq. (2.11):

$$H_\phi = \frac{V}{\eta \ln \frac{b}{a}} \frac{1}{\rho}. \quad (2.11)$$

By applying the Ampere's law around the loop of radius ρ encircling the inner conductor, the current I [A] can be defined as:

$$I = 2\pi\rho H_\phi = \frac{2\pi V}{\eta \ln \frac{b}{a}}. \quad (2.12)$$

It follows that the characteristic impedance of the line Z , which is typically 50 Ω , can be expressed as:

$$Z = \frac{V}{I} = \eta 2\pi \frac{b}{a}. \quad (2.13)$$

Thus, the transmitted power P_T [W] can be expressed either in terms of the voltage V or in terms of the maximum value of the electric field inside the line, which occurs at $\rho = a$ and is equivalent to E_a , as in Eq. (2.15) [68]:

$$E_a = \frac{V}{\ln \frac{b}{a}} \frac{1}{a}, \quad (2.14)$$

$$P_T = \frac{1}{2Z} |V|^2 = \frac{\pi |V|^2}{\eta \ln \frac{b}{a}} = \frac{1}{\eta} |E_a|^2 (\pi a^2) \ln \frac{b}{a}. \quad (2.15)$$

Furthermore, in TEM mode, the propagation constant γ [$\frac{1}{m}$] is related only to the wave phase constant β , which is equivalent to the wave number k . The propagation constant is then defined as follows:

$$\gamma = j\beta = jk = j\omega\sqrt{\mu\epsilon_0\epsilon_r}. \quad (2.16)$$

Consequently, the voltage and the current of the incident signal at a certain length of the coaxial line z can be expressed as:

$$V(z) = V e^{-j\beta z}, \quad (2.17)$$

CHAPTER 2. DIELECTRIC PROPERTIES OF BIOLOGICAL TISSUES

$$I(z) = \frac{1}{Z} V e^{-j\beta z}. \quad (2.18)$$

The expressions in Eq. (2.17) and Eq. (2.18) take into account only the incident or forward signal. However, at the probe sample interface, when there is an impedance mismatch between the probe and the sample, part of the signal is reflected and goes backwards. Thus, by taking into account both forward and backward signals, the signals $V(z)$ and $I(z)$ can be defined as:

$$V(z) = V^+ e^{-j\beta z} + V^- e^{j\beta z}, \quad (2.19)$$

$$I(z) = \frac{1}{Z} (V^+ e^{-j\beta z} + V^- e^{j\beta z}), \quad (2.20)$$

where the voltage signal is expressed as a sum of a forward and a backward moving wave, with V^+ referring to the magnitude of the forward signal and V^- to the magnitude of the backward signal [68].

The ratio between reflected and incident voltage signals is related to the impedances of the probe and the sample, Z and Z_S , respectively. The expression of the reflection coefficient at the probe-sample interface, Γ , is given by:

$$\Gamma = \frac{V^-}{V^+} = \frac{(Z_S - Z)}{(Z_S + Z)} = \frac{(1 - \frac{Z}{Z_S})}{(1 + \frac{Z}{Z_S})}. \quad (2.21)$$

The reflection coefficient can be calculated at any point of the coaxial line by using the propagation equation. Thus, the reflection coefficient Γ_L between two points, z_1 and z_2 , along the line separated by distance $L = z_2 - z_1$ is given by:

$$\Gamma_L = \Gamma e^{-2j\beta L}. \quad (2.22)$$

Due to the frequency-dependence of the signals, the reflection coefficient Γ , also defined as S_{11} , is complex and its magnitude ranges from -1 to 1. From Eq. (2.21), it can be observed that, when the impedance of the sample tends to infinity ($Z_S \gg Z$), in the case of the probe in contact with air (i.e., open circuit), or to zero, in the case of the probe in contact with a metal plate (i.e., short circuit), all of the incident signal is reflected back, and the magnitude of Γ is equal to 1. Specifically, Γ is equal to 1 for the case of open circuit and equal to -1 for the case of short circuit due to the opposite phase. Also, from Eq. (2.21), it can be deduced that the lower the impedance mismatch, the lower the magnitude of Γ . In fact, in the case of matching impedances ($Z_S = Z$), no part of the incident signal is reflected back and Γ is equal to 0.

Furthermore, from the calculation of the reflection coefficient, the expressions of reflected and dissipated power, P_R and P_D , respectively, can be obtained as follows:

$$P_R = |\Gamma|^2, \quad (2.23)$$

$$P_D = 1 - |\Gamma|^2. \quad (2.24)$$

Both reflected and dissipated power depend on the frequency and dielectric properties of the sample interrogated by the probe. Specifically, the dissipated power is related to the penetration depth of the signal transmitted into the sample, which gives an extent of the sensing volume of the coaxial probe. Further discussion regarding the sensing volume of a coaxial probe and its calculation is provided in Chapter 4 of this dissertation.

In dielectric measurements involving the coaxial probe connected to one port of the VNA, the reflection coefficient Γ is typically automatically converted into permittivity by the VNA embedded software. However, the permittivity can also be obtained through applying mathematical models to the measured reflection coefficient. Further details regarding the conversion of the reflection coefficient into permittivity are reported in the next section.

2.3.2 Reflection coefficient conversion into permittivity

Different methods to model the probe and convert the measured complex reflection coefficient into complex permittivity have been developed [91], [92], [95], [98], [100], [101].

These methods can be divided into two categories: full wave formulation techniques and lumped equivalent circuit models [92], [102]. The former provide more accurate permittivity values at the expense of the computational cost, while the latter are computationally simple and fast and can be accurate for limited ranges of frequency and permittivity. Both categories are discussed below.

2.3.2.1 Full wave formulation methods

Full wave formulation methods attempt a rigorous solution of the EM field equations appropriate for a coaxial probe in contact with a dielectric sample [92]. In the full wave formulation methods, the reflection coefficient of the fundamental TEM mode in the coaxial probe is obtained numerically by matching the electromagnetic fields at the interface between the coaxial probe and the external dielectric material. The fields inside the line are

CHAPTER 2. DIELECTRIC PROPERTIES OF BIOLOGICAL TISSUES

expressed in terms of a superposition of the forward travelling TEM wave, and the reflection from the interface is considered as a series of reflected, but evanescent, TM_{0n} modes. Mathematical formulation of the forward problem is provided in several studies [92], [99], [102]. The solution of the forward problem provides the reflection coefficient for a given material permittivity, while the inverse problem finds the material permittivity for a given reflection coefficient. Solutions to both the forward and inverse problems are required for the calculation of the permittivity. Due to the complexity of the inversion process, simplified approximate expressions can be used to determine the dielectric properties [95]. Most of these relations are derived from TEM variational formulation expressions, which are valid for the calculation of the system admittance under certain assumptions [95], [102]. Also, in some cases, the parameters of the probe were empirically optimised by using known values of permittivity of dielectric media, such as air and water [102].

Nowadays, these complex algorithms are generally embedded in the VNA software [102]. However, conversion algorithms are still used to convert the reflection coefficient obtained from numerical simulations into permittivity. To this extent, the lumped equivalent circuit models are generally used due to their simplicity and low computational cost [92].

2.3.2.2 Lumped equivalent circuit models

Lumped equivalent circuit models involve modelling the discontinuity at the termination of the coaxial probe as an equivalent lumped circuit [103]. Different lumped equivalent circuit models, such as the capacitive model [51], [93], [101], the antenna model [101], [104], [105], and the virtual line model [101], [106], were developed for use in conversion algorithms. These models, illustrated in Fig. 2.4, all solve for the system admittance and then sample permittivity using knowledge of both the reflection coefficient and the permittivity of different numbers of known materials.

In particular, in the capacitive model, the discontinuity at the termination of the coaxial probe is assumed to be purely capacitive, and is then modelled as a lumped admittance Y with a capacitance C_f originating from the field within the probe insulator and a capacitance $C(\epsilon^*)$ deriving from the fringing field across the sample. Due to the two lumped elements, the capacitive model has two unknowns, C_f and $C(\epsilon^*)$, which can be calculated from knowledge of both the reflection coefficient and permittivity of two known reference materials.

In the antenna model, the sample losses are taken into account by adding a resistor with conductance G in parallel to the probe capacitance C_f and

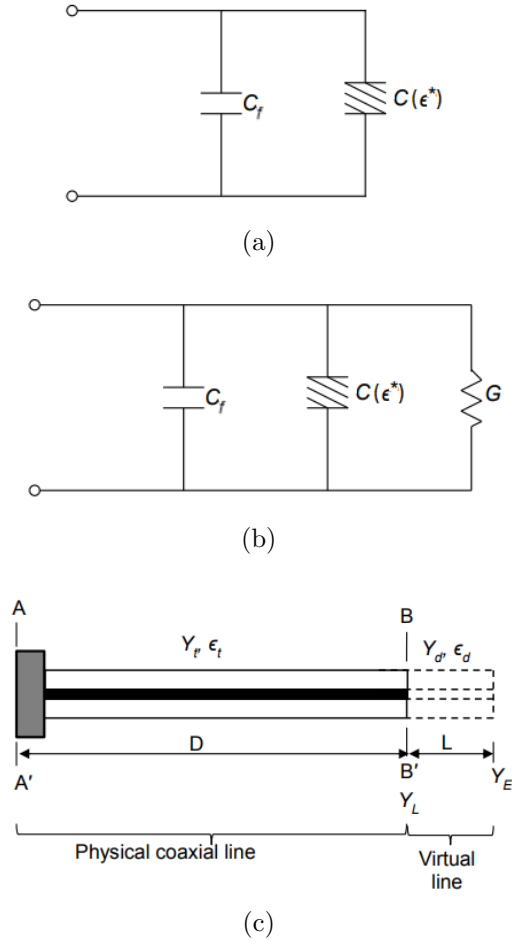


Figure 2.4: Schema of the lumped equivalent circuit models used to convert the reflection coefficient into permittivity: (a) capacitive model, (b) antenna model, and (c) virtual line model (adapted from [107]). In the capacitive model (a), the termination of the coaxial probe is assumed to be purely capacitive, and is then modelled as a lumped admittance Y [S] with a capacitance C_f [F] originating from the fringing field within the probe insulator, and a capacitance $C(\epsilon^*)$ deriving from the sample fringing field. In the antenna model (b), the sample losses are taken into account by adding a resistor with conductance G [S] in parallel to the probe capacitance C_f and the sample capacitance $C(\epsilon^*)$. Lastly, in the virtual line model (c), the dielectric sample is modelled with a virtual transmission line of length L , which has the same dimensions as the physical probe of length D and terminates with an open circuit.

CHAPTER 2. DIELECTRIC PROPERTIES OF BIOLOGICAL TISSUES

the sample capacitance $C(\epsilon^*)$. The presence of an additional lumped element (i.e., the resistor) in the antenna model results in the need for knowledge of both the reflection coefficient and permittivity of three known materials in order to achieve the conversion to dielectric properties of an unknown material.

Lastly, in the virtual antenna model, the dielectric sample is modelled with a virtual transmission line of length L , which has the same dimensions as the physical probe of length D . The virtual transmission line terminates with an open circuit, as shown in Fig. 2.4c. Due to the two unknown variables, L and D , the virtual line model requires both the reflection coefficient and permittivity of two known materials.

The accuracy of these models are related to the dielectric properties of the reference materials used for the calculation of the permittivity of the interrogated sample. Generally, the model accuracy is higher when the dielectric properties of the known materials are spread uniformly across the dielectric spectrum, and the reflection coefficient of the interrogated sample is close to one of the reflection coefficients from the reference materials. Furthermore, in the study conducted by Berube *et al.* [101], the accuracy of the capacitive, antenna and virtual line models was investigated for a specific subset of reference materials having different dielectric properties. Among the three models, it was found that the virtual line model and the antenna model are more appropriate for the calculation of the dielectric properties of biological tissues [101].

Thus, the antenna model has been implemented in the work of this dissertation, to process the simulation data that is presented in Chapter 4 and Chapter 5. For this reason, this model is described in more detail below, before providing the state-of-the-art of the coaxial probe in terms of the design and fabrication in Section 2.3.3.

In the antenna model, the permittivity of the sample interrogated by an open-ended coaxial probe is calculated from the admittance at the probe-sample interface [101]. Fig. 2.4b shows the equivalent circuit of the antenna model. The admittance at the probe-sample interface is represented by two capacitances and a conductance. Specifically, C_f is the capacitance originating from the field within the probe, $C(\epsilon^*)$ is the capacitance originating from the fringing field across the sample, and G is the conductance of the sample and is in parallel to the other capacitances. The normalised admittance of this equivalent circuit Y_c (Fig. 2.4b) is provided in Eq. (2.25):

$$\frac{Y_c}{Y} = j\omega C_f Z + j\omega C(\omega, \epsilon^*) Z + G(\omega, \epsilon^*) Z, \quad (2.25)$$

where Z is the characteristic impedance of the coaxial probe (50Ω), $Y = \frac{1}{Z}$ is

CHAPTER 2. DIELECTRIC PROPERTIES OF BIOLOGICAL TISSUES

the characteristic admittance of the coaxial probe, and ϵ^* is the permittivity of the sample interrogated by the probe.

In this model, the coaxial probe inserted into a lossy material mimics an antenna radiating in a lossy medium. Thus, the admittance can be expressed as in Eq. (2.26) [108]:

$$Y_c(\omega, \epsilon^*) = \sqrt{\epsilon^*} Y_c(\sqrt{\epsilon^*} \omega, \epsilon_0). \quad (2.26)$$

Thus, Eq. (2.25) becomes:

$$\frac{Y_c}{Y} = j\omega C_f Z + j\omega \epsilon^* C Z + \epsilon^{*\frac{5}{2}} G Z. \quad (2.27)$$

Equation Eq. (2.27) can be also expressed in the form:

$$\frac{Y_c}{Y} = K_1 + K_1 \epsilon^* + K_3 \epsilon^{*\frac{5}{2}}, \quad (2.28)$$

where the factors K_1 , K_2 and K_3 are generally complex constants that are calculated from the knowledge of reflection coefficient and permittivity of three known reference materials. Then, once the complex values of K_1 , K_2 and K_3 are known, the permittivity of the (unknown) interrogated sample can be calculated from the normalised admittance. Discrepancies of 10% or more may occur between the measured and the expected values of permittivity [92], [101]. However, the accuracy can be improved by using references materials with very similar properties to those of the investigated sample [101].

2.3.3 State-of-the-art of coaxial probe designs and fabrication materials

Since the late 1970s, numerous studies involving the dielectric measurements of biological tissues have been focused on probe design and fabrication, system development, and systemic error correction techniques [42], [44], [76], [93], [100], [109]. The majority of the custom probes were fabricated from 50 Ω semi-rigid coaxial cables [42], [44], [50], [76], [93], [100]. Probes were customised based on the type and size of the tissue sample to be investigated, and on the desired frequency range of the dielectric measurement study.

In terms of the probe fabrication and design, many custom-made probes have been made of metal and Teflon [42], [44], [76], [100]. Burdette *et al.* used a 2.1 mm diameter probe to perform *in vivo* and *ex vivo* measurement on animal tissue over the frequency range of 0.1-10 GHz [42]. This probe had a flange (i.e., a ground plane) to contain the electromagnetic field at

CHAPTER 2. DIELECTRIC PROPERTIES OF BIOLOGICAL TISSUES

the tip [42]. Kraszewski *et al.* performed *in vivo* animal measurements over the frequencies 0.1-12 GHz using a Teflon-filled metal probe with a 3.2 mm external diameter [44]. Gabriel *et al.* used two Teflon-filled metal probes for *in vivo* and *ex vivo* animal studies in order to acquire tissue dielectric properties at both low and high frequencies [46]. The probe used in the low frequency range (100 Hz-200 MHz) had an external diameter of about 10 mm, and the smaller probe, used for dielectric measurements at the frequency range between 0.2-20 GHz, had an external diameter of 2.9 mm [110]. Larger probes require larger sample size due to the increased sensing volume (i.e., the region of the tissue that is interrogated by the electric field of the probe). In both studies by Burdette *et al.* [42] and Gabriel *et al.* [46], the probe tips of the inner and outer conductors were plated with an inert metal, such as gold and platinum, to modify the effect of electrode polarisation, which is a manifestation of chemical reactions between the probe and the electrolytes (water molecules and hydrated ions) in the tissue. Specifically, this plating process shifts the electrode polarisation, normally occurring at low frequencies, to even lower frequencies (thereby reducing the impact of polarisation in the frequency range of interest) [42], [45], [110]. Popovic *et al.* reported that Teflon-filled copper probes, usually used for broadband reflection coefficient measurements, can cause inaccurate measurements because the probe aperture deteriorates easily and mechanical flaws can occur [111]. The effects of small mechanical imperfections at the probe tip were quantified on the measured reflection coefficient, and it was found that mechanical flaws at probe tip can impact the measurements by altering the reflection coefficient by up to 30% [111]. Notably, Teflon-filled copper probes do not meet bio-compatibility requirements nor can they be autoclaved (steam sterilised), both of which are required for safe *in vivo* measurements on human patients [109].

More recently, borosilicate glass-filled stainless-steel open-ended coaxial probes were designed and fabricated [75], [109]. For instance, the probe fabricated in the study by Popovic *et al.* [109] consists of a 9.5 mm line filled with low-loss porous silica, followed by a shorter line (2.3 mm) filled with a borosilicate glass, with a 2.9 mm air-filled line between the two lines to cancel out the parasitic effects in the transition region. Due to the use of thermally constant and matched, inert, refractory materials, the borosilicate glass-filled probes are biocompatible and suitable for high-temperature sterilisation [109].

Over the last decade, a growing number of dielectric studies have been conducted using commercial probes having designs similar to the probe by Popovic *et al.* [12], [48], [54], [109], [112]. Modern commercial probes are accurate [113], yet require specific sample dimensions and characteristics. In

CHAPTER 2. DIELECTRIC PROPERTIES OF BIOLOGICAL TISSUES

Table 2.1: Use of the commercial probes in recent works. Studies involving breast tissues are shaded in grey. The others involve liver tissues, apart from the porcine skin study conducted by Karacolak *et al.* [114].

Study	Probe	Frequency [GHz]	Tissue type	Sample size
Halter <i>et al.</i> [12]	Slim form (<i>in vivo</i>) High temperature (<i>ex vivo</i>)	0.1-8.5	<i>Ex vivo</i> and <i>in vivo</i> breast tumour (human)	5 mm thick
Karacolak <i>et al.</i> [114]	High temperature	0.3-3	<i>Ex vivo</i> skin (porcine)	45x45x4 mm ³
Lopresto <i>et al.</i> [30]	Slim form	2.45	<i>Ex vivo</i> liver tissue (bovine)	20x20x50 mm ³
Sabouni <i>et al.</i> [112]	Performance	0.5-20	<i>Ex vivo</i> breast tissue (human)	NA
Abdilla <i>et al.</i> [54]	Slim form	0.5-50	<i>Ex vivo</i> muscle and liver (bovine, porcine)	60x60x40 mm ³
Sugitani <i>et al.</i> [15]	Slim form	0.5-20	<i>Ex vivo</i> breast tissue (human)	50-300 mm diameter
Peyman <i>et al.</i> [48]	Slim form	0.1-5	<i>Ex vivo</i> liver tissue (human)	20 mm thick
Martellosio <i>et al.</i> [49]	Slim form	0.5-50	<i>Ex vivo</i> breast tissue (human)	6 mm thick and volume between 700 and 1500 mm ³

particular, Keysight probes, including the slim form probe, the performance probe, and the high temperature probe, have been used in most of the recent tissue dielectric studies [15], [49], [54], [112], [114]. Out of these, the slim form probe is a common choice for tissue measurements due to its small diameter and the fact that it can be steam-sterilised and thus used *in vivo* [15], [49], [54]. The tissue dielectric measurements performed using these commercial probes are summarised in Table 2.1.

2.4 State-of-the-art of dielectric properties of biological tissues

This section presents the state-of-the-art of dielectric studies of biological tissues in order to identify the topics that require further investigation.

Dielectric properties of biological tissues have been analysed since the 1940s [38]–[41]. Early studies focused on the theoretical aspects regarding the interaction of electrical signals with cell suspensions and biological tissues [39], [41].

Then, in the 1980s, the dielectric relaxation processes of biological tissues

CHAPTER 2. DIELECTRIC PROPERTIES OF BIOLOGICAL TISSUES

were further examined and modelled [45], [67], and increasingly the open-ended coaxial line became the most common sensor for the acquisition of the dielectric properties of animal and human tissues [42], [51], [52], [104], [115]–[119]. The open-ended coaxial measurement technique was preferred to the transmission line and cavity perturbation methods, since the open-ended coaxial technique is non-destructive, and allows for *ex vivo* and *in vivo* broadband measurements [42], [51], [93], [100], [104], as was discussed in detail in Section 2.2.

In the 1990s, due to the increasing interest of developing numerical models to simulate the interaction between EM signals and biological tissues, dielectric studies focused on improving the open-ended coaxial probe technique and the dielectric measurement protocol with the aim of obtaining more consistent dielectric data [46], [98], [120], [121].

In the last two decades, additional studies have been conducted to further refine the protocol for the acquisition of dielectric properties with a coaxial probe due to design requirements of novel medical devices, such as MWI, ablation and hyperthermia systems [10]–[12], [28], [30]–[32], [48], [49], [53], [122]. In fact, since the target of these novel EM-based systems is cancerous tissue, knowledge of the dielectric properties of cancerous tissue and the respective contrast with the dielectric properties of the surrounding healthy tissue is fundamental to optimising the design of such technologies. To this extent, several studies were conducted to improve the dielectric characterisation of cancerous tissues, which generally present complex structures and thus high variance in terms of dielectric properties [11], [47], [49].

Overall, there have been a substantial number of dielectric studies reported in the literature. Therefore, in Section 2.4.1, the state-of-the-art of the dielectric measurement of animal and human biological tissues with a coaxial probe is reported. Although several studies were conducted with the aim of refining the dielectric measurement protocol and increasing measurement repeatability, dielectric data is still inconsistent for a subset of tissues, such as healthy adrenal gland and kidney, cancerous liver, and healthy and cancerous breast. Thus, these data inconsistencies are presented in Section 2.4.2, after introducing two types of sources of uncertainty, which may have affected and still affect dielectric measurements. However, each source of uncertainty is analysed in more detail in Chapter 3.

2.4.1 Seminal dielectric studies of biological tissues

Since the late 1940s, a number of studies have been conducted ranging from the development and refinement of dielectric models of biological tissues to the design and optimisation of novel open-ended coaxial probes, which

CHAPTER 2. DIELECTRIC PROPERTIES OF BIOLOGICAL TISSUES

contributed to expanding human and animal tissue dielectric repositories [38]–[41]. While a discussion on coaxial probe design and fabrication was reported in Section 2.3.3, this section describes the state-of-the-art in tissue-based dielectric studies, presented in chronological order.

In 1957, Schwan reported the dielectric properties of tissues and cell suspensions after describing the measurement techniques and the dielectric theories applicable to biological tissues [41]. About two decades later, in 1980, Schwan and Foster presented new data to accurately define the main dielectric processes of biological tissues occurring across a wide range of frequencies (from extra low frequency to MW range) [67].

In the same year, Stuchly and Stuchly, after reviewing and comparing different coaxial line designs for measuring dielectric properties of biological materials at RF and MW frequencies [104], tabulated the dielectric properties of different tissues in the frequency range between 10 kHz and 10 GHz [43]. Furthermore, Burdette *et al.* presented a novel probe technique to accurately perform *in vivo* tissue dielectric measurements at MW frequencies [42], and Schepps *et al.* reported animal normal and tumour tissue data and their dependence on tissue water content in the MW range [69].

In 1982, Athey *et al.* provided detailed information for the design and development of a precision open-ended coaxial line sensor for dielectric measurements of biological tissues [93]. The developed open-ended coaxial probe was used successfully for the acquisition of *in vivo* animal tissue data in the frequency range from 0.01 to 1 GHz [51].

Through the 1980s until the early 1990s, besides the dielectric characterisation of animal and human tissues [42], [43], [76], [123], the tissue dielectric properties were analysed as a function of their physiological properties [67], [115], [124]. For instance, the dependence of dielectric properties on tissue water content at MW frequencies was analysed [69], [117], the *in vivo* and *ex vivo* dielectric properties were compared [44], the difference between healthy and malignant tissues were examined [69], [124], and the change of tissue dielectric properties post-mortem were reported [115].

In 1996, Gabriel *et al.* published a comprehensive literature review reporting animal and human dielectric data across ten frequency decades, from 10 Hz to 20 GHz [125]. The data found in the literature was compared, but inconsistencies were noted due to the use of different equipment and samples (from different species). For this reason, Gabriel *et al.* bridged the gaps in the literature and consolidated the dielectric repository with new *in vivo* and *ex vivo* animal and human tissue data acquired in the frequency range from 10 Hz to 20 GHz [46]. Measurements were performed using three different techniques, depending on the acquisition frequency. Wherever possible, *in vivo* measurements on human patients were selected

CHAPTER 2. DIELECTRIC PROPERTIES OF BIOLOGICAL TISSUES

in preference to *ex vivo* or animal measurements. Where *ex vivo/in vitro* tissue was used, measurements were acquired as soon as possible after death. The data collected and measured by Gabriel *et al.* became the generally accepted standard for dielectric properties of human tissues. This data was made publicly available on the Federal Communications Commission (FCC) website first [126], and on the Italian National Research Council (CNR) website subsequently [127]. This broad availability allowed widespread use of the data among the scientific community and contributed to its diffusion.

In the following years, the dielectric measurement instrumentation and procedure were further improved. Specifically, the volume of the sample interrogated by the coaxial probe was investigated to accurately assign the acquired dielectric data to the actual tissue involved in the measurement [65], [96], [128]. Based on the analysis of the probe sensing volume, precision probes were manufactured for localised dielectric spectroscopy of both low and high permittivity tissues [109].

In 2005, following an extensive measurement programme to dielectrically characterise several animal tissues, Peyman *et al.* described the most relevant challenges related to biological tissue measurements, such as tissue temperature variation, tissue dehydration and probe-sample contact, and reported methods to address them [47]. In 2006, Gabriel and Peyman reviewed tissue dielectric properties with the aim of examining sources of uncertainty and their effect on existing dielectric measurements [55].

In 2007, Lazebnik *et al.* examined breast tissues in terms of dielectric properties, with the aim of assessing the viability of using MWI to detect early stage breast cancer [10], [11]. Through histological categorisation of each breast tissue sample, Lazebnik *et al.* found the breast to be dielectrically heterogeneous, and the dielectric contrast between fibroglandular tissue and cancerous tissue to be as little as 1.1:1 in the range between 0.5 GHz and 20 GHz [11]. These findings were in conflict with a number of former datasets, which had predicted considerably higher dielectric contrast of the order of 10:1 in the same frequency range [60], [61]. In 2014, through a quantitative tissue histological analysis, Sugitani *et al.* suggested that variations in tissue dielectric properties reported in such historical studies may be at least partially attributed to variations in the number of cells of each tissue type (e.g., fat or tumour) within a sample [15]. The findings of the study reported by Sugitani *et al.* [15] underscore the need to take into consideration tissue heterogeneity and histopathology when assigning measured properties to tissue types, something that was lacking in the literature prior to this point.

Finally, recent studies have been conducted to investigate the contrast in dielectric properties between healthy and malignant tissues in order to improve the design of existing medical devices or expand the clinical

application of both imaging and therapeutic devices [12], [48], [53], [112], [122]. Also, a number of works investigated the dependence of the dielectric properties of biological tissues on temperature [28], [31], [36]. The dielectric properties of biological tissues at discrete frequencies and temperatures were measured and presented in terms of linear temperature coefficients, which are fundamental for the optimisation of therapeutic applications, such as hyperthermia and ablation [27]–[32], [36].

The following section highlights inconsistencies in the reported dielectric data of a subset of investigated biological tissues and reviews sources of uncertainty, which may have contributed to the data inconsistencies.

2.4.2 Dielectric measurement of tissues: Inconsistencies and sources of uncertainty

Due to the simplicity of the measurement process with an open-ended coaxial probe, this technique has been used to investigate the dielectric properties of a number of biological tissues [11], [42], [44], [46], [47], [61], [129]. Nonetheless, different sources of uncertainty can affect the measurements and compromise the interpretation of dielectric data, thus resulting in inconsistencies in the reported data [46], [47], [55].

In 1996, dielectric data inconsistencies were highlighted for the first time by Gabriel *et al.*, which grouped the dielectric measurements acquired across the previous five decades according to the investigated tissue type [125]. Specifically, the analysis involved thirteen tissue types. For instance, among these tissue types, Gabriel *et al.* noticed that the dielectric properties of fat and lung were characterised by a high standard deviation in the MW range. In particular, systematic differences were found for fat coming from various species, thus suggesting that those differences were due to the natural variation of fat tissue composition across different species. Thus, human tissues were preferred to animal tissues. Further, the large variation in the dielectric properties of lung was attributed to the different degrees of inflation, since the higher the air content, the lower the dielectric properties. Over all tissues, repeated measurements were performed to increase the reliability of the measurements [46], [71]. Moreover, other factors, such as measurement time from excision, tissue temperature, tissue dehydration, and sample characteristics intrinsic to the tissue type, were taken into consideration to reduce the data uncertainty [46]. Such factors were also considered and compensated for in subsequent studies [11], [47], [54], [130].

With the aim of reducing uncertainty in dielectric data, in the study conducted by Peyman *et al.* [47], different sources of uncertainty in the

CHAPTER 2. DIELECTRIC PROPERTIES OF BIOLOGICAL TISSUES

dielectric measurements were listed and divided into random or “type A” errors, and systematic or “type B” errors, according to the guidelines defined by the NIST in 1994 [55], [131].

In general, the overall performance of the measurement system is assessed by conducting measurements on reference liquids with well-known dielectric properties. The type B errors are associated with the systematic errors of the measurement system. The difference between the measured and reference dielectric values provides an extent of the system performance and represent the main contribution to type B error [47], [55]. However, other factors can contribute to the type B error, such as:

- Quality of the calibration of the system;
- VNA drift occurring after the calibration;
- Temperature variation within the system;
- Movement of cable/probe assembly.

The above factors are generally monitored by repeating the measurement of reference liquids within a calibration [47]. However, the most common practices adopted to monitor or compensate for the type B errors are reported in detail in Section 3.1 of the next chapter.

On the other hand, the main type A error in tissue dielectric measurements is the repeatability of the data, which may contribute to the highest value of uncertainty [47], [55]. The error in repeatability can be related to both measurement system and tissue sample. However, measurements on tissue samples have lower repeatability than measurements on other materials. In fact, type A error is mostly associated with the characteristics of the investigated tissue sample and the interaction of the sample with the system. The main factors that are associated with the tissue characteristics and may contribute to the type A error are the following:

- Sample water content variation/dehydration;
- Sample temperature change;
- Sample handling;
- Sample probe-tissue contact and pressure;
- Sample heterogeneity.

Details regarding monitoring or compensation techniques used to reduce type A errors are provided in Section 3.2.

Since the 1980s, standard techniques have been used to monitor and compensate for type B errors [47], [54], [55], [104], [116], [120]; however, there are not standard techniques yet to monitor and compensate for many type A errors. Although there are good benchmarks to reduce type A errors [47], there are not consistent techniques to reduce the dielectric data variability related to highly heterogeneous tissue samples. Due to the fact that the open-ended coaxial probe technique is based on the assumption

CHAPTER 2. DIELECTRIC PROPERTIES OF BIOLOGICAL TISSUES

that the measured sample is homogeneous, measurements on homogeneous sample regions have generally higher repeatability than measurements on heterogeneous sample regions [47]. To this extent, it is appropriate to conduct dielectric measurements on homogeneous regions of the sample. However, homogeneous regions may not be found across highly heterogeneous tissue samples (such as cancerous samples), which consequently present large variation in terms of dielectric properties [11], [48], [49]. To this extent, the impact of tissue heterogeneity on dielectric data variability (that causes data inconsistencies) is discussed below by reporting the dielectric data for healthy adrenal gland and kidney tissues, cancerous liver tissue, and healthy and cancerous breast tissues.

An example of tissue heterogeneity introducing data inconsistencies involves healthy adrenal gland and kidney tissues. In fact, while adrenal gland and kidney were considered dielectrically homogeneous in several past studies [46], [61], [132], in more recent studies [133], [134], the existence of three distinct dielectric regions corresponding to the capsule, cortex and medulla regions was demonstrated for both the adrenal gland and the kidney. The updated dielectric models consisting of three dielectrically different regions within the adrenal gland and kidney were developed by using a different measurement methodology. Specifically, while previous studies involved dielectric measurements conducted only on the sample surface (i.e., the capsule of adrenal gland and kidney) [46], [61], [132], more recent studies involved dielectric measurements along the sample cross-section, where the capsule, cortex and medulla could be easily distinguished [133], [134]. Thus, these results, illustrated in the relative permittivity and conductivity plots in Fig. 2.5, highlight the importance of considering the anatomy of the organs and their natural heterogeneity when dielectric properties are acquired.

Generally, the higher the natural heterogeneity of the sample, the more complicated the interpretation of the dielectric data from the sample. For instance, by considering both healthy and diseased (i.e., cancerous and cirrhotic) liver tissues, consistent results were found for healthy liver tissue [31], [46], [53], [54], [57], [61], while a wider range of dielectric properties were measured for diseased liver tissues [48], [53]. The difference in dielectric properties between healthy and diseased liver tissue can be observed in the relative permittivity and conductivity plots of Fig. 2.6. The spread dielectric values of diseased liver tissue was attributed to the different types of cancerous tissues analysed by O'Rourke *et al.* [53] and Peyman *et al.* [48], since each cancerous liver sample presented different histological characteristics.

Another example of a highly heterogeneous sample that is challenging to characterise dielectrically is provided by breast tissues. The heterogeneity of healthy and cancerous breast tissues is shown in Fig. 2.7. As highlighted in

CHAPTER 2. DIELECTRIC PROPERTIES OF BIOLOGICAL TISSUES

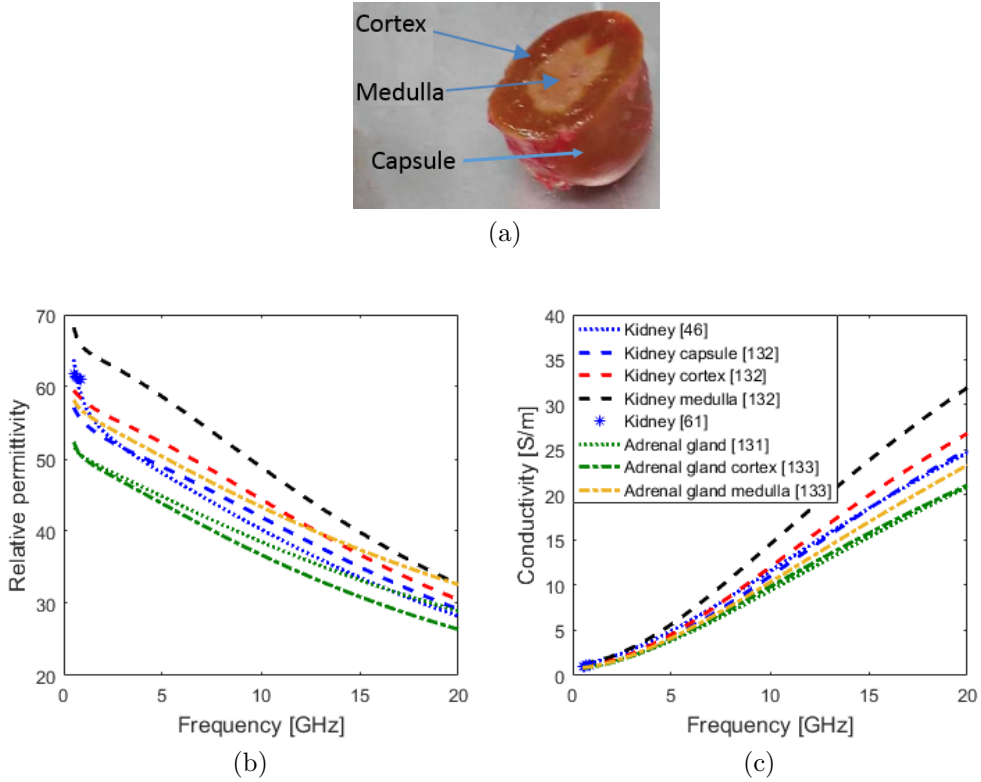
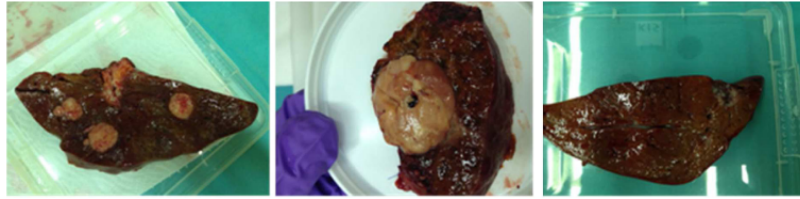
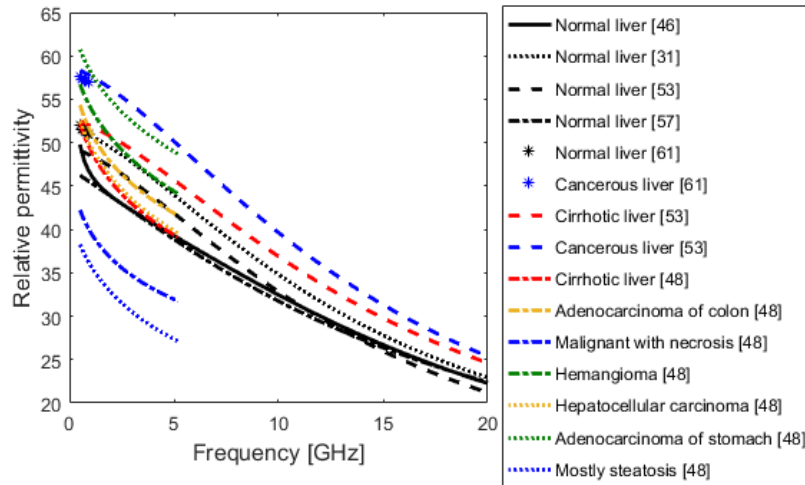


Figure 2.5: Relative permittivity and conductivity plots from adrenal gland and kidney associated with the tissue sample anatomy: (a) diagram illustrating the three anatomical regions, capsule, cortex and medulla, which characterise both adrenal gland and kidney (figure adapted from [134]); (b) relative permittivity plot and (c) conductivity plot summarising adrenal gland data from [132], [134] and kidney data from [46], [133]. In both (b) and (c), it can be noted that, in past studies [46], [132], measurements were performed only on the capsule (that is the external anatomical region of adrenal gland and kidney), while, in more recent studies [133], [134], cortex and medulla (i.e., the other two anatomical regions of adrenal gland and kidney) were also considered for the dielectric characterisation of adrenal gland and kidney.

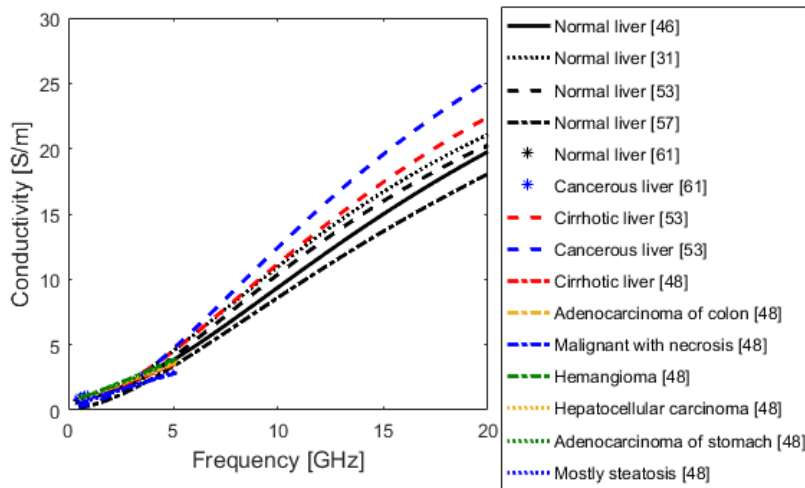
CHAPTER 2. DIELECTRIC PROPERTIES OF BIOLOGICAL TISSUES



(a)



(b)



(c)

Figure 2.6: Relative permittivity and conductivity plots from healthy and cancerous liver tissue: (a) figure from [48] illustrating a subset of diseased liver samples; (b) relative permittivity plot and (c) conductivity plot summarising healthy liver data from [31], [46], [53], [54], [57], [61] and diseased liver data from [48], [53]. In both (b) and (c), it can be noted that consistent data was found for healthy liver tissue [31], [46], [54], [57], [61], while a wider range of dielectric properties were acquired for diseased liver tissues [48], [53].

CHAPTER 2. DIELECTRIC PROPERTIES OF BIOLOGICAL TISSUES

Section 2.4.1, the dielectric properties of breast tissue reported by Lazebnik *et al.* [10], [11] were in contrast with the results presented by Chaudhary *et al.* [60] and Joines *et al.* [61]. The causes of such differences in dielectric properties can be attributed to differences regarding tissue handling and tissue categorisation. For instance, Joines *et al.* [61] categorised healthy samples as normal adjacent muscle and mammary gland, while Lazebnik *et al.* [10], [11] classified healthy tissues in three categories according to their adipose content: Group 1 with 0–30% adipose content, Group 2 with 31–84% adipose content, and Group 3 with 85–100% adipose. Furthermore, Chaudhary *et al.* [60] immersed samples in physiological saline solution prior to dielectric measurements, while, Lazebnik *et al.* [10], [11] and Joines *et al.* [61] did not treat the samples with any solution.

However, inconsistencies in breast tissue data can also be found across more recent studies, as illustrated in the relative permittivity and conductivity plots of Fig. 2.8. For instance, Sugitani *et al.* [15] and Martellosio *et al.* [49] found a high variability in the properties across each tissue type and across patients, which complicates the dielectric differentiation between healthy and malignant tissue. The findings presented by Sugitani *et al.* [15] cannot be compared to the outcomes of the studies previously performed [10], [11], [60], [61] due to the different categorisation of the breast samples, which were classified based on the content of cancer, stroma and adipose tissues. Due to the high variability of dielectric properties across each category, no statistically significant difference was found between cancer and stroma and between stroma and adipose tissue, which compromises the interpretation of dielectric properties acquired from breast samples [15]. On the other hand, Martellosio *et al.* reported the dielectric properties of breast tissue with similar sample classification as that used in the study conducted by Lazebnik *et al.* [10], [11], and the samples were categorised as: low density (80–100% adipose content), medium density (20–80% adipose content) and high density (0–20% adipose content) [49]. Consequently, a contrast in relative permittivity ranging from 1.1 to 5 was found between healthy and cancerous breast tissues across the range of 0.5–20 GHz [49], which partially agrees with the results of Lazebnik *et al.* [10], [11]. However, small dielectric inconsistencies were found between the dielectric data from Martellosio *et al.* [49] and Lazebnik *et al.* [10], [11]. These inconsistencies can be attributed to differences in the size of the histological slices considered to associate the measured dielectric properties with the sample histological content. In fact, although the two studies were conducted with probes having similar geometries (with a diameter of 3 mm for [10], [11] and 2.2 mm for [49]), 7 mm and 2 mm wide breast tissue slices were analysed histologically, respectively, in the studies conducted by Lazebnik *et al.* [10], [11] and Martellosio *et al.* [49].

CHAPTER 2. DIELECTRIC PROPERTIES OF BIOLOGICAL TISSUES

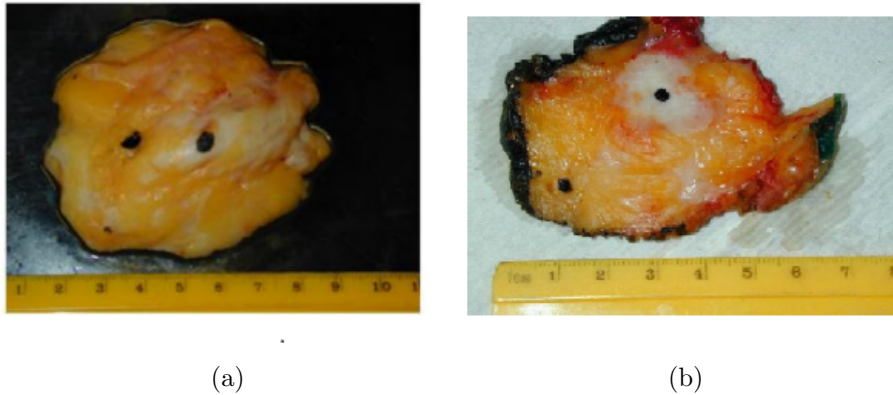


Figure 2.7: Examples of (a) healthy and (b) cancerous breast samples from [10], [11].

Thus, histological slices covering tissue regions located at different distances from the probe may have impacted the tissue sample categorisation and, consequently, the interpretation of the acquired dielectric data.

All of the studies presented above highlight the importance of taking into consideration the heterogeneity of the measured tissue sample and underscore the challenges in accurately attributing the measured dielectric properties to the tissue content of the heterogeneous sample. Thus, for heterogeneous samples, histopathology is generally conducted within the sensing volume of the coaxial probe after completing the dielectric measurement [10]–[12], [15], [49]. However, this procedure adds more steps to the dielectric characterisation of the samples and can lead to other sources of uncertainty, which can consequently result in dielectric data inconsistencies. As seen for breast tissue, data inconsistencies can originate from inaccurate or inconsistent values of sensing volume, differences in the histological categorisation of the samples, and inconsistent dielectric data interpretation.

To this extent, recent studies have been conducted to examine the sensing volume of the commercial dielectric probes commonly used in dielectric studies and evaluated the dependence of the measured dielectric properties on the sample tissue composition [63], [64], [66], [135]. However, further research is still needed to improve the correspondence between histological and dielectric properties for an accurate and consistent characterisation of biological heterogeneous tissues, thus underscoring the motivation of this dissertation.

CHAPTER 2. DIELECTRIC PROPERTIES OF BIOLOGICAL TISSUES

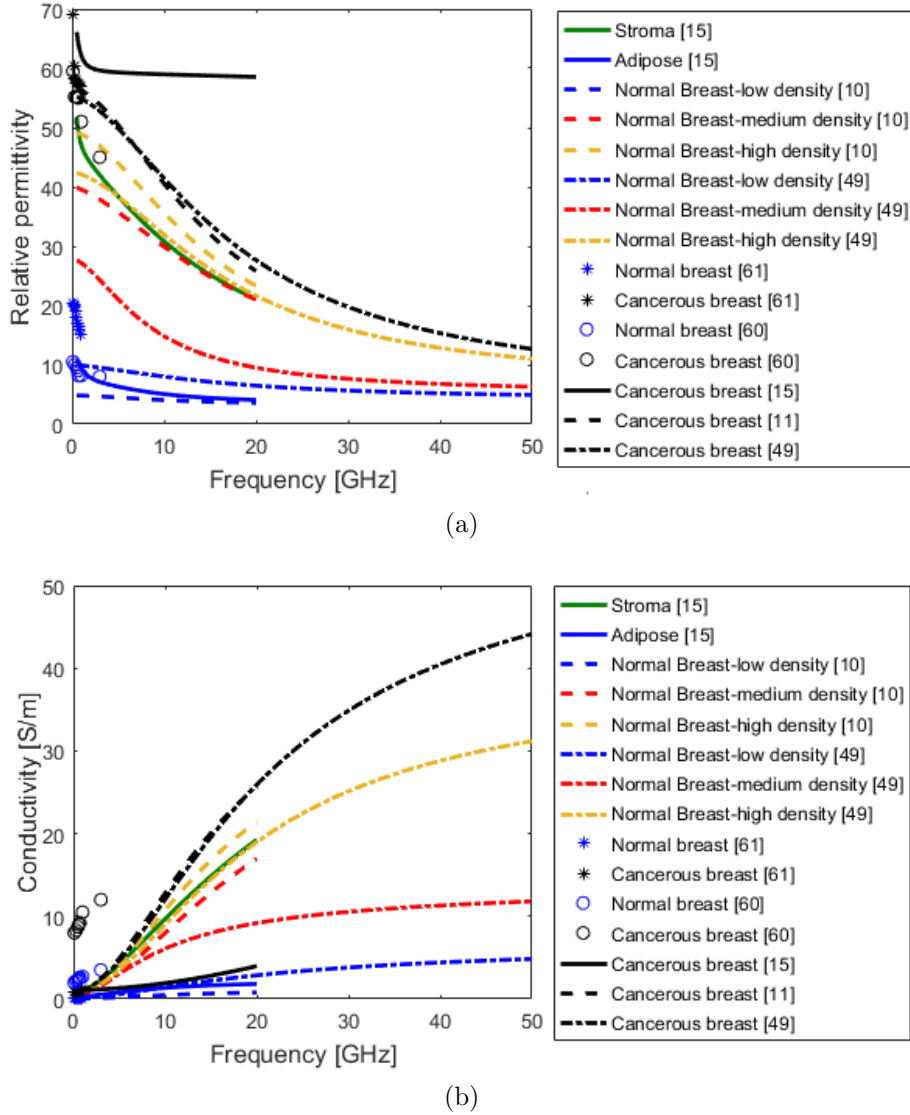


Figure 2.8: (a) Relative permittivity and (b) conductivity plots summarising healthy and cancerous breast tissue data from [10], [11], [15], [49], [60], [61]. In the legend in (a), the low, medium and high density healthy breast tissue refer to the three categories, Group 3 with 85–100% adipose content, Group 2 with 31–84 % adipose content, and Group 1 with 0–30% adipose content, respectively, in the study by Lazebnik *et al.* [10], and to the three categories, 80–100% adipose content, 20–80% adipose content and 0–20% adipose content, respectively, in the study by Martellosio *et al.* [49]. Furthermore, from (a) and (b), it can be noted that the reported dielectric data is inconsistent for both healthy and cancerous breast tissue, mostly due to tissue heterogeneity and differences in sample categorisation across the literature.

2.5 Summary

In this chapter, dielectric properties of biological tissues have been defined and the state-of-the-art in the acquisition of dielectric properties of biological tissues with an open-ended coaxial probe has been presented in terms of measurement techniques and seminal dielectric studies.

Specifically, in Sections 2.1.1 and 2.1.2, the principle theoretical aspects regarding the interaction of EM fields with biological tissues were reviewed, and, in Section 2.1.3, the mathematical models used to compactly represent the dielectric dispersions of polar solutions and biological tissues (that can be then included in numerical EM solvers) were presented.

In Section 2.2, the most common techniques used to dielectrically characterise biological tissues in the MW range were presented along with the known advantages and drawbacks of each. Specifically, the transmission line, cavity perturbation and open-ended coaxial probe techniques were reported in Section 2.2.1, Section 2.2.2, and Section 2.2.3, respectively. For each measurement technique, the characteristics of the system, such as broadband or single-frequency system, system/measurement complexity, measurement accuracy, and the requirements of the measurement samples, such as *in vivo*/*ex vivo* samples, sample size restrictions and sample handling, were reported. Furthermore, in Section 2.2.3, the open-ended coaxial probe technique was identified as the most appropriate method for the dielectric characterisation of biological samples in the MW range, since this technique is broadband, does not require custom sample handling, and allows both the measurement of *in vivo* samples and the analysis of *ex vivo* samples at different temperatures.

Thus, the open-ended coaxial probe technique was the focus of Section 2.3. In Section 2.3.1, the EM transmission along the coaxial probe and the EM interaction of the probe with a biological sample, resulting in the reflected signal that is expressed by the reflection coefficient, were described. Consequently, in Section 2.3.2, the main algorithms used to convert the reflection coefficient into permittivity were presented, and one of the lumped equivalent circuit models (the antenna model) was described in more detail, since the antenna model has been implemented to process the numerical data of this dissertation. After presenting the theoretical basis of the open-ended coaxial probe technique, the state-of-the-art of coaxial probe designs and fabrication materials was provided in Section 2.3.3. At the end of Section 2.3.3, the commercial probes most commonly used in recent dielectric studies were highlighted and the corresponding experiments on biological tissues tabulated.

Lastly, in Section 2.4.1, key dielectric studies performed on biological

CHAPTER 2. DIELECTRIC PROPERTIES OF BIOLOGICAL TISSUES

issues using the open-ended coaxial probe technique since the 1940s were reported and, in Section 2.4.2, the inconsistencies in reported dielectric data for a subset of tissue samples were highlighted. Specifically, in Section 2.4.2, the main sources of data uncertainty (and thus inconsistencies) were reviewed, resulting in the following findings.

- Sources of uncertainty in the dielectric measurements can be divided into random or “type A” errors, and systematic or “type B” errors. Generally, type A errors are intrinsic to the characteristics of the measured sample, such as temperature, probe-sample contact, probe-sample pressure, sample handling procedure, *in vivo* versus *ex vivo* experiments, sample tissue morphology, and heterogeneity. On the other hand, type B errors are related to measurement equipment choice, and measurement calibration and validation;
- While standard techniques have been developed to monitor or compensate for type B errors, type A errors contribute most to the uncertainty in more recent dielectric studies.
- Type A errors are mostly related to the measurement repeatability that is higher for heterogeneous tissues than for homogeneous tissues.

The above findings provide the motivation for conducting a thorough analysis of both type A and type B errors, with more focus on type A errors, which constitute a higher source of uncertainty in dielectric data. Specifically, type A and type B errors are defined in Chapter 3 as tissue-related and equipment-related confounders, respectively, since type A errors are mainly due to factors related to the characteristics of the investigated tissue samples, and type B errors are mainly related to the characteristics of the measurement system and its performance. In Chapter 3, equipment-related and tissue-related confounders are examined together with their different compensation techniques throughout each step of the dielectric measurement process. Due to experimental challenges in reducing the variability in dielectric data associated with the sample tissue heterogeneity, the last sections of Chapter 3 focus on the techniques used to improve the correspondence between the dielectric properties and histological content of measured heterogeneous samples. Thus, Chapter 3 helps in defining a measurement protocol able to reduce uncertainty and inconsistencies in dielectric data, and introduces the experimental objectives of this dissertation.

Dielectric measurement protocol for biological tissues: Confounders and best practices

Related publications

*A summary of each step of the open-ended coaxial probe measurement procedure, with the best practices adopted to reduce errors in the dielectric measurement of biological tissues, has been published in the journal of Diagnostics in a review paper entitled “Open-ended Coaxial Probe Technique for Dielectric Measurement of Biological Tissues: Challenges and Common Practices”, in 2018 (A. La Gioia, E. Porter, I. Merunka, S. Salahuddin, A. Shahzad, M. Jones, and M. O’Halloran, “Open-ended Coaxial Probe Technique for Dielectric Measurement of Biological Tissues: Challenges and Common Practices,” *Diagnostics*, 8, 40, 2018).*

Furthermore, the content of this paper has supported the identification of the minimum types of raw data and metadata necessary for interpreting and replicating a dielectric study, which led to the development of the Minimum Information for Dielectric mEasurEments of biological tissues (MINDER) standard. The MINDER standard enables reproducibility of measurements, ease of interpreting and re-using data, and comparison of data across studies. The MINDER standard has also been published in the journal of RF and MW Computer-Aided Engineering in a paper entitled “Minimum information for dielectric measurements of biological tissues (MINDER): A framework for repeatable and reusable data”, in 2017.

As seen in Chapter 2, the open-ended coaxial probe has been the most commonly used technique for dielectrically characterising biological tissues in the MW frequency range since the 1940s, due to its operating principles that enable *in vivo*, non-destructive measurements. However, the protocol for the dielectric measurement of biological tissues with an open-ended coaxial probe consists of multiple steps that require control over a number

CHAPTER 3. DIELECTRIC MEASUREMENT PROTOCOL

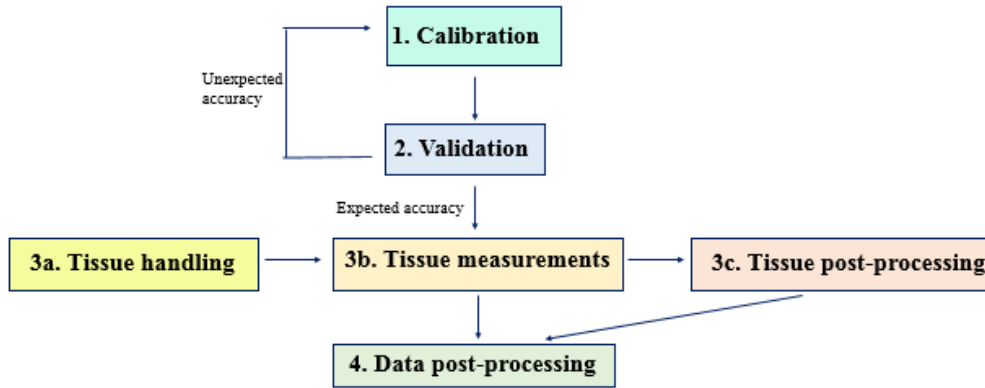


Figure 3.1: Flowchart of the main steps of the protocol for measuring the dielectric properties of biological tissues.

of factors, or confounders, which can erroneously affect the measurement and compromise the interpretation of the measured dielectric data. Notably, no standard protocol for the dielectric measurement of tissues exists.

Thus, this chapter reviews the measurement protocol across past and recent dielectric studies from the literature. This review is conducted by examining each step of the protocol together with known and potential sources of errors. For each source of error that can be either equipment-related or tissue-related, the most common compensation techniques used in the literature are examined, along with their respective weaknesses and strengths. This thorough review of the dielectric measurement process with an open-ended coaxial probe has the aim of identifying the main sources of errors and the corresponding most suitable techniques for minimising the uncertainty of the measured data.

Specifically, in the following sections, the steps involved in an open-ended coaxial measurement, ranging from the calibration of the system, to the actual measurement process and the corresponding data and sample post-processing, are detailed. The main steps of the protocol for measuring the dielectric properties of biological tissues are schematised in the flowchart in Fig. 3.1.

In Section 3.1, the standard calibration method, the typical system validation procedure and the measurement uncertainty estimation are discussed. The steps regarding the probe selection, tissue handling and measurement procedure are discussed in Section 3.2, along with the associated tissue-related confounders. In Section 3.3, the steps involving data and sample tissue post-processing are detailed. While the data post-processing supports

the interpretation of the data measured from all tissue samples, the tissue post-processing only applies to the dielectric characterisation of samples that have heterogeneous tissue structures. Lastly, the chapter concludes with Section 3.4.

3.1 Characterisation of the dielectric measurement system

This section focuses on the steps of the dielectric measurement protocol that relate to the measurement equipment itself. The topics of the calibration and validation of the measurement system are discussed, along with the determination of the measurement uncertainty.

3.1.1 System calibration

The reliability of dielectric measurements is principally determined by the accuracy of the acquired input impedance. The accuracy of impedance measurements can be substantially improved by performing a standard calibration procedure before each set of measurements [44], [76], [93], [120]. In this section, a description of the calibration process for the open-ended coaxial probe is provided, followed by an in-depth analysis of the related confounders.

In general, coaxial probe measurements use a three load standard calibration procedure for one-port error correction. Any three different standard materials can be used for calibration, as long as the dielectric properties of those standards are well known [120], [136], [137]. The choice of standard materials to use may be based on the ease of use, availability, or similarity to the materials under test [50], [120]. The three most common standards used for coaxial probe calibration are: open-circuit, short-circuit, and a broadband load [138]. The calibration is performed at the reference plane of the probe while the probe is connected to the VNA through a specialised cable or an L-shaped connector. The calibration procedure aims to find a relation between the expected complex reflection coefficient and the measured complex reflection coefficient and, thus, to correct for systematic errors.

The three standards are necessary to determine and compensate for the three main sources of error: directivity error, impedance mismatch and frequency tracking error [138]. The directivity error occurs when a part of the generated signal does not come in contact with the sample. This error is due to a direct leakage of the directional coupler or imperfect connectors. Impedance mismatch between the system components causes

CHAPTER 3. DIELECTRIC MEASUREMENT PROTOCOL

Table 3.1: The standard calibration process with confounders and compensation techniques listed for each step, with open-circuit, short-circuit, and a liquid load material shown as the three calibration standards.

	Confounders	Compensation
Equipment set-up	<ul style="list-style-type: none"> • Environmental parameter change [131] • Probe contamination [28], [42], [53], [139] • Imperfect connections [42] • Cable movement [10], [47], [66], [113] 	<ul style="list-style-type: none"> • Environmental parameter control [56], [58] • Probe inspection and cleaning [30], [46], [47], [52] • Connection check [42] • Cable fixing with tape [30], [54], [112]
Open	<ul style="list-style-type: none"> • Particles on probe tip [75] 	<ul style="list-style-type: none"> • Probe cleaning [30], [46], [47], [52] • Smith Chart check [140]
Short	<ul style="list-style-type: none"> • Poor probe-short block contact [75] 	<ul style="list-style-type: none"> • Short block and probe cleaning [75] • Short block repositioning [75] • Smith chart check [140]
Load	<ul style="list-style-type: none"> • Accuracy of liquid model [50], [120] • Liquid temperature [47], [50], [121], [141] • Air bubbles [65], [72], [98] • Liquid contamination [47] • Probe position in liquid [65] 	<ul style="list-style-type: none"> • Deionised water model has best accuracy [120] • Temperature monitoring/ control [30], [47], [54], [139] • Probe re-immersion in liquid [75] • Limited exposure to air [47] • Probe distant from beaker sides [65]

undesired reflected signals. The frequency tracking error involves the changes in magnitude and phase flatness versus frequency between the reference and the reflected signal. This error is generally due to differences in directional and test couplers [138].

If performed correctly, a good calibration procedure considerably reduces systematic errors. The quality of the calibration depends on the accuracy in the measurements of the three standards and on the level of control over the factors that can affect the process. In the following subsections a list of the calibration steps required to reduce the confounders is reported. In addition, the confounders and the corresponding methods for their control and compensation are summarised in Table 3.1.

3.1.1.1 Equipment set-up and confounders

Before performing the calibration, environmental parameters, such as temperature, pressure and humidity, are generally controlled or monitored [56], [58] because environmental changes may impact measurement results [131]. Furthermore, system components need to be checked [42], the probe tip cleaned and verified by visual inspection [30], [46], [47], [52], and the cable fixed in place [30], [54], [112] as imperfect connections [42], probe contamination [28], [42], [53], [139], and cable movement [10], [12], [47], [66], [113] can all result in a poor calibration and thus unreliable measurements.

3.1.1.2 Acquisition settings and confounders

Prior to calibration, the frequency range needs to be selected based on the planned measurements. Subsequently, the number of acquisition frequency points must be defined. Frequency points may be equidistant according to a linear or a logarithmic scale or non-equidistant, thus distributed more densely in some regions rather than others. The use of a logarithmic scale can be advantageous when data is acquired over a frequency range covering more dispersion regions, as there will be more points taken at the frequency points where the largest change in dielectric properties occurs (due to dispersions) [142]. The signal power and measurement bandwidth must also be selected in the VNA software. The choice of number of frequency points and bandwidth requires a trade-off between the measurement accuracy and speed of data acquisition. In fact, a smaller number of points and a larger bandwidth result in less accurate but faster data acquisition, while a higher number of points and a narrower bandwidth result in more accurate but more time-consuming data acquisition.

3.1.1.3 Measurement of the three standards and confounders

Once the measurement settings are selected, the calibration measurements of the three standards (i.e., open-circuit, short-circuit and broadband load) can be performed. The set-up for the measurements of open-circuit, short-circuit and broadband load is schematised in Fig. 3.2.

As highlighted in Table 3.1, visualisation of the complex impedance on the VNA Smith chart is key to identifying the unwanted presence of particles at the probe tip and confirming the quality of the open or short-circuit [75], [117]. In particular, having a good quality short-circuit is vital to a successful calibration [50]. Therefore, proper contact between the short and the probe must be ensured. Other than this, the open and short measurements are relatively straightforward and do not require any additional consideration.

Conversely, several confounders can introduce error into the load measurement. In the literature, different liquids have been examined as potential load materials [116], [120]. The standard liquid is generally selected such that the complex impedance of the load is considerably different from the other two standards [116]. The most typical liquid used as a load is deionised (DI) water [15], [28], [66], [112], [114], [143]. Polar liquids (for example, ethanol, methanol, and saline) also meet the requirements [116] and exhibit high conductivity and permittivity as a function of frequency. Nyshadham *et al.* conducted a quantitative analysis of the effect of the uncertainty of the models of different standard materials on the uncertainty of the measured

CHAPTER 3. DIELECTRIC MEASUREMENT PROTOCOL

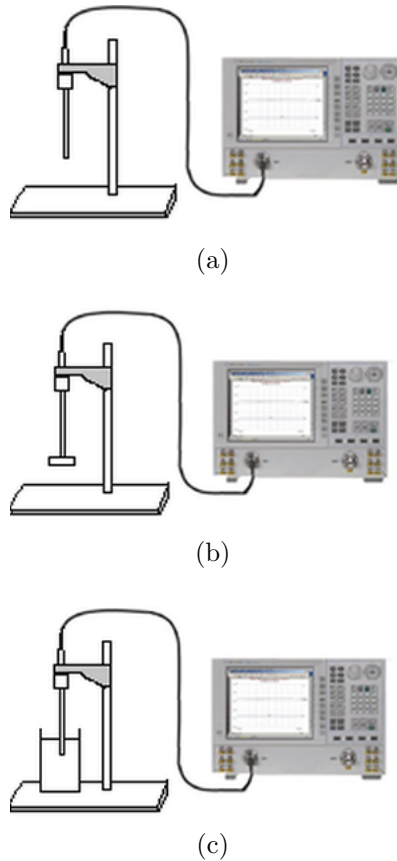


Figure 3.2: Schematised set-up for the calibration of the coaxial probe. The calibration procedure involves the measurement of the three standards: (a) open-circuit, (b) short-circuit and (c) broadband load. Portions of this figure were adapted from [75].

permittivity [120]. In this study [120], different liquids (having different models) were used for calibration and it was verified that DI water represents a better calibration standard than methanol and saline because there are smaller uncertainties in the Cole-Cole model of DI water (in other words, the dielectric properties of deionised water are the most well-known and well-characterised). Indeed, the accuracy of the model represents one of the confounders affecting the calibration procedure and the uncertainty of the measured permittivity. Specifically, a quantitative analysis that examined the impact of errors in the model of one of the calibration standards (in this case, acetone), found that model errors of 2% induced a similar magnitude of error into the measured relative permittivity [144].

During the calibration process, the temperature of the load liquid needs to be maintained and monitored, since the dielectric properties are temperature-dependent [47], [50], [121], [141]. The permittivity of liquids vary by up to

2.2% per degree Celsius [121]. The measurement of deionised water, or any standard liquid, as a calibration load may be performed at room temperature or at any fixed temperature. The liquid temperature can be monitored using a thermometer [75] and the temperature may be maintained using a water bath [30], [47], [54], [139]. However, the study by Gabriel and Peyman [55] advises to perform the calibration at a temperature close to that of the sample temperature, otherwise an uncharacterised amount of error could be introduced in the dielectric measurement.

Aside from the liquid temperature and model accuracy, other confounders, such as liquid contamination [47], air bubbles between the probe and the liquid [65], [72], [75], [98], and probe position in the liquid-filled beaker [65], have been investigated. In order to avoid any impurity in the DI water, the beaker filled with liquid is generally kept closed [47]. The presence of air bubbles between the probe tip and the standard liquid can result in deviations in the dielectric measurement data by up to 20%, due to the fact that the material within the sensing region is then a mixture of air and liquid [98]. A transparent beaker is recommended so that air bubbles can clearly be seen. If bubbles are present, they need to be removed prior to measurement. The removal of bubbles may be achieved by gently tapping the probe tip on the bottom of the beaker, or by lowering the beaker away from the liquid and then re-immersing it on an angle [75]. A soft brush (non-metallic, to avoid scratches) may also be used to remove any bubbles without having to move the probe or the beaker. In addition, the probe needs to be immersed in the liquid and positioned in the beaker such that the liquid is the only material within the probe sensing volume. Accurate positioning avoids undesirable reflections from the beaker walls. Hagl *et al.* provided a process for finding the minimum distance between the probe and the beaker sides according to the probe size; these distances also depend on the properties of the liquid material in the beaker, and the frequency range of interest [65].

3.1.1.4 Confounders introduced in the system after calibration

Following the calibration procedure, two additional equipment-related confounders can introduce errors in dielectric measurements: VNA drift over time and cable movement [10], [12], [28], [47], [54], [66], [112], [113]. The system drift can be characterised and taken into account in the measured dielectric data [47], [54]. This factor can be quantified by taking several measurements on a standard liquid at defined time instants in the period after calibration [47]. When a cable is moved, given the difficulty in precisely characterising the systematic error introduced by the cable movement, a

new calibration is required. However, low loss and phase stable cables have the potential to minimise the impact of the error of the cable stability on the results [11], [50], [65]. In some studies, the cable was fixed in place (using adhesive tape) to limit the effect of the cable movement in the dielectric data [30], [54], [112]. An alternative approach may be to replace the cable with an L-shaped connector, when such a rigid set-up does not overly restrict dielectric data acquisition [142].

After each calibration, it is good practice to first confirm proper calibration by re-measuring one of the calibration standards, commonly the short [54]. However, re-measuring the properties of materials used during calibration does not guarantee that the system is functioning error-free, it just indicates that the calibration error-correction algorithms were successfully applied. Thus, a measurement of a known liquid, other than the one used in calibration, is also required in order to validate the accuracy of the calibration. Details about the validation procedure and the measurement uncertainty calculation are discussed in the next sections.

3.1.2 Measurement validation

The validation procedure consists of measuring the dielectric properties of a known reference liquid, in order to determine the quality of the calibration and to monitor systematic errors [47], [54], [55], such as VNA drift and noise due to cable movement [47]. Thus, it is good practice to perform validation immediately following calibration [42], [47], [65], [139], [145] and again after acquiring a set of tissue dielectric data [10]. The validation procedure can also be conducted whenever anomalies are observed in the dielectric data of the investigated material in order to isolate the source of error. For instance, if the same anomalies are observed in the reference liquid dielectric trace, the error is due to changes in the system and a new calibration is needed; if the anomalies are not evident in the liquid trace, the error is likely sample-related and further investigation is needed to identify the source of the error.

During the validation procedure, the dielectric properties of a standard liquid are measured and compared to the properties of the corresponding known model [54], [55], [96], [120], [121], [145]. Since the dielectric properties of reference liquids are temperature- and frequency-dependent, monitoring or controlling the temperature of the liquid during the validation process is required [47], [54], [145]. Liquids in general are selected for validation purposes as they are homogeneous and are free of many of the confounders affecting solids or semi-solids (e.g., incorrect probe-sample contact, inconsistent probe-sample pressure). However, several confounders can still introduce

CHAPTER 3. DIELECTRIC MEASUREMENT PROTOCOL

errors in the measurement of the validation liquid. The factors that affect the validation quality are similar to those present in the load measurement during the calibration procedure. Thus, details regarding confounders in the liquid dielectric measurement and how they are addressed can be found in the previous section.

Alcohols and saline are the most common polar reference liquids used in the validation procedure [10], [42], [55], [65], [121], [146]. Polar solutions are particularly suitable as validation liquids because they have comparatively high relative permittivity and high dielectric loss at radio and MW frequencies. Both the relative permittivity and conductivity have a strong frequency dependence, which is a feature of the pronounced molecular dielectric relaxation behaviour [50]. Details regarding alcohols, saline solutions, and other reference liquids are, respectively, reported in the following subsections.

3.1.2.1 Alcohols

Methanol, ethanol, ethanediol and butanol are the types of alcohols generally used to characterise the system and calculate the uncertainty in the dielectric measurements [10], [54], [65], [96], [120], [121], [145] prior to tissue measurements. Methanol, ethanol, and butanol, in particular, are used as standard liquids because they represent the high, intermediate, and low dielectric property values, respectively, within the range of those expected for human breast tissue at MW frequencies [10], [96], [145]. The alcohols also have well-established permittivity models [10], [96], [121], [145]. Ethanediol, which has also been modelled in the MW frequency range [54], [145]–[147], has a static permittivity about half that of pure water [147]. Standard methods for obtaining the known dielectric property values for each of these alcohols have been detailed thoroughly [145].

Although alcohols present properties similar to those of biological tissues, there are some constraints that must be taken into account when using them as reference liquids. For instance, the alcohol models are accurate in restricted frequency ranges and at discrete temperatures only [120], [141], [145], [147], [148]. Furthermore, the dielectric properties of alcohols can change during storage and handling. For example, methanol has very low vapour pressure and evaporates rapidly. These properties of methanol can contribute to a decrease in the liquid temperature and, consequently, to a dielectric property change over the course of just a few minutes when exposed to air [96], [145]. In order to minimise these effects, the dielectric properties of methanol are generally measured immediately after it is poured into the measurement beaker [96] and the temperature is monitored. Lastly, since alcohols are inflammable and have an acute inhalation toxicity, working with

these liquids requires a safety protocol, such as the use of special fire-proof storage cabinets and handling under a fumehood [145].

3.1.2.2 Saline

The dielectric properties of different concentrations of NaCl (saline) solutions at various temperatures have been modelled in the MW frequency range [55], [73], [149]–[151]. Specifically, Stogryn provided models in the gigahertz range for computing the complex permittivity of saline as a function of temperature and concentration (between 0.25 and 0.5 M) in order to allow these liquids to be used as references [149]. More recent models, based on extended experimental data, are now available for solutions having concentrations between 0.001 and 5 mol/L in the frequency range of 0.10–40 GHz, for any temperature between 0–60°C [73], [143], [146], [150], [151]. Although saline models were obtained from non-traceable dielectric data, saline solutions are the most convenient reference liquids used to assess the uncertainty in measuring the dielectric properties of biological materials [146].

Among all of the saline solutions, 0.1 M NaCl solution is the most commonly used reference liquid, since it has similar dielectric properties to those of biological tissues [47], [54], [146]. Furthermore, 0.1 M NaCl is stable in temperature and electrical properties during storage and handling. At room temperature, saline does not evaporate quickly like alcohols. Saline solutions are also straightforward to prepare (with commercially-bought solutions being cost-effective) [146] and to use. Saline solutions are also less dangerous than alcohols, and thus they do not require the use of fire-proof storage cabinets or handling under a fumehood. For 0.1 M NaCl, models that cover relatively wide frequency and temperature ranges are available [146]. However, due to poor traceability of the data used to obtain the models by Peyman *et al.* [146] (since the data was acquired with only a single measurement system and a single measurement technique, and then compared to reference data measured under unknown conditions), the saline models are likely not as accurate as the models for alcohols.

3.1.2.3 Other liquids

Several other liquids, such as formamide [48], [55], [147], [150], DI water [50], [141], [145], dimethyl sulphoxide (DMSO) [50], [141], [145], and acetone [50], [145], [152], have been used as reference liquids.

Formamide is a polar organic solvent, which has a relative permittivity of approximately 110 at frequencies below 1 GHz that drops down to a value of around 7 at frequencies above 50 GHz (when handled at room

temperature) [147]. The temperature-dependent model for characterising the dielectric properties of formamide across the MW frequency range was developed by Jordan *et al.* [147] and more recently by Barthel *et al.* [148] using waveguide interferometry [55], [147], [148]. The parameters of different models were found at discrete temperatures in the frequency range between 0.2-89 GHz. The reliability of the model from Jordan *et al.* [147] is affected by the limited discrete frequency points used in the dielectric measurements from which the model has been obtained. In both studies by Jordan *et al.* [147] and Barthel *et al.* [148], the dielectric models are available only for limited discrete temperatures. Also, since formamide is toxic, a custom handling protocol is required.

When it is not used as broadband load in the calibration procedure, DI water represents an advantageous validation liquid [120], [141]. In fact, DI water has dispersive properties similar to those of biological tissues and has been accurately modelled in the MW frequency range, for any temperature between -4.1-60°C [141]. DI water has also the advantage of being a stable liquid and does not require special handling.

DMSO is a highly polar organic reagent that has a high relaxation frequency. DMSO has relative permittivity values similar to those of muscle tissue. Although DMSO dielectric models covering a wide frequency range [141] and different temperatures [145] have been developed, DMSO does not represent a convenient reference liquid, since it is particularly hygroscopic [50], [145]. In particular, when DMSO evaporates, the liquid temperature increases, causing an increase in relative permittivity values [145].

Acetone is a polar organic solvent having intermediate permittivity values, which have been modelled only in the upper MW frequency range [152]. Acetone requires special handling because it has a boiling point of 56°C and has the potential to soften some plastics [50], [145].

Liquid properties and information about available models and storage/handling procedure related to the most common categories of reference liquids are reported in Table 3.2. The column “Models” contains the most referenced models, i.e., those that cover the widest frequency range and largest, most continuous temperature interval.

3.1.3 Measurement uncertainty calculation

The uncertainty of measurements is generally calculated according to the guidelines defined by the NIST [47], [54], [55], [131]. Thus, in this subsection, the uncertainty of the measurement is discussed in terms of “standard” uncertainty. Multiple measurements performed on the same material of known dielectric properties enables determination of the uncertainty of the

CHAPTER 3. DIELECTRIC MEASUREMENT PROTOCOL

Table 3.2: Reference liquid properties, available models, and storage and handling procedures (where f =frequency, T =temperature).

Liquid	Models	Storage and Handling
Methanol	Debye model [50]: <ul style="list-style-type: none"> • $f = 0.1-5$ GHz • $T = [10^{\circ}\text{C}, 50^{\circ}\text{C}]$, 5°C increments Cole-Cole model [147]: <ul style="list-style-type: none"> • $f = 0.01-70$ GHz • $T = [10^{\circ}\text{C}, 40^{\circ}\text{C}]$, 10°C increments 	Alcohols are flammable and have an acute inhalation toxicity. Fire-proof storage cabinets required. Handling in fumehood required. Rapid evaporation may occur and should be avoided (particularly with methanol and ethanediol). Ethanediol is hygroscopic and when it evaporates the liquid temperature increases, causing an increase in relative permittivity [50].
Ethanediol	Davidson-Cole model [50]: <ul style="list-style-type: none"> • $f = 0.1-5$ GHz • $T = [10^{\circ}\text{C}, 50^{\circ}\text{C}]$, 5°C increments 	
Ethanol	Debye- Γ model [50]: <ul style="list-style-type: none"> • $f = 0.1-5$ GHz • $T = [10^{\circ}\text{C}, 50^{\circ}\text{C}]$, 5°C increments 	
Butanol	Double Debye model [50]: <ul style="list-style-type: none"> • $f = 0.1-5$ GHz • $T = [10^{\circ}\text{C}, 40^{\circ}\text{C}]$, 5°C increments 	
Saline (NaCl)	Davidson-Cole [73] and Cole-Cole models [146]: <ul style="list-style-type: none"> • Concentrations = $[0.001, 5$ mol/l] • $f = 0.13-20$ GHz [146] or $f = 0.1-40$ GHz [73] • $T = [5^{\circ}\text{C}, 35^{\circ}\text{C}]$ (any intermediate T) [146] or at 17 temperatures in the interval $T = [10^{\circ}\text{C}, 60^{\circ}\text{C}]$: 10°C, 20°C, increments of 2°C in $[24^{\circ}\text{C}, 50^{\circ}\text{C}]$, and 60°C [73]. 	Storage in sealed containers. No special handling required.
Formamide	Davidson-Cole model [148]: <ul style="list-style-type: none"> • $f = 0.2-89$ GHz • $T = [10^{\circ}\text{C}, 25^{\circ}\text{C}]$, 5°C increments • $T = [25^{\circ}\text{C}, 65^{\circ}\text{C}]$, 10°C increments 	Fire-proof storage cabinets required. Handling in fumehood required.
DI water	Debye model [153]: <ul style="list-style-type: none"> • $f = 1.1-57$ GHz • $T = [-4.1^{\circ}\text{C}, 60^{\circ}\text{C}]$ (any intermediate T) 	Storage in sealed containers. No special handling required.
Dimethyl sulphoxide (DMSO)	Debye model [50]: <ul style="list-style-type: none"> • $f = 0.1-5$ GHz • $T = [10^{\circ}\text{C}, 50^{\circ}\text{C}]$, 5°C increments Davidson-Cole model [153]: <ul style="list-style-type: none"> • $f = 0.001-40$ GHz • $T = 25^{\circ}\text{C}$ 	DMSO has an acute inhalation toxicity. Since, DMSO is exceptionally hygroscopic, it needs to be measured as soon as the container lid is removed [50].
Acetone	Static permittivity [50]: <ul style="list-style-type: none"> • $f = 0.1-5$ GHz • $T = [10^{\circ}\text{C}, 50^{\circ}\text{C}]$, 5°C increments Budo model/confined rotator models [152]: <ul style="list-style-type: none"> • $f = 50-310$ GHz • $T = 20^{\circ}\text{C}$ 	Acetone boiling point is at 56°C [50]. Special handling is required, since it is a powerful liquid able to soften some plastics [50] and it is flammable.

CHAPTER 3. DIELECTRIC MEASUREMENT PROTOCOL

measurement system in terms of the repeatability and accuracy. The repeatability of the measurement may be expressed quantitatively in terms of the characteristics (e.g., standard deviation) of data repeatedly acquired under the same measurement condition [131]. The accuracy of the measurement may be defined as the average percentage difference between the dielectric properties of the acquired data and those of the corresponding model [47], [54]. The repeatability varies between measurements and gives the extent of random errors, while the accuracy is constant across measurements and is related to systematic errors, which are introduced by inaccuracies in the calibration procedure. For these reasons, repeatability and accuracy uncertainties are represented by Gaussian and rectangular distributions, respectively [131]. The uncertainties in repeatability and accuracy contribute to the total uncertainty in the dielectric measurements [47], [54], [55], [131]. In particular, the total combined uncertainty is the sum of individual uncertainties related to repeatability, accuracy, VNA drift and cable movement, with each uncertainty value divided and multiplied by standard divisors and sensitivity coefficients (associated to the probability distribution of each corresponding individual uncertainty according to the NIST guidelines [131]). Furthermore, the expanded uncertainty can be calculated by multiplying the combined uncertainty by a coverage factor (k) that is related to a specific confidence interval. For instance, a coverage factor of 2 provides a confidence level of approximately 95%. An example of the combined and expanded uncertainty calculation by Peyman *et al.* [47] is reported in Table 3.4, where the numerical values of uncertainty associated with repeatability, accuracy, VNA drift and cable movement are referred to relative permittivity values obtained from measurements on 0.1 M NaCl solution in the MW range between 300 MHz and 10 GHz. Later, Gabriel and Peyman also reported the uncertainties for additional validation liquids, including alcohols and formamide, but only in repeatability and accuracy, since the uncertainties related to VNA drift and cable movement were the same for all liquids [55]. In fact, in the two studies [47], [55], measurements were conducted with the same equipment, and thus the systematic uncertainties related to VNA drift and cable movement were calculated only on 0.1 M NaCl. Alternatively, in the studies conducted by Gregory *et al.*, uncertainties associated with specific input parameters were evaluated by means of Monte Carlo modelling [145], [154].

The uncertainties related to systematic errors (i.e., uncertainty in accuracy, and uncertainties related to VNA drift and cable movement) are taken into account when interpreting dielectric data. In addition, in order to quantify the random error associated with a given tissue measurement, the mean and standard deviation are generally calculated from multiple

CHAPTER 3. DIELECTRIC MEASUREMENT PROTOCOL

Table 3.4: Example of the calculation of standard individual, combined and extended uncertainties for relative permittivity measured on 0.1 M NaCl in the frequency range 300 MHz–10 GHz in the study conducted by Peyman *et al.* [47]. The nomenclature and methodology follow the guidelines defined by the NIST [131]. The calculation was performed at each measurement frequency and averaged across the frequency range.

Sources of Uncertainty	Uncertainty component a (%)	Probability distribution	Divisor b	Sensitivity coefficient c_i	Standard uncertainty (%) $u_i = (\frac{a}{b})c_i$
Repeatability	0.18	Gaussian	1	1	0.18
Accuracy	0.26	Rectangular	$\sqrt{3}$	1	0.15
VNA drift	0.07	Rectangular	$\sqrt{3}$	1	0.04
Cable movement	0.00	U-shaped	$\sqrt{2}$	1	0.0
Combined uncertainty	N/A	$u = \sum_1^4 u_i^2$	N/A	N/A	0.24
Expanded uncertainty ($k=2$)	N/A	ku	N/A	N/A	0.48

independent measurements conducted on the same tissue sample. Specifically, according to the NIST guidelines, the best practice for expressing uncertainty is to report the mean measured value along with a coverage probability of 95% [131].

Next, details regarding the measurement procedure are reported in Section 3.2 and the analysis of the measured dielectric data is discussed in Section 3.3.1. In particular, while the focus of this section has been on the equipment-related confounders, in Section 3.2, techniques related to minimisation or compensation of tissue-related confounders are described.

3.2 Dielectric measurement of biological tissues

Dielectric measurement of biological tissues with an open-ended coaxial probe is affected by a number of confounders related to the characteristics of the tissue samples. Tissue-related confounders may be the major cause of measurement uncertainty, since the total combined uncertainty for measurements on liquids is relatively small compared to that of tissue measurements [47]. Uncertainties associated with measuring tissue properties seem to be primarily related to the complex structure of biological tissues [42], [47], [56].

In order to reduce tissue-related confounders, it is useful to plan each set of measurements according to the experimental goal. The first step in planning involves choosing the source animals (since their age or weight could affect the dielectric properties [47], [56], [57]) and the sample tissue

CHAPTER 3. DIELECTRIC MEASUREMENT PROTOCOL

type. Aside from the source species, the number of samples needs to be chosen based on the scientific question. Following these decisions, the next steps include the analysis of the various tissue-related confounders and the evaluation of different methods that aim to reduce or compensate for these confounders.

In the next subsections, the confounders related to probe choice, sample preparation and handling are first described. Then, a discussion of the confounders that need to be considered during the dielectric measurement procedure with biological tissues is provided.

3.2.1 Probe selection considerations

Open-ended coaxial probes are suitable to use with materials that are liquid or semi-solid [75], homogeneous [75], have flat surfaces [75], [100], and have a semi-infinite thickness [42], [47], [75]. Tissues are generally semi-solid (with the exception of bone), but they are not always homogeneous or have flat surfaces, and tissue samples that are much thicker and larger than the probe tip are not always available or easy to prepare. Thus, while any probe can be used for measuring the dielectric properties of liquids (if contained in large beakers), the selection of the probe for measuring the dielectric properties of tissues is affected by three main factors: sample size, heterogeneity, and tissue surface.

3.2.1.1 Sample size and heterogeneity in relation to sensing volume

Dielectric spectroscopy techniques permit the acquisition of the average complex permittivity of the interrogated volume. Thus, the probe is generally selected such that sensing volume only contains the tissue sample of interest and no other material. Since probes with a small diameter have smaller sensing volumes compared to large flanged probes, the sample size has to be taken into account and compared to the sensing volume of the probe [10], [65], [96]. For low frequency dielectric measurements, larger probes, with outer conductor diameter normally greater than 1 cm, are typically used and tissue samples larger than the diameter are required. Conversely, for high frequency dielectric measurements, smaller probes with outer conductor diameter less than 1 cm are typically used and smaller tissue samples can be measured.

Heterogeneity of biological samples is a further factor to consider when choosing a probe, since it is challenging to determine the tissue-specific dielectric properties in an extended heterogeneous volume interrogated

by the probe [10], [42], [47]. Thus, since it is more likely that smaller probes contain less complex tissue heterogeneities than larger probes, smaller probes are generally more suitable for characterising heterogeneous samples. However, the dielectric characterisation of highly heterogeneous tissues, such as breast tissue, can be challenging even with the use of smaller probes. Therefore, in order to support the dielectric characterisation of highly heterogeneous tissues, post-measurement histological analysis can be conducted. Further details regarding this procedure and the challenges in combining the histological characteristics of a heterogeneous sample with the corresponding measured dielectric data are reported in Section 3.3.2.

3.2.1.2 Tissue surface characteristics

In addition to the sample size and heterogeneity, the quality of the tissue surface is another consideration when selecting the appropriate probe to use. Surface irregularities may contribute to inadequate probe-tissue contact and poor repeatability of dielectric measurements [46], [47], [93]. Examination of the tissue surface permits the identification of the tissue region most suitable for the acquisition of dielectric information [155]. For instance, thick samples and even surfaces are preferable to thin and uneven surfaces in order to ensure good probe contact with the tissue sample [46], [75], [93]. The use of a smaller probe on uneven tissue surfaces can result in more reliable measurements, especially if these areas are limited or spatially restricted [42]. Lower uncertainty in the measurements from smaller probes on uneven surfaces may be attributed to smaller forces being applied on smaller surfaces. Indeed, large uneven surfaces require the application of higher forces (and consequently higher pressures) to prevent the presence of air gaps between the probe and the tissue. An increased probe-sample pressure may cause fluid accumulation at the probe tip [42], [47] or tissue damage [75], both of which can affect the tissue dielectric properties and lead to inaccurate data.

In summary, the probe needs to be selected not only on the basis of the probe characteristics and specifications (i.e. frequency range, permittivity range, temperature range, mechanical resistance) previously discussed in Section 2.2.3, but also based on the properties of the tissue under investigation. The size of the selected probe has to be consistent with the sample surface, size and heterogeneity in order to achieve good probe-tissue contact and accurate measurements in a homogeneous region.

After selecting the probe, but before measuring the dielectric properties, it is recommended to carefully plan the tissue preparation and handling procedures in order to reduce tissue-related confounders, such as sample

cooling, dehydration and damage. These confounders are examined in the next section.

3.2.2 Tissue handling and confounders

Tissue measurements can be performed *in vivo* or *ex vivo*; the tissue preparation and handling will be different in each case. Often, for reasons of convenience (i.e., patient safety, ethics) or due to difficulties in establishing a good probe-sample contact with *in vivo* tissues, dielectric measurements of animal and human tissues are performed *ex vivo*. However, *in vivo* measurements may be preferred since the tissues are in their natural environment, with blood perfusion and well-hydrated. This section discusses these tissue-related issues in more detail.

3.2.2.1 *In vivo* vs. *ex vivo* measurements

Several authors have reported on whether or not differences exist between tissue dielectric properties acquired *in vivo* and *ex vivo*. These studies are discussed below in chronological order. Initially, Burdette *et al.* performed *in vivo* measurements on canine muscle, kidney cortical tissue and fat tissue, and differences were found between acquired *in vivo* data and reported *ex vivo* data [42]. For all of the *in vivo* tissues, the measured permittivity was higher than the permittivity reported by previous *ex vivo* studies [41], [42], [156]. In particular, for *in vivo* canine fat tissue, the measured permittivity values were a factor of approximately 1.5 to 3 times larger than the *ex vivo* permittivity values acquired previously by other authors [41], [42], [156]. This difference in dielectric properties was most likely due to differences in water content, in temperature, or actual physiological differences between living and non-living tissues [42]. Next, Kraszewski *et al.* performed both *in vivo* and *ex vivo* dielectric measurements on rat and cat tissues, finding only dielectric differences less than the uncertainty at frequencies between 100 MHz and 8 GHz [44]. Schwartz and Mealing observed that the permittivity and conductivity of frog heart, in the frequency range 0.2-8 GHz, were higher *in vivo* than *ex vivo*, with the difference being attributed to blood perfusion changes [52]. More recently, significant differences between *in vivo* and *ex vivo* dielectric properties were found by Gabriel *et al.* [46] and Peyman *et al.* [47], [57] in skin, spinal cord, skull, long bone and bone marrow in the MW frequency range. Similar differences were not observed in other tissues but might indicate unavoidable contamination of tissues with blood or other body fluids [47]. From the analysis of normal and malignant human liver tissue, O'Rourke *et al.* found a statistically significant difference between

CHAPTER 3. DIELECTRIC MEASUREMENT PROTOCOL

in vivo and *ex vivo* normal liver tissue, but not between *in vivo* and *ex vivo* malignant liver tissue [53]. Furthermore, Halter *et al.* evaluated the changes of breast cancer dielectric properties between *in vivo* and *ex vivo* measurements and found an approximately 30% drop in the magnitude of the permittivity in tissues analysed 300 minutes after excision [12]. More recently, Shahzad *et al.* found that over the 210 minutes immediately following excision, the relative permittivity of liver tissue, as measured on the surface of the sample, decreased by 32 points [130]. However, this decrease was attributed fully to dehydration of the surface of the tissue sample, as dielectric measurements conducted on the interior of the sample did not change considerably over the same time period [130].

As is clear from the varied results of these studies, there is no consensus on: i) whether a difference in the dielectric properties of *in vivo* and *ex vivo* tissues exists over the MW frequency range, and ii) if a difference does exist, the magnitude and direction of it. Despite these results, the difference between *in vivo* and *ex vivo* data in the MW frequency range is generally attributed to the temperature change and tissue dehydration [12], [31], [42], [47], [112], and recent studies following best practice in dealing with these confounders suggest no significant difference in the dielectric properties measured from *in vivo* and *ex vivo* measurements [48], [157]. Therefore, following best measurement practice, it is advantageous to keep the temperature constant during dielectric measurement using a temperature controlled container or a water bath [30], [44], [47], [54], [56]–[58] and to minimise dehydration by limiting the time between excision and measurement to a few hours [10], [28], [31], [44], [46], [47], [57], [58], [61], [69], [76], [112], [158]–[160].

However, at frequencies lower than 100 MHz (i.e., below the MW range), a larger variation between *in vivo* and *ex vivo* properties can be found. This difference is generally attributed to physiological parameters, such as blood flow in vessels [28], [42], [69], [112], [160], ischemia [12], [112], [159], [160], heart rate [47], arterial pressure [47], [112], [159], respiration rate [47], air content in lungs [158], which can affect the permittivity and conductivity values at frequencies below the MW range.

In the following subsections, the best-practice steps involved in both *in vivo* and *ex vivo* measurements are described: from surgical intervention, to sample access and excision, transportation, handling and processing. In each step, all potential tissue-related confounders, as well as the different methods used in previous studies to compensate for them, are reported.

3.2.2.2 *In vivo* procedure: surgical intervention, sample access and excision

The first step in defining a sample handling procedure involves identifying the surgical methods to be used for tissue access and excision. It is necessary to define a surgical protocol that minimises tissue property modification. The main factors interfering with the dielectric acquisition concern the use of chemicals that alter the body physiological condition [42], [58], the use of tools or techniques that may damage tissues [12], and tissue exposure and cooling during the surgical operation [42], [44], [47], [52], [161].

It may be useful to test for, and take into account, the effect of anaesthesia or other pharmaceuticals, which are used on animals and humans during surgery, and which may impact physiological parameters. For instance, Burdette *et al.* observed a decrease in body temperature due to anaesthesia [42]. However, this phenomenon has not been studied extensively and future research in this area is needed.

During the surgery preceding the dielectric measurements, contact with the tissue needs to be minimised in order to avoid any damage or contamination. For human *in vivo* studies, the measurement tools need to be sterilised prior to surgery. Normally, steam sterilisation is performed prior to calibration [12], [53] and a calibration refresh is performed in the sterile environment before the *in vivo* measurements [12].

Other important confounders to take into consideration in the operating room during *in vivo* measurements are those related to the tissue exposure to air. Specifically, air contributes to tissue cooling (from body temperature to room temperature) and to tissue dehydration. Different techniques have been adopted in *in vivo* measurements to prevent tissue cooling and dehydration. For example, Ranck and BeMent performed experiments within a few minutes from the surgical incision used to expose the interior tissues, and used warm saline to wet the measurement region [161]. Schwartz and Mealing rinsed the tissues and kept them moist with frog physiological solution [52]. Hart and Dunfee applied Ringer's solution with a medicine dropper to muscle to prevent drying between the measurements [162]. However, these methods to reduce dehydration can impact the dielectric property measurement, since the solutions used have their own dielectric properties that will then contribute to the dielectric measurement of the tissue. Thus, the use of solutions, especially saline, needs to be avoided. More commonly, tissue dehydration during an *in vivo* measurement is minimised by reducing the time between the surgical incision performed to expose the tissue and the dielectric measurement and by covering the area of interest with another tissue between measurement times [42], [44], [47]. This technique does not

alter the tissue properties and also minimises tissue cooling.

The tissue temperature still needs to be measured frequently, so that any temperature change is taken into account during data analysis. In previous studies, the *in vivo* tissue temperature was monitored using thermocouple probes [28], [30], [76] and, more recently, fibre-optic thermometers [30], [31]. Infrared thermometers may also be used for tissue temperature monitoring, since they are portable and do not require sample contact [49]. The same sensors can also be used in *ex vivo* measurements.

A further crucial point in *in vivo* measurements concerns the probe positioning. Typically, in *ex vivo* scenarios the probe-tissue contact can be verified by visual inspection; this approach can be challenging in a surgical setting. The probe positioning cannot be accurately planned prior to surgery; thus, it is normally decided in the surgical theatre.

3.2.2.3 *Ex vivo* procedure: transportation and tissue handling

When *ex vivo* measurements are performed, the excised sample may be transported from the operating theatre to a secondary location for measurement, characterisation, or histology (details on histological analysis are presented in Section 3.3.2). The time between excision and *ex vivo* measurements is minimised to prevent tissue dehydration [28], [31], [44], [46], [47], [61], [76], [112]. Aside from water content change due to dehydration, care is generally taken during tissue transportation to avoid changes in the sample temperature. Since the temperature has a systematic impact on the measured dielectric spectrum of biological tissues, it is usually necessary to transport the tissue in hermetically-sealed temperature-controlled containers [10], [30], [54], [57].

In order to prevent tissue contamination, dehydration and damage, sample handling prior to the *ex vivo* measurements needs to be minimised [11], [42], [57], [65]. The sample temperature can be kept constant during the measurements using a water bath [30], [44], [47], [56], [57]. As the temperature setting of the water bath may not be equivalent to the tissue temperature, the tissue temperature needs still to be verified using an infrared or fibre-optic thermometer [30], [31]. In this way, the tissue temperature variation can be taken into account during data analysis. Details on how tissue temperature affects the measured dielectric properties are reported at the end of Section 3.2.3.

If the tissue sample undergoes post-measurement histological analysis, the measurement sites on the sample have to be marked. Sample marking is necessary to ensure that the histological analysis involves the portion of tissue corresponding to the volume interrogated by the probe. In this way, a

good correspondence between the tissue histological and dielectric properties can be found. Further details about the histological characterisation of tissue samples are reported in Section 3.3.2. In previous studies, acrylic ink [10], [49] or pins [12] have been used as site markers. When *ex vivo* measurements are performed on the same sites where *in vivo* measurements were taken, the effect of the marker on the tissue dielectric properties should be tested before experimental implementation in order to prevent tissue modification or damage by the marker. Lastly, in order to maintain the integrity of the tissue, the use of additives and preservatives is generally avoided until the measurement is completed [58].

Having presented the confounders to consider during the planning of the tissue measurement procedure, in the next subsection, the actual measurement procedure and the key confounders that affect tissue dielectric property measurements are discussed.

3.2.3 Acquisition of dielectric properties and confounders

After the equipment set-up, calibration, and validation, the measurements on *in vivo* or excised tissues can be performed.

In order to minimise the effects of the environmental parameters on tissue dielectric properties, it is advantageous to perform measurements in a climate (temperature, pressure and humidity) controlled room [47], [58].

It is important to note that the confounders related to the physical conditions and characteristics of the tissue sample can be controlled, monitored or compensated for only during the measurement phase.

Thus, in the following paragraphs, the main confounders occurring during the measurement phase and affecting the measurement region choice, the probe-tissue contact and pressure, as well as the tissue sample temperature, are discussed.

3.2.3.1 Measurement region choice

The confounders mentioned in Section 3.2.1 (i.e., probe sensing volume, tissue thickness, tissue surface, and sample heterogeneity) need not only be considered in the planning phase, but also need to be controlled and managed in relation to the choice of the measurement region. Additional considerations may also be needed, for instance, in order to prevent undesirable reflections negatively affecting the measured data, Abdilla *et al.* placed a shorting block under the sample to check for any reflections from

the sample boundaries [54]. Confounders intrinsic to the tissue type include: fibre orientation in anisotropic tissues, presence of blood vessels, and high heterogeneity. It was observed that anisotropic tissues, such as muscles, present different dielectric properties according to the measurement directions along or across the fibre [125]. At lower frequencies (10 Hz-1 MHz) the fibre direction can change the relative permittivity by 100% [125]. However, in the MW frequency range, the permittivity values between these two sets of measurements are not substantially different [47]. Blood vessels are non-uniformly distributed in tissues and may make up roughly 30% of their volume [163], so the probe position relative to that of blood vessels has to be checked by visual inspection [69], [160]. In highly heterogeneous and mechanically stiff tissues the uncertainty is generally higher and, in order to minimise the random errors arising from tissue heterogeneity and complexity, it is useful to repeat the measurements at multiple sites [47], [54], [55]. For instance, Peyman *et al.* stated that as many measurements as possible should be taken on each sample tissue, and took at least six measurements per sample [47]. In most other dielectric studies, three to five measurement sites were generally selected on each tissue sample [28], [44], [54].

3.2.3.2 Probe-tissue contact

Having selected the most suitable measurement region, the probe is placed in contact with the sample. In order to reduce the uncertainty due to probe and cable movement, in both *ex vivo* and *in vivo* measurements (in *in vivo* measurements only when the animal size is relatively small), it is convenient to move the sample towards the probe using a lift table until the entire probe aperture makes firm contact with the tissue sample, as opposed to moving the probe during the measurement procedure.

Measured reflection coefficient data is extremely sensitive to the probe positioning relative to the sample surface. A high variability in the dielectric properties can be attributed to variability in probe-tissue contact. Thus, a firm contact between the probe and the tissue is key [10], [81]. A good quality contact reduces the impact of confounders that increase the measurement uncertainty, such as pressure differences [42], [47], [66], [158], air gaps [75], [81], [98], [164] and biological fluid accumulation at the probe tip [42], [47]. In most studies, these factors have been monitored by a close visual inspection [10], [30], [47], [52], [75]. In order to keep the applied pressure constant in *ex vivo* measurements, weighing scales or force sensors can be placed underneath the sample holder [49]. In fact, the application of a steady pressure contributes to more repeatable measurements [42]. However, in the

CHAPTER 3. DIELECTRIC MEASUREMENT PROTOCOL

literature to date there is no study that quantifies the error in the measured data in terms of the variation of the applied pressure. Therefore, in the experimental work of this dissertation, measurements to quantify the error introduced by probe pressure variations were conducted, but it was observed that the outcome found for one measurement site could not be extended to all measurement sites across a sample. For instance, within the same tissue sample, there can be some differences in terms of sample thickness, tissue mechanical properties, water content, and surface irregularities, which may require the application of different probe pressures on the same sample. Thus, no specific, fixed pressure can be reported for all samples. However, a technique that may be used to obtain a good quality contact is as follows. First, a low pressure is applied to the probe to contact the sample. This low pressure, if too low, can lead to data inconsistencies when repeated measurements are taken at the same site (due to air gaps). If this occurs, a pressure adjustment can be undertaken until measurements at the same site are repeatable.

Other factors are also related to the applied pressure. For instance, a low pressure applied on uneven tissue surfaces can result in poor contact due to the presence of air gaps. Conversely, high pressure can cause tissue compression and can prompt fluid from within the tissue to rise to the tissue surface, or worse, can cause tissue damage [58], [158]. In previous studies, sample contamination by biological fluids has been reduced by using cotton wipes/swabs [47], [57], [58], [161] or suction [47]. However, the suction method is more invasive and has the potential to dehydrate the sample.

3.2.3.3 Temperature effects

During dielectric measurements, as discussed in the Section 3.2.2, the temperature needs to be controlled and monitored. While different techniques used to monitor or control the temperature have been discussed in earlier sections, the effect of temperature on the dielectric properties of tissues is examined below. In previous studies, the dielectric properties of biological tissues at discrete frequencies and temperatures were measured and, for small temperature variations, they were presented in terms of linear temperature coefficients, which are defined as the percent change in either relative permittivity or conductivity per degree Celsius [40]. The provided linear temperature coefficients are limited to a number of specific discrete frequencies and temperatures [28], [31], [76]. Outside of these frequencies and temperatures, the impact of temperature on the dielectric properties may no longer be linear [31]. A brief summary of the previously published temperature-dependent dielectric properties data is presented in Lazebnik

CHAPTER 3. DIELECTRIC MEASUREMENT PROTOCOL

et al. [31]. In the MW frequency range, the change in relative permittivity is at most 2% per degree Celsius and the change in conductivity is between 1% and 2% per degree Celsius, depending on the tissue and on the frequency and temperature range considered. Generally, the relative permittivity and conductivity trends with temperature differ over frequency. However, the magnitude change in both relative permittivity and conductivity per degree Celsius tends to be higher at lower frequencies in most biological tissues [28], [31], [76].

Lazebnik *et al.* developed a model to characterise the temperature-dependence of liver tissue dielectric properties over the MW frequency range [31]. In particular, from the liver dielectric measurements, Lazebnik *et al.* identified different “cross-over” points in the trends of both relative permittivity and conductivity with temperature [31]. In relative permittivity, the cross-over point was found at about 4 GHz. Below the cross-over point, the relative permittivity decreases slowly as temperature increases and, above the cross-over point, the permittivity increases with temperature. For conductivity, two cross-over points were found: one near 2–3 GHz and the other near 16 GHz. Below the first cross-over point, the conductivity increases slowly as temperature increases. Between the two cross-over points, the trend reverses, and above the second cross-over point, the conductivity again increases as temperature increases. The same trends were also found for water [31].

More recently, temperature coefficients were provided for a wider temperature range (up to 100°C) at the discrete frequencies 915 MHz and 2.45 GHz, which are of interest for microwave liver tissue ablation [30], [32]. The study conducted by Brace [32] reported linear temperature coefficients across the 5–50°C range in agreement with the results from Lazebnik *et al.* [31], with coefficients of -0.22 and -0.18 in relative permittivity for the two frequency points, respectively, and coefficients of 1.29 and -0.2 for conductivity. From 50°C to 100°C, both relative permittivity and conductivity were found to decrease by as much as 50%, due to both irreversible damage of the tissues and tissue dehydration [32].

In summary, the temperature coefficients for both relative permittivity and conductivity depend on tissue-type, on frequency, and on the considered temperature range. Knowledge of these temperature coefficients can be used to compensate for the effect of the temperature change during tissue dielectric measurements.

In this section, the importance of preplanning the measurement procedure was highlighted, the measurement process overviewed, and the main confounders involved in the measurement were described. The most common practices adopted to minimise tissue-related errors are summarised in

Fig. 3.3.

In the next section, the steps involving data and sample post-processing are discussed. Both data and sample post-processing are conducted to support dielectric data interpretation.

3.3 Post-measurement processing

This section is divided into two subsections: the first presents the steps involved in data post-processing, along with their sources of errors and compensation techniques, and the second describes the steps involved in sample post-processing, along with their confounders, challenges and common practices. Data post-processing generally consists of data fitting, data consistency verification (and exclusion of data), and statistical data analysis. On the other hand, sample post-processing generally consists of histological analysis, which determines the tissue types present in the sample and their relative spatial distribution and enables attributing measured dielectric properties to the appropriate tissue type.

Both data and sample post-processing support interpretation of the measured dielectric properties. While data post-processing is conducted after the acquisition of the dielectric properties of any tissue sample, sample post-processing is especially required after the acquisition of the dielectric properties of a heterogeneous tissue sample. In fact, since homogeneous samples are composed of only a single tissue type, histological analysis may not provide any additional information for those samples. However, for heterogeneous samples, histological analysis enables the identification of the constituent tissue types that may have contributed to the acquired dielectric properties, thus facilitating the association of the acquired dielectric data with the tissue types constituting the sample.

3.3.1 Data post-processing

The measured tissue dielectric data is generally fitted to the dielectric models presented in Section 2.1.3. Then, the quality of the fit is assessed by the calculation of the error between the fitted model and the measured data. After removing inconsistent data, the remaining data is then processed, and often the average dielectric properties across the samples is reported. Lastly, the fitted tissue dielectric data may be analysed statistically. Since uncertainties may be introduced by post-processing the data, in this section, the common practices adopted to process the acquired dielectric data are discussed.

CHAPTER 3. DIELECTRIC MEASUREMENT PROTOCOL

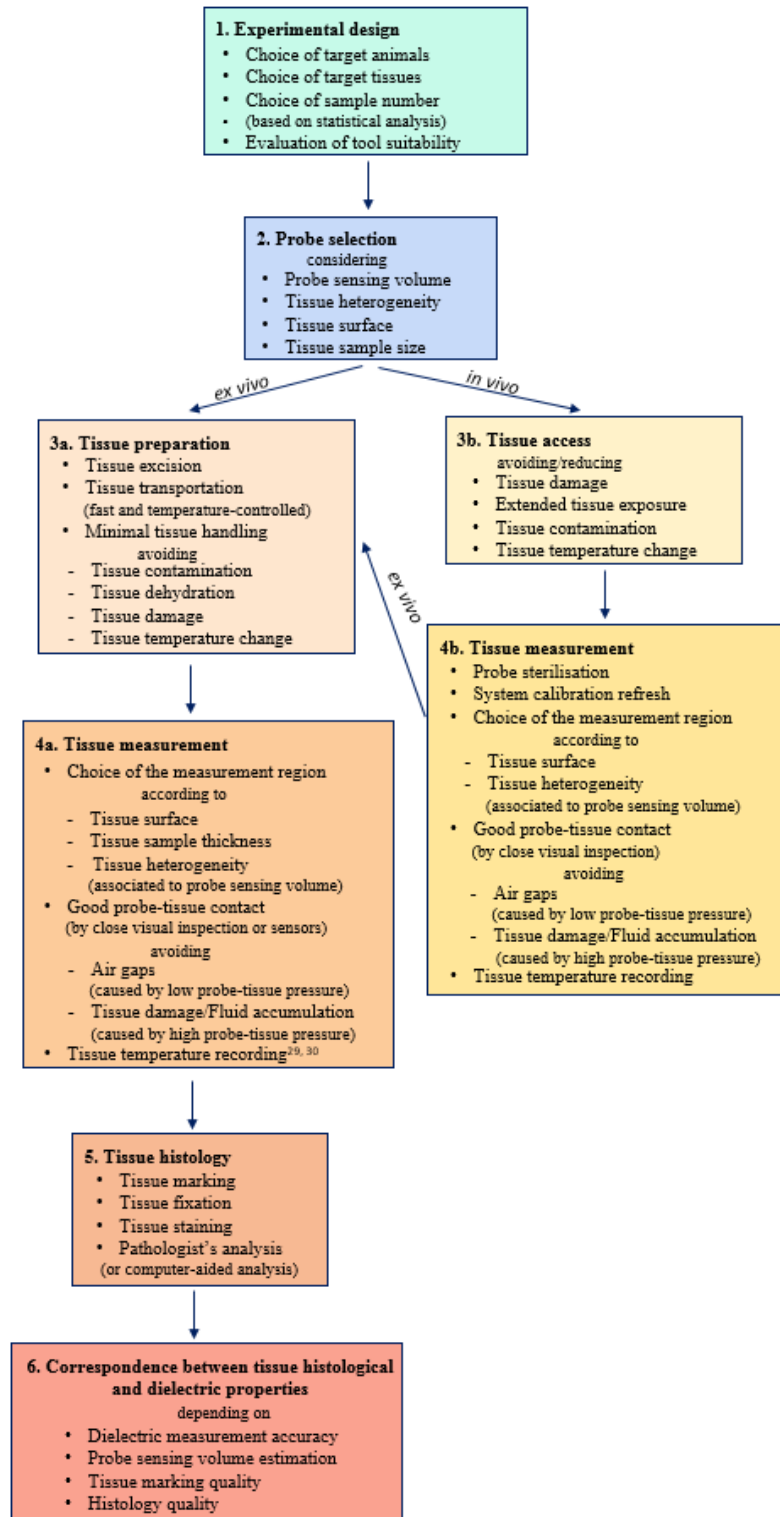


Figure 3.3: Flowchart of the common steps to minimise tissue-related errors in *in vivo* and *ex vivo* dielectric measurements.

3.3.1.1 Choice of the dielectric model

The choice of the dielectric model depends on the data trend and the measurement frequency range. The width of the frequency band typically determines the number of poles, which is generally related to the number of relaxation regions spanning that frequency range [67], [71]. The curve fitting is empirical and requires knowledge of the mathematical function that relates the model parameters [48], [71]. Optimisation algorithms are used to find the model parameters that best fit the dielectric data. The optimisation procedure is generally terminated when further parameter refinement does not produce a significant change in the fit error. While mathematical models are fitted to data based on the physical behaviour of tissues, the obtained parameters do not typically reflect any physical meaning [15], [72].

Different models and data fitting techniques have been adopted in previous studies. In 1996, Gabriel *et al.* developed a parametric model to describe the variation with frequency of the dielectric properties of seventeen different tissue types. Although the dielectric spectrum of biological tissues is characterised by three major relaxation regions in the frequency range from 10 Hz to 100 GHz, a four pole Cole–Cole model was used. The additional poles provide more flexibility to achieve a better fit to the data, yet the complexity increases due to the increased number of parameters [125]. In a number of studies, a single Cole-Cole model was used in the MW frequency range. Abdilla *et al.* compared multiple-pole Cole–Cole models (up to four poles) fitted to the measured data and the one-pole Cole-Cole model together with a conductivity term was found to be the most suitable model to characterise high-water content biological data [54]. This result is in agreement with Peyman *et al.* [57]. In the frequency range from 0.5 to 20 GHz, Lazebnik *et al.* and O’Rourke *et al.* adopted a single-pole Cole-Cole model to fit liver tissue data after verifying that the single-pole model was sufficient to represent the tissue data [31], [53]. Specifically, it was observed that a two-pole model did not result in increased accuracy in the data fitting [31]. On the other hand, over the same frequency range, Sugitani *et al.* used a two-pole Cole-Cole model to fit breast cancer tissue data, since the conventional one-pole Debye and Cole-Cole plots did not adequately fit the measurement results in the entire frequency range of 0.5–20 GHz [15].

3.3.1.2 Optimisation algorithms

Once the dielectric model and the number of poles are selected, the model parameters are obtained by optimisation algorithms and fitting evaluation methods. Several optimisation algorithms have been used to find param-

eters that give the best fit to measured dielectric data. Generally, for single-pole Debye or Cole-Cole models, which have a small number of parameters, traditional optimisation techniques such as the non-linear least squares method [10], [11], [48], [54], [71], [109], [120], [128], [162], [165] and Nelder–Mead direct search optimisation [53] are used. These techniques require careful attention to the initial parameter estimates and the selected parameter ranges, since the parameters of the model are interrelated to the extent that the solution is not unique. Thus, it may be possible to find a local, rather than a global, minimum of the error [71], [166], [167]. Evolutionary optimisation methods such as genetic algorithm (GA) [167]–[169] and particle swarm optimisation (PSO) [170], [171] avoid this problem, despite being computationally more complex. These methods are suitable for fitting dielectric data over a broad frequency range [167]. For instance, in Kelley *et al.*, PSO was used to fit Debye dispersions to the Havriliak–Negami equation over the frequency range 107–1011 Hz [171]. Furthermore, Clegg *et al.* used a GA to minimise the difference between a multi-pole Debye model and muscle dielectric data tabulated by Hurt *et al.* from 20 Hz to 17 GHz [167], [172].

In the literature, the most common optimisation method is the non-linear least squares algorithm and the most common fitting evaluation method is the root mean square error (RMSE) [10], [48], [54], [120]. Specifically, Lazebnik *et al.* obtained the single-pole Cole-Cole model parameters for human breast tissue in the frequency range of 0.5–20 GHz by minimising the criterion that can be viewed as the squared, scaled Euclidean distance between the measured data and the fitted curve in the permittivity and conductivity space [10]. The measured and fitted values were divided by the overall measured median value for that tissue sample to enable direct comparison between tissue samples [10].

After fitting the tissue data to the most suitable dielectric model, it is generally ensured that the optimised parameters give similar quality of fit to the real and imaginary parts of permittivity.

3.3.1.3 Sample data exclusion criteria and data analysis

Unusual dielectric trends may be observed when measured data does not truly reflect the tissue dielectric properties, e.g., when the trace presents ripples or when the relative permittivity/conductivity increases/decreases with frequency. The consistency in the measured data is determined by the relationship between the real and imaginary parts of the complex permittivity. This relationship can be verified by the Kramers-Kronig theory, which shows that for linear systems the frequency response of the conductivity is related

CHAPTER 3. DIELECTRIC MEASUREMENT PROTOCOL

to the relative permittivity, and vice versa, through the time constant [67], [76]. In other words, the relative permittivity and conductivity cannot vary independently.

An alternative method to test if the data is consistent comprises of evaluating the quality of the Cole-Cole fit, since the Cole–Cole model obeys the Kramers–Kronig relation. For instance, in the studies by Lazebnik *et al.* [10], [11], the quality of the Cole–Cole fit was evaluated by defining an acceptability threshold for the fitting criterion and excluding any data set with a value exceeding that threshold. In Lazebnik *et al.* less than 5% of the characterised tissue samples were excluded based on this physics-based exclusion criterion [10], [11].

Furthermore, erroneous data sets can be identified from the comparison of all the measurement results taken from the same tissue sample [28], [44]. For instance, Kraszewski *et al.* analysed animal tissue samples with dielectric measurements recorded at three to five sites on each tissue type [44]. If one or two sites out of the three to five measurement sites deviated by more than one standard deviation, these sites were excluded from the data set. Whereas, if three or more sites deviated by more than one standard deviation, the measurements were repeated [44]. Also, Stauffer *et al.* conducted dielectric measurements at multiple sites on each tissue type and some results were not recorded if evident errors were visualised in the relative permittivity (or conductivity) plot on the network analyser screen [28]. Some of these errors were attributed to probe movement and poor probe-tissue contact [28]. However, this method is quantitative and numerical or quantitative methods are preferred for data consistency assessment.

Once the best fit to the measured dielectric data is found and the data reliability and consistency is verified, the fitted data may be analysed across the frequency range and across tissue samples. Statistical methods can be used to evaluate the variability of the tissue dielectric measurements by calculating the mean and standard deviation of both relative permittivity and conductivity across the sample data at each acquisition frequency. Data post-processing may involve additional statistical analysis, such as statistical hypothesis tests or analysis of variance (ANOVA), in order to compare tissue data sets acquired in different conditions and to find statistically relevant trends in the dielectric properties of specific biological tissues [10], [11]. In these data analysis steps, it is of fundamental importance to take into consideration the acquisition settings of the system, and the physical conditions and the characteristics of the samples.

In the next section, the histological analysis of tissue samples is discussed as a method to support the interpretation of dielectric data acquired from heterogeneous biological tissues.

3.3.2 Sample post-processing

Many studies performed in the literature involve only homogeneous (or assumed homogeneous) tissues (for example, liver tissue [28], [54]), and thus the samples do not undergo histological analysis. However, in this section, the focus is on heterogeneous tissue samples. Measuring the dielectric properties of heterogeneous tissues is inherently challenging, as spectroscopy has the effect of averaging the dielectric properties throughout the sensing volume that is illuminated by the electromagnetic field [10]. Thus, in the following subsections, histological analysis methods used in the literature for attributing dielectric properties to heterogeneous samples are overviewed, after a general description of the histology process and its confounders. Finally, the confounders that are of specific concern for dielectric characterisation of heterogeneous samples are examined.

3.3.2.1 Histological analysis and confounders

Histology is the study of the microscopic structure of cells and tissues; while histopathology refers to the same but with diseased tissue [173], [174]. There are multiple steps involved in the histological analysis of a tissue sample: the sample must be fixed, processed, embedded in wax, sliced, mounted on slides, stained, then imaged [175]. Following these steps, the images of the slices are ready to be analysed by a pathologist. The pathologist is able to determine: i) the types of tissues present; ii) if diseased tissue is present, the disease grade and other characterisations (for example, with breast cancer, the hormone receptor status) [174]; and iii) the distribution of the tissue types within the sample.

The histological procedure is time-consuming not only because it consists of multiple steps, but also because each step can be affected by numerous factors, such as poor fixation, uneven levels of staining, different procedures of slide digitation, and poor histological interpretation. In particular, poor fixation of the sample can lead to changes in the tissue structure [10], [175], and uneven levels of staining can result in images that are incomplete or out of focus [175]. Slide digitation can have variations in lighting conditions and magnification that can affect interpretation of the results, particularly when comparing across slices [175]. Furthermore, the histological interpretation of a slice is subjective, and variability in results between pathologists are possible [176]–[178]. Computer-aided diagnosis (CAD) and prognosis (CAP) methods are currently being investigated to create a fully automated analysis that is faster and more consistent than a human-based analysis [175]. An excellent review of challenges associated with histopathological analysis can

CHAPTER 3. DIELECTRIC MEASUREMENT PROTOCOL

be found in the study by Veta *et al.* [175].

A limited number of studies involving histological analysis to support the interpretation of the measured dielectric properties of heterogeneous tissues have been presented in the literature [10], [12], [15], [49], [112]. All of these studies have been performed on breast tissue, due to the need for breast tissue dielectric properties in microwave breast imaging. While the histological procedure was not detailed in the studies conducted by Sabouni *et al.* [112] and Martellosio *et al.* [49], the histological procedure was reported in other studies, which are described and compared below.

In the studies conducted by Lazebnik *et al.* [10], [179], several hundred dielectric measurements were taken from normal and malignant excised breast tissue samples using an open-ended coaxial probe. The measurement sites were marked on the tissue samples using a spot of black ink. Lazebnik *et al.* conducted a histological analysis of each sample based on the tissue composition inside the region of the sensing volume of the probe that was 7 mm wide and 3 mm deep, as determined by Hagl *et al.* [65]. In this way, a cross-section of each tissue sample was taken directly below the measurement site (i.e., the ink spot). Digital microscopy images were obtained and visually inspected. The tissue composition within the sensing volume was quantified based on the percentage of each tissue type residing within the slice under consideration. The 2-dimensional cross-section was used to obtain an estimate of the tissue composition in the full 3-dimensional sensing volume. The percentages of each tissue type, including adipose (fat), glandular and fibroconnective tissue, along with benign and malignant tissue, were estimated visually by qualified pathologists [10], [179] and supported the sample categorisation discussed in Section 2.4.2. A Kappa statistic was used to confirm consistency in the analysis between different pathologists. Several exclusion criteria were applied during the histological process. In particular, samples were eliminated from further consideration if the ink spot was not visible, if the ink had leaked into the tissue, or if the cross-sectional slice was deformed. In these studies, nearly half of all samples (49.8%) were excluded based on difficulties during the histological procedure [10], [179].

Following the studies by Lazebnik *et al.* [10], [179], Halter *et al.* performed a study that also examined the region under the probe using histological analysis [12]. In the study conducted by Halter *et al.* [12], the dielectric properties of *in vivo* and *ex vivo* breast tissue were measured in the MW frequency range with open-ended coaxial probes. After the *in vivo* tissue measurement was recorded, a biopsy clip was embedded in the tissue at the measurement site. The tissue was then excised and sectioned into 5 mm thick pieces. The excised samples were measured again (at the same site as for *in vivo*, as identified by the clip). Initially, the pathologist examined

CHAPTER 3. DIELECTRIC MEASUREMENT PROTOCOL

a 1 cm x 1 cm square area around the measurement site, and thus the tissue types were estimated based on a large area. Later, the strategy was improved by inserting two pins covered in ink into the tissue on either side of the depression left by the probe in order to mark the measurement site. The tissue sample was fixed with formalin, stained, and then slides were prepared. The pin holes were then used during the analysis to determine the probed region in which the tissue types were estimated by the pathologist. The pathologist examined the tissue histology within the 1 cm x 1 cm region, which was a slice parallel to the probe-sample interface (i.e., perpendicular to the plane of the probe axis), unlike the vertical (or axial) slice used in the study conducted by Lazebnik *et al.* [10], [11]. However, in both cases, the full tissue composition within the sensing volume was estimated based on the one given slice. Furthermore, as only one pathologist was involved in the study, a Kappa analysis similar to that in the study by Lazebnik *et al.* [10], [11] was not needed. In this study, details were not provided regarding whether or not samples had to be excluded from consideration due to histological challenges.

Most recently, in the study conducted by Sugitani *et al.* [15], excised breast tissue samples were obtained and their complex permittivities measured using an open-ended coaxial probe. The samples contained a combination of cancerous tissue, normal fat tissue, and normal stroma (connective) tissue. The study aimed to calculate the effective permittivity of the cancerous tissue based on the idea that each sample is an inhomogeneous mixture of cells with different permittivities. It was proposed, and confirmed, that since the cancerous tissue is composed of cancer cells mixed in with normal cells, the volume fraction of cancer cells in a sample affects the dielectric properties. In particular, each sample was treated with a hematoxylin-eosin stain and then digital images of each slice (parallel to the probe-sample interface) were taken. The slide images were analysed by counting the number of pixels of cancer cells and cells of other tissue types presented. The ratios of each type of tissue cell, relative to all of the cells in the slice, were calculated. The three-dimensional fractional volume of each cell type was calculated based on the two-dimensional slice using Bruggeman's effective medium approximation theory [180]. This method has the advantage of being highly quantifiable – each cell is counted – however, the process is tedious and time-consuming. In this study, the sample analysis was not restricted to a specific region of the sample (sample sizes ranged from 5–30 mm). Furthermore, the study does not mention if any samples had to be discarded or were contaminated during the histological procedures. A similar study on various types of malignancies was presented by Sugitani *et al.* [122], for which the pathological procedures were the same as those by Sugitani *et*

al. [15].

From the studies mentioned above, it is clear that there is no consensus to date on the best practice for conducting histology in relation to dielectric measurements. Since no comparison of the different histology techniques has been reported in the literature, it is not known if some methods are more accurate than others. However, it is likely that some features from each of the studies lend themselves to obtaining more accurate data.

For instance, it is straightforward to conclude that a marker that is resistant to the histology process and is non-invasive (i.e., does not damage the measurement region) has the potential to reduce the uncertainty due to the probe location marking on tissue samples. In the study by Lazebnik *et al.* [10], [11], the use of a non-invasive black ink caused the rejection of nearly half of all samples, because the ink was not always resistant to the chemicals used in the histology process. Conversely, pins and stitches as used by Halter *et al.* [12] are resistant to the histology process, although they can damage the tissue. For this reason, the results from these two studies suggest that it can be preferable to use pins and stitches (instead of black ink), but around and not within the measurement region, in order to avoid tissue damage.

Furthermore, recent studies have suggested limitations in the methodology used in the breast tissue studies conducted by Lazebnik *et al.* [10], [11] to combine the acquired dielectric data with the histological content of the sample [66]. Specifically, the study conducted by Meaney *et al.* [66] reported that the inconsistencies in breast tissue data in the literature may be attributed to an inaccurate evaluation of the sensing depth of the probe, and thus to an imprecise correspondence between the sensing volume and the dielectric contribution of each tissue type to the acquired data.

Due to the numerous challenges in accurately evaluating the sensing volume and the dielectric contribution of each tissue type within the sensing volume, the sensing volume and the correlation between dielectric and histological data are thoroughly discussed in the next subsection.

3.3.2.2 Challenges in attributing dielectric data to heterogeneous samples

The first challenge of attributing the acquired dielectric data to the histological content of the heterogeneous sample relates to an accurate calculation of the sensing volume of the probe. Once the sensing volume is defined, another challenge involves the correlation of the histological content of the sample with the acquired dielectric properties. In this section, the sensing

CHAPTER 3. DIELECTRIC MEASUREMENT PROTOCOL

volume is examined first, followed by the issue of correlating tissue content with bulk tissue properties.

The sensing volume of an open-ended coaxial probe consists of sensing radius and sensing depth, which define the radial and longitudinal extents of the volume, respectively. The sensing radius and depth also delineate the radial and longitudinal sizes, respectively, of the region of sample that undergoes histological analysis, i.e., histology region, as shown in the diagrams of Fig. 3.4.

The sensing radius and depth can be determined by preliminary experiments and numerical simulations with different combinations of materials, as in numerous past studies [63], [64], [66], [128], [135], [163], [181], [182]. Specifically, across these studies, although similar methodologies and probe geometries have been used, considerably different values of sensing radius and depth have been reported [63]–[66]. Differences in sensing radius and depth estimates can be attributed to the different definitions, on which the estimation of the sensing radius and depth is based. To this extent, Porter and O’Halloran [63] demonstrated how different definitions of sensing depth can impact the estimates of the sensing depth.

Hence, although similar coaxial probes operating at MW frequencies were used across the breast tissue studies (the Keysight slim form probe with a diameter of 2.2 mm was used in [12], [15], [49] and a custom made probe with a diameter of 3 mm was used in [10], [11]), inconsistent values of sensing radius and depth were considered for the histological analysis (due to the different criteria adopted for defining and estimating the sensing volume). Specifically, the following values of sensing radius \times sensing depth were considered:

- 1 cm \times 1 cm in Halter *et al.* [12];
- 7 mm \times 3 mm in Lazebnik *et al.* [10], [11];
- 5-30 mm size samples in Sugitani *et al.* [15];
- 2 mm \times 2 mm in Martellosio *et al.* [49].

The different values of sensing volume, and the resulting high variability of the histology regions considered across the above studies, may have contributed to the inconsistencies in the reported dielectric data of the breast tissue, as was discussed in Section 2.4.2.

To this extent, the impact of the defined and calculated sensing volume on the interpretation of the dielectric data from heterogeneous tissues is demonstrated in Fig. 3.4. In particular, this figure demonstrates the importance of matching the sensing volume with the histology region in order to achieve an accurate interpretation of the dielectric data. All of the diagrams in Fig. 3.4 refer to a simplified, single longitudinal breast histology slice (parallel to the plane of the probe axis) consisting of eight fat modules

CHAPTER 3. DIELECTRIC MEASUREMENT PROTOCOL

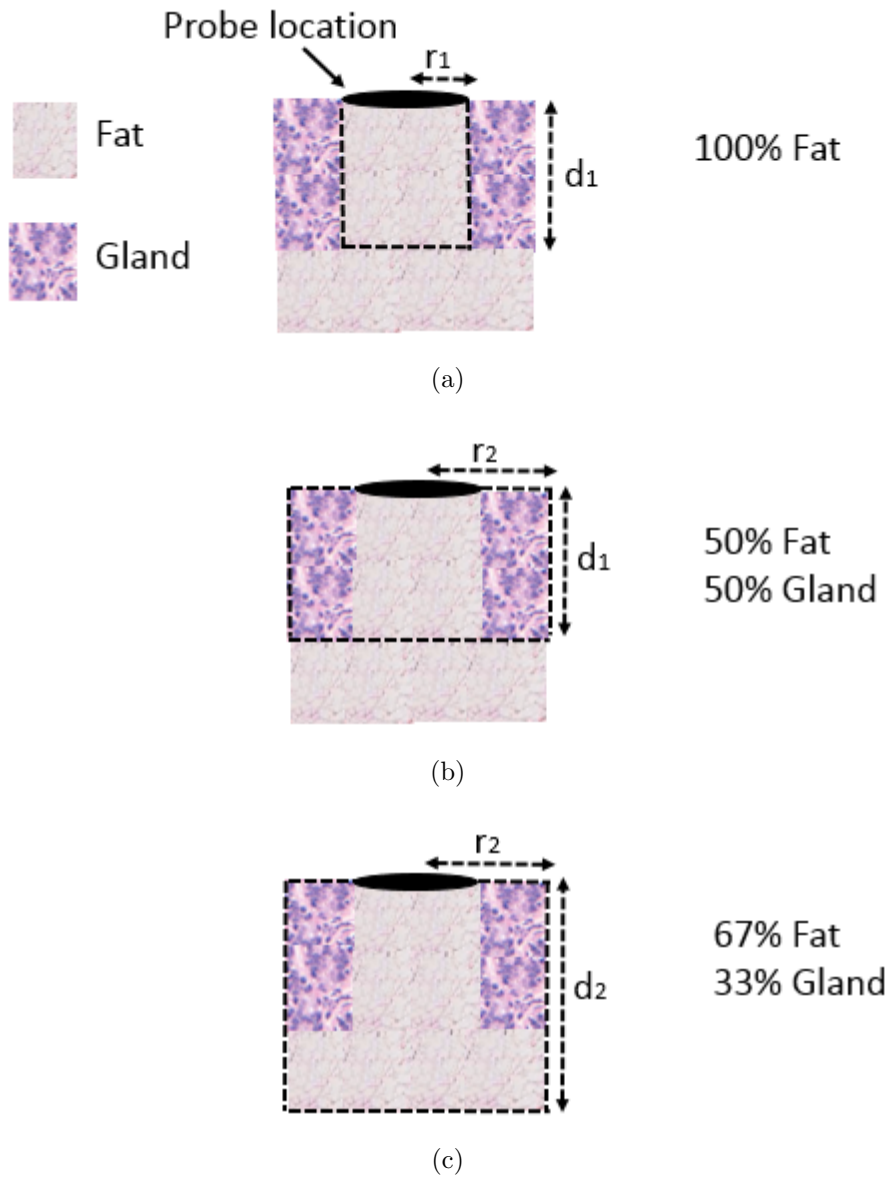


Figure 3.4: Histology diagrams of a breast sample composed of fat and gland modules (distinguishable by their distinctive colours) highlighting the impact of the sensing volume on the tissue categorisation and thus on the interpretation of the acquired dielectric data. In (a-c), the probe location is denoted with a black oval on the top of the side view of the sample histology, where different values of sensing radius and depth are marked with dotted lines. Specifically, in (a), the sensing volume is expressed by r_1 and d_1 and delineates the histology region occupied by 100% fat, in (b), the sensing volume is expressed by r_2 and d_1 and delineates the histology region occupied by 50% fat and 50% gland, and, in (c), the sensing volume is expressed by r_2 and d_2 and delineates the histology region occupied by 67% fat and 33% gland.

and four gland modules. The two different tissue modules are distinguishable by their distinctive colours, white for fat and pink for gland. Furthermore, the probe location is denoted with a black oval on the top of the side view of the sample histology, where different values of sensing radius and depth are marked with dotted lines in each of the diagrams. By comparing these diagrams, Fig. 3.4 illustrates how the tissue composition of the histology region changes by modifying in turn the values of sensing radius and depth, respectively. For instance, in Fig. 3.4a, a sensing radius and a sensing depth having r_1 and d_1 values, respectively, delineate the histology region that is composed entirely of homogeneous fat tissue. Alternatively, as represented in Fig. 3.4b, if the sensing volume is expressed by r_2 (which is double the size of r_1) and d_1 , then the histology region occupied by 50% fat and 50% gland is delineated. Finally, if the sensing volume is expressed by r_2 and d_2 (which is now 50% larger than d_1), the histology region consists of 67% fat and 33% gland.

With these diagrams, the significance of the sensing volume in categorising the tissue types present in the sample, and then in interpreting the acquired dielectric data, is highlighted. For instance, if r_2 and d_2 are the accurate values of sensing radius and depth, respectively, and instead r_1 and d_1 are the values considered for the definition of the histology region, then a considerable error is introduced in the dielectric characterisation of that heterogeneous sample. In fact, although both fat and glandular tissue contribute to the acquired dielectric data in this case, the dielectric data is erroneously associated only to fat tissue.

Furthermore, as the sensing volume can be tissue-specific, as reported in the studies conducted by Porter *et al.* [63], [64], the types of tissues and their relative locations within the sample also need to be considered while defining the histology region and attributing the dielectric data to the heterogeneous tissue sample. Due to the tissue-specificity of the sensing volume, the dielectric contribution of each tissue type cannot be considered proportional to the volume occupied by the tissue within the sensing volume, as it was erroneously assumed in the breast tissue dielectric studies [10]–[12], [15], [49]. Specifically, most recent studies demonstrated that the measured dielectric properties are dominantly influenced by the materials that are the closest to the probe tip [63], [64], [66]. Thus, although the histology regions in Fig. 3.4b and Fig. 3.4c have different tissue compositions, they are likely to correspond to dielectric measurements of similar magnitude, since the bottom fat layer is likely to have a very small dielectric impact to the acquired signal compared to the top layers. In addition, although the histology region in Fig. 3.4b consists of 50% fat and 50% gland, the corresponding dielectric signal could be closer to the permittivity of fat than

the permittivity of gland, since the acquired dielectric signal could be more influenced by fat than gland due to the fact that fat is the tissue closest to the probe tip. However, in the literature, the differences in dielectric contribution among tissues based on their location relative to the probe tip has been accurately quantified only for layered tissue samples [63], [64], [66], [135]. Thus, further studies are needed to quantify the dielectric contribution of tissues across samples with different heterogeneities.

Lastly, another factor that complicates the attribution of the dielectric data to the heterogeneous tissue sample is that not every tissue is occupied fully by cells of that tissue type [15]. Obviously, as more tissue types are involved in the histological analysis and the histology region becomes more heterogeneous, the more challenging it becomes to conclusively determine the tissue composition breakdown.

The numerous confounders involved in interpreting the acquired dielectric data, together with the lack of a consistent histological procedure, provide the motivation for the experimental objectives of this dissertation, which are discussed in the following chapters.

3.4 Summary

This chapter has discussed each step of the open-ended coaxial probe measurement procedure, highlighting common practices, challenges, and techniques for controlling and compensating for confounders.

The main focus of the chapter is the topic of tissue-related confounders, which generally contribute to higher values of uncertainty compared to equipment-related confounders and do not have standardised compensation methods. Based on previous dielectric studies, the tissue-related confounders that introduce higher errors in tissue dielectric properties are:

- Probe-sample contact;
- Sample moisture content;
- Heterogeneity.

In Sections 3.2.2 and 3.2.3, compensation techniques for these confounders were also described. In particular, along with a close visual inspection of the probe tip and the tissue surface, the probe-sample contact can be improved by applying a steady pressure with the probe on the sample, which can be monitored by conducting repeated measurements on the same exact site.

In addition, the sample moisture content can be controlled and dehydration reduced by minimising the time between tissue surgical removal and dielectric data acquisition, and by keeping the sample in temperature-

CHAPTER 3. DIELECTRIC MEASUREMENT PROTOCOL

controlled rooms (or containers, in case transportation is involved) or in a water bath.

Lastly, the measurement issues related to tissue heterogeneity could be reduced by carefully selecting the tissue measurement regions and marking them on the sample surface. This procedure ensures that the histological analysis is performed exactly at the measurement site. However, in order to find an accurate correspondence between dielectric and histological properties, it is appropriate to consider additional steps involving the histological procedure and the selection of the portion of the sample to image digitally at the microscope (i.e., selection of the dimension and the number of the histology slices, which constitute the histology region). Furthermore, the histological procedure and the selection of the histology region can be affected by a number of confounders that have not been thoroughly investigated in the literature. Specifically, general confounders (i.e., not tissue-specific) that can affect the histology procedure are the following:

- Poor fixation;
- Uneven levels of staining;
- Different procedures of slide digitation;
- Inconsistent histological interpretation and tissue categorisation.

Moreover, challenges in the selection of the histology region and, consequently, in the interpretation of dielectric data involve:

- Calculation of the size of sensing radius and sensing depth, which constitute the sensing volume of the probe;
- Calculation of the dielectric contribution of each tissue within the sensing volume to the acquired dielectric data.

The sensing volume and the tissue dielectric contributions are generally determined by preliminary experiments and numerical simulations, as in the study by Hagl *et al.* [65] and in most recent studies [63], [64], [66], [135]. The calculation of the sensing volume and the dielectric contribution of each tissue occupying the sensing volume are not straightforward, since both sensing volume and dielectric contribution can be sample-specific, i.e., dependent on the characteristics of the tissue sample [63], [64], [66]. For instance, the sensing volume may vary with the dielectric properties of the investigated tissue, not only with the size of the probe [63], [64], [66]. Furthermore, the dielectric contribution of a tissue to the acquired signal can depend on the location of the tissue within the sensing volume, not necessarily only on the volume occupied by the tissue within the sensing volume [63], [64].

Due to these challenges and the lack of research studies investigating methods to address them, in the next chapters of this dissertation, experimental measurements and numerical simulations are reported to support

CHAPTER 3. DIELECTRIC MEASUREMENT PROTOCOL

the calculation of the sensing volume and the tissue dielectric contribution (within the sensing volume) for heterogeneous biological samples. Thus, the experimental objectives of this dissertation support the interpretation of dielectric properties acquired from heterogeneous tissue samples.

In summary, Chapter 3 has provided the framework for best practice in the dielectric measurement of biological tissues, which supports the measurement protocol adopted in the following chapters. This chapter has also highlighted gaps in the dielectric characterisation of heterogeneous samples (which require knowledge of the sensing volume and the dielectric contribution of each tissue within the sensing volume to the acquired data). These gaps are addressed through the work of this thesis.

Analysis of the sensing radius of an open-ended coaxial probe

Related publications

The experimental and numerical studies presented in this chapter have been reported in two journal papers. In particular, the analysis of the sensing radius based on the probe dimensions has been summarised in the paper entitled “Predicting the Sensing Radius of a Coaxial Probe based on the Probe Dimensions”, which is under review in the journal of IEEE Transactions on Antennas and Propagation.

*The analysis of the sensing radius based on the sample dielectric properties has been published in the paper entitled “Modelling the Sensing Radius of a Coaxial Probe for Dielectric Characterisation of Biological Tissues” in the journal of IEEE Access (A. La Gioia, M. O’Halloran, and E. Porter, “Modelling the Sensing Radius of a Coaxial Probe for Dielectric Characterisation of Biological Tissues,” *IEEE Access*, vol. 6, pp. 46516–46526, 2018).*

In Chapter 2, inconsistencies in dielectric data from the literature were presented and it was demonstrated that these inconsistencies tend to increase with the heterogeneity of the investigated biological sample. By critically examining the measurement protocol for accurate dielectric characterisation of biological tissues in Chapter 3, data inconsistencies in heterogeneous samples were attributed primarily to discrepancies in the methodology adopted to interpret the acquired dielectric data in relation to the sample tissue content. Included among these discrepancies are the inconsistent procedures for calculating the sensing volume of the measurement probe, which consists of sensing radius and sensing depth, and defines the portion of sample that undergoes post-measurement histological analysis.

Since recent research studies have investigated the impact of the sensing depth definition and calculation on the dielectric characterisation of a number of biological tissue samples, this chapter focuses on the investigation of the sensing radius. Similarly to the sensing depth investigations in the literature,

CHAPTER 4. SENSING RADIUS OF COAXIAL PROBES

which were conducted by performing dielectric experiments and numerical simulations on layered material samples, in this chapter, the sensing radius is investigated both experimentally and numerically by examining concentric tissue-mimicking materials and biological tissues. In particular, the sensing radius is calculated in a number of scenarios involving different coaxial probes and concentric samples in order to evaluate the dependence of the sensing radius on both the physical dimensions of the probe and the dielectric properties of the investigated sample.

Firstly, Section 4.1 reports the state-of-the-art in analysing the sensing volume, which provides the motivation for the experimental and numerical studies discussed in the following sections of this chapter.

Secondly, in Section 4.2, the experimental and numerical methodology for the calculation of the sensing radius across various scenarios is motivated and detailed. Specifically, Section 4.2.1 reports the experimental methodology, which consists of the following steps:

- Assessment of the overall performance of the measurement system by conducting measurements on reference liquids and calculating the measurement uncertainty;
- Selection of the measurement probes and samples;
- Design of the dielectric measurement protocol.

Section 4.2.2 reports the numerical geometry, the simulation design and settings used to reproduce, validate and then extend the experimental study. Lastly, Section 4.2.3 concludes the methodology section with the description of the implemented models used for predicting the sensing radius from knowledge of probe dimensions and tissue dielectric properties.

Furthermore, the results are presented and discussed in Section 4.3 in three different subsections as follows:

- Section 4.3.1 analyses the dependence of the sensing radius on the inner conductor, insulator width, and inner radius of the outer conductor of the probe;
- Section 4.3.2 analyses the dependence of the sensing radius on the tissue dielectric magnitude and contrast;
- Section 4.3.3 reports the accuracy of the linear regression and neural network models at predicting the sensing radius from knowledge of the probe dimensions and tissue dielectric properties.

The main findings of the above results are finally summarised in Section 4.4.

4.1 Sensing radius of an open-ended coaxial probe

As the open-ended coaxial probe became the most common technique to measure the dielectric properties of biological tissues, a number of probes were fabricated, as discussed in Chapter 2. Generally, after designing and fabricating the probe, the measurement uncertainty and the sensing volume of the probe are evaluated. Knowledge of the sensing volume enables accurate dielectric characterisation of the tissue of interest for both homogeneous and heterogeneous samples. However, as mentioned in Chapter 3, different procedures to define the sensing volume have been adopted in the literature. Therefore, the importance of an accurate evaluation of the sensing volume is provided in Section 4.1.1, the state-of-the-art in sensing volume investigations is reported in Section 4.1.2, and the definition of sensing radius considered in this thesis is provided in Section 4.1.3.

4.1.1 Importance of an accurate evaluation of the sensing volume

Dielectric measurement with the coaxial probe is based on the assumption that the measured sample is homogeneous and has infinite size in the transverse and longitudinal directions [183]. In practice, all samples have limited size. In addition, biological tissues generally show heterogeneous structures, which further complicate dielectric measurements with a coaxial probe.

Generally, biological tissue samples are dielectrically characterised by either determining the dielectric properties of each tissue type constituting the sample [48], [61] in the case of simple heterogeneous structures (where homogeneous tissue regions are at least as large as the sensing volume), or by correlating the dielectric data acquired from the heterogeneous sample region with the sample histological content in the case of complex heterogeneous structures [10], [11]. However, in both scenarios, knowledge of sensing volume is fundamental for an accurate dielectric characterisation of the samples.

In the case of simple heterogeneous structures, knowledge of the sensing radius and depth allows definition of the minimum width and thickness, respectively, of the homogeneous tissue that can be accurately dielectrically characterised, without the influence of the surrounding tissues [183]. In fact, if the width (or thickness) of the homogeneous tissue is smaller than the sensing radius (or depth), the dielectric measurements of the tissue of

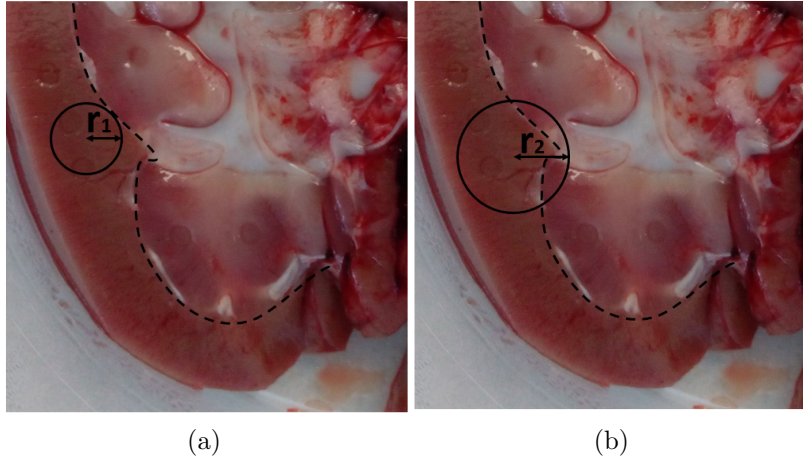


Figure 4.1: Example illustrating the importance of knowledge of the sensing radius of the measurement probe for the dielectric characterisation of single tissue types within heterogeneous samples. Both (a) and (b) illustrate a portion of porcine kidney, where the cortex is separated from the medulla with a black dashed line. In (a) and (b) the transversal sensing areas corresponding to the sensing radii r_1 and r_2 , respectively, are marked with a black solid line. The figure highlights how an inaccurate evaluation of the sensing radius can lead to an inaccurate dielectric characterisation of tissues: if the sensing radius r_1 is erroneously considered (instead of the correct sensing radius r_2), the measured dielectric data is erroneously associated only to the cortex, although the medulla is within the sensing area and is likely to contribute to the dielectric measurement.

interest are not accurate, since the properties are affected by other tissues or materials surrounding the tissue of interest. On the other hand, if only the homogeneous tissue region is contained within the probe sensing volume, the dielectric properties of the homogeneous tissue are accurately measured.

In particular, in Fig. 4.1, the importance of rigorously evaluating the sensing radius for an accurate dielectric characterisation of the kidney cortex is highlighted. In Fig. 4.1, an image of a porcine kidney sample is shown with a black dashed line indicating the interface between the cortex and the medulla. In Fig. 4.1a and Fig. 4.1b, the transversal sensing areas for the sensing radius r_1 and r_2 , respectively, are marked with a black solid line. In fact, if the sensing radius r_1 is erroneously considered (instead of the correct sensing radius r_2), the measured dielectric data is erroneously associated only to the cortex, although the medulla is within the sensing area and is likely to contribute to the dielectric measurement. Thus, Fig. 4.1 highlights how an inaccurate evaluation of the sensing radius can lead to an inaccurate dielectric characterisation of the cortex.

In the case of highly heterogeneous structures, knowledge of the sensing

radius and depth enables delineating the radial and longitudinal extents, respectively, of the portion of sample to characterise histologically in order to accurately correlate the dielectric data obtained from the heterogeneous measurement region to the histological information within that region [10], [63]. The importance of the sensing radius and depth for the dielectric characterisation of heterogeneous samples with the support of histological analysis is illustrated in Fig. 3.4 of Chapter 3.

Having demonstrated the importance of the sensing volume in different dielectric measurement scenarios, the different methodologies adopted for evaluating the sensing volume across past studies are reported in the following section.

4.1.2 State-of-the-art in sensing volume studies

In the 1970s, mathematical models reproducing the interaction of a coaxial probe with samples of finite thickness have been developed [184] and replaced the models based on the assumption of sample of infinite size [99]. Subsequently, the sensing volume of coaxial probes has been investigated to determine the minimum sample size necessary for accurate dielectric measurements of custom materials surrounded by other materials [181]. Specifically, a number of studies have investigated the sensing depth across scenarios involving different probes and tissue-mimicking/biological samples [63], [65], [66], [128], [181]–[183], [185]–[187]. Conversely, only a few studies including limited numbers of probes and tissue-mimicking samples have examined the sensing radius in the literature [65], [181], [183], [187]. The historical sensing depth and sensing radius investigations are reported in chronological order in Table 4.1 and Table 4.2, respectively.

In the studies summarised in Table 4.1, the sensing depth has been investigated experimentally and/or numerically with bi-layered structures consisting of a top material of varying thickness backed by a material of fixed large thickness (much larger than the sensing depth) [63], [65], [66], [181]–[183], [185]. In a similar way, in the studies summarised in Table 4.2, the sensing radius has been investigated experimentally and/or numerically with concentric structures consisting of an inner material of varying radius surrounded by a surrounding material of fixed large radius (much larger than the sensing radius) [65], [181], [183], [187]. In most studies, the sensing depth has been defined as the minimum thickness required for the top material so that the dielectric contribution of the backed material (in terms of either total equivalent capacitance C_T of the sample, reflection coefficient Γ , or permittivity ϵ) is negligible (under a certain level, generally ranging from 1 to 10%) [63], [65], [66], [181]. Similarly, the sensing radius has

CHAPTER 4. SENSING RADIUS OF COAXIAL PROBES

Table 4.1: Summary of sensing depth investigations in the literature.

Study	Frequency [GHz]	Sample materials	Sensing depth definition	Sensing depth value
Anderson et al. [181] (Experimental and numerical)	0.20-2	1 st layer: water 2 nd layer: metal/air	1 st layer thickness at which: $\frac{C_T - C_{1^{st}layer}}{C_{1^{st}layer}} \leq 0.01$	6 mm for a 6.4 mm diameter probe
Chen et al. [185] (Experimental and mathematical)	0.60-2	1 st layer: rubber band/ wax 2 nd layer: DI water/ saline	Mathematical formulation by combining the equivalent capacitance model of the probe and the admittance expression	N/A
Bakhtiari et al. [186] (Numerical and mathematical)	0.10-12	1 st layer: lossy media 2 nd layer: metal	Mathematical formulation with admittance expressions supported by simulations	N/A
De Langhe et al. [183] (Experimental and numerical)	0.50-1.5	1 st layer: water 2 nd layer: metal	1 st layer thickness at which: $\frac{\Gamma_{meas} - \Gamma_{1^{st}layer}}{\Gamma_{1^{st}layer}} \leq 0.01$	$\approx 2b$
Folgerø et al. [182] (Experimental and numerical)	0.50-15	1 st layer: reference liquid 2 nd layer: Teflon	1 st layer thickness at which: $\frac{\epsilon_{meas} - \epsilon_{1^{st}layer}}{\epsilon_{1^{st}layer}} \leq 0.02$	$\approx b$
Alanen et al. [128], [164] (Experimental, numerical and mathematical)	0.30	1 st layer: reference liquids 2 nd layer: Teflon/ acrylic	Variational formulation with the support of experiments and simulations	N/A
Hoshina et al. [187] (Experimental and numerical)	0.86	1 st layer: saline 2 nd layer: metal	1 st layer thickness within which: $\bar{\epsilon}_{meas} - 3std \leq \epsilon_{meas} \leq \bar{\epsilon}_{meas} + 3std$	5.4 mm for a probe with $b=5$ mm
Hagl et al. [65] (Experimental and numerical)	1-20	1 st layer: reference liquids 2 nd layer: beaker bottom	1 st layer thickness at which: $\frac{\Gamma_{meas} - \Gamma_{1^{st}layer}}{\Gamma_{1^{st}layer}} \leq 0.01$ and $\frac{\epsilon_{meas} - \epsilon_{1^{st}layer}}{\epsilon_{1^{st}layer}} \leq 0.1$	1.5 mm for a 2.2 mm diameter probe 3 mm for a 3.58 mm diameter probe
Meaney et al. [66], [135] (Experimental and numerical)	0.30-10	1 st layer: reference liquids 2 nd layer: Teflon/ acrylic	1 st layer thickness at which the curve of measured properties versus 1 st layer thickness deviates from a straight line by 20%	$d = 0.1793x - 0.0091$ where x is the probe diameter
Porter et al. [63], [64] (Experimental and mathematical)	0.30-8.5	1 st layer: reference liquids/tissues 2 nd layer: phantoms/tissues	1 st layer thickness at which: $\frac{\epsilon_{meas} - \epsilon_{1^{st}layer}}{\epsilon_{1^{st}layer}} \leq u_c$ where u_c is the measurement combined uncertainty. The results were also embedded in models to predict the material dielectric contribution.	from 1.20 mm to 3.59 mm for a 2.2 mm diameter probe (based on frequency and sample)

CHAPTER 4. SENSING RADIUS OF COAXIAL PROBES

Table 4.2: Summary of sensing radius investigations in the literature.

Study	Frequency [GHz]	Sample materials	Sensing radius definition	Sensing radius value
Anderson et al. [181] (Numerical)	0.20-2	Inner material: water Outer material: metal	Inner material radius at which the electric field is negligible	\simeq probe total radius
De Langhe et al. [183] (Numerical)	0.50-1.5	Inner material: water Outer material: metal	Inner material radius at which: $\frac{\Gamma_{meas}-\Gamma_{inner}}{\Gamma_{inner}} \leq 0.01$	Satisfies the relationship: $\frac{\pi R^2}{(\pi b)^2} > 2$ with R =sensing radius
Hoshina et al. [187] (Numerical)	0.86	Inner material: saline Outer material: metal	Radial extent at which the normalised power is -39.4 dB (i.e., the power at which the effect of the outer material is negligible)	2.95 mm for a probe with $b=5$ mm
Hagl et al. [65] (Experimental and numerical)	1-20	Inner material: reference liquids Outer material: beaker wall	Inner material radius at which: $\frac{\Gamma_{meas}-\Gamma_{inner}}{\Gamma_{inner}} \leq 0.01$ and $\frac{\epsilon_{meas}-\epsilon_{inner}}{\epsilon_{inner}} \leq 0.1$	1.25 mm for a 2.2 mm diameter probe 3.75 mm for a 3.58 mm diameter probe

been defined as the minimum radius required for the inner material so that the dielectric contribution of the surrounding material (in terms of either reflection coefficient Γ , or permittivity ϵ) is negligible (under a certain level, generally ranging from 1 to 10%) [65], [181]. The two materials used to calculate experimentally and/or numerically the sensing depth and the sensing radius are specified in the column ‘‘Sample materials’’ of Table 4.1 and Table 4.2, respectively. The two tables report also the different definitions of sensing depth and sensing radius adopted in each study and the respective numerical values, wherever calculated.

Furthermore, from Table 4.1, it can be observed that several studies provided mathematical formulations of bi/three-layered materials, in the context of determining the sensing depth. These formulations allow for the calculation of the permittivity of a layer of material from knowledge of the geometry of the layered structure and the bulk measured permittivity. On the other hand, no mathematical formulations of concentric materials were provided in the sensing radius investigations reported in Table 4.2.

Hence, from the studies summarised in Table 4.1 and Table 4.2, it is clear that, contrary to the sensing depth, the sensing radius has not been investigated thoroughly in the literature. Notably, only Hagl *et al.* investigated the sensing radius experimentally. However, in the study by Hagl *et al.*, the sensing radius was analysed with experiments and simulations

including only a limited number of reference liquids and no biological tissues. For this reason, this chapter examines the sensing radius across a number of scenarios involving probes with different geometries and biological samples with different permittivities.

Before introducing the experimental and numerical methodology, the following subsection motivates the definition of sensing radius used in this thesis.

4.1.3 Sensing radius definition

In this thesis, the sensing radius is investigated both experimentally and numerically with concentric samples consisting of an inner cylindrical material of increasing radius surrounded by an outer material of larger size. This concentric sample structure is consistent with the literature and the axially symmetric EM field radiation around the probe. The sensing radius is then determined as the distance at which the outer material ceases to contribute to the measured dielectric properties, within the uncertainty of the measurement (i.e., the distance at which only the permittivity of the inner material is detectable, within the uncertainty of the measurement). Thus, while an arbitrary value of 10% was chosen for the calculation of the sensing radius in the study conducted by Hagl *et al.* [65], in this thesis, the determination of the sensing radius is empirically related with the uncertainty of the measurement system (the calculation of which is reported in Section 4.2.1). The methodology for the calculation of the sensing radius in this thesis is discussed and illustrated in Sections 4.2.1 and 4.2.2.

Furthermore, in this thesis, the definition of maximum sensing radius is also introduced, based on the awareness that the sensing radius may vary with the dielectric properties of the investigated tissue sample. Thus, the maximum sensing radius is defined in this thesis as the sensing radius obtained from materials having the maximum contrast expected in the properties of biological tissues at MW frequencies. This maximum sensing radius can be used for the histological analysis when the tissue composition of the sample is unknown, due to the fact that the sensing radius for any unknown sample cannot be larger than the maximum sensing radius. On the other hand, when the tissue composition of the sample is known, the sensing radius can be estimated by customised preliminary experiments or simulations.

Based on the definition of sensing radius and maximum sensing radius given above, concentric samples consisting of Teflon and 0.1 M NaCl solution (saline) were selected in this thesis as materials that allow for the calculation of the maximum sensing radius. In fact, the maximum dielectric contrast

CHAPTER 4. SENSING RADIUS OF COAXIAL PROBES

found between biological tissues is less than the contrast between Teflon and saline. Thus, the sensing radius for biological tissues is likely to be smaller than for samples consisting of Teflon and saline. In order to clarify how the sensing radius depends on the tissue contrast in permittivity, an example is provided in the paragraph below.

As an example, two concentric heterogeneous samples, both composed of 0.1 M NaCl (inner material) contributing 80% to the total measured permittivity (regardless of the volume occupied) are considered. In this hypothetical example, the outer material then contributes 20% to the total permittivity in each of two samples, with one sample composed of an outer material of Teflon, and the other of DI water. At 0.5 GHz, the relative permittivities of saline (at 20°C), DI water (at 20°C), and Teflon, are 77, 79, and 2.1, respectively. Therefore, the sample composed of saline and Teflon has a much higher contrast in relative permittivity (77:2.1) than the sample composed of saline and water (77:79). For both samples, the measured relative permittivity, $\epsilon_{r,meas}$, is calculated as follows:

$$\epsilon_{r,meas} = w_1\epsilon_{r1} + w_2\epsilon_{r2}, \quad (4.1)$$

where ϵ_{r1} is the relative permittivity of the inner material; ϵ_{r2} is the relative permittivity of the outer material; w_1 is the weight of the contribution of the dielectric properties of the inner material (0.8), and w_2 the weight of the properties of the outer material (0.2), to the bulk measured dielectric properties. In this particular case, although the outer material has equal dielectric contribution in both samples, the relative permittivity values measured from the two samples are very different. The respective numerical values of the two samples are reported in Fig. 4.2.

As is clear from Fig. 4.2, the relative permittivity of the 80% saline and 20% Teflon sample is 62, while the relative permittivity of the 80% saline and 20% water sample is 77.4. Although Teflon and water contribute equally to the measured dielectric properties of their respective samples, the relative permittivity from the 80% saline and 20% Teflon sample is approximately 20% lower than the relative permittivity from the 80% saline and 20% water sample. Furthermore, the 80% saline and 20% water sample is only 0.5% different from the relative permittivity of a homogeneous saline sample. Thus, concentric materials with a high contrast in relative permittivity substantially affect the measured dielectric properties, but concentric materials with a low contrast in relative permittivity introduce only a small change in the measured dielectric properties, which may be within the uncertainty. This outcome motivates the selection of Teflon and saline for the calculation of the maximum sensing radius in this thesis.

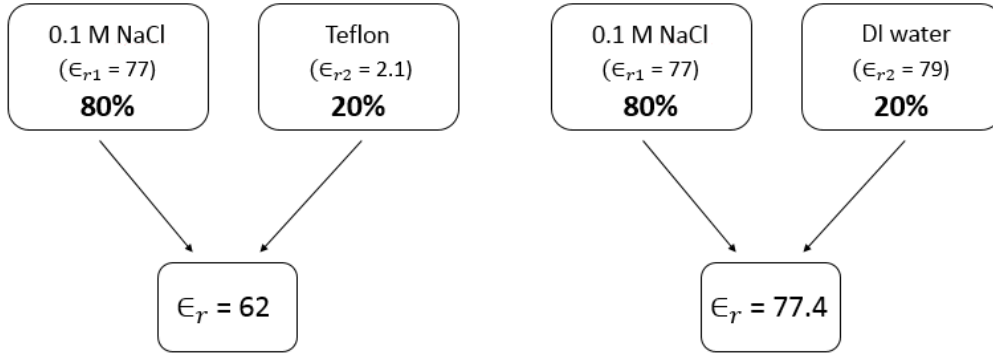


Figure 4.2: Diagram schematising the dielectric impact of individual materials within two concentric samples: one sample with saline as inner material (dielectrically contributing 80%) and Teflon as outer material (dielectrically contributing 20%), and the other sample with saline as inner material (dielectrically contributing 80%) and DI water as outer material (dielectrically contributing 20%). The respective values of relative permittivity (corresponding to 0.5 GHz) of the two samples demonstrate how concentric materials with a high contrast in relative permittivity (like that of saline and Teflon) substantially affect the measured dielectric properties, while concentric materials with a low contrast in relative permittivity (like that of saline and DI water) introduce only a small change in the measured dielectric properties, which may be within the uncertainty.

The definitions of sensing radius and maximum sensing radius provided above support the investigation conducted in this chapter. In fact, firstly, the investigation involves the calculation of the maximum sensing radius for a number of probes having different physical dimensions. Then, the sensing radius is further investigated across a number of biological tissues.

4.2 Methodology for the sensing radius investigation

The methodology of this study consists of initial dielectric experiments, followed by a number of numerical scenarios involving coaxial probes of different geometries and different concentric samples.

Firstly, the calculation of the measurement uncertainty is presented to support the definition of the sensing radius.

Secondly, an initial analysis of the maximum sensing radius of each of the Keysight slim form, performance, and high temperature probes is conducted. Then, the outcome of the initial experiments is validated with numerical simulations. After verifying consistency between experimental and numerical

CHAPTER 4. SENSING RADIUS OF COAXIAL PROBES

results, the sensing radius analysis is completed numerically, since numerical simulations allow for the calculation of the sensing radius across a number of scenarios involving a controlled variety of probe geometries and concentric material/tissue samples.

Both experiments and simulations cover the frequency range of 2-6 GHz, which is the operating frequency of many MW imaging systems and MW ablation applicators [12], [30], [53], [62].

Lastly, the sensing radius data obtained numerically is used to develop linear regression models and neural networks able to predict the sensing radius of a coaxial probe based on the probe dimensions and the dielectric properties of the interrogated sample.

In this section, the methodology is reported in different subsections, which discuss, in turn, the experimental methodology, the numerical methodology and the implemented models used for predicting the sensing radius.

4.2.1 Experimental methodology

The experimental procedure consists of different steps that are reported in this section. Firstly, measurements on standard liquids with known dielectric properties are reported to calculate the measurement uncertainty, which evaluates the overall performance of the system and supports the calculation of the sensing radius. Then, the geometry of the measurement probes is detailed, and the design of the investigated samples motivated and described. Lastly, the dielectric measurement protocol and the sensing radius calculation methodology are reported and discussed.

4.2.1.1 Uncertainty calculation

In this subsection, the calculated uncertainty for the measurement system consisting of the Keysight slim form probe [113] connected to the Agilent E8362B network analyser [188] is presented. The complete uncertainty analysis, calculated according to the NIST guidelines [131] (as discussed in Section 3.1.3), is reported only for the Keysight slim form probe, since similar values of uncertainties are obtained with the Keysight performance and high temperature probes. Furthermore, most of the dielectric measurements and simulations described in the following sections are conducted with the Keysight slim form probe because the slim form probe is the most commonly used probe in recent tissue dielectric studies [12], [15], [48], [49], [54], [63], [66] (due to the small dimensions of the probe that facilitate measurements on irregular and heterogeneous tissue structures, as seen in Section 3.2.3).

CHAPTER 4. SENSING RADIUS OF COAXIAL PROBES

In particular, this subsection reports the uncertainty values associated with measurements of 0.1 M NaCl, methanol, ethanediol, and 1-butanol solutions. These reference liquids cover a wide range of permittivities across the operating frequency range of the measurement system, i.e., 0.5-20 GHz [109], and thus enable a thorough assessment of the performance of the system within this frequency range.

The uncertainty was calculated from the analysis of repeated measurements taken on the same solution across different calibrations, as in the study conducted by Gabriel *et al.* [55]. Before each measurement session, the system was calibrated using the three-load standard procedure. Errors within each calibration were minimised by following the best practice guidelines listed in Section 3.1.1. For instance:

- Errors due to cable movement were avoided by using an L-shaped connector between the slim form probe and the VNA;
- Drift errors were minimised by allowing the VNA to warm up for over two hours prior to use and by conducting measurements immediately after calibration;
- Errors associated with the measurement of the load and validation liquids were minimised by bringing the sample in contact with the probe by a lift table, positioning the probe away from the beaker walls, accurately recording the temperature of the measurement solution, and removing air bubbles from the probe tip (whenever present).

Furthermore, the following settings were used for the measurement of the reference liquids:

- 401 linearly spaced frequency points between 0.5 and 20 GHz (the number of frequency points is a trade-off between accuracy and acquisition time, and a linear scale was used since the frequency range covers only two overlapped dispersion regions);
- A power level of -5 dBm and an intermediate frequency bandwidth (IFBW) of 30 Hz (to reduce the trace noise of the VNA).

By following the calibration steps with the above measurement settings, the total combined uncertainty was calculated for each reference liquid, for both relative permittivity, ϵ_r , and conductivity, σ . As reported in Section 3.1.3, the total combined uncertainty was calculated from the standard uncertainties associated with repeatability, accuracy and VNA drift (the system does not present uncertainties due to cable movement, since the cable was replaced by an L-shaped connector). Each of these standard uncertainties were obtained as follows:

- The standard uncertainty in repeatability was assessed for each reference liquid by conducting 10 repeated measurements after each of the three calibrations. Then, across the total 30 measurements taken from

CHAPTER 4. SENSING RADIUS OF COAXIAL PROBES

each reference liquid, the standard uncertainty in repeatability was calculated as the average percent deviation of the measured dielectric data from the mean measured dielectric data for each acquisition frequency point.

- The standard uncertainty in accuracy was assessed for each reference liquid from the set of measurements described in the point above, and was calculated by computing the percent difference between the fitted mean measured dielectric data and the dielectric model from the literature for each acquisition frequency point. For each reference liquid, the fitted mean measured dielectric data was obtained by fitting the dielectric model, i.e., Debye, Cole-Cole or Cole-Davidson (the same as the model reported in the literature for that specific liquid), to the mean measured dielectric data using the non-linear least squares error algorithm [169]. Specifically, fitted models with a fractional fit error lower than 1% were accepted. Furthermore, in the literature, the parameters of the dielectric models are generally reported across a 95% confidence interval [55], [145]; however, the percent difference between fitted mean measured data and model from the literature was computed by considering the mean values of the model parameters reported in the literature.
- The standard uncertainty associated with the VNA drift was assessed only for the 0.1 M NaCl solution, since such uncertainty is systematic, and thus has the same value for each solution [47], [55]. Specifically, the dielectric effect of the VNA drift was assessed by 20 repeated measurements performed within 2 hours from the calibration (since the dielectric measurements reported in the following subsections were all conducted within 2 hours from the calibration), with measurements taken with an interval of 5 minutes. The uncertainty was then obtained by computing the percent difference between the first measurement (performed right after the calibration was completed) and the last measurement (conducted 2 hours after calibration), after subtracting the uncertainty in repeatability.

After calculating the single standard uncertainties above, the combined and extended uncertainties can be obtained for both relative permittivity and conductivity across specific subranges of frequencies, as reported in the literature [47], [55] and illustrated in Section 3.1.3.

By replicating the table structure from the study by Peyman *et al.* [47] (Table 3.4 in the previous chapter), Table 4.3 reports the single uncertainties, the total combined uncertainty, and the extended uncertainties (with $k = 2$ and $k = 3$) calculated for the relative permittivity of 0.1 M NaCl across the subrange of 0.5-10 GHz. With the same methodology, the combined

CHAPTER 4. SENSING RADIUS OF COAXIAL PROBES

Table 4.3: Calculation of standard uncertainty for relative permittivity measured on 0.1 M NaCl in the frequency range 0.5–10 GHz. The nomenclature and methodology follow the guidelines defined by the NIST [131], as reported in Section 3.1.3. The calculation was performed at each measurement frequency and averaged across the frequency range. The uncertainty in accuracy is calculated by considering the model by Peyman *et al.* [146] as reference data.

Sources of Uncertainty	Uncertainty component a (%)	Divisor b	Sensitivity coefficient c_i	Standard uncertainty (%) $u_i = (\frac{a}{b})c_i$
Repeatability	0.25	1	1	0.25
Accuracy	1.29	$\sqrt{3}$	1	0.75
VNA drift	0.19	$\sqrt{3}$	1	0.11
Cable movement	0.00	$\sqrt{2}$	1	0.0
Combined uncertainty	N/A	N/A	N/A	0.80
Expanded uncertainty ($k=2$)	N/A	N/A	N/A	1.6
Expanded uncertainty ($k=3$)	N/A	N/A	N/A	2.4

Table 4.4: Standard uncertainty for 0.1 M NaCl in terms of both relative permittivity and conductivity across the entire measurement frequency range, divided in two frequency subranges, 0.5-10 GHz and 10-20 GHz.

Standard uncertainty (%)	ϵ_r		σ	
	0.5-10 GHz	10-20 GHz	0.5-10 GHz	10-20 GHz
Repeatability	0.25	0.20	0.33	0.26
Accuracy	0.75	0.55	1.50	0.72
VNA drift	0.11	0.01	0.29	0.12
Combined	0.80	0.59	1.56	0.60
Extended ($k = 2$)	1.60	1.18	3.12	1.20
Extended ($k = 3$)	2.40	1.77	4.60	1.80

and extended uncertainties calculated for both relative permittivity and conductivity across the entire frequency range, divided in two frequency subranges (0.5-10 GHz and 10-20 GHz, as in the study by Peyman *et al.* [47]), are reported in Table 4.4.

The uncertainty in accuracy reported in Table 4.4 was calculated by computing the percent difference between the average dielectric data measured from 0.1 M NaCl at 23.7°C and then fitted with a one-pole Cole-Cole model and the one-pole Cole-Cole model from the study conducted by Peyman *et al.* [146]. The model reported in the study by Peyman *et al.* [146] was selected as reference data because this model is valid for all temperatures between the range 2-30°C, as discussed in Section 3.1.2. Thus, the measured data can be compared with the reference data obtained at the measurement temperature of 23.7°C.

As is clear from both Table 4.3 and Table 4.4, among the single standard uncertainties, the uncertainty associated with the VNA drift is the lowest, which is in agreement with the study by Peyman *et al.* [47]. From the tables,

CHAPTER 4. SENSING RADIUS OF COAXIAL PROBES

it is also evident that the standard uncertainty in accuracy is the highest.

In Fig. 4.3, the measured average data of saline is reported, with a blue dotted line. The fitted average dielectric data, together with the standard deviation covering 95% of the confidence interval, and the reference dielectric data are also plotted, for both relative permittivity and conductivity (the fitted data is reported with a black solid line, the standard deviation with black dotted lines, and the reference data from the study by Peyman *et al.* [146] with a red dash-dotted line). Furthermore, in Fig. 4.3, the measured data is compared with other dielectric data from the literature, such as the one-pole Cole-Davidson model from the study by Gulich *et al.* [73] obtained at 23.7°C (reported with a dash-dotted yellow line) and the one-pole Cole-Cole model from the study by Buchner *et al.* [143] for temperatures of 20°C and 25°C. As is clear from both relative permittivity and conductivity plots in Fig. 4.3, both models from the studies of Peyman *et al.* [146] and Gulich *et al.* [73] overlap with the measured data. The highest dielectric difference between the measured and reference traces are for frequencies lower than 5 GHz, thus confirming that the uncertainty in accuracy is higher at lower frequencies, as reported in Table 4.4. Furthermore, the measured data at 23.7°C is in agreement with the data from the study by Buchner *et al.* [143], since the measured data is within the two dielectric traces given by the one-pole Cole-Cole models at 20°C and 25°C that are indicated with green dashed and dash-dotted lines, respectively (since the average measured data is at 23.7°C, the measured trace is a bit closer to the 25°C trace than to the 20°C trace).

Along with the VNA drift, the standard uncertainty in repeatability should be the same for every reference liquid, since the repeatability is associated with the internal trace noise of the VNA [189]. In fact, the standard uncertainty in repeatability obtained for saline is approximately the same as that obtained for methanol, ethanediol and 1-butanol. Due to the fact that the single standard uncertainties associated with the repeatability and the VNA drift are the same for all liquid solutions, in Table 4.5, only the standard uncertainty in accuracy, for both relative permittivity and conductivity, is reported for the three alcohols: methanol, ethanediol, and 1-butanol. Specifically, the uncertainty values in Table 4.5 are reported for the subrange of frequencies 0.5-5 GHz, since such values were obtained by comparing the measured average data with the models reported in Gregory *et al.* [145], which are from traceable data (obtained from a number of measurements conducted by different systems and appropriately documented to allow comparison with the highest standards) but only available up to 5 GHz. The results in Table 4.5 indicate that the accuracy is the lowest for methanol, and the highest for 1-butanol. All three alcohols show higher

CHAPTER 4. SENSING RADIUS OF COAXIAL PROBES

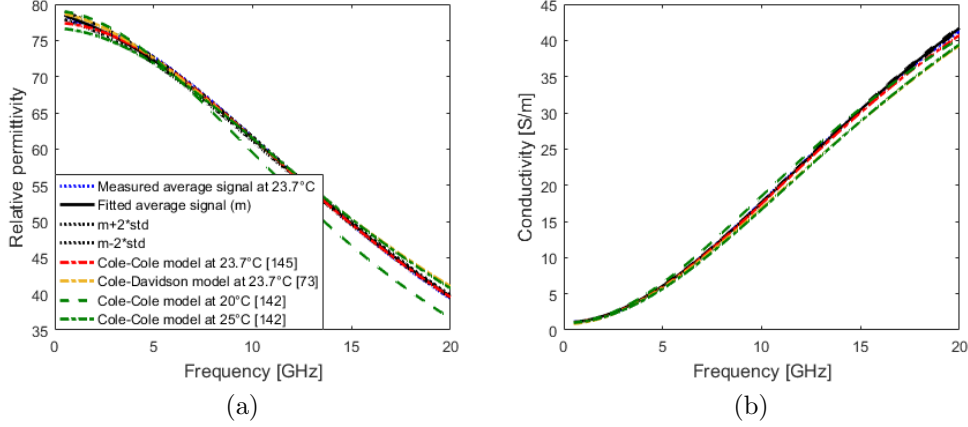


Figure 4.3: (a) Relative permittivity and (b) conductivity plots of the average measured and reference data from the literature for 0.1 M NaCl. In both relative permittivity and conductivity plots, the average measured data at 23.7°C is reported with a blue dotted line, the fitted data with a black solid line, together with the standard deviation (covering 95% of the confidence interval) indicated with black dotted lines, the data at 23.7°C by Peyman *et al.* [146] with a red dash-dotted line, the data at 23.7°C by Gulich *et al.* [73] with a dash-dotted yellow line, and the data at 20°C and 25°C by Buchner *et al.* [143] with green dashed and dash-dotted lines, respectively. The plots show that the measured data is in agreement with the data from the literature.

Table 4.5: Standard uncertainty in accuracy for the three alcohols, methanol, ethanediol and 1-butanol across the frequency range of 0.5-5 GHz. The uncertainty values are reported for the subrange of frequencies 0.5-5 GHz, since such values were obtained by comparing the measured average data with the models reported in Gregory *et al.* [145], which are from traceable data but only available up to 5 GHz.

Reference alcohol	Accuracy in ϵ_r (%)	Accuracy in σ (%)
Methanol	0.78	2.70
Ethanediol	1.30	3.58
1-Butanol	1.66	4.28

uncertainty in conductivity than in relative permittivity, as was also the case for saline. However, overall, the uncertainty in accuracy (in both relative permittivity and conductivity) is lower for saline than any of the alcohols, likely because the dielectric properties of saline are similar to the dielectric properties of DI water, which was used as standard liquid in calibration.

For a better comparison, measured and reference data of the three alcohols are reported for both relative permittivity and conductivity in Fig. 4.4 and Fig. 4.5. Specifically, the plotted reference data from the study by Gregory *et al.* [145] were obtained for the measurement temperature by interpolating the model parameters, which are available only for discrete

CHAPTER 4. SENSING RADIUS OF COAXIAL PROBES

temperature (every 5°C), as discussed in Section 3.1.2.

In all plots in Fig. 4.4, the measured average dielectric data is plotted with a blue dotted line, the fitted average dielectric data with a black solid line (together with the standard deviation covering 95% of the confidence interval that is illustrated with black dotted lines), the model at the measurement temperature from the study by Gregory *et al.* [145] with a red dash-dotted line, and the models from the study by Jordan *et al.* [147] at 20°C and 30°C with green dashed and dash-dotted lines, respectively. In particular, one-pole Debye model and one-pole Cole-Davidson model were fitted to the average measured data from methanol and ethanediol, respectively, in order to compute the percent different between measured data and reference data by Gregory *et al.* [145] for the calculation of the uncertainty in accuracy. For both methanol and ethanediol, while the model by Gregory *et al.* [145] overlaps with the measured data at lower frequencies, the difference between the measured dielectric data and the reference data by Jordan *et al.* [147] is higher for relative permittivity and conductivity values above 8 GHz and 5 GHz, respectively. The discrepancy at higher frequencies may be due to the operating limitations of the Keysight dielectric probes, which are not recommended for materials with a loss tangent lower than 0.5 with relative permittivity higher than 5 [113]. In fact, the loss tangent of both methanol and ethanediol tends to 0.5 at such higher frequencies.

Lastly, in Fig. 4.5, the relative permittivity and conductivity values from both measured and reference data of 1-butanol are reported. Specifically, in both plots of Fig. 4.5, the measured average dielectric data is plotted with a blue dashed line, together with the standard deviation covering 95% of the confidence interval (illustrated with blue dotted lines), the fitted average dielectric data with a black solid line, and the model at the measurement temperature from the study by Gregory *et al.* [145] with a red dash-dotted line. The fitted data was obtained by fitting the two-pole Debye model to the measured average data for a better comparison with the two-pole Debye model by Gregory *et al.* [145]. From both plots of Fig. 4.5, the measured data is in agreement with the reference data up to 5 GHz. However, the measured data is not reliable for frequencies above 5 GHz, where the loss tangent of 1-butanol is below the minimum recommended value of 0.05 reported in the probe datasheet [113].

In summary, the uncertainty calculation for 0.1 M NaCl, methanol, ethanediol and 1-butanol provides an understanding of the overall performance of the measurement system, and defines the permittivity range within which accurate dielectric measurements can be conducted.

Furthermore, the extended uncertainty calculated for saline supports the calculation of the sensing radius based on the definition provided in Section

CHAPTER 4. SENSING RADIUS OF COAXIAL PROBES

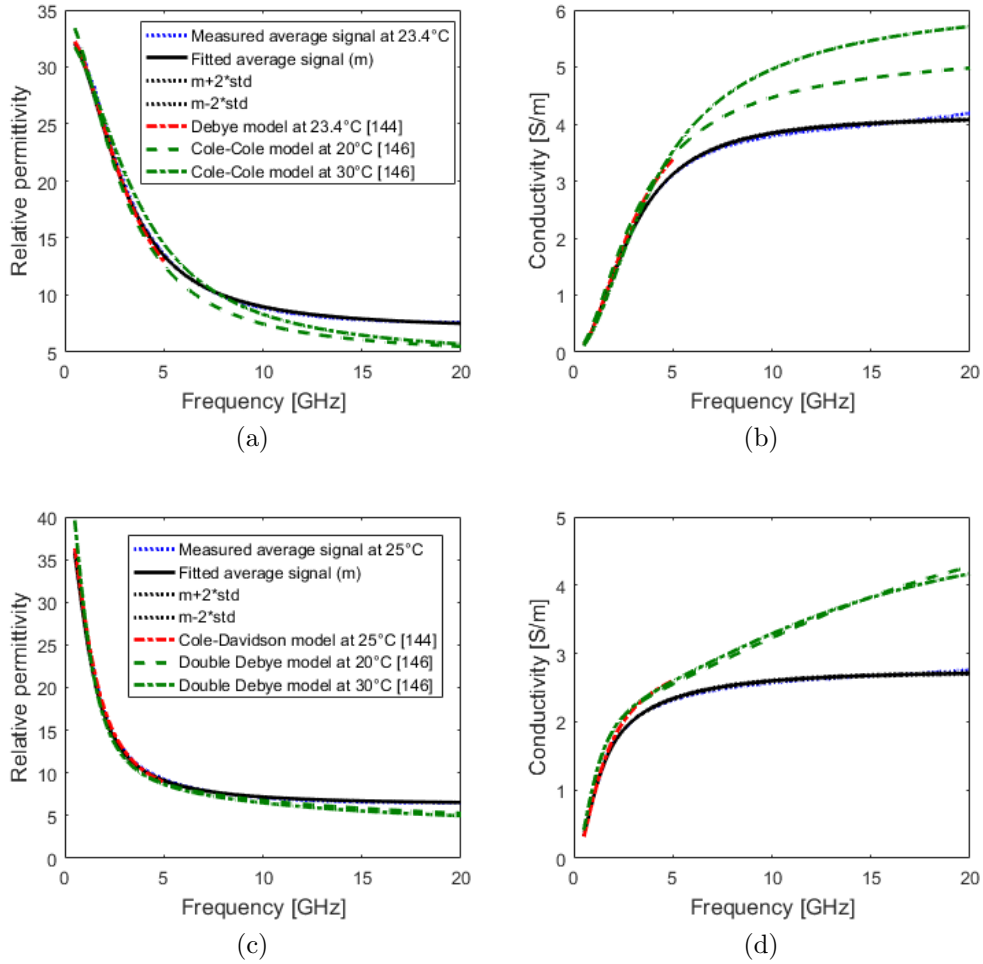


Figure 4.4: Relative permittivity and conductivity plots of the average measured and reference data from the literature for methanol (a-b) and ethanediol (c-d). In all plots, the average measured data is reported with a blue dotted line, the fitted data with a black solid line, together with the standard deviation (covering 95% of the confidence interval) indicated with black dotted lines, the data at the measurement temperature by Gregory *et al.* [145] with a red dash-dotted line, and the data at 20°C and 25°C by Jordan *et al.* [147] with green dashed and dash-dotted lines, respectively. The plots show that the measured data is in agreement with the data by Gregory *et al.* [145] and gradually diverges from the data by Jordan *et al.* [147] for frequencies above 5 GHz.

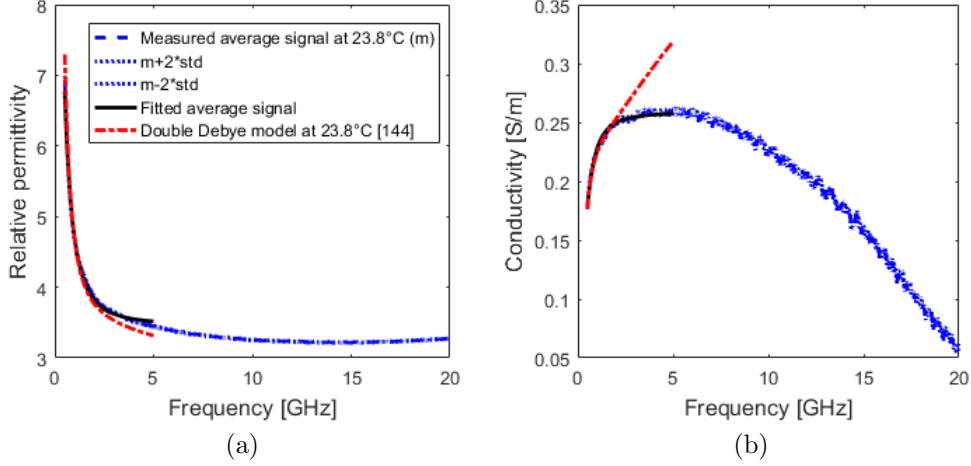


Figure 4.5: (a) Relative permittivity and (b) conductivity plots of the average measured and reference data from the literature for 1-butanol. In both plots, the average measured data at 23.8°C is reported with a blue dashed line, together with the standard deviation (covering 95% of the confidence interval) indicated with blue dotted lines, the fitted data with a black solid line (only up to 5 GHz), and the data at 23.8°C by Gregory *et al.* [145] with a red dash-dotted line. Both plots show that the measured data is in agreement with the reference data up to 5 GHz. However, measured data is not reliable for frequencies above 5 GHz, where the loss tangent of 1-butanol is below the minimum recommended value of 0.05 reported in the Keysight probe datasheet [113].

4.1.3. Further information regarding the calculation of the sensing radius is reported in the following subsections.

4.2.1.2 Experimental design

The maximum sensing radius for each of the Keysight slim form, performance and high temperature probes was calculated by performing dielectric experiments on concentric samples consisting of Teflon and 0.1 M NaCl solution. Keysight probes were selected for the experimental study since, in recent dielectric studies [15], [48], [49], [54], [114], the dielectric properties of biological tissues were mostly measured with the Keysight probes, as reported in Section 2.3.3. In addition, the three Keysight probes are suitable for an initial analysis of the dependence of the sensing radius on the physical dimensions of the probe, since these probes present different dimensions of inner conductor, insulator, and outer conductor. The probe dimensions, which are illustrated in Fig. 4.6, are reported in Table 4.6 for each of the Keysight probes. Since the datasheet reports only information regarding the size of the outer conductor, the other probe dimensions were measured

CHAPTER 4. SENSING RADIUS OF COAXIAL PROBES

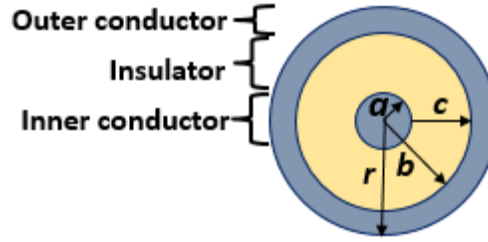


Figure 4.6: Dimensions of the coaxial probe: a is the radius of the inner conductor, c is the insulator width, b (obtained by summing a and c) is the inner radius of the outer conductor, and r is the total radius of the probe.

Table 4.6: Dimensions of the three Keysight probes: a , b , c and r refer to the probe dimensions illustrated in Fig. 4.6.

Keysight probe	a (mm)	c (mm)	b (mm)	r (mm)
Slim form	0.25	0.50	0.75	1.10
Performance	0.30	0.50	0.80	4.75
High Temperature	0.35	1.00	1.35	9.50

with a calliper through reverse engineering.

Furthermore, Teflon and 0.1 M NaCl were selected as materials for the measurement samples, since they allow for the calculation of the maximum sensing radius, as demonstrated in Section 4.1.3. In fact, Teflon and saline represent the scenario with the highest contrast in complex permittivity that can be found across biological tissues. Thus, the sensing radius for measurements of biological tissues is expected to be equal to or smaller than the maximum sensing radius.

The measurement samples used to calculate the maximum sensing radius were manufactured by drilling circular apertures of different radii into a Teflon block and immersing the drilled block into the 0.1 M NaCl solution. Both the thickness of the Teflon block and the size of the Teflon apertures were chosen based on the results of preliminary experiments analysing the sensing radius and depth of each Keysight probe. For instance, a Teflon block with a thickness of 10 mm was selected, since dielectric measurements performed with each of the three Keysight probes on a Teflon block of 10 mm thickness were found to be equivalent to dielectric measurements performed on a Teflon block of 50 mm thickness. Thus, these preliminary experiments suggested that the 10 mm thick Teflon block is larger than the sensing depth of each Keysight probe. Furthermore, the radius of the Teflon aperture was chosen by ensuring that the sensing radius of each probe was within the smallest and the largest aperture. In particular, the aperture radii were selected based on the precision of the drilling machine, and the results

CHAPTER 4. SENSING RADIUS OF COAXIAL PROBES

of preliminary experiments demonstrating that, for each Keysight probe, dielectric measurements of saline performed in a Teflon aperture of 5 mm radius were equivalent to dielectric measurements of saline performed in a beaker with a radius of 25 mm. Specifically, the Teflon apertures have radii of: 0.5 mm, 1 mm, 1.25 mm, 1.75 mm, 2.5 mm, 3 mm, 4 mm, and 5 mm, respectively. Dielectric measurements were performed with each of the three probes across all Teflon apertures immersed in the 0.1 M NaCl solution. A depiction of a given measurement is shown in Fig. 4.7a, while a diagram schematising the measurement scenarios is provided in Fig. 4.7b. Specifically, in Fig. 4.7a, the Keysight performance probe is in contact with the Teflon block immersed into the 0.1 M NaCl solution. On the Teflon block, the sizes of the apertures are labelled and, for apertures smaller than the total radius r of the probe, the size of the probe is marked in black around the apertures in order to facilitate probe positioning. In Fig. 4.7b, the measurements of each aperture, with aperture radius ranging from 0.5 mm to 5 mm, are schematised. The red circle outlines the probe position, and the solid and dotted circles concentric to the probe denote the smallest and largest radius of the saline solution, respectively, within Teflon, which is represented by the yellow square.

4.2.1.3 Dielectric measurement protocol and sensing radius calculation

Before each set of measurements, the system (i.e., the Keysight probe connected to the Agilent E8362B network analyser with an L-shaped connector) was calibrated using the three-load standard procedure and the quality of the calibration was verified by measuring the dielectric properties of 0.1 M NaCl. Before and after each calibration, the temperature of the calibration and validation liquids were recorded. Recordings of 0.1 M NaCl were compared to the known model properties, confirming that the measurement uncertainty was consistently below the uncertainty for saline reported in Table 4.4. Thus, calibration and validation procedures were conducted by following the steps specified in Sections 3.1.1 and 3.1.2. For each set of measurements, the following settings were used:

- 21 frequency points on a linear scale over the frequency range of 2-6 GHz (the choice of the number points does not impact the calculation of the sensing radius, since the sensing radius is generally calculated at single frequencies and then averaged across frequency);
- A power level of -5 dBm and an intermediate frequency bandwidth (IFBW) of 30 Hz (to reduce the trace noise of the VNA).

For each measurement, relative permittivity and conductivity values were

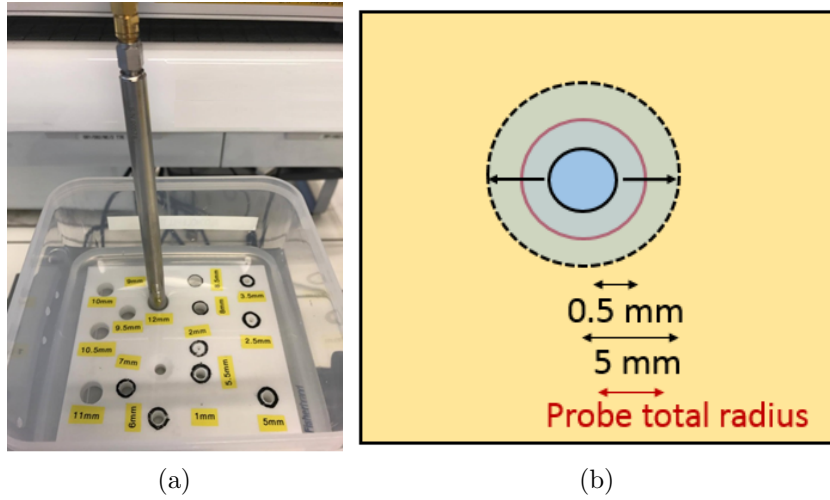


Figure 4.7: (a) Photograph and (b) diagram of the measurement scenario for the calculation of the maximum sensing radius. In the photograph (a), the Keysight performance probe is in contact with the Teflon block immersed in the 0.1 M NaCl solution. On the Teflon block, the sizes of the apertures are labelled and, for apertures smaller than the total radius r of the probe, the size of the probe is marked in black around the apertures in order to facilitate probe positioning. In the diagram (b), the measurements of each aperture, with radius ranging from 0.5 mm to 5 mm, are schematised. The red circle outlines the probe position, and the solid and dotted circles concentric to the probe denote the smallest and largest radius of the saline solution, respectively, within Teflon, which is represented by the yellow square.

acquired by bringing the sample to the probe tip using a lift table. A stable contact between the probe and the sample was ensured by visual inspection. The temperature of the immersion solution (0.1 M NaCl) surrounding the Teflon block was also recorded. For apertures smaller than the size of the probe, the measurement was more difficult to perform due to difficulty in visualising the presence of air bubbles at the probe tip, and the position of the probe with respect of the Teflon walls. Therefore, in order to ensure that the probe location was concentric to the Teflon aperture (i.e., that the Teflon aperture was centred with respect to the probe), the probe size was marked around the smaller apertures, as illustrated in Fig. 4.7. Furthermore, for each probe, measurements were repeated three times after each of three calibrations.

For each probe and each calibration, the maximum sensing radius was obtained by comparing single frequency measurements acquired across all apertures, since it is known that the sensing radius depends on the frequency [65]. Then, for each measurement frequency, the maximum sensing

CHAPTER 4. SENSING RADIUS OF COAXIAL PROBES

radius was estimated as the radius of the Teflon aperture at which the measured relative permittivity and conductivity were equal to the relative permittivity and conductivity of saline, respectively, within the extended uncertainty of saline in the range of 0.5-10 GHz. Specifically, the extended uncertainty obtained with a coverage factor of 3, which provides a confidence level of approximately 99%, was selected for the calculation of the sensing radius. The choice of such extended uncertainty, which is 2.4% for relative permittivity and 4.6% for conductivity (as reported in Table 4.4), is due to the fact that dielectric measurements from Teflon apertures filled with saline are less repeatable than dielectric measurements of saline from a beaker. The higher uncertainty in repeatability in such scenarios can be attributed to the presence of small air bubbles on the Teflon walls that cannot be visualised during the measurement, and the variation of the immersion depth of the probe. In fact, in the cases with apertures smaller than the size of the probe, the probe is placed on top of the Teflon aperture. Conversely, in the cases with apertures larger than the size of the probe, the probe is placed within the Teflon aperture.

The maximum sensing radius values obtained experimentally with the procedure described above were then validated with numerical simulations reproducing the experimental scenarios. Before presenting the numerical methodology, an example demonstrating how the maximum sensing radius was calculated from the experiments is provided.

In Fig. 4.8, the relative permittivity and conductivity traces obtained from one measurement set conducted with the performance probe are reported over 2-6 GHz. In Fig. 4.8, each trace corresponds to a given radius of the Teflon aperture filled with saline (i.e., a specific concentric sample with saline as inner material and Teflon as outer material), as specified in the legend. It should be noted that the plot does not include the apertures of radii 1.25 mm, 3 mm and 4 mm. In particular, the measurement from the aperture having 1.25 mm radius was not considered due to the persistent presence of air bubbles on the interface between Teflon and saline. On the other hand, the measurements from the apertures of radii 3 mm and 4 mm are not illustrated in Fig. 4.8 to improve the decipherability of the plot, since the traces from the apertures of radii 3 mm and 4 mm would overlap with the traces from the apertures of radii 1.75 mm, 2.5 mm, and 5 mm. From both relative permittivity and conductivity plots, it is clear that as the aperture radius increases, the traces tend to that of saline. For example, when the radius of the aperture is 0.5 mm, the acquired relative permittivity and conductivity are, on average, 40% and 45% different from relative permittivity and conductivity of saline, respectively. Conversely, when the radius of the aperture is 5 mm, the acquired dielectric properties

CHAPTER 4. SENSING RADIUS OF COAXIAL PROBES

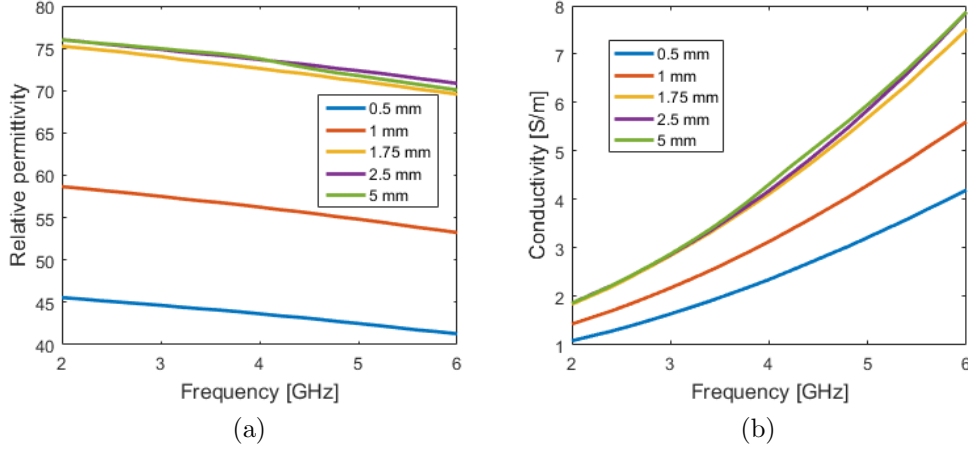


Figure 4.8: (a) Relative permittivity and (b) conductivity traces obtained from measurements involving the Keysight performance probe and the sample consisting of Teflon apertures filled with saline. In the legend, the radius of the Teflon apertures, ranging from 0.5 mm to 5 mm, is specified. As the radius of the Teflon aperture increases, the relative permittivity tends toward that of the saline solution.

are equivalent to those of saline in isolation.

In this example, the maximum sensing radius was calculated by comparing the dielectric properties acquired from different apertures to the dielectric properties of saline from the 5 mm aperture. Thus, the relative permittivity obtained from the 5 mm aperture was used as reference data for each measurement set (as shown in Fig. 4.8). In particular, for each probe, the percent difference in dielectric properties between data from each aperture with variable radius and the reference data was calculated across the frequency range. Fig. 4.9 illustrates the calculation of the maximum sensing radius of the performance probe at three single frequencies, 2 GHz, 4 GHz and 6 GHz. The 2 GHz trace is indicated with a blue solid line, the 4 GHz trace with a red dash-dotted line, and the 6 GHz trace with a green dashed line. In Fig. 4.9, it is clear that both the percent differences in relative permittivity and conductivity decrease as the aperture radius increases. Based on the definition, the sensing radius corresponds to the radius of saline at which the measured relative permittivity and conductivity of the sample differ by 2.4% (i.e., the extended uncertainty for relative permittivity of saline) and 4.6% (i.e., the extended uncertainty for conductivity of saline), respectively, from the relative permittivity and conductivity of the reference data. As is clear from the plots in Fig. 4.9, the percent differences in relative permittivity are comparable with the percent

CHAPTER 4. SENSING RADIUS OF COAXIAL PROBES

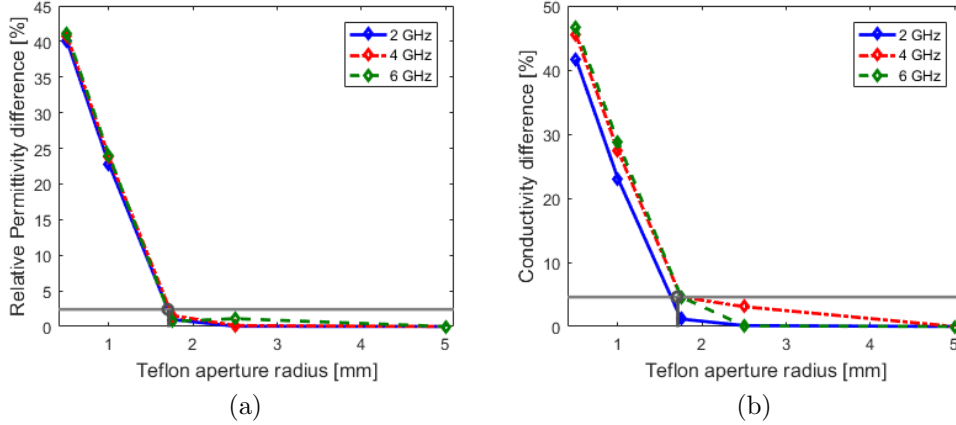


Figure 4.9: Plot of the percent difference in (a) relative permittivity and (b) conductivity between the measurements from each aperture (plotted in Fig. 4.8) and the reference data, for the frequencies of 2 GHz, 4 GHz and 6 GHz. The reference data is the measurement at the 5 mm aperture, which is representative of saline in isolation. In both plots, the 2 GHz data is indicated with a blue solid line, the 4 GHz data with a red dash-dotted line, and the 6 GHz data with a green dashed line. The 2.4% and 4.6% threshold values are indicated with horizontal grey lines in (a) and (b), respectively, for the calculation of the maximum sensing radius. In fact, the maximum sensing radius is calculated as the radius at which the outer material (Teflon) ceases to contribute to the acquired dielectric properties, within the measurement uncertainty of 2.4% for relative permittivity and 4.6% for conductivity. In both plots, the maximum sensing radius values of approximately 1.7 mm are marked with a vertical grey line, where the (a) relative permittivity and (b) conductivity percent difference lines intercept the horizontal threshold trace.

differences in conductivity, resulting in a maximum sensing radius estimated at 1.7 mm for both relative permittivity and conductivity. However, for materials or tissues that present different values of relative permittivity and conductivity, the sensing radius estimated from relative permittivity can differ from the sensing radius estimated from conductivity. In these cases, the highest value between the two estimates of sensing radius should be considered, to ensure that the sensing radius includes all the materials that can impact the measured dielectric properties.

Furthermore, in Fig. 4.9, the maximum sensing radius values calculated at the three frequencies are approximately equivalent (within 5% from each other). The maximum sensing radius obtained for each of the three frequencies (2 GHz, 4 GHz and 6 GHz) was also compared with the maximum sensing radius obtained by averaging all the sensing radius values across the frequency range. From this comparison, it was verified that the maximum sensing radius averaged across frequency is within 5% from the maximum

sensing radius calculated for the central simulation frequency (4 GHz).

The methodology described above was also adopted for the calculation of the maximum sensing radius and sensing radius from data obtained with numerical simulations, which are detailed in the following subsection.

4.2.2 Numerical methodology

This subsection reports the numerical geometry, and the simulation design and settings used to reproduce, validate and then extend the experimental study. The numerical simulations extend the analysis of the sensing radius based on the probe dimensions and allow for the analysis of the dependence of the sensing radius on the dielectric properties of biological tissues.

Specifically, the analysis of the sensing radius based on the tissue dielectric properties was only conducted numerically, due to the impossibility of finding a controlled range of concentric biological tissues in nature to enable thorough calculation of the sensing radius.

4.2.2.1 Geometrical model

Simulations were performed using COMSOL Multiphysics (version 5.3), which uses the finite element method (FEM) to solve electromagnetic wave problems. According to the concentric geometry of the probe and the interrogated sample, a 2D axially-symmetric environment was used to conduct the numerical simulations presented in this chapter.

For each simulation set, firstly, the probe model was developed by creating the probe geometry and assigning the dielectric properties of the probe insulator and conductors. Secondly, concentric sample geometries were created and the dielectric properties were assigned to each geometry simulating a material or a biological tissue.

The models of the three Keysight probes were developed with the features reported in Table 4.6. For all probes, nickel ($\epsilon_r=1$, $\sigma=1.43e7$ S/m) was assigned as the material for the inner and outer conductors, and Teflon ($\epsilon_r=2.1$, $\sigma=1e-23$ S/m) was assigned as the material for the insulator. Since information regarding the materials of the probes is not reported in the Keysight probe datasheet [113], different combinations of materials were tested in preliminary numerical simulations. Nickel and Teflon were selected since these materials ensure the best match between simulated and measured dielectric properties. To match the experiments, the dielectrically interrogated samples were modelled with concentric cylinders consisting of an inner cylinder with varying radius and a surrounding cylinder with size considerably larger than the total radius r of the probe.

CHAPTER 4. SENSING RADIUS OF COAXIAL PROBES

Table 4.7: Summary of the three simulation sets.

Simulation set 1	3 scenarios: 3 probes x 1 sample (made of saline and Teflon)
Simulation set 2	48 scenarios: 12 probes x 4 samples
Simulation set 3	1 probe (Keysight slim form probe) x 38 samples

Once the geometry of the sample was created, the dielectric properties were assigned to each cylinder. Dielectric properties were obtained by either fitting the experimental data or from the IT'IS database [190], depending on the simulation scenario. Detailed information regarding the design of each simulation set are provided next.

4.2.2.2 Numerical design

Different sets of numerical simulations were designed for the investigation of the sensing radius. A first set of simulations reproducing the dielectric measurement scenarios with the three Keysight probes and the Teflon and saline samples was conducted to validate the experimental outcome. A second set of simulations involving 12 probe geometries and a subset of 4 dielectric samples was conducted to model the dependence of the sensing radius on the probe dimensions, i.e., the inner conductor radius, insulator width and outer conductor inner radius, across a subset of materials and biological tissues. A third set of simulations reproducing the interaction of the Keysight slim form probe with a number of biological tissues was conducted to examine the dependence of the sensing radius on the dielectric properties of the investigated sample. The three simulation sets are summarised in Table 4.7.

In the first simulation set, the three Keysight probes were modelled as described in the subsection above and, as with the experiments, cylindrical samples with different radii of saline solution concentrically surrounded by Teflon were created. However, more samples with intermediate values of radius were included in the simulations, thanks to the ease in developing numerical models. Thus, the saline solution was modelled with variable radius ranging from 0.5 to 5 mm in 0.25 mm discrete steps, surrounded by Teflon having radius much larger than that of saline and considerably larger than the total radius r of the probe. Furthermore, the dielectric properties of saline and Teflon were assigned to the simulation samples. Specifically, one-pole Cole-Cole models were fitted to the dielectric data measured experimentally from the 0.1 M NaCl solution (at room temperature between 20°C and 24°C) and Teflon using the non-linear least squares error algorithm. One-pole Cole-Cole models were chosen, since the models were able to fit the data with an error lower than 0.8%. The parameters of the

CHAPTER 4. SENSING RADIUS OF COAXIAL PROBES

Table 4.8: One-pole Cole-Cole parameters for simulated saline and Teflon.

Parameters	Saline	Teflon
ϵ_∞	5.1700	1.4600
ϵ_s	78.1000	2.4600
τ [s]	8.78e-12	1e-12
α	0.0071	0.0010
σ_s [S/m]	0.9600	0.0030

one-pole Cole-Cole model for saline and Teflon are summarised in Table 4.8, where ϵ_∞ , ϵ_s , τ , α and σ_s were defined in Section 2.1.3.

In the second simulation set, in order to expand the investigation of the sensing radius beyond the fixed dimensions of the Keysight probes, a number of other probes with different geometries were modelled with the same conductor and insulator materials, i.e., nickel and Teflon. Specifically, the dimensions of the inner conductor and insulator were varied, by either maintaining or increasing the dimension of the inner radius of the outer conductor. Since preliminary simulations demonstrated that the width of the outer conductor does not impact the sensing radius, an outer conductor having a fixed width of 1 mm was used for all probe geometries.

For the probe geometry, the minimum probe size was defined by the slim form probe, and the maximum probe size was selected by considering the coaxial line cut-off frequency, which is inversely proportional to the dimensions of the inner conductor and insulator. In total, 12 probes were modelled with different dimensions and assigned to four subsets of probe dimension combinations, as listed in Table 4.9. Each subset, consisting of four probes having different size, was designed as follows:

- For the first subset (S1), the insulator width c was kept fixed, and the radius of the inner conductor a was gradually increased by 0.25 mm; thus also the inner radius of the outer conductor b gradually increased by 0.25 mm;
- For the second subset (S2), a was kept fixed, and c was gradually increased by 0.5 mm; thus also b gradually increased by 0.5 mm;
- For the third subset (S3), b was kept fixed, and a was gradually increased by 0.25 mm while c was gradually decreased by 0.25 mm;
- For the fourth subset (S4), a was gradually increased by 0.25 mm while c was gradually increased by 0.5 mm; thus b gradually increased by 0.75 mm.

The subsets S1, S2 and S4 have the slim form probe CP1 as the initial probe size, for ease of analysis. Similarly, the probes CP4 and CP9 are included also in S3 and S4, respectively. Among the probes listed in Table 4.9, the performance probe is not included due to its dimensions a , b and c

CHAPTER 4. SENSING RADIUS OF COAXIAL PROBES

Table 4.9: List of probe dimension combinations (CP1,...,CP12) grouped in four subsets (S1,...,S4). a , b and c refer to probe features in Fig. 4.6. Each probe has an outer conductor of 1 mm width.

Subset	Coaxial probes	a (mm)	c (mm)	b (mm)
S1	CP1	0.25	0.50	0.75
	CP2	0.50	0.50	1.00
	CP3	0.75	0.50	1.25
	CP4	1.00	0.50	1.50
S2	CP1	0.25	0.50	0.75
	CP5	0.25	1.00	1.25
	CP6	0.25	1.50	1.75
	CP7	0.25	2.00	2.25
S3	CP8	0.25	1.25	1.50
	CP9	0.50	1.00	1.50
	CP10	0.75	0.75	1.50
	CP4	1.00	0.50	1.50
S4	CP1	0.25	0.50	0.75
	CP9	0.50	1.00	1.50
	CP11	0.75	1.50	2.25
	CP12	1.00	2.00	3.00

that are very close to the slim form probe CP1 (the slim form probe and the performance probe have different total radius r because of the width of the outer conductor that does not affect the sensing radius). The high temperature probe is not included either, since its dimensions are very close to the probe CP5.

For each probe geometry, simulations across different concentric samples were conducted in order to verify that the correlation between the sensing radius and the probe geometry was consistent across materials having different dielectric properties. Concentric samples modelled as in the first simulation set were simulated with the four material combinations detailed in Table 4.10. The sample having saline as inner material and Teflon as outer material was selected, since it enables calculation of the maximum sensing radius. The locations of the two materials were then swapped to model another sample. The dielectric properties assigned to Teflon and saline are as reported in Table 4.8. Furthermore, two samples consisting of breast gland and fat tissues were modelled to enlarge the dielectric spectrum of the investigated sample and to support breast tissue dielectric characterisation, which is crucial for the design of breast MW imaging systems (generally operating within 2-6 GHz). The dielectric properties of breast tissue assigned to the modelled samples are taken from the IT'IS database [190]. Thus, the second simulation set consists of a total of 48 scenarios involving 12 different coaxial probes and 4 different dielectric samples (12 probes x 4 samples).

In the third simulation set, in order to complete the sensing radius investigation, the interaction between the Keysight slim form probe and concentric biological tissues, with different dielectric properties and contrasts,

CHAPTER 4. SENSING RADIUS OF COAXIAL PROBES

Table 4.10: Modelled concentric materials with their contrast in relative permittivity. The average relative permittivity values of the materials across the range 2–6 GHz are specified in brackets.

Samples	Inner material	Outer material	Contrast in ϵ_r
Saline In-Teflon Out	Saline ($\epsilon_r=74.00$)	Teflon ($\epsilon_r=2.15$)	34:1
Teflon In-Saline Out	Teflon ($\epsilon_r=2.15$)	Saline ($\epsilon_r=74.00$)	1:34
Gland In-Fat Out	Gland ($\epsilon_r=53.50$)	Fat ($\epsilon_r=4.80$)	10:1
Fat In-Gland Out	Fat ($\epsilon_r=4.80$)	Gland ($\epsilon_r=53.50$)	1:10

was examined to analyse the sensing radius dependence on the dielectric properties of the interrogated biological tissues. The probe was modelled with the dimensions of the Keysight slim form probe, since, among the three Keysight probes, the slim form probe is the most commonly used in tissue dielectric studies (especially in studies involving breast tissue dielectric characterisation) [15], [48], [49], [54], [63], [66], as discussed in Section 2.3.3. Furthermore, the dielectrically interrogated samples were modelled as concentrically heterogeneous biological tissues consisting of a cylindrical inner tissue with variable radius ranging from 0.1 to 3 mm, surrounded by a concentric outer tissue that extends to a radius considerably larger than the total radius r of the probe. The discrete radii of the inner tissue were selected given that the sensing radius falls within the range of 0.1-3 mm. In fact, for the Keysight slim form probe, the sensing radius cannot be smaller than 0.1 mm (i.e, smaller than the inner conductor radius) and cannot be larger than the maximum sensing radius of the Keysight slim form probe estimated from the first simulation set. Specifically, the value of 3 mm chosen for the maximum radius of the inner tissue allows a margin of error above the maximum sensing radius estimated from the second simulation set.

Once the geometrical model was designed, a number of simulations were conducted by assigning specific values of dielectric properties to the samples. The assigned dielectric properties were selected in order to span different magnitudes and contrasts in permittivity. Specifically, 15 different tissues were combined into 38 distinct simulated samples. The relative permittivity and conductivity of each of the 15 tissues were obtained from the IT'IS database [190]. In Fig. 4.10, the relative permittivity and conductivity are plotted for all of the selected tissues. As is clear from Fig. 4.10, the 15 tissues span a wide range of relative permittivity and conductivity values. In fact, the average tissue relative permittivity and conductivity range from 10.4 to 77.2 and from 0.5 to 5.4 S/m, respectively, across the frequency range of 2-6 GHz. The trends in relative permittivity and conductivity are the same for most of the tissues, with the exclusion of lung, muscle, blood

CHAPTER 4. SENSING RADIUS OF COAXIAL PROBES

and lymph node. In fact, while the relative permittivity of lung is higher than that of bone, the conductivity of lung is lower than that of bone. A similar difference between relative permittivity and conductivity values was found for the muscle and thalamus, and similarly for the esophagus and blood. Furthermore, although the lymph node tissue is the one with the highest relative permittivity, the conductivity of lymph node is relatively lower (between that of fat and bone).

Since the sensing radius may depend on the contrast in permittivity between the two concentric tissues, the 38 concentrically heterogeneous samples were composed of tissues spanning a wide range of contrasts in relative permittivity and conductivity. Due to the fact that the selected tissues cover a wider range of contrasts in relative permittivity than in conductivity, in Section 4.3.2 the sensing radius is examined only in terms of the dependence on the relative permittivity of tissues, or their contrast in relative permittivity (although the sensing radius was calculated by considering both relative permittivity and conductivity values as illustrated in Fig. 4.9).

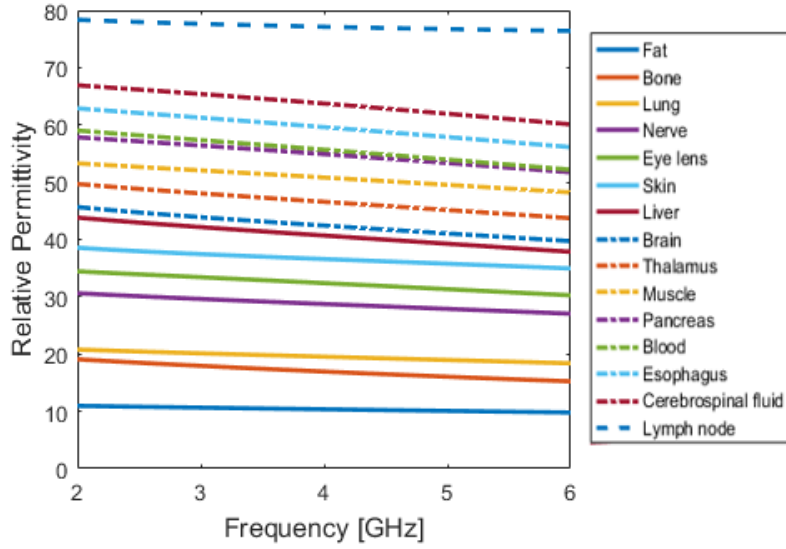
Specifically, in this chapter, the contrast in relative permittivity is defined as the percent difference in relative permittivity between the two tissues constituting a given sample. Thus, the contrast in relative permittivity between the two tissues was calculated as:

$$\Delta\epsilon_r\% = \frac{\epsilon_{r,max} - \epsilon_{r,min}}{\epsilon_{r,max}} \times 100, \quad (4.2)$$

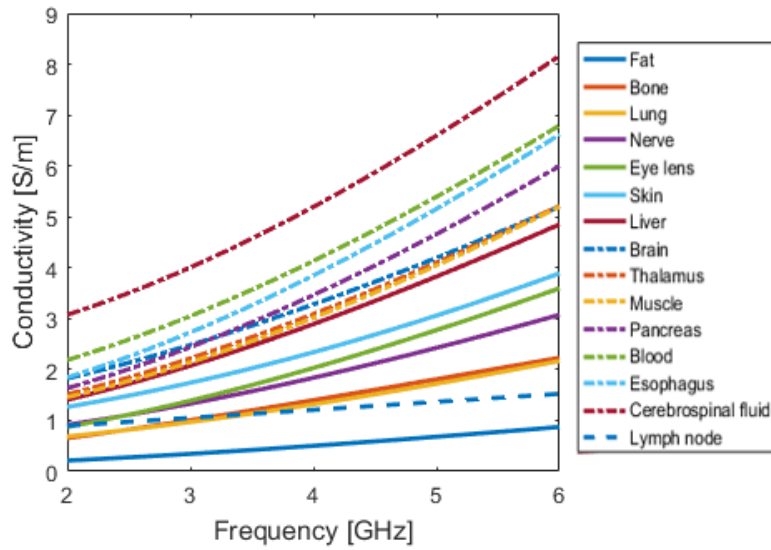
where $\epsilon_{r,max}$ is the relative permittivity of the constituent tissue with the highest relative permittivity and $\epsilon_{r,min}$ is the relative permittivity of the other constituent tissue (thus, having lower relative permittivity). The quantities $\epsilon_{r,max}$ and $\epsilon_{r,min}$ can refer to relative permittivity values at single frequencies or to mean relative permittivity values averaged across the measurement frequency range of 2-6 GHz. The contrast in relative permittivity averaged across frequency varies between 7.4%, for the sample composed of muscle and pancreas (with average relative permittivities of 50.8 and 54.9, respectively), up to 86.5%, for the sample composed of fat and lymph node. (with average relative permittivities of 10.4 and 77.2, respectively).

Although the selected combinations of tissues are not practically significant, they cover the full spectrum of dielectric properties of biological tissues. Tissue sample compositions involving both healthy tissues and the corresponding malignant tissues would be more appropriate for this investigation. However, to date, data on the dielectric differences between healthy and malignant tissues are known only for limited tissue types, such

CHAPTER 4. SENSING RADIUS OF COAXIAL PROBES



(a)



(b)

Figure 4.10: (a) Relative permittivity and (b) conductivity of the 15 biological tissues selected for the 38 simulated samples constituting the third simulation set samples. The 15 tissues were selected in order to span a wide range of relative permittivity and conductivity values. The relative permittivity and conductivity of each of the 15 tissues were obtained from the IT'IS database [190].

CHAPTER 4. SENSING RADIUS OF COAXIAL PROBES

as breast, liver, kidney and lung, and across restricted frequency ranges [48], [61].

Once the design of the numerical investigation was completed, simulations were conducted with the settings specified below. Then, the relative permittivity and conductivity data obtained from each set of simulations were processed and analysed to calculate the sensing radius across all simulation scenarios.

4.2.2.3 Numerical settings and data processing

Before executing the simulations by the multifrontal massively parallel sparse direct solver (MUMPS), for each numerical model (composed of a probe and two different concentric materials), the procedure as described below was followed:

- The coaxial EM source generating a signal of 1 V across the measurement frequency (21 linearly spaced frequency points in the range of 2-6 GHz) was positioned on the top of the probe;
- The absorbing conditions were assigned to the model boundaries;
- The tetrahedral mesh was created.

For all simulations, the minimum and maximum mesh elements sizes were 0.01 mm and 0.05 mm, respectively. Such mesh settings ensured that the largest mesh element was at least twice smaller than the smallest geometry of the model, and at least 100 elements were included within the wavelength of the EM signal. In fact the smallest geometry of the model is 0.1 mm and the free-space wavelength of the EM signal ranges from 149.9 mm (for the lowest frequency of 2 GHz) down to 49.96 mm (for the highest frequency of 6 GHz). The entire geometry includes, on average, approximately 50000 domain elements and 20000 boundary elements.

After the FEM simulations were solved, the EM field across the sample materials in the proximity of the probe tip was analysed in terms of the magnitude decay, and the complex S_{11} parameters from the probe-sample interface were analysed. In particular, the S_{11} parameters obtained from the top of the probe were translated to the probe aperture interfacing the interrogated sample by taking into account the following mathematical relationship [92]:

$$S_{11} = S_{11}^* e^{+j\beta 2L}, \quad (4.3)$$

where S_{11} and S_{11}^* refer to the values at the probe aperture and the top of the probe, respectively, β is the propagation constant across the probe and L is the length of the probe (i.e., the distance between the top of the probe and the probe aperture). Specifically, Eq. (4.3) is equivalent to Eq. (2.22), which

CHAPTER 4. SENSING RADIUS OF COAXIAL PROBES

derives from the mathematical formulation defining the EM propagation within perfectly matched transmission lines. Thus, Eq. (4.3) is used for probe de-embedding, i.e., to cancel out the effect of the propagation along the probe on the acquired S_{11} parameters. Due to the fact that the propagation along the probe affects both incident and reflected signals, from which the S_{11} parameter are obtained (as detailed in Section 2.3.1), Eq. (4.3) considers twice the length L of the probe as the propagation distance.

Furthermore, the de-embedded S_{11} parameters from the first simulation set (reproducing the dielectric measurements) were compared with the S_{11} parameters obtained from the measurements. A systematic S_{11} mismatch between simulations and measurements was found, likely attributable to differences in probe materials. However, the systematic mismatch error was compensated for by converting the S_{11} parameters into permittivity values, using the open-ended coaxial probe antenna model [101], presented in Section 2.3.2. As detailed in Section 2.3.2, the antenna model conversion algorithm uses known permittivity and corresponding S_{11} parameters of three media to calculate the three parameters necessary to estimate the probe admittance. Specifically, across all simulation scenarios, different sets of three known media were considered for the estimation of the probe admittance according to the permittivity of the simulated sample. Generally, the three media were selected to cover the permittivity range comprising the permittivity of the simulated sample, due to the fact that media with similar properties to those of the investigated sample are likely to improve the conversion of the S_{11} parameters into permittivity [101].

Across all simulations, both relative permittivity and conductivity values obtained from the converted S_{11} parameters were considered for the calculation of the sensing radius as illustrated in Fig. 4.9. The same definition of sensing radius reported in Section 4.2.1 for the experimental scenarios was considered for the numerical scenarios. Specifically, the sensing radius was estimated numerically as the radius of the inner material at which the acquired relative permittivity and conductivity were equal to the relative permittivity and conductivity, respectively, of the inner material in isolation, within the extended measurement uncertainty, which is 2.4% for relative permittivity and 4.6% for conductivity. Thus, the numerical estimates of sensing radius are based on the measurement uncertainty. Furthermore, as with the measurement scenarios, the sensing radius values obtained across all simulation scenarios were compared for each frequency point. Also, for each simulation scenario, the sensing radius was averaged across the frequency range.

After calculating the average sensing radius from each scenario, the numerical data was grouped into specific subsets and modelled to facilitate

CHAPTER 4. SENSING RADIUS OF COAXIAL PROBES

Table 4.11: Schematic information regarding the three categories of samples included within the third simulation set (indicated in Table 4.7).

C1	Samples having the same outer tissue, but different inner tissues
C2	Samples having the same inner tissue, but different outer tissues
C3	Samples consisting of the same two tissues, but with swapped locations

the analysis of the dependence on the sensing radius on the probe dimensions and the simulated samples. In particular, in order to model the sensing radius dependence on the probe dimensions, the average sensing radius values from the second simulation set were interpolated with first or second degree polynomial curves (fitting the average sensing radius data). Specifically, sensing radius values from each probe combination subset and for each sample (comprising the second simulation set) were represented with first or second degree functions. The parameters of the functions fitting the numerical sensing radius data are reported in Section 4.3.1 according to Eq. (4.4) and Eq. (4.5):

$$f(x) = p_3x^2 + p_2x + p_1, \quad (4.4)$$

$$f(x) = p_2x + p_1, \quad (4.5)$$

where x is one of the probe dimensions, $f(x)$ is the sensing radius, p_1 is the intercept, p_2 is the first degree coefficient and p_3 is the second degree coefficient.

Similarly to the data from the second simulation set, the average sensing radius values from the third simulation set were divided in three different categories. The three categories are based on the tissue composition of the simulated samples and, as specified in Table 4.11, involve:

- samples having the same outer tissue, but different inner tissues;
- samples having the same inner tissue, but different outer tissues;
- samples consisting of the same two tissues, but with swapped locations.

The average sensing radius data from each category (within the third simulation set) is reported in Section 4.3.2 with the first or second degree polynomials (interpolating the data) defined by Eq. (4.4) and Eq. (4.5), where x now represents either the relative permittivity of the inner (or outer tissue) or the contrast in relative permittivity between inner and outer tissues, $f(x)$ is the sensing radius, p_1 is the intercept, p_2 is the first degree coefficient and p_3 is the second degree coefficient.

Lastly, the average sensing radius data was used to develop linear regression and neural network models able to predict the sensing radius of a coaxial probe based on the probe dimensions and the dielectric properties of the interrogated sample. The methodology for these prediction models are reported in the following subsection.

4.2.3 Mathematical prediction of sensing radius

Machine learning techniques enable data prediction from *a priori* information after creating a generalisation of the input-output relationship derived from a set of training data.

From the average sensing radius obtained numerically, two regression models and two feedforward neural networks were developed. In particular, firstly, a linear regression model and a neural network were developed from the second set of simulations composed of 48 scenarios (12 probes x 4 sample combinations). Secondly, a linear regression model and a neural network were developed from the third set of simulations composed of 38 scenarios (1 probe x 38 sample combinations).

For the first set of linear and neural network models, each observation is from the second set of simulations and consists of four input features and one output target. The four inputs of the models are: the radius of the inner conductor, a , the inner radius of the outer conductor, b , and the average relative permittivity across frequency of the two materials constituting the concentric sample, ϵ_{r1} and ϵ_{r2} . The insulator width c was not used as an input parameter since it is not an independent parameter; in fact, c is the mathematical difference between b and a . The output target for each observation is the sensing radius calculated from the second set of simulations.

For the second set of linear and neural network models, each observation is from the third set of simulations and consists of two input features and one output target. The two inputs of the linear regression and neural network are the average relative permittivity across frequency of the two materials constituting the concentric sample, ϵ_{r1} and ϵ_{r2} . The output target for each observation is the sensing radius calculated from the third set of simulations.

All models were trained with 90% of the data, and then tested with the remaining 10%.

Specifically, for the first regression model, the training dataset was used to obtain a regression line that relates the sensing radius to the probe dimensions and relative permittivity values of the two concentric tissues, as follows:

CHAPTER 4. SENSING RADIUS OF COAXIAL PROBES

$$f(x) = p_1 + p_2a + p_3b + p_4\epsilon_{r1} + p_5\epsilon_{r2}, \quad (4.6)$$

where $f(x)$ is the sensing radius, a and b are the dimensions of the probe as illustrated in Fig. 4.6, ϵ_{r1} and ϵ_{r2} are the average relative permittivities of the inner and outer tissues, respectively, p_1 is the intercept, and p_2 , p_3 , p_4 and p_5 are the coefficients obtained from the data fitting. The resulting regression model was then tested with the remaining data.

For the second regression model, the training dataset was used to obtain a regression line that relates the sensing radius of the Keysight slim form probe to the relative permittivity values of the two concentric tissues, as follows:

$$f(x) = p_1 + p_2\epsilon_{r1} + p_3\epsilon_{r2}, \quad (4.7)$$

where $f(x)$ is the sensing radius, ϵ_{r1} and ϵ_{r2} are the average relative permittivities of the inner and outer tissues, respectively, p_1 is the intercept, and p_2 and p_3 are the coefficients obtained from the data fitting.

Furthermore, the design of the neural networks was selected after preliminary testing runs aimed at minimising the error between network outputs and training data. As a result, the two neural networks were constructed with 2 hidden layers, consisting of a different number of neurons. In particular, the first neural network was designed with a first layer of 5 neurons and a second layer of 2 neurons. The second neural network was designed with a first layer of 3 neurons and a second layer of 2 neurons. Both networks were trained and tested (with the same datasets used for the linear regression) across ten iterations using the Levenberg–Marquardt algorithm [191], [192]. Each iteration produced one trained network. Across each iteration, the Levenberg-Marquardt algorithm updates the weights and bias associated to each neuron so that the vector of network errors (obtained by comparing the network output with the training data) is minimised. Then, among the 10 resulting nets (obtained from each iteration), the network providing the lowest mean squared error (MSE) in the testing stage was selected as the final trained network.

The performance of all models was then evaluated by comparing the predicted sensing radius values with the output targets from the testing datasets.

Details regarding the performance of the two sets of linear regression and neural network models are reported in Section 4.3.3.

4.3 Results and Discussion of the sensing radius investigation

This section examines the sensing radius values estimated from the dielectric measurements and the simulation scenarios described in Section 4.2 and reports the results in three subsections as follows. In the first subsection, the dependence of the sensing radius on the probe dimensions is examined and modelled based on the experimental and numerical data. In the second subsection, the dependence of the sensing radius of the Keysight slim form probe on the dielectric properties of the investigated sample is examined and modelled from numerical data. Lastly, in the third subsection, the performance of the linear regression models and the neural networks developed from the numerical data are detailed.

4.3.1 Dependence of sensing radius on probe dimensions

In this subsection, the sensing radius values from the dielectric measurements and the first and second simulation sets are reported to analyse the dependence of the sensing radius on the probe dimensions. In particular, each reported sensing radius value refers to the average sensing radius (calculated as an average across the frequency range of 2-6 GHz). The average sensing radius was found to be approximately equivalent to the sensing radius calculated for the central simulation frequency (4 GHz). In addition, it was determined that variations of the sensing radius with frequency were due primarily to differences in the dielectric contrast between the two concentric tissues across the frequency range. For instance, if the dielectric contrast between the tissues increases with the frequency, so does the sensing radius.

Firstly, both experimental and numerical results from the first simulation set aimed at calculating the maximum sensing radius of the Keysight probes are reported for an initial analysis of the sensing radius based on the probe size and to verify consistency between measurements and simulations.

Then, the data obtained from the second simulation set is reported to analyse the dependence of the sensing radius on the probe dimensions. Specifically, the sensing radius dependence on the inner conductor radius, insulator width, and inner radius of the outer conductor is examined and modelled.

4.3.1.1 Maximum sensing radius of the Keysight probes

In Fig. 4.11, both experimental and numerical data for the three Keysight probes is illustrated for the calculation of the maximum sensing radius. In the measurement plot (Fig. 4.11a), the percent difference between the relative permittivity acquired from each Teflon aperture and the relative permittivity of saline in isolation (i.e., from the 5 mm aperture) is plotted as a function of the radius of the Teflon aperture. In the same way, in the simulation plot (Fig. 4.11b), the percent difference between the relative permittivity acquired from each of the different sized concentric samples (consisting of saline as inner material and Teflon as outer material) and the relative permittivity of the saline solution is plotted as a function of the radius of the Teflon aperture, i.e. the radius of saline. Both measurement and simulation plots refer to acquired data averaged across frequency. Also, in both plots, the value of the extended uncertainty for relative permittivity (2.4%) is highlighted to graphically facilitate the estimation of the sensing radius. In particular, for each trace, the sensing radius corresponds to the radius at which the percent difference is approximately 2.4%. The sensing radius is reported only from relative permittivity values, since similar values were found for conductivity.

From the measurement plot in Fig. 4.11a, it can be observed that the sensing radius estimated for the slim form, performance, and high temperature probes is approximately 1.25 mm, 1.7 mm and 2.5 mm, respectively. From the simulation results in Fig. 4.11b, the sensing radius was found to be 1.4 mm, 1.5 mm and 2.25 mm for slim form probe, performance probe, and high temperature probe, respectively. The slight differences in values between the measurement and simulation are attributed to the absence of measurement confounders in the simulations, such as air bubbles across the Teflon aperture and temperature variation, and to the increased number of Teflon apertures which were numerically modelled. Therefore, a higher resolution in the transition of dielectric properties relative to changes in radii is achieved in simulation. Since the difference between the measured and simulated sensing radius data is always within 0.25 mm, it can be concluded that the simulations are able to reproduce accurately the measurements.

These initial results showed that the sensing radius increases with the size of the probe. In fact, as reported in Table 4.6, the inner radius of the outer conductor of the slim form probe, performance probe and high temperature probe is 0.75 mm, 0.8 mm, and 1.35 mm, respectively. The dependence of the sensing radius on the probe size is better examined through numerical results in the following subsections. In particular, the average sensing radius data obtained from the second simulation set are plotted, in turn, for each

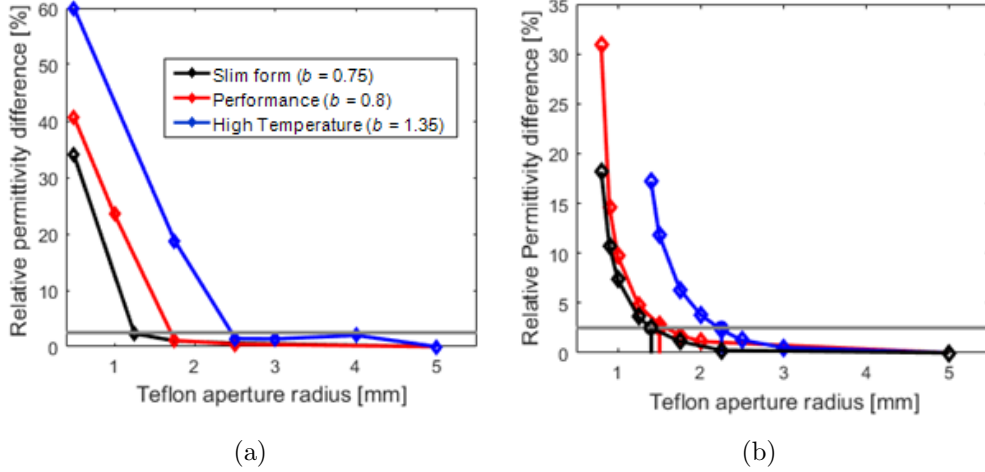


Figure 4.11: Determination of the maximum sensing radius for the three Keysight probes through (a) measurements and (b) simulations. In both plots, the percent relative permittivity difference is calculated by considering the relative permittivity of 0.1 M NaCl averaged across frequency as the reference signal. The percent difference was calculated between each Teflon aperture (saline as inner material surrounded by Teflon), and the reference signal. In both plots, the 2.4% threshold value used for the calculation of the sensing radius is indicated with a horizontal line, and the black trace refers to the slim form probe, the red trace to the performance probe, and the blue trace to the high temperature probe. In (b), the sensing radius values are marked where the relative permittivity difference lines intercept the horizontal threshold trace.

Table 4.12: Parameters, R^2 value and RMSE of the regression lines in Fig. 4.12.

Samples	p_2	p_1	R^2	RMSE
Saline In-Teflon Out	2.08	0.95	0.987	0.0949
Teflon In-Saline Out	1.70	0.68	0.996	0.0433
Gland In-Fat Out	1.96	0.85	0.994	0.0592
Fat In-Gland Out	1.54	0.60	0.999	0.0194

subset of probe dimension combinations (reported in Table 4.9).

4.3.1.2 Dependence of sensing radius on inner conductor radius

In order to examine the trend of the sensing radius for the subset S1, in Fig. 4.12, the average sensing radii calculated for the four probes (CP1, CP2, CP3 and CP4) are plotted versus the inner conductor radius.

From the plot in Fig. 4.12, it is clear that the sensing radius increases approximately linearly with the inner conductor radius. The linear trend is highlighted by fitting regression lines to the data points. The coefficients, R^2 values and RMSE of the regression lines are reported in Table 4.12, for

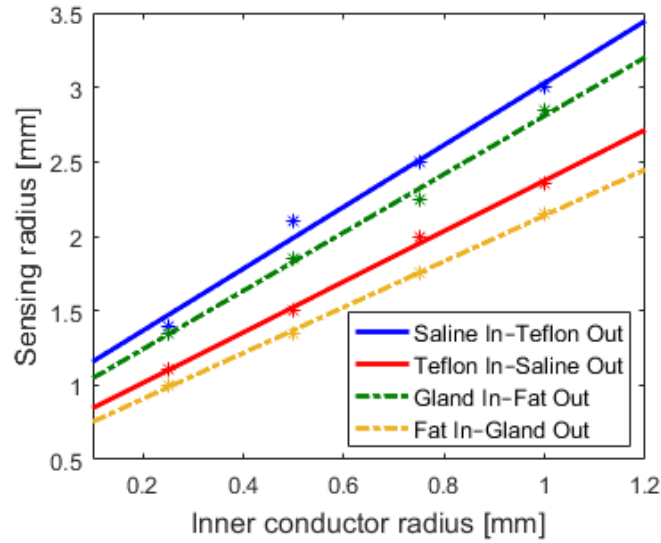


Figure 4.12: Regression lines (solid for saline and Teflon samples and dash-dotted for breast fat and gland samples) fitting the sensing radius data (stars) obtained for different radii of inner conductor. The data refers to the scenarios S1, where only a and then b are increased. The lines, with parameters reported in Table 4.12, show the same trend across all samples. Specifically, the sensing radius is found to increase with increasing inner conductor radius; however, the rate of increase is dependent on the sample composition.

each of the four simulated samples. The R^2 and RMSE values listed in the table confirm the quality of the fitting.

Although the trend is approximately linear across all simulated samples, the sensing radius values vary according to the materials constituting the samples. In fact, from Fig. 4.12, it can be observed that the smallest values of sensing radius are obtained for the sample having breast fat as inner tissue and breast gland as outer tissue. On the other hand, the largest values of sensing radius are obtained for the sample having saline as inner material and Teflon as outer material, thus motivating the selection of Teflon and 0.1 M NaCl solution as materials for the estimation of the maximum sensing radius (since these materials have the highest contrast in permittivity that can be found across biological tissues, as discussed in Section 4.1.3).

In particular, for any given probe geometry, it can be observed that the sensing radius trend across samples increases with the contrast in permittivity between the two concentric materials constituting the sample. In fact, the sensing radius values for the two samples with higher contrast in relative permittivity, the Teflon and saline samples, are higher than for the breast samples that have lower contrast in relative permittivity (contrasts are as

CHAPTER 4. SENSING RADIUS OF COAXIAL PROBES

reported in Table 4.10).

Furthermore, between two samples consisting of the same materials but with swapped locations, the sensing radius is higher for the sample having an inner material with higher relative permittivity than the outer material. For instance, between the two Teflon and saline samples, the sensing radius is higher for the sample with saline as inner material than it is for the sample with Teflon as inner material. Lower values of sensing radius for samples having an inner material with lower relative permittivity can be due to the impedance mismatch between the probe and the inner material, which tends to be higher for lower permittivity materials. The high impedance mismatch between the probe and the lower permittivity materials, Teflon and fat, is illustrated in Fig. 4.13 in terms of S_{11} parameters. In fact, for Teflon and fat, the S_{11} magnitude and phase tend to the S_{11} magnitude and phase of the open-circuit, which are 1 and 0, respectively. As reported in Section 2.3.1, in the case of an open-circuit, the impedance mismatch is the highest (i.e., tends to infinite) and the incident signal is all reflected back. Thus, the high impedance mismatch between the probe and Teflon and the probe and fat, indicated by the S_{11} parameters plotted in Fig. 4.13, results in a large reflection of the incident EM signal at the probe-Teflon and probe-fat interfaces with only limited transmission into the material beyond Teflon (or fat). Thus, the sensing radius trend across samples is consistent with EM propagation theory.

The same trend of the sensing radius varying with the sample composition is observed across all other scenarios of different probe dimension combinations. For instance, the same trend of the sensing radius varying with the sample composition is found across the scenarios S4 in Fig. 4.14, where the average sensing radii calculated across the scenarios S4 are plotted versus the inner conductor radius. The four probes of the subset S4 have increasing inner conductor radii and insulator widths. As in Fig. 4.12, the data in Fig. 4.14 illustrates the approximately linear relationship between the sensing radius and the inner conductor radius across all samples. Thus, the data was interpolated with regression lines, the parameters of which are listed in Table 4.13 for each simulated sample. As indicated from the R^2 and RMSE values, in this case, the quality of the fitting is a bit lower than in the previous cases; however, the data are still well-represented by the fitted lines. For the subset S4, since the insulator width increases while the inner conductor radius increases, a trend similar to that of the dependence of the sensing radius on the inner conductor radius was found for the dependence of the sensing radius on the insulator width. However, the dependence of the sensing radius on the insulator width is examined better in the following subsection.

CHAPTER 4. SENSING RADIUS OF COAXIAL PROBES

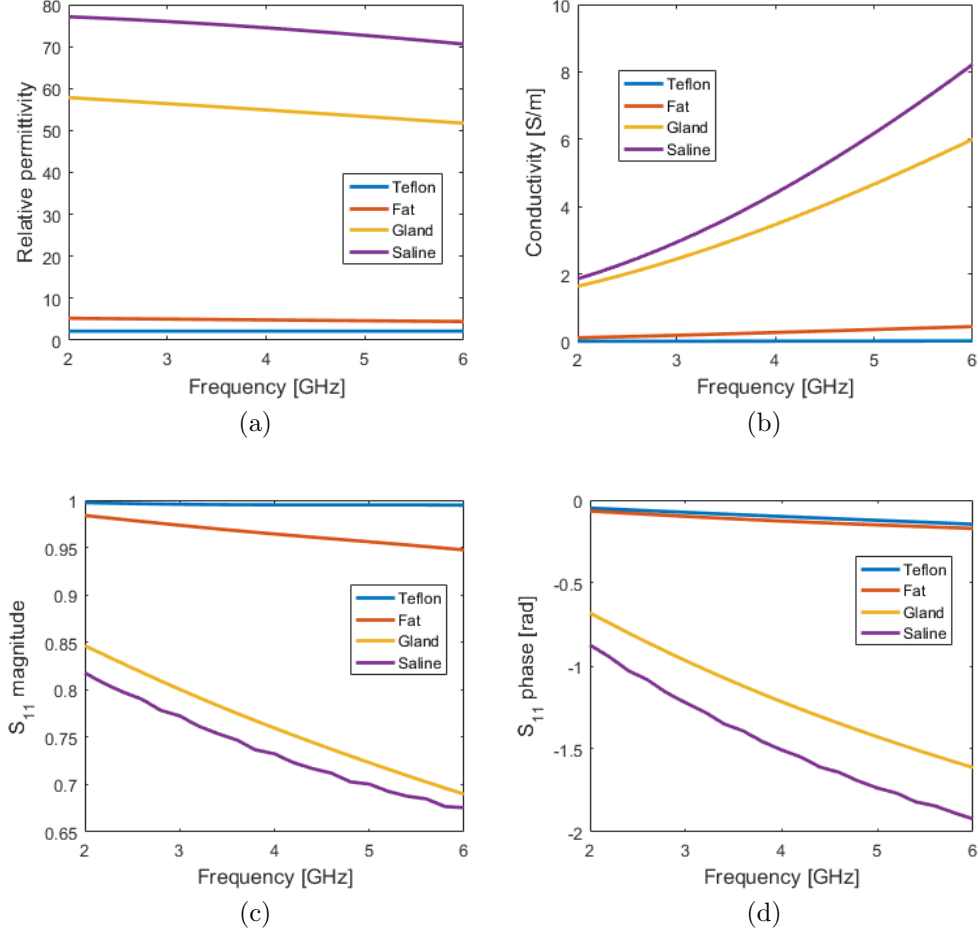


Figure 4.13: (a) Relative permittivity, (b) conductivity, (c) S_{11} magnitude and (d) S_{11} phase of the materials constituting the four samples within the second simulation set: Teflon, fat, gland and saline. The relative permittivity (a) and conductivity (b) traces were obtained from the conversion of the S_{11} magnitude (c) and S_{11} phase (d) obtained from the simulations reproducing the interaction of the probe CP1 with each of the four materials, in isolation. As illustrated in (c) and (d), the S_{11} magnitude of Teflon and fat is close to 1, and the S_{11} phase of Teflon and fat is close to 0. Such values reflect the high impedance mismatch between the probe and Teflon, and the probe and fat.

Table 4.13: Parameters, R^2 value and RMSE of the regression lines in Fig. 4.14.

Samples	p_2	p_1	R^2	RMSE
Saline In-Teflon Out	3.62	0.65	0.971	0.2470
Teflon In-Saline Out	3.24	0.40	0.980	0.1830
Gland In-Fat Out	3.48	0.60	0.987	0.1550
Fat In-Gland Out	3.36	0.18	0.999	0.0474

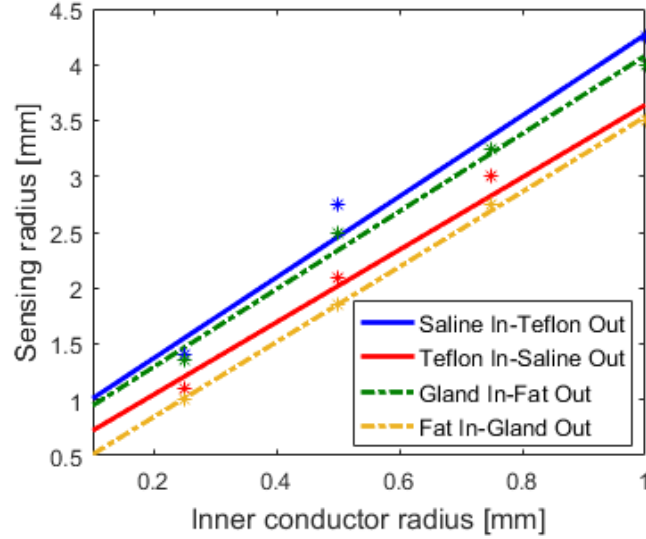


Figure 4.14: Sensing radius vs. inner conductor radius for the scenario S4, where both a and c are increased with b . The regression lines fitting the sensing radius data, with parameters reported in Table 4.13, show the same trend for different samples. Solid and dash-dotted lines are the fitted lines for saline and Teflon samples and for breast fat and gland samples, respectively, while the data is indicated with stars.

Table 4.14: Parameters, R^2 value and RMSE of the regression lines in Fig. 4.15.

Samples	p_2	p_1	R^2	RMSE
Saline In-Teflon Out	1.04	0.95	0.987	0.0949
Teflon In-Saline Out	1.11	0.55	0.999	0.0296
Gland In-Fat Out	0.97	0.93	0.987	0.0887
Fat In-Gland Out	0.94	0.55	0.997	0.0387

4.3.1.3 Dependence of sensing radius on insulator width

In Fig. 4.15, the average sensing radii calculated across the scenarios S2 are plotted versus the insulator width. The four probes of the subset S2 have increasing insulator widths but the same inner conductor radius. The data in Fig. 4.15 illustrates the approximately linear relationship between the sensing radius and the insulator width across all samples. Thus, the data was interpolated with regression lines, the parameters of which are listed in Table 4.14 for each simulated sample.

From the simulations performed with the probes in S1, S2 and S4, it can be observed that the sensing radius increases linearly by increasing the inner radius of the outer conductor b . In fact, an increase of b results in an increase of the radial extent of the sample interrogated by the electric field, and, thus, in an increase of the sensing radius.

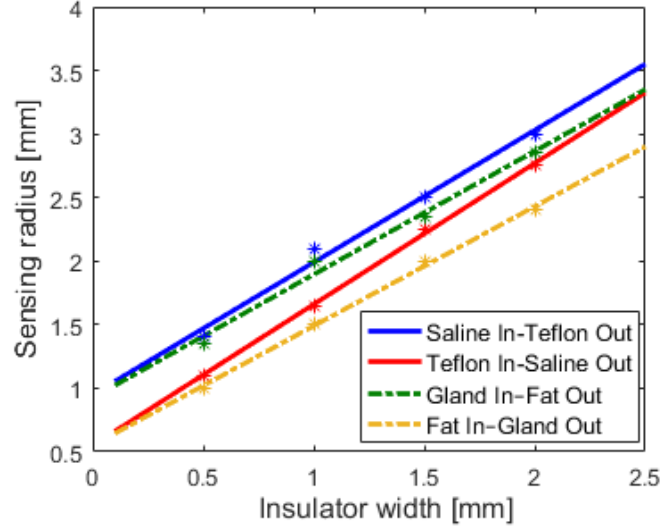


Figure 4.15: Regression lines (solid for saline and Teflon samples and dash-dotted for breast fat and gland samples) fitting the sensing radius data (stars) obtained for different insulator widths. The data refers to the scenario S2, where c and thus b are increased. The lines, with parameters reported in Table 4.14, show the same trend across all samples.

Furthermore, the sensing radius value obtained for the probe CP1, which has dimensions similar to those of the 2.2 mm diameter probe used in the study by Hagl *et al.* [65], is comparable with the sensing radius value estimated by Hagl *et al.* [65]. Specifically, a maximum sensing radius of 1.4 mm was obtained for the CP1 probe (illustrated by the leftmost blue star in Fig. 4.12, Fig. 4.14 and Fig. 4.15), which total radius is 1.1 mm (i.e., which total diameter is 2.2 mm). Similarly, in the study by Hagl *et al.* [65], a sensing radius of 1.25 mm was obtained for the 2.2 mm diameter probe. Also, the maximum sensing radius values obtained from the simulation subsets S1, S2 and S4 satisfy the relationship between sensing radius and probe aperture, defined by the inner radius of the outer conductor, reported in the study by De Langhe *et al.* [183]. For instance, by considering the differences in dimensions between the probe CP1 and the probe used in the study by De Langhe *et al.* [183], the maximum value of sensing radius for the CP1 (i.e., 1.4 mm) is within the maximum sensing radius estimated by De Langhe *et al.* [183] (i.e., 1.55 mm).

In order to conclude the analysis of the sensing radius based on the probe dimensions, the sensing radius values obtained across the probes having fixed inner radius of the outer conductor and varying inner conductor radius and insulator width are examined in the following subsection.

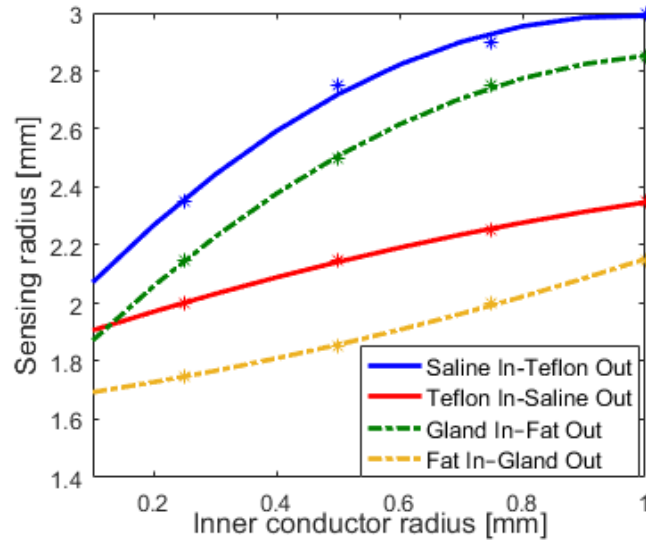


Figure 4.16: Sensing radius vs. inner conductor radius for the scenario S3, where b is kept constant while a increases and c decreases. The data is interpolated with second degree polynomials, with parameters reported in Table 4.15. Solid and dash-dotted lines are the fitted polynomials for saline and Teflon samples and for breast fat and gland samples, respectively, while the data is indicated with stars.

4.3.1.4 Dependence of sensing radius on inner radius of outer conductor

In Fig. 4.16, the average sensing radii estimated from subset S3, across probes having fixed inner radius of the outer conductor, are plotted versus the inner conductor radius. In this case, the trends were not found to be linear. Thus, the data was interpolated with second degree polynomials, with coefficients and RMSE values summarised in Table 4.15. The fitting curves illustrate that the sensing radius is greatly dependent on the radius of the inner conductor. For the subset S3, the relationship between the sensing radius and the inner conductor radius is directly proportional. Conversely, the relationship between the sensing radius and the insulator width is inversely proportional, as expected. These different trends are due to the fact that the probes within subset S3 have increasing inner conductor radii and decreasing insulator widths.

Furthermore, the curves of Fig. 4.16 follow different exponential trends across samples. The sensing radius increases faster with the inner conductor radius for samples with higher contrast in relative permittivity and/or inner materials with higher dielectric properties than for samples with lower contrast in relative permittivity and/or inner materials with lower dielectric

CHAPTER 4. SENSING RADIUS OF COAXIAL PROBES

Table 4.15: Parameters and RMSE of the second degree polynomial curves in Fig. 4.16.

Samples	p_3	p_2	p_1	RMSE
Saline In-Teflon Out	-1.20	2.34	1.85	0.0224
Teflon In-Saline Out	-0.20	0.71	1.84	0.0056
Gland In-Fat Out	-1.00	2.19	1.66	0.0056
Fat In-Gland Out	0.20	0.29	1.66	0.0056

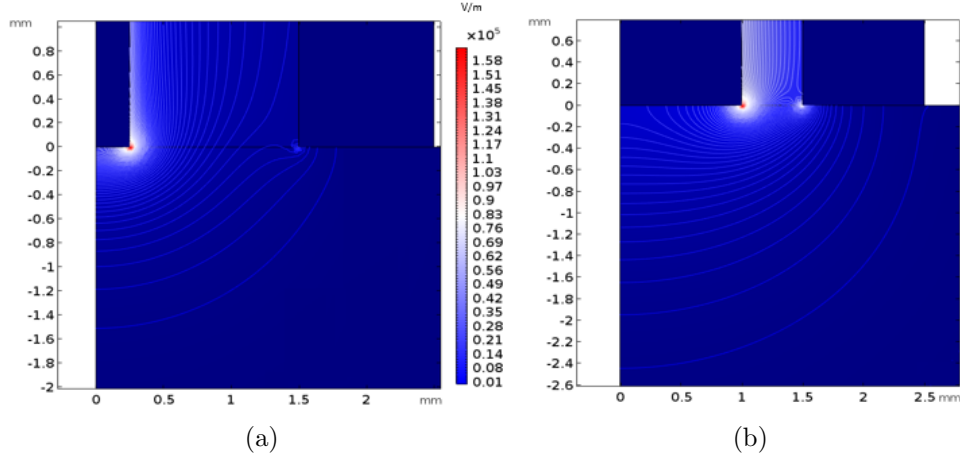


Figure 4.17: Contour plot of the electric field magnitude (V/m) at 4 GHz of the simulated probes (a) CP8 and (b) CP4 in contact with Teflon surrounded by saline. In the simulations, a simplified 2D axis-symmetric model was used and, in both plots, radial and axial distances are shown in mm horizontally and vertically, respectively. In both plots, to the right of the symmetry axis ($x = 0$), is the half cross-section of the probe tip and the interrogated sample (Teflon). The electric field isolines are marked, with the last isoline referring to the location where the electric field decays 40 dB. The two probes CP8 and CP4 both have the inner radius of the outer conductor equal to 1.5 mm, but different inner conductor radii and insulator widths, which affect the electric field magnitude such that it is higher in (b) than (a) at the radial distance of 1.5 mm. Also, in (a), the last isoline includes a smaller geometrical region than the region delineated by the last isoline in (b), thus suggesting that the inner conductor radius has higher impact than the insulator width on the sensing radius.

properties. The greater impact of the inner conductor radius on the sensing radius with respect to the insulator width is also illustrated in terms of electric field distribution across the probe tip and the interrogated sample in Fig. 4.17. This figure depicts a simplified 2D axially-symmetric geometry, with the radial and axial distances shown in mm horizontally and vertically, respectively. The electric field isolines at 4 GHz are marked across the half cross-section of the end of the probe and the interrogated sample (Teflon surrounded by saline in this case), with the last isoline referring to the location where the electric field decay is 40 dB.

CHAPTER 4. SENSING RADIUS OF COAXIAL PROBES

Fig. 4.17a illustrates the simulated probe CP8, which has an inner conductor radius of 0.25 mm and an insulator width of 1.25 mm, while Fig. 4.17b illustrates the simulated probe CP4, which has an inner conductor radius of 1 mm and an insulator width of 0.5 mm. In both cases, the sample is composed of Teflon (with a radius of 5 mm), surrounded by saline. Although the two probes CP4 and CP8 have both an outer conductor inner radius of 1.5 mm, the electric field magnitude across CP4 is significantly higher than the magnitude across CP8. Also, in Fig. 4.17a, the last isoline circumscribes a smaller geometrical region of the sample than the region delineated by the last isoline in Fig. 4.17b, thus confirming that the inner conductor radius has larger impact on the sensing radius than does the insulator width.

These results are in agreement with the findings of the study by Anderson *et al.* [181], for which the sensing radius does not exceed the total radius of the probe and the magnitude of the EM field is the highest in proximity of the inner conductor of the probe. This last outcome is also confirmed by Gauss's theorem, which relates the radial component of the electric field within the coaxial probe to the applied input voltage and the probe dimensions, as reported in Eq. (2.8) (in Chapter 2). Specifically, from Eq. (2.8), it can be concluded that, if b is fixed, the electric field at a fixed point ρ increases with a . Since the size of the sensing radius is proportional to the electric field magnitude across the probe, Gauss's theorem confirms that, at a certain location ρ , when b is fixed, the sensing radius increases with the radius of the inner conductor a .

Furthermore, as in the study conducted by Hoshina *et al.* [187], by observing the electric field across all simulated samples, it was found that the magnitude of the electric field is negligible out of the hemispherical region delineated by the -40 dB isoline (the outer isoline depicted in both illustrations of Fig. 4.17). Outside of this region, the effect of the outer material is within the measurement uncertainty.

Finally, the numerical study confirmed that the trends of the sensing radius with the probe dimensions are consistent across samples having different dielectric properties. However, for each probe geometry, a different trend of the sensing radius was observed across samples, thus confirming that the size of the sensing radius does depend on the permittivity of the interrogated sample. The dependence of the sensing radius on the permittivity of the sample is further examined in the following subsection.

4.3.2 Dependence of sensing radius on tissue dielectric properties

In this subsection, the sensing radius values from the third simulation set are reported to analyse the dependence of the sensing radius on the relative permittivity of the constituent tissues. As in the previous subsection, the sensing radius values are reported in terms of average sensing radius (i.e., sensing radius values averaged across the range of 2-6 GHz).

Firstly, the average sensing radius data from each of the 38 concentric samples is plotted as a function of the relative permittivity of the inner and outer tissues constituting the specific samples. From a general analysis of the data from all 38 scenarios, the sensing radius dependence on the contrast in relative permittivity between the sample inner and outer tissues is examined and modelled.

Then, the sensing radius dependence on the relative permittivity values of the inner and outer tissues constituting the concentric samples is further examined and modelled across the three sample categories specified in Table 4.11.

4.3.2.1 General dependence of sensing radius on tissue permittivity magnitude

In order to examine the trend of the sensing radius with varying relative permittivities of the constituent tissues, in Fig. 4.18, the average sensing radii (i.e., sensing radii averaged across frequency) calculated from the 38 scenarios are plotted versus the average relative permittivity values (i.e., relative permittivity values averaged across frequency) of the corresponding concentric samples. In the 3D plot, two different trends were detected and organised in two clusters. The two clusters are related to the magnitude of the average relative permittivity of the inner tissue compared to that of the outer tissue. Specifically, in Fig. 4.18, the cluster representing samples composed of an inner tissue with relative permittivity lower than that of the outer tissue is indicated in blue, and the cluster representing the samples composed of an inner tissue with relative permittivity higher than that of the outer tissue is indicated in red. From the trend of the blue cluster, the sensing radius generally increases with the relative permittivity of the outer tissue; while, from the trend of the red cluster, the sensing radius also generally increases with the relative permittivity of the inner tissue.

In order to understand the trend of the sensing radius according to the contrast in relative permittivity between the two tissues constituting each sample, the sensing radius from the two clusters is next plotted versus the

CHAPTER 4. SENSING RADIUS OF COAXIAL PROBES

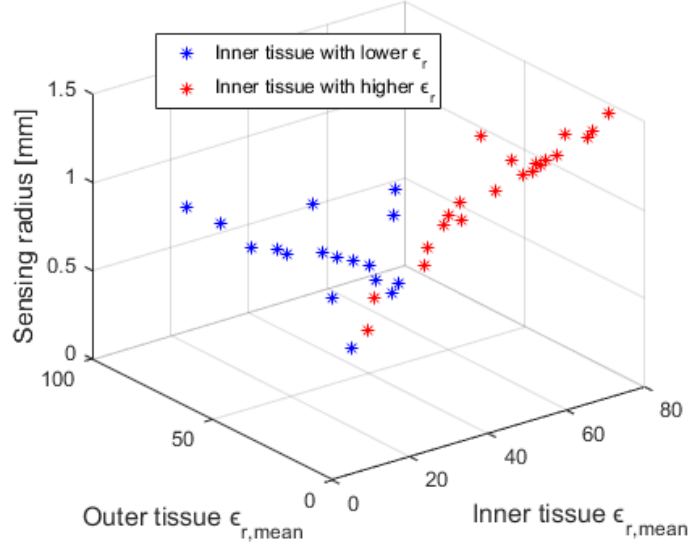


Figure 4.18: 3D plot of the average sensing radii (i.e., sensing radii averaged across frequency) from all simulation scenarios vs. the average relative permittivities (i.e., relative permittivities averaged across frequency) of the inner and outer tissues constituting each concentric sample. Two different clusters were identified: the cluster including samples composed of an inner tissue with relative permittivity lower than that of the outer tissue is indicated in blue, and the cluster of samples composed of an inner tissue with relative permittivity higher than that of the outer tissue is indicated in red.

percent contrast in relative permittivity in Fig. 4.19. In order to highlight the trends of the two clusters, the data from each cluster is interpolated with a linear polynomial. Specifically, the polynomial interpolating the data from the blue cluster (representing the samples composed of an inner tissue with relative permittivity lower than that of the outer tissue) is defined by Eq. (4.8) and the polynomial interpolating the data from the red cluster (representing the samples composed of an inner tissue with relative permittivity higher than that of the outer tissue) is defined by Eq. (4.9), as follows:

$$f_{blue}(x) = 0.006x + 0.480, \quad (4.8)$$

$$f_{red}(x) = 0.010x + 0.540, \quad (4.9)$$

where $f(x)$ is the average sensing radius and x is the average contrast in relative permittivity between the two tissues constituting each sample. The

CHAPTER 4. SENSING RADIUS OF COAXIAL PROBES

RMSE calculated between the data and the fitted polynomials is 0.0764 for the blue cluster and 0.0819 for the red cluster.

In Fig. 4.19, it can be observed that the two linear polynomials have similar trends, although the corresponding sensing radius values are lower for the samples with inner tissues having lower relative permittivity than for the samples with inner tissues having higher relative permittivity. However, for both clusters, the sensing radius increases as the contrast in relative permittivity increases. This outcome is consistent with the trend of the sensing radius across the four samples from the second simulation set. In particular, in Section 4.3.1, it was observed that the sensing radius values are lower for the samples with inner tissues having lower permittivity because of the high impedance mismatch between the probe and the lower permittivity tissues.

From Fig. 4.19, it is also clear that the average sensing radius varies from 0.4 mm and 1.5 mm, depending on the tissues constituting the sample and the tissue location within the sample. The minimum and maximum sensing radii found correspond, respectively, to the samples composed of concentric tissues having the minimum and maximum contrast in relative permittivity. As specified in Section 4.2.2, the minimum contrast in relative permittivity was found for the sample consisting of muscle and pancreas, and the maximum contrast in permittivity was found for the sample consisting of fat and lymph node. Thus, the average sensing radius of 0.4 mm (the minimum sensing radius) is for the sample composed of muscle as inner tissue and pancreas as outer tissue, and the corresponding data in Fig. 4.19 is represented by the leftmost blue marker (this marker is part of the blue cluster, since the average relative permittivity of muscle is lower than that of pancreas). Similarly, the average sensing radius of 1.5 mm (the maximum sensing radius) is found for the sample composed of lymph node as inner tissue and fat as outer tissue, and the corresponding data in Fig. 4.19 is represented by the red marker on the extreme right (this marker is part of the red cluster, since the average relative permittivity of lymph node is higher than that of fat).

Furthermore, the markers farthest away from the fitted polynomials, generally, correspond to the samples presenting higher contrast in conductivity than in relative permittivity. In fact, since the sensing radius was calculated by considering both relative permittivity and conductivity values, relatively higher values of sensing radius can be found for samples with lower contrast in relative permittivity, if those samples present a higher contrast in conductivity. For instance, in Fig. 4.19, the red marker corresponding to the contrast in relative permittivity of 17.59% and sensing radius of 1 mm (i.e., the farthest away from the red polynomial) is from the sample consisting of

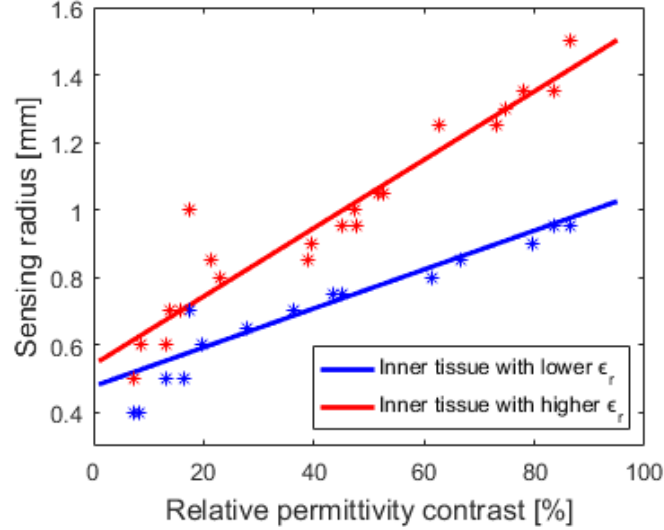


Figure 4.19: Sensing radius vs. contrast in relative permittivity for the two clusters identified in Fig. 4.18: the blue cluster consisting of the samples with an inner tissue having lower relative permittivity, and the red cluster consisting of the samples with an inner tissue having higher relative permittivity. The plot also shows the linear polynomials interpolating the two data subsets (with solid lines). Specifically, the blue line is defined by Eq. (4.8), with an RMSE of 0.0764 between data and polynomial, and the red line is defined by Eq. (4.9), with an RMSE of 0.0918.

lymph node as inner tissue and cerebrospinal fluid as outer tissue, which is characterised by a low contrast in relative permittivity and a high contrast in conductivity (as can be observed from the plots in Fig. 4.10). For this reason, the sensing radius for the sample consisting of lymph node as inner tissue and cerebrospinal fluid as outer tissue is higher than the sensing radius values obtained for other samples with tissues presenting a contrast in relative permittivity similar to that of lymph node and cerebrospinal fluid.

Finally, it should be noted that all sensing radius values obtained from the 38 scenarios are within the maximum sensing radius estimated from the second simulation set except for the sensing radius from the sample consisting of lymph node as inner tissue and fat as outer tissue (that is 1.5 mm). The sensing radius estimated for the sample consisting of lymph node and fat is 0.1 mm higher than the maximum sensing radius reported in Section 4.3.1 for the Keysight slim form probe (simulated as CP1), although the contrast in relative permittivity between lymph node and fat (that is 86.5%) is lower than the contrast in relative permittivity between saline and Teflon (that is 97%). However, the two values of sensing radius differ approximately 6% from each other and such difference can be due to errors

in the conversion from S_{11} parameters into permittivity, which can be up to 10% [101].

The data from the 38 scenarios is further examined across the three categories of samples specified in Table 4.11 (i.e., samples having the same outer tissue, but different inner tissue; samples having the same inner tissue, but different outer tissue; and samples consisting of the same two tissues, but with swapped locations) in the subsection below.

4.3.2.2 Dependence of sensing radius on tissue permittivity magnitude across three categories of samples

Firstly, the data from C1, the category consisting of samples having the same outer tissue but different inner tissues, is presented in Fig. 4.20, where the average sensing radius is plotted versus the average relative permittivity of the inner tissue. Specifically, for all scenarios plotted in Fig. 4.20, muscle is the outer tissue. In the plot of Fig. 4.20, two trends are detected and the data is distinguished into two clusters as in Fig. 4.18 and Fig. 4.19. The clusters refer to the average relative permittivity of the inner tissue relative to the average relative permittivity of the outer tissue. Specifically, in Fig. 4.20, the data corresponding to the scenarios with inner tissues having relative permittivity lower than that of muscle is illustrated in blue, and the data corresponding to inner tissues having relative permittivity higher than that of muscle is illustrated in red. In Fig. 4.20, the trends of the two clusters are delineated by two second degree polynomial curves that interpolate the two data subsets. The polynomials interpolating the blue and red data clusters are defined by Eq. (4.10) and Eq. (4.11), respectively, as follows:

$$f_{blue}(x) = -0.0003x^2 + 0.005x + 0.856, \quad (4.10)$$

$$f_{red}(x) = -0.0007x^2 + 0.103x - 3.092, \quad (4.11)$$

where $f(x)$ is the average sensing radius and x is the average relative permittivity of the outer tissue for the samples having muscle as inner tissue. The RMSE calculated between the data and the fitted polynomials is 0.0248 for the blue cluster and 0.0339 for the red cluster. From the two polynomial trends, it is clear that the sensing radius is lower when the average relative permittivity of the inner tissue is closer to the average relative permittivity of muscle, i.e., 50.8. Furthermore, it is found that the sensing radius increases as the average relative permittivity of the inner tissue diverges from that of muscle.

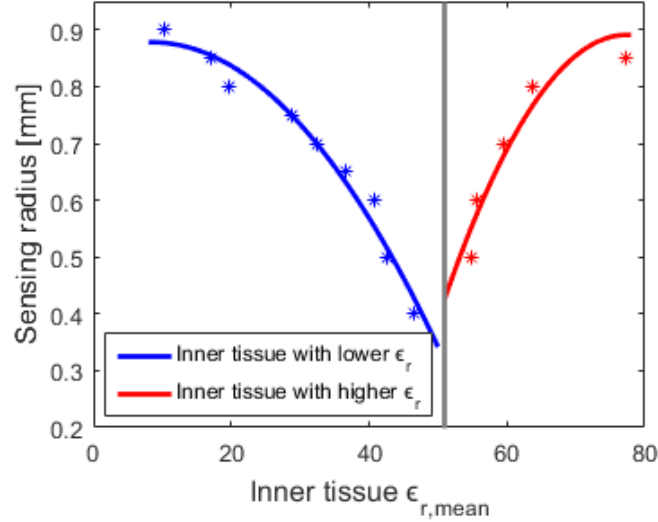


Figure 4.20: Plot of the average sensing radius vs. average relative permittivity of the inner tissue for scenarios consisting of samples having the same outer tissue, i.e., muscle, but different inner tissues (included within the category C1). The average relative permittivity of muscle (50.8) is marked with a grey vertical line in the plot and separates the data into two clusters: on the left, in blue, the cluster including samples composed of an inner tissue with relative permittivity lower than that of muscle, and, on the right, in red, the cluster of samples composed of an inner tissue with relative permittivity higher than that of muscle. The data from the two clusters show different trends. To better define the trends, the two data subsets are interpolated with second degree polynomials, which are defined by Eq. (4.10) and Eq. (4.11) for the blue and red curves, respectively. The RMSE calculated between the data and the fitted polynomials is 0.0248 for the blue cluster and 0.0339 for the red cluster. From both trends, it is clear that the sensing radius is lower when the average relative permittivity of the inner tissue is closer to that of muscle.

Next, in Fig. 4.21, examples of results from the category C2 of samples having the same inner tissue but different outer tissues are plotted. Specifically, the sensing radius versus the relative permittivity of the outer tissue is shown, for data from two clusters. One cluster refers to samples having fat as inner tissue with a range of other tissues as outer tissue (in blue) and the other cluster refers to samples having lymph node as inner tissue with a range of other outer tissues (in red). The two clusters have opposite trends, since the corresponding inner tissues, fat and lymph node, have very different relative permittivities which delimit the range of relative permittivity values of the tissues selected for this study (as shown in Fig. 4.10). Specifically, the average relative permittivity of fat is 10.4, and the average relative permittivity of lymph node is 77.2. As such, the data from samples having

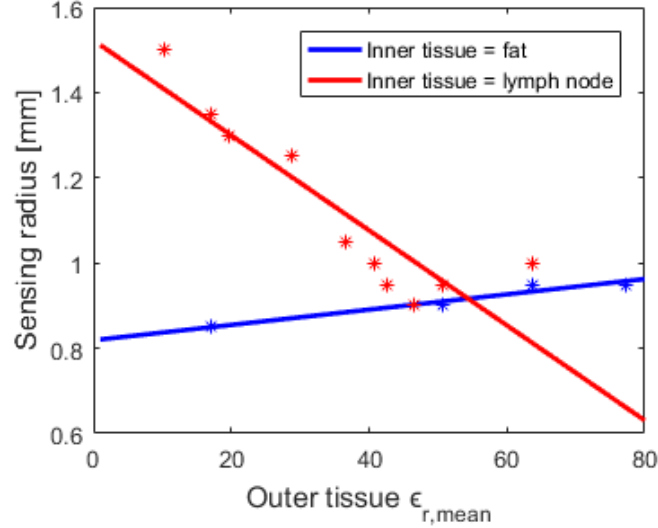


Figure 4.21: Sensing radius vs. outer tissue relative permittivity for two clusters corresponding to the category C2 of samples having the same inner tissue, but different outer tissues. The data in blue refers to samples having fat as inner tissue with a range of other tissues as outer tissue, and the data in red refers to samples having lymph node as inner tissue with a range of other outer tissues. The two clusters have different trends, since in one case, fat has an average relative permittivity lower than that of all the outer tissues, and in the other case, lymph node has an average relative permittivity higher than that of all the outer tissues. The blue and red data clusters are interpolated with linear polynomials defined by Eq. (4.12) and Eq. (4.13), respectively. Furthermore, the RMSE is 0.0105 and 0.0868 for the clusters from samples with fat as inner tissue and lymph node as inner tissue, respectively.

fat as inner tissue are part of the cluster of samples with inner tissues having lower relative permittivity, and, vice versa, the data from samples having lymph node as inner tissue are part of the cluster of samples with inner tissues having higher relative permittivity than the outer tissues. In fact, in one case, fat has an average relative permittivity lower than that of all the outer tissues, and in the other case, lymph node has an average relative permittivity higher than that of all the outer tissues.

In Fig. 4.21, the two opposite trends are highlighted by the two linear polynomials interpolating the red and blue data clusters. Specifically, the polynomial interpolating the data from the blue cluster (representing the samples having fat as inner tissue) is defined by Eq. (4.12) and the polynomial interpolating the data from the red cluster (representing the samples having lymph node as inner tissue) is defined by Eq. (4.13), as follows:

CHAPTER 4. SENSING RADIUS OF COAXIAL PROBES

$$f_{blue}(x) = 0.002x + 0.819, \quad (4.12)$$

$$f_{red}(x) = -0.011x + 1.522, \quad (4.13)$$

where $f(x)$ is the average sensing radius and x is the average relative permittivity of the outer tissue for the samples having fat and lymph node as inner tissues. The RMSE calculated between the data and the fitted polynomials is 0.0105 for the blue cluster and 0.0868 for the red cluster.

Although the two subsets show opposite trends in Fig. 4.21, they present the same trends in the sensing radius versus relative permittivity contrast plot in Fig. 4.22. In both cases, the sensing radius increases as the contrast in relative permittivity increases. In addition, as in Fig. 4.19, the sensing radius values are lower for the samples having fat as inner tissue (i.e., samples with the lower relative permittivity inner tissue) than for the samples having lymph node as inner tissue (i.e., samples with the higher relative permittivity inner tissue). Also in this case, the two data clusters are interpolated with polynomials defined by the equations below:

$$f_{blue}(x) = 0.002x + 0.770, \quad (4.14)$$

$$f_{red}(x) = 0.009x + 0.639, \quad (4.15)$$

where $f(x)$ is the average sensing radius and x is the average contrast in relative permittivity between inner and outer tissues (for the samples having fat and lymph node as inner tissues). Specifically the data cluster from the samples having fat as inner tissue is interpolated with the polynomial defined by Eq. (4.14), with an RMSE of 0.0162, and the data cluster from the samples having lymph node as inner tissue is interpolated with the polynomial defined by Eq. (4.15), with an RMSE of 0.0942. The RMSE is higher for the red polynomial (interpolating the data from the samples having lymph node as inner tissue), than for the blue polynomial (interpolating the data from the samples having fat as inner tissue), since the red cluster includes more spread out data. In particular, the red cluster includes the sensing radius (calculated by considering both relative permittivity and conductivity values) from the sample with lymph node as inner tissue and cerebrospinal fluid as outer tissue, which, as specified in the previous subsection, is characterised by a higher contrast in conductivity than in relative permittivity.

Finally, in Fig. 4.23, the average sensing radius from three couplets of datasets corresponding to the category C3 of samples composed of the same tissues but with swapped location are plotted versus the average relative

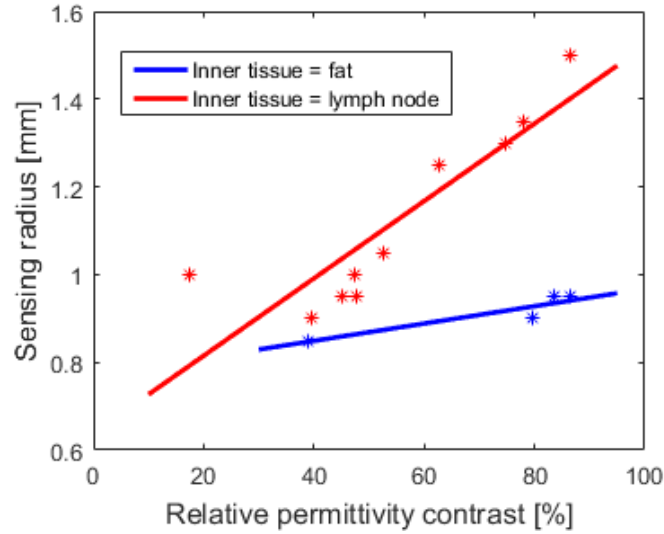


Figure 4.22: Sensing radius vs. relative permittivity contrast for the two clusters illustrated in Fig. 4.21. For both clusters, the sensing radius increases with the contrast in relative permittivity. The blue and red data clusters are interpolated with linear polynomials defined by Eq. (4.14) and Eq. (4.15), respectively. Furthermore, the RMSE is 0.0161 and 0.0942 for the clusters from samples with fat as inner tissue and lymph node as inner tissue, respectively.

permittivity of the inner tissue. One couplet refers to the two samples composed of fat and lymph node (in blue), another couplet refers to the two samples composed of muscle and pancreas (in red), and the last refers to the two samples composed of brain and lymph node (in green). The three couplets of datasets show similar trends, although they have different contrasts in relative permittivity. Specifically, the sample composed of fat and lymph node has the highest contrast in relative permittivity (86.57%), the sample composed of muscle and pancreas has the lowest contrast in relative permittivity (7.40%), and the sample composed of brain and lymph node has a contrast in relative permittivity of 44.96%. From Fig. 4.23, it can be observed that the higher the contrast between the two tissues, the higher the difference in sensing radii between the two samples within a couplet. Furthermore, in each couplet, the lowest sensing radius corresponds to the case with the lower permittivity tissue occupying the inner region of the concentric sample. Similarly, the highest sensing radius corresponds to the case with the higher permittivity tissue occupying the inner region of the concentric sample. The outcome of these case scenarios confirms the trend of the sensing radius based on the inner tissue permittivity (reported in the

CHAPTER 4. SENSING RADIUS OF COAXIAL PROBES

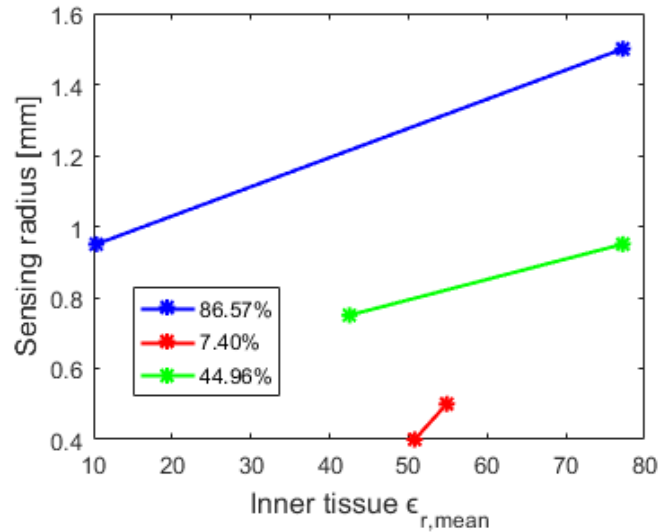


Figure 4.23: Sensing radius vs. inner tissue relative permittivity for three couplets of datasets corresponding to the category of samples C3, having same tissues but with the locations swapped. The two tissues from each couplet have different percent contrasts in relative permittivity, which are reported in the legend. The data in blue is from the sample composed of fat and lymph node, the data in red is from the sample composed of pancreas and muscle, and the data in green is from the sample composed of brain and lymph node. In each couplet, the lowest sensing radius corresponds to the case of the lower permittivity tissue occupying the inner region of the concentric sample.

paragraphs above), which can be attributed to the impedance mismatch between the probe and the inner tissue constituting the sample. Consequently, from the three couplets of datasets, it can be concluded that the higher the difference in impedance mismatch between the probe and the inner tissue and the probe and the outer tissue (and thus the difference in permittivity between inner and outer tissue), the higher the difference in sensing radius across each data couplet.

In summary, across all data from all categories the third simulation set, it was observed that the inner tissue greatly impacts the size of the sensing radius. Based on the relative permittivity of the inner tissue compared to that of the outer tissue, two different trends in sensing radius were detected. In particular, the sensing radius values were found to be lower when the relative permittivity of the inner tissue was lower than that of the outer tissue. On the other hand, the sensing radius values were higher when the relative permittivity of the inner tissue was higher than that of the outer tissue. It was also found that the sensing radius trend varies with the contrast in relative permittivity between the two concentric tissues. In

CHAPTER 4. SENSING RADIUS OF COAXIAL PROBES

general, the higher the contrast, the higher the sensing radius.

Furthermore, the quantitative results obtained from the third simulation set are only valid for the Keysight slim form probe, since the sensing radius also depends on the geometry and features of the probe used, as examined in Section 4.3.1. However, the trend of the sensing radius, depending on the relative permittivity magnitude of the interrogated tissues, can be extended to any type of probe.

Lastly, the trend of the sensing radius on tissue conductivity was not examined in this subsection. For a complete analysis of the sensing radius based on the dielectric properties of the interrogated tissue sample, the sensing radius dependence on tissue conductivity in combination with tissue relative permittivity can be analysed in future studies. However, since the trend in conductivity of the 15 tissues selected for the 38 samples is similar to the trend in relative permittivity (as reported in Fig. 4.10) and the sensing radius was estimated by considering both relative permittivity and conductivity values (as illustrated in Fig. 4.9), for the 38 selected samples, a trend similar to that of the sensing radius with relative permittivity is expected for the sensing radius analysis based on conductivity.

Before summarising the main findings and highlighting the significance of the experimental and numerical results, the performance of the linear regression and the neural network models, developed from the numerical results as tools to predict the sensing radius from information regarding the probe dimensions and tissue dielectric properties, are detailed in the next subsection.

4.3.3 Mathematical prediction of sensing radius

In this subsection, the performance of the two sets of linear regression models and neural networks, presented in Section 4.2.3, are reported and discussed. Firstly, the first set of linear regression and neural network models, developed from the second set of simulations composed of 48 scenarios including 12 probes of different geometry with 4 samples of different dielectric properties, is examined in terms of accuracy at predicting the sensing radius of probes having different dimensions across a subset of biological tissues. Secondly, the second set of linear regression and neural network models, developed from the third set of simulations composed of 38 scenarios including the Keysight slim form probe with 38 samples of different dielectric properties, is examined in terms of accuracy at predicting the sensing radius of the Keysight slim form probe across a number of biological tissues.

4.3.3.1 Mathematical prediction of sensing radius from probe dimensions

The ability to predict the sensing radius from knowledge of the probe dimensions and dielectric properties of the interrogated sample was examined through a linear regression model, defined by Eq. (4.6). From this modelling, a fitting line with the following equation was obtained:

$$f(x) = -0.13 + 0.703a + 0.907b + 0.013\epsilon_{r1} + 0.005\epsilon_{r2}, \quad (4.16)$$

where $f(x)$ is the sensing radius and a , b , ϵ_{r1} and ϵ_{r2} are the input features defined in Section 4.2.3.

Next, the neural network approach was considered. Across the ten iterations of training and testing the neural network, an average MSE of 0.0821 was calculated, ranging between 0.0128 and 0.2048. The network with the lowest MSE was selected to be used as the optimised neural network for the prediction of the sensing radius from probe dimensions and sample dielectric properties.

By comparing the performance of the linear regression and neural network models across the testing dataset, an average difference of 0.1 mm was obtained between the targets and the estimates from the linear regression (with the lowest difference of 0.005 mm and the highest difference of 0.193 mm), and an average difference of 0.048 mm was obtained between the targets and the estimates from the neural network (with the lowest difference of 0.004 mm and the highest difference of 0.09 mm). In addition, across the estimates from the testing stage, an average RMSE of 0.13 was obtained for the linear regression and an average RMSE of 0.05 was obtained for the network, suggesting a good match between the predicted sensing radius and the target value for both models.

The performance of this set of linear regression and neural network models (developed from the second simulation set data) are graphically compared in Fig. 4.24, where the predicted sensing radius values from the testing dataset are plotted versus the target values obtained numerically. For a better interpretation of the data, in Fig. 4.24, an ideal line obtained by considering a perfect match between estimates and targets ($y = x$) is plotted.

Since the values predicted from the neural network are closer to the ideal line than the values predicted from the linear regression model, Fig. 4.24 demonstrates that the trained neural network can predict the sensing radius with a higher accuracy than the linear regression model. Specifically, while an average accuracy (obtained from the average percent difference between

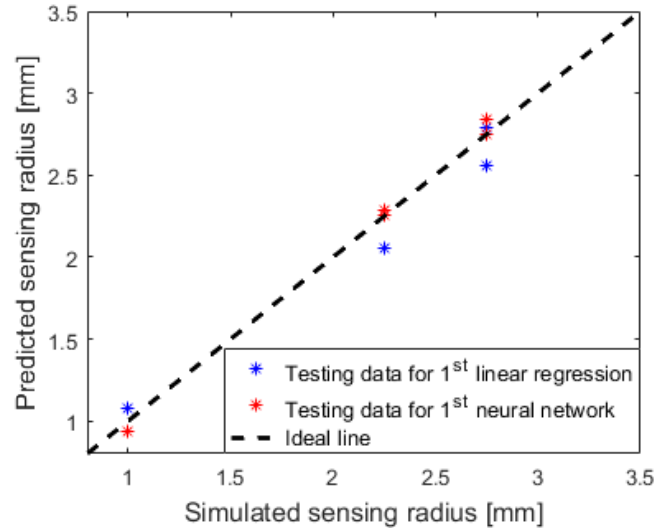


Figure 4.24: Plot comparing the sensing radius data predicted by the first set of linear regression and neural network (estimates) with the sensing radius data obtained numerically from the second simulation set (targets). The testing data obtained from the linear regression is indicated in blue and the testing data from the neural network is indicated in red. The dashed black line, which is obtained by matching the estimates with the targets, facilitates the data comparison and illustrates that the neural network is more accurate than the linear regression at predicting the sensing radius.

estimates and targets) to within 10% is obtained for the linear regression model, an average accuracy to within 5% is obtained for the neural network. The performance of the two models was further tested by evaluating the sensing radius predicted from the performance and high temperature probes within the first simulation set. The performance and high temperature probes are not included among the 12 simulated probes used for the 48 simulation scenarios, which were employed to develop and test the linear regression and the neural network models. However, by comparing the dimensions of the performance and high temperature probes summarised in Table 4.6 with those of the simulated probes listed in Table 4.9, the performance probe features are close to those of the probe CP1, and the high temperature probe has features close to those of the probe CP5.

By providing the linear regression model with the probe dimensions and material relative permittivities, an estimate of 1.73 mm and 2.29 mm was found for the sensing radius of the performance and high temperature probes, respectively. By providing the neural network with the same inputs, estimates of 1.54 mm and 2.37 mm were found, respectively. The comparison of these predicted values with the values obtained numerically,

CHAPTER 4. SENSING RADIUS OF COAXIAL PROBES

which are 1.5 mm and 2.25 mm for the performance and high temperature probes, respectively, suggest that, while both models may be practically implemented, a neural network can potentially outperform linear regression. Thus, these results demonstrate the potential for using neural networks, or similar algorithms, to predict the sensing radius of a coaxial probe based on knowledge of the probe dimensions and the dielectric properties of the investigated sample, with an accuracy to within 10%.

In summary, the neural network is able to predict the sensing radius from knowledge of the probe geometry and relative permittivity of the interrogated sample, with an accuracy approximately 5% higher than that of the linear regression model. With predictions always within 0.2 mm of the target sensing radius values, the neural network provides estimates that are appropriately accurate for use in experimental studies. Since the network was trained with a discrete number of geometries and a small number of interrogated materials, the neural network is likely only able to predict the sensing radius with high accuracy for breast tissue or tissues with similar dielectric properties, such as heart tissue. However, the neural network performance can be extended to any type of biological tissue by training it with an increased number of sample tissues for each probe geometry.

To this extent, a second set of linear regression and neural network models, developed for the prediction of the sensing radius of the Keysight slim form probe for a number of biological tissues, is reported and analysed below.

4.3.3.2 Mathematical prediction of sensing radius from tissue dielectric properties

A second linear regression model, defined by Eq. (4.7), was developed as tool to predict the sensing radius of the Keysight slim form probe from knowledge of the dielectric properties of the interrogated sample. From this regression model, a fitting line with the following equation was obtained:

$$f(x) = 1.127 + 0.0023\epsilon_{r1} - 0.0093\epsilon_{r2}, \quad (4.17)$$

where $f(x)$ is the sensing radius and ϵ_{r1} and ϵ_{r2} are the input features defined in Section 4.2.3.

Subsequently, ten iterations of training and testing were run for the second neural network, and an average MSE of 0.0310 was calculated, ranging between the lowest value of 0.0046 and the highest value of 0.1320. As with the neural network discussed above, the neural network with the lowest MSE was selected to be used as the optimised neural network for the

CHAPTER 4. SENSING RADIUS OF COAXIAL PROBES

prediction of the sensing radius of the slim form probe from the dielectric properties of the interrogated biological sample.

By comparing the performance of this second set of models across the testing dataset, an average difference of 0.179 mm was obtained between the targets and the estimates from the linear regression (with the lowest difference of 0.026 mm and the highest difference of 0.415 mm), and an average difference of 0.062 mm was obtained between the targets and the estimates from the neural network (with the lowest difference of 0.03 mm and the highest difference of 0.11 mm). In addition, across the estimates from the testing stage, an average RMSE of 0.24 was obtained for the linear regression and an average RMSE of 0.07 was obtained for the neural network, suggesting a better match between the predicted sensing radius and the target value with the neural network than with the linear regression model.

The performance of this second set of linear regression and neural network models (developed from the third simulation set data) are graphically compared in Fig. 4.25, in a plot similar to the one illustrated in Fig. 4.24. As with the previous set of models, the values predicted from the neural network are closer to the ideal line $y = x$ (obtained by considering a perfect match between estimates and targets) than the values predicted from the linear regression model. Thus, Fig. 4.25 demonstrates that the trained neural network can predict the sensing radius with a higher accuracy than the linear regression model. Specifically, while an average accuracy to within 15% is obtained for the linear regression model, an average accuracy to within 5% is obtained for the neural network.

The performance of the two models was further tested by evaluating the sensing radius of the Keysight slim form probe for breast gland and fat tissues and comparing the predicted values with the values obtained from the two simulations (within the second simulation set) involving the probe CP1 (i.e., the model for the slim form probe) and the two samples consisting of breast gland and fat tissues.

By providing the linear regression model with the relative permittivities of breast gland and fat tissues, an estimate of 1.21 mm and 0.64 mm was found for the sample having breast gland as inner tissue and breast fat as outer tissue and for the sample having breast fat as inner tissue and breast gland as outer tissue, respectively. By providing the neural network with the same inputs, estimates of 1.30 mm and 0.94 mm were found, respectively. The values predicted from the neural network are comparable with the two values obtained from the second simulation set, which are 1.35 mm and 1 mm, for the sample having breast gland as inner tissue and breast fat as outer tissue and for the sample having breast fat as inner tissue and breast gland as outer tissue, respectively. Conversely, the value of sensing

CHAPTER 4. SENSING RADIUS OF COAXIAL PROBES

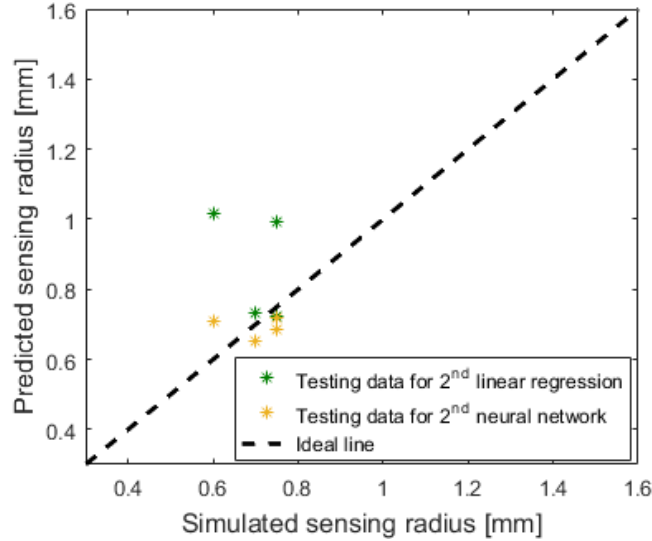


Figure 4.25: Plot comparing the sensing radius data predicted, for the Keysight slim form probe, by the second set of linear regression and neural network (estimates) with the sensing radius data obtained numerically from the third simulation set (targets). The testing data obtained from the linear regression is indicated in green and the testing data from the neural network is indicated in yellow. The dashed black line, which indicates the ideal match between the estimates and the targets, facilitates data comparison and illustrates that the neural network is more accurate than the linear regression at predicting the sensing radius.

radius obtained from the linear regression model for the same sample is significantly different from the value obtained numerically.

From a general comparison of the predicted values with the values obtained numerically, it can be concluded that the neural network generally outperforms linear regression for the prediction of the sensing radius from knowledge of the dielectric properties of the interrogated biological sample. In fact, the neural network is able to predict the sensing radius of the slim form probe from the relative permittivities of the interrogated sample, with an average accuracy 10% higher than that of the linear regression model. With predictions always within 0.11 mm of the target sensing radius values, the neural network provides estimates that are appropriately accurate for use in experimental studies involving the Keysight slim form probe.

Lastly, it should be noted that the two sets of linear regression and neural network models discussed above were developed from sensing radius values obtained numerically based on the definition of sensing radius empirically related with the uncertainty of the measurement system, as provided in Section 4.1.3 and illustrated in Section 4.2.1. Different definitions of sensing

radius, or different measurement uncertainty values (associated with different measurement systems), are likely to result in different estimates of sensing radius. However, different definitions or estimates of sensing radius do not affect the trend of the sensing radius across varying probe dimensions and tissue constituents, which is detailed in Section 4.3.1 and Section 4.3.2, and finally summarised in the following section.

4.4 Summary

The estimation of the sensing volume of an open-ended coaxial probe is fundamental, not only to dielectrically characterise highly heterogeneous biological samples (as previously discussed in Section 3.3.2), but also to define the minimum size of the homogeneous tissue region that ensures accurate tissue dielectric measurements, without the influence of the tissues or materials surrounding the tissue of interest.

In the literature to date, the sensing radius has only been analysed in select scenarios with limited number of probes and tissue-mimicking materials. Therefore, in this chapter, the sensing radius has been examined both numerically and experimentally with a range of probes of different dimensions and a wide variety of materials including biological tissues. In particular, for the estimation of the sensing radius, concentric samples were used and modelled, in the same way as layered samples have been used in the literature for the estimation of the sensing depth. The measured and simulated samples were then analysed to model the dependence of the sensing radius of a coaxial probe on the probe dimensions and on the dielectric properties of the interrogated sample.

After providing the definition of sensing radius and maximum sensing radius based on the measurement uncertainty in Section 4.1.3, an initial analysis of the sensing radius dependence on the probe dimensions was conducted by performing measurements and simulations with the three Keysight probes, i.e., slim form, performance and high temperature probes, which are the most commonly used probes in recent dielectric studies [15], [48], [49], [54], [114]. From this initial analysis, maximum sensing radius values of 1.4 mm, 1.5 mm, and 2.25 mm were estimated numerically for the slim form probe, performance probe, and high temperature probe, respectively, which are consistent with the maximum sensing radius values obtained experimentally. Since the three Keysight probes have increasing sizes (specifically, increasing outer conductor inner radii), this initial outcome demonstrated that the sensing radius of a coaxial probe increases with increasing the inner radius of the outer conductor.

CHAPTER 4. SENSING RADIUS OF COAXIAL PROBES

Subsequently, the sensing radius dependence on the probe dimensions was further examined by conducting numerical simulations across a subset of 4 samples with 12 probes having varying dimensions of, in turn, inner conductor, insulator, and outer conductor. From the analysis of the sensing radius obtained from each simulation, the following findings were observed:

- The sensing radius is not affected by the width of the outer conductor;
- The sensing radius increases approximately linearly with the inner radius of the outer conductor (and thus with the radius of the inner conductor and the width of the insulator);
- The sensing radius is primarily affected by the radius of the inner conductor.

Furthermore, although the trend of the sensing radius as a function of the probe dimensions was found to be consistent across samples having different dielectric properties, for each probe geometry, different sensing radius values were obtained depending on the dielectric properties of the simulated sample.

Hence, the dependence of the sensing radius on the sample dielectric properties was examined by conducting numerical simulations involving the Keysight slim form probe and 38 biological samples with varying relative permittivity values of the concentric constituent tissues. From the analysis of the sensing radius values obtained across all the 38 samples, the following two key observations were noted.

- The sensing radius increases with the contrast in relative permittivity between the two concentric tissues.
- The relative permittivity of the inner tissue greatly impacts the acquired signal and, as a consequence, it also affects the value of the sensing radius. Specifically, the lower the impedance mismatch between the probe and the inner tissue (i.e., the higher the permittivity of the inner issue), the higher the estimated sensing radius.

Lastly, the sensing radius values obtained numerically were used for the development of two sets of regression line and neural network models. Specifically, the first set of models requires as input features the radius of the inner conductor, the inner radius of the outer conductor, and the relative permittivity of two concentric materials to predict the sensing radius from knowledge of the probe dimensions and sample dielectric properties. On the other hand, the second set of models requires as input features only the relative permittivity of two concentric materials in order to predict the sensing radius of the Keysight slim form probe from knowledge of the sample dielectric properties. For both sets of models, it was observed that the neural network generally outperforms the regression line and is able to predict the sensing radius with an average accuracy to within approximately 5%.

CHAPTER 4. SENSING RADIUS OF COAXIAL PROBES

Hence, with some additional investigation, such as the combined analysis of the dependence on the sensing radius on both relative permittivity and conductivity of the constituent tissues, extended to a larger number of probes and biological tissues, the development of neural networks has the potential to support the dielectric measurement of biological tissues in providing a fast and easy method to estimate the sensing radius in future studies.

In summary, the findings reported in this chapter highlight the importance of taking into account not only the dimensions of the probe, but also the dielectric properties of the constituent tissues of the investigated sample when estimating the sensing radius. In particular, in the case of highly heterogeneous tissue samples, or samples with completely unknown composition, it is recommended to consider the maximum sensing radius as the starting point for the tissue sample dielectric characterisation. In the case of tissue samples with known constituents, a sensing radius smaller than the maximum sensing radius may be considered, based on the results of preliminary simulations or experiments.

The outcomes of this study are the foundation for a rigorous estimation of the sensing radius, which supports accurate and consistent dielectric measurement of biological tissues. However, even with a rigorous estimation of the sensing radius, inaccuracies in the dielectric characterisation of highly heterogeneous tissue samples can occur, due to the lack of knowledge of the dielectric contribution of the tissues included within the sensing radius to the acquired dielectric data. For this reason, the dielectric contribution of the sample constituents to the acquired dielectric data is investigated in Chapter 5.

Analysis of the dielectric contribution of individual materials within the sensing radius

Related publications

The experimental and numerical studies presented in this chapter have been published in two journal papers.

In particular, a general analysis of the dielectric contribution of individual materials within the sensing radius has been published in the paper entitled “Investigation of Histology Radius for Dielectric Characterisation of Heterogeneous Materials” in the journal of IEEE Transactions on Dielectrics and Electrical Insulation (A. La Gioia, S. Salahuddin, M. A. Elahi, M. O’Halloran, and E. Porter “Investigation of histology radius in dielectric measurements of heterogeneous materials,” IEEE Transactions on Dielectrics and Electrical Insulation, vol. 25, no. 3, pp. 1065–1080, 2018).

A detailed analysis of individual tissue dielectric contribution within porcine samples has been published in the paper entitled “Quantification of the Sensing Radius of a Coaxial Probe for Accurate Interpretation of Heterogeneous Tissue Dielectric Data” in the journal of IEEE Journal of Electromagnetics, RF, and Microwaves in Medicine and Biology (A. La Gioia, S. Salahuddin, M. O’Halloran, and E. Porter, “Quantification of the Sensing Radius of a Coaxial Probe for Accurate Interpretation of Heterogeneous Tissue Dielectric Data,” IEEE Journal on Electromagnetics, RF, and MWs in Medicine and Biology, vol. 2, no. 3, pp. 145–153, 2018).

The sensing radius analysis completed in Chapter 4 supports accurate dielectric characterisation of heterogeneous biological tissues. However, for an accurate dielectric characterisation of highly heterogeneous biological tissues, knowledge of the sensing volume needs to be accompanied by knowl-

edge of the dielectric contribution of each tissue constituting the sensing volume, in order to appropriately correlate the acquired dielectric data to the histology of the sample (as already mentioned in the previous chapters). In past studies, the dielectric contribution of layered materials within the sensing depth has been thoroughly examined. However, only a few studies in the literature have investigated the dielectric contribution of radially heterogeneous materials within the sensing radius, and the reported results were only qualitative [193].

For this reason, in this chapter, after highlighting the motivation of the study (in Section 5.1), the dielectric contribution of individual materials is quantitatively analysed within tissue-mimicking and biological samples that consist of two side-by-side or concentric materials (or tissues). In particular, such analysis involves both dielectric measurements and numerical simulations, the methodology of which is described in Section 5.2. Thus, the experimental and numerical findings are discussed in Section 5.3 for both sample configurations, i.e., samples consisting of side-by-side and concentric materials. Furthermore, the numerical findings regarding a subset of biological tissues are modelled in order to support prediction of the dielectric contribution of an individual tissue from knowledge of the sample tissue content, i.e., types of tissues and the distribution/volume of each. Lastly, the main findings of this investigation are summarised in Section 5.4.

5.1 Dielectric contribution of individual materials within a heterogeneous sample

As discussed in Chapter 4, knowledge of the sensing volume enables accurate dielectric measurement of homogeneous tissues within heterogeneous tissue samples presenting simple heterogeneities. However, in the case of highly heterogeneous tissue samples, within which it is not possible to find a homogeneous tissue region with size larger than the sensing volume, it is crucial to know the contribution of each tissue type within the sensing volume to the acquired dielectric data. In fact, in this case, knowledge of the sensing volume and the dielectric contribution of tissues within the sensing volume supports associating the acquired dielectric data with the tissue content of the sample, generally investigated by post-measurement histology. The importance of knowing the dielectric contribution of tissues within the sensing radius was highlighted in Section 3.3.2, with the support of the illustrations in Fig. 3.4.

CHAPTER 5. MATERIAL DIELECTRIC CONTRIBUTION

However, in all dielectric studies to date that have correlate the dielectric data with the histology of the sample, it has been assumed that the contribution of each tissue to the measured dielectric data is proportional to the volume occupied by each tissue within the sensing volume [10], [11], [15], [49]. Thus, the data inconsistencies regarding heterogeneous biological tissues (presented in Chapter 2) can be attributed not only to inconsistent estimations of the sensing radius (as discussed in Chapter 4), but also to the erroneous assumption that the measured dielectric data is proportional to the volume occupied by the tissue. Specifically, Porter *et al.* found up to 50% discrepancy between acquired data and data calculated based on the assumption that the contribution of each tissue to the measured dielectric data is proportional to the volume occupied by that tissue [64].

In particular, in the studies conducted by Porter *et al.* [63], [64] the dielectric contribution of individual materials to the acquired signal was investigated with layered structures, in the context of determining the sensing depth. Other recent studies by Meaney *et al.* [66], [135] also demonstrated that, within layered structures, the closest tissue to the probe has the highest impact on the acquired dielectric data. Furthermore, the dielectric impact of individual materials within radially heterogeneous samples was analysed only in the study by Ozalp [193]. Specifically Ozalp conducted dielectric measurements with an open-ended coaxial probe across different radially heterogeneous regions within tissue-mimicking samples consisting of two materials placed side-by-side. This set of measurements demonstrated that the acquired dielectric data varies considerably across regions close to the interface between the two materials; however, quantitative results were not provided.

Hence, due to the fact that previous studies focused on examining the dielectric contribution of individual materials within the sensing depth, in this chapter, the dielectric contribution of individual materials within the sensing radius is quantified. Specifically, both dielectric measurements and numerical simulations were conducted on tissue-mimicking and biological tissue samples presenting two configurations of radial heterogeneities:

- Linear heterogeneity configuration, with side-by-side materials (or tissues);
- Concentric heterogeneity configuration, with concentric materials (or tissues).

Besides differences in structure, the investigated samples consist of materials having different dielectric properties, since recent studies demonstrated that the dielectric contribution of a material to the acquired data depends on both the spatial distribution (i.e., volume occupied) and the dielectric properties of each material constituting the interrogated sample [63], [64],

[135]. Thus, in this investigation, the dependence of the dielectric contribution of an individual material on the spatial distribution and dielectric properties of each material within the sensing radius is examined.

While the two types of heterogeneities above represent simplified scenarios relative to the heterogeneities present in actual biological tissues, the analysis of these types of heterogeneities provides the basis for more complex structural variations. Therefore, an understanding of how materials in these different spatial distributions influence dielectric measurements supports the interpretation of the dielectric data from biological tissues presenting more complex heterogeneities.

Further details regarding the experimental and numerical methodology of the study are reported in the following section.

5.2 Methodology

This section details the methodology used to investigate the dielectric contribution of individual materials within the sensing radius. Specifically, methodologies for both experimental and numerical investigations are presented.

Initially, dielectric measurements performed on tissue mimicking materials and biological tissues presenting side-by-side heterogeneities are reported in Section 5.2.1, for different radial distances from the material/tissue interface.

Secondly, in order to examine how the dielectric contribution of a material varies with the sample structure, dielectric measurements performed on tissue mimicking materials and biological tissues presenting concentric heterogeneities are detailed in Section 5.2.1. In particular, in order to examine how the dielectric contribution of a material varies with the dielectric properties of the materials constituting the sample, different materials and tissues spanning a wide range of permittivities were used to manufacture the samples in both configurations (i.e., samples with side-by-side and concentric heterogeneities).

Furthermore, due to the high number of measurement confounders that can affect dielectric experiments (as seen in Chapter 3), the experimental findings were validated with numerical simulations reproducing the experimental scenarios, which thus provided more quantitative information regarding the contribution of each tissue constituting a radially heterogeneous sample.

Lastly, further numerical simulations were performed to model the dielectric contribution of individual biological tissues across a subset of radially heterogeneous samples. The design of the numerical simulations performed

to validate the experimental outcome and to model the individual tissue dielectric contribution is detailed in 5.2.2.

5.2.1 Experimental methodology

This subsection presents the experimental methodology used to examine how the dielectric contribution of an individual tissue to the measured permittivity of the bulk sample depends on the individual dielectric properties and spatial distribution of the tissues constituting the sample.

Dielectric experiments were performed with the Keysight slim form probe connected to the Agilent E8362B VNA in the MW range of 2-6 GHz. The slim form probe was selected for this investigation since it is the most commonly used probe in recent tissue dielectric studies [12], [15], [48], [49], [54], [63], [66]. Thus, the use of the slim form probe allows for re-interpreting the results obtained with such probes in recent studies involving the dielectric characterisation of heterogeneous tissue samples [12], [15], [48], [49]. Furthermore, the range of 2-6 GHz was selected because it includes the operating frequency of many MW imaging systems and MW ablation applicators, as mentioned in Chapter 4.

Dielectric experiments were conducted on two types of well-controlled radially heterogeneous samples, which were manufactured with side-by-side and concentric materials. Specifically, only these types of radially heterogeneous samples were fabricated due to the challenges of manufacturing well-controlled heterogeneous phantoms with different geometrical structures within the sensing radius of the slim form probe, which does not exceed the size of 1.5 mm, as observed in Section 4.3.

For each dielectric experiment, measurements were repeated three times within each of three different calibrations. The same measurement settings were used and the same measurement procedure was followed as for the experiments conducted to estimate the sensing radius (as specified in Section 4.2.1). Thus, before each measurement set, the system was calibrated using the three-load standard procedure. After each calibration, the system performance was validated by measuring the dielectric properties of 0.1 M NaCl and by comparing the measured dielectric properties with the dielectric properties from the model by Peyman *et al.* [146]. The temperature of the calibration and validation liquids were recorded within each calibration. Measurements were performed after the calibration only if the recordings of 0.1 M NaCl confirmed the measurement uncertainty was consistently within the values presented in Section 4.2.1 (i.e., 2.4% for relative permittivity and 4.6% for conductivity), otherwise, the calibration was repeated.

CHAPTER 5. MATERIAL DIELECTRIC CONTRIBUTION

Table 5.1: Summary of heterogeneous samples measured in linear configuration. The average relative permittivity values of the materials/tissues across the range 2-6 GHz are specified in brackets.

Samples	Material 1	Material 2
L1	Phantom A ($\epsilon_r=7.20$)	Phantom B ($\epsilon_r=46.10$)
L2	Phantom A ($\epsilon_r=7.20$)	Saline ($\epsilon_r=74.00$)
L3	Vegetable oil ($\epsilon_r=2.53$)	Phantom B ($\epsilon_r=46.10$)
L4	Porcine fat ($\epsilon_r=9.20$)	Porcine muscle ($\epsilon_r=42.10$)
L5	Phantom A ($\epsilon_r=7.20$)	Vegetable oil ($\epsilon_r=2.53$)
L6	Saline ($\epsilon_r=74.00$)	Phantom B ($\epsilon_r=46.10$)

Further details regarding the experimental design and protocol are reported in the following subsections for the two types of radially heterogeneous samples. Specifically, the design of the dielectric measurements conducted on side-by-side tissue-mimicking materials and biological tissues is firstly discussed; then followed by the description of the experimental design regarding concentric tissue-mimicking materials and biological tissues.

5.2.1.1 Investigation of dielectric contribution of materials in linear heterogeneity configuration

For the fabrication of samples with a linear heterogeneity configuration, two different materials were placed side-by-side, resulting in one bulk heterogeneous sample. The samples consist of Material 1 (on the left) and Material 2 (on the right). Material 1 and Material 2 are specified for each heterogeneous sample (denoted L1 to L6) in Table 5.1. The materials/tissues were selected to maximise the range of material properties and dielectric contrasts involved in the measurement scenarios. In this way, the impact of the materials on the measured dielectric properties could be examined based on the individual material dielectric properties and/or on the dielectric contrast of the materials.

In Table 5.1, the average relative permittivity values of the materials/tissues across the range of 2-6 GHz are reported in brackets beside the material name. As is clear from Table 5.1, the materials involved in Samples L1, L2, L3, and L4 have high contrast in permittivity, while the materials comprising Samples L5 and L6 have lower contrast in permittivity.

In particular, different solid or liquid phantoms having both high and low permittivity were assembled, such as 0.1 M NaCl, vegetable oil, and rubber-based tissue-mimicking phantoms. The tissue-mimicking phantoms are based on those developed by Santorelli *et al.* [194], and have a durable, semi-solid structure. Two types of such rubber-based phantoms were used: a fat-mimicking phantom having low permittivity, denoted here as “Phantom

CHAPTER 5. MATERIAL DIELECTRIC CONTRIBUTION

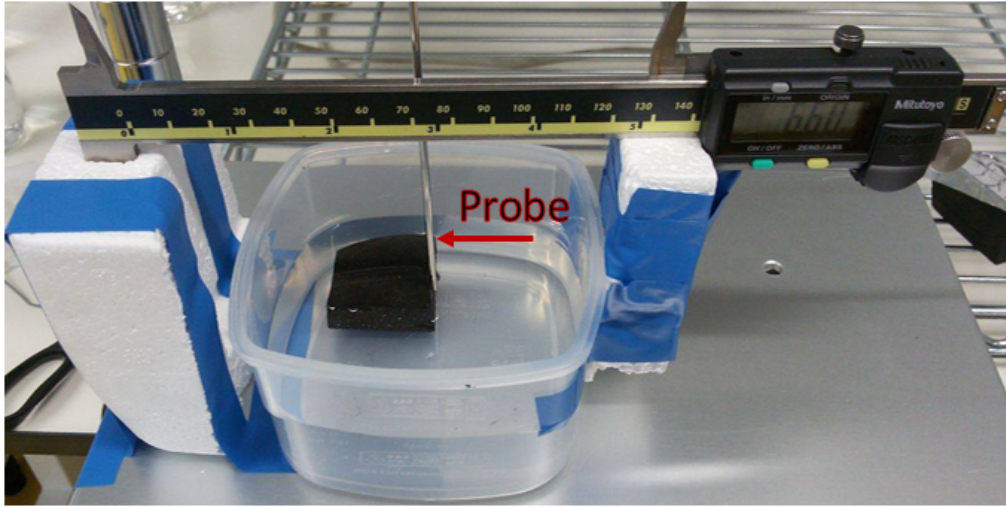


Figure 5.1: Set-up for the measurement scenario used to evaluate how radial heterogeneities in linear configuration impact the measured dielectric properties. In the picture, the probe is positioned on sample L2 at the interface between Phantom A and saline. Phantom A is the low permittivity rubber-based phantom and was attached to the bottom of the plastic box using double-sided tape. The probe position on the sample was controlled, radially, by the calliper attached to the right extremity of the box and, longitudinally, by the lift table.

A”, and a breast glandular phantom having high permittivity, denoted here as “Phantom B”.

Measurements were performed at the interface of the two materials as well as at controlled distances away from the interface. The position of the sample with respect to the probe was controlled by connecting a calliper between the box containing the heterogeneous sample and a rigid support. In this way, the probe was kept in a fixed position (to avoid cable movements and system perturbations) and the sample was moved underneath the probe by moving the calliper in discrete steps of 0.5-1 mm. It was ensured that no contact occurred between the probe and the sample while the calliper was moved. Specifically, before the probe position on the sample was changed, the sample was lowered away from the probe using the lift table. In Fig. 5.1, a photograph of the measurement set-up is provided and, in Fig. 5.2, a picture of the heterogeneous sample L1 and a diagram of this measurement scenario are reported.

The dielectric properties were first measured with the probe positioned on Material 1, at 10 mm from the interface. Then, the probe was brought closer to the material interface in small increments. At each position, the dielectric properties were measured. After performing multiple dielectric

CHAPTER 5. MATERIAL DIELECTRIC CONTRIBUTION

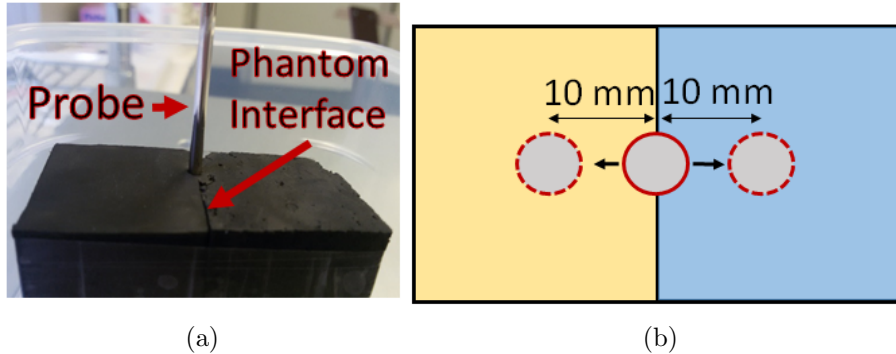


Figure 5.2: (a) Side view picture and (b) top view diagram of the measurement scenario used to evaluate how radial heterogeneities in linear configuration impact the measured dielectric properties. In the photograph, the probe is positioned on sample L1 at the interface between Phantom A and Phantom B. In the diagram, the red bordered circles represent the probe and the two sample materials are represented with the colours yellow and blue. Measurements were performed at the material interface and at different distances from the interface (from -10 mm to +10 mm).

measurements on the interface, the probe was positioned on Material 2. At this point, the probe was gradually moved away from the material interface. Dielectric measurements were performed at each position until the probe was located on Material 2 at 10 mm from the interface. All distances were measured using the material interface as the origin, i.e., as distance “zero”. The distance from the centre of the probe from the position “zero” (material interface) was considered “negative” if the probe was placed on the left material (Material 1), and “positive”, if the probe was placed on the right material (Material 2). Furthermore, a maximum distance of 10 mm from the interface was chosen for the experiments, since such distance is notably larger than the sensing radius, and measurements within such distance could provide further information about the sensing radius. In fact, each set of experiments enables estimation of the radial distance between the probe and the material interface at which only the dielectric properties of one material were detected (i.e., the radial distance at which the effect of the other material ceased). Thus, this set of experiments not only enables estimation of the contribution of each material to the measured dielectric properties, but also supports the estimation of the sensing radius.

As is clear from Table 5.1, dielectric measurements were also performed on porcine tissue. Specifically, porcine tissue samples, obtained from a local butcher, were chosen for the measurements because of the well-defined heterogeneous structure consisting of two easily distinguishable tissues: fat and muscle. During the measurement procedure, tissue dehydration was

CHAPTER 5. MATERIAL DIELECTRIC CONTRIBUTION

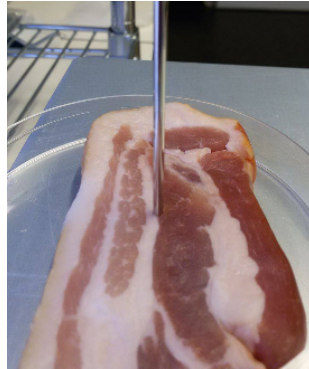


Figure 5.3: Example of measurement sample used to estimate the contribution of side-by-side tissues to the measured permittivity. The picture illustrates Sample L4, a porcine sample consisting of side-by-side fat and muscle tissues. In the figure, the probe is positioned on the fat-muscle interface, where both fat and muscle tissues occupy approximately 50% of the sensing volume.

minimised by limiting the exposure of each sample to air. Specifically, prior to measurements, tissue samples were kept in hermetically closed containers and between measurement times, the measurement sites were covered with excess tissue. Furthermore, during tissue measurements, each sample was brought to the probe tip using a lift table, a firm contact between the probe and the tissue was established, and the tissue temperature was measured with an infrared thermometer.

Due to the heterogeneity of the porcine sample, it was not possible to perform measurements at controlled distances from the fat-muscle interface, as was done for the tissue-mimicking materials. Thus, measurements were conducted on three different porcine tissue sites: on only fat, on only muscle, and at the fat-muscle interface, where both fat and muscle tissues occupy approximately 50% of the sensing volume. Three measurements were performed at each of the three sites and averaged. The same measurement procedure was repeated on three different porcine tissue samples exhibiting the same tissue distribution. The permittivity values were then examined to determine the contribution of the fat and muscle tissues to the total dielectric properties at the fat-muscle interface. The probe position at the fat-muscle interface of a porcine sample is shown in Fig. 5.3.

For a more quantitative evaluation of the contribution of side-by-side tissue-mimicking materials and porcine tissues to the dielectric data, numerical simulations were conducted. The design of the numerical simulation is presented in Section 5.2.2, after discussing the experimental design of the dielectric measurements conducted on concentric tissue-mimicking materials

and biological tissues.

5.2.1.2 Investigation of dielectric contribution of materials in concentric heterogeneity configuration

For the fabrication of samples with a concentric heterogeneity configuration, fewer materials were combined, given the complexity of fabricating a round inner material with a radius smaller than the sensing radius of the Keysight slim form probe (that does not exceed 1.5 mm, as seen in Section 4.3). As such, besides using concentric heterogeneous porcine tissue samples, Teflon or polylactic acid (PLA) and saline solution were combined to fabricate four different tissue-mimicking samples with concentric heterogeneities. Similarly to porcine muscle and fat, Teflon (or PLA) and saline have a high contrast in permittivity in order to facilitate the interpretation of the acquired data (i.e., the separation of the contribution of each material to the measured dielectric properties). In fact, it is simpler to discern the dielectric contribution of an individual material from a sample with two materials having high contrast in permittivity than from a sample with two materials having low contrast in permittivity.

In particular, the tissue-mimicking materials were combined in two ways:

- In the first configuration, saline was used as the inner material and Teflon as the outer material;
- In the second configuration, PLA was used as the inner material and saline as the outer material.

In the first configuration, similarly to the experimental design used for the estimation of the sensing radius (detailed in Section 4.2.1), a drilled Teflon plate with apertures having radii of 0.75 and 1 mm was immersed into saline (these samples are similar to the ones illustrated in Fig. 4.7). In the other configuration, PLA 3D-printed cylinders having radii of 0.75 and 1 mm were immersed into saline. It was not possible to fabricate inner materials with radius smaller than 0.75 mm due to the limited resolution of the drilling machine and the 3D printer. The four tissue-mimicking concentric samples described above are listed in Table 5.2. In addition, Table 5.2 reports Samples C5 and C6, which consist of concentric fat and muscle tissues. As is clear from Table 5.2, Samples C1, C2 and C5 have a high permittivity material as the inner material, with a low permittivity material as the outer material, while Samples C3, C4 and C6 have a low permittivity material as the inner material and a high permittivity material as the outer material.

In contrast to the tissue-mimicking samples, Samples C5 and C6 include different sized concentric regions of five porcine samples. Specifically, Sample

CHAPTER 5. MATERIAL DIELECTRIC CONTRIBUTION

Table 5.2: Summary of heterogeneous samples measured in linear configuration. The average relative permittivity values of the materials/tissues across the range 2-6 GHz are specified in brackets.

Samples	Inner Material	Outer Material
C1	0.75 mm radius saline ($\epsilon_r=74.00$)	Teflon ($\epsilon_r=2.15$)
C2	1 mm radius saline ($\epsilon_r=74.00$)	Teflon ($\epsilon_r=2.15$)
C3	0.75 mm radius PLA ($\epsilon_r=3.00$)	Saline ($\epsilon_r=74.00$)
C4	1 mm radius PLA ($\epsilon_r=3.00$)	Saline ($\epsilon_r=74.00$)
C5	0.5-0.9 mm radius porcine muscle ($\epsilon_r=42.10$)	Fat ($\epsilon_r=9.20$)
C6	0.5-0.9 mm radius porcine fat ($\epsilon_r=9.20$)	Muscle ($\epsilon_r=42.10$)

C5 includes concentrically heterogeneous tissue regions consisting of muscle as the inner tissue, with radii ranging from 0.5 mm to 0.9 mm, surrounded by fat. Conversely, Sample C6 includes concentrically heterogeneous tissue regions consisting of fat as the inner tissue, with radii ranging from 0.5 mm to 0.9 mm, surrounded by muscle. The inner and outer tissues of the concentrically heterogeneous regions were approximately homogeneous. Also, the radius of the inner tissue was always within the sensing radius. In Fig. 5.4, a concentrically heterogeneous region with muscle as the inner tissue and fat as the outer tissue is shown. In Fig. 5.4, the size of the probe diameter (2.2 mm) is also included to better illustrate the size of the inner region occupied by the small approximately homogeneous muscle tissue.

Dielectric measurements on concentrically heterogeneous samples were performed by positioning each inner material/tissue in contact with the inner part of the probe tip. In this way, the samples were heterogeneous in the radial axis but unvarying in the longitudinal axis. Uniform contact between the probe and the sample was ensured through close visual inspection. A photograph and diagram of the measurements conducted on tissue-mimicking samples are shown in Fig. 5.5. The photograph in Fig. 5.5 illustrates a measurement being conducted on Sample C3, composed of an inner material of 0.75 mm radius PLA and an outer liquid of saline. The diagram in Fig. 5.5 summarises the set of measurements performed on the concentrically heterogeneous tissue-mimicking samples. The inner material is indicated in blue and has a radius ranging from 0.25 mm to 1 mm, surrounded by the outer material that has a radius much larger than that of the probe.

Following the measurements, the dielectric properties measured from the concentric tissue-mimicking samples were quantitatively compared to those estimated based on the assumption that the dielectric contribution of a material is proportional to the volume occupied by that material within the sensing volume. Such quantitative comparison was not conducted for concentric biological samples due to the challenges of accurately measure the size of the inner tissue. In fact, for each tissue sample, the average

CHAPTER 5. MATERIAL DIELECTRIC CONTRIBUTION

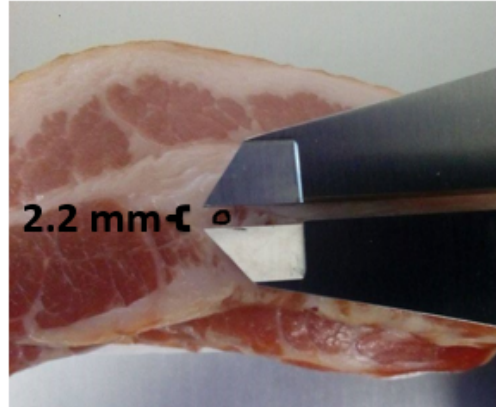


Figure 5.4: Example of measurement sample used to estimate the contribution of concentric tissues to the measured permittivity. The picture illustrates Sample C5, a concentrically heterogeneous porcine sample having muscle as the inner tissue and fat as the outer tissue. The size of the inner muscle tissue is highlighted in the picture with reference to the diameter of the slim form probe (2.2 mm).

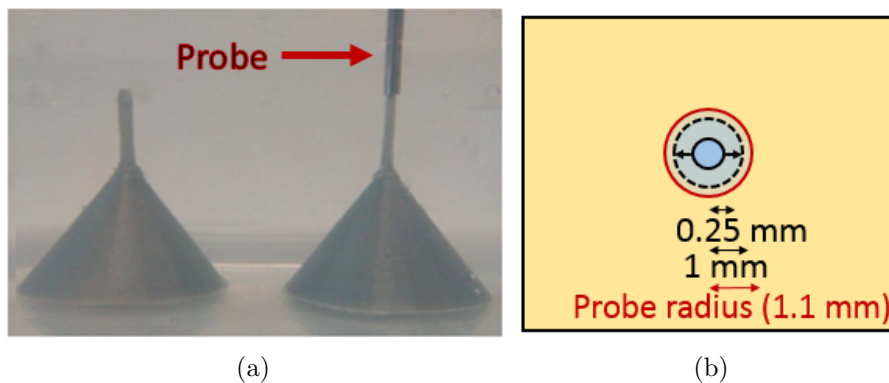


Figure 5.5: (a) Side view picture and (b) top view diagram of the measurement scenario used to evaluate how radial heterogeneities in concentric configuration impact the measured dielectric properties. In the photograph, the probe is positioned on Sample C3, consisting of the 0.75 mm radius PLA cylinder immersed in saline. In the diagram, the red bordered circle represents the probe and the two sample materials are represented with the colours yellow and blue. The inner material (in blue) has a radius ranging from 0.25 to 1 mm, and the outer material (in yellow) extends outside of this extent.

CHAPTER 5. MATERIAL DIELECTRIC CONTRIBUTION

permittivity values from the concentrically heterogeneous measurement regions were only qualitatively compared with the average permittivity values from homogeneous fat and muscle regions.

On the other hand, for each tissue-mimicking sample consisting of Teflon (or PLA) and saline, the material composition was calculated as a percentage (by volume occupied within the sensing volume) and associated with the corresponding dielectric data acquired by the probe. The percent volume occupied by the inner material of each tissue-mimicking sample was calculated based on the estimated sensing radius as follows:

$$\text{Inner material } [\%] = 100 \frac{\pi r_1^2}{\pi R^2}, \quad (5.1)$$

where r_1 is the radius of the inner material, and R is the sensing radius of the Keysight slim form probe reported in Section 4.3.2 for samples consisting of saline and Teflon (or PLA, since Teflon and PLA have approximately equivalent dielectric properties as shown in Table 5.2). Specifically, from the simulation results presented in Section 4.3.2, a sensing radius of 1.4 mm was found for the sample having saline as the inner material and Teflon as the outer material, while a sensing radius of 1.1 mm was found for the sample having Teflon as the inner material and saline as the outer material. Finally, the percent volume occupied by the outer material of each sample was calculated by subtracting the inner material percentage composition from the total percent composition of 100:

$$\text{Outer material } [\%] = 100 - \text{Inner material } [\%]. \quad (5.2)$$

Before showing the experimental results, the numerical methodology used to validate the outcome from dielectric measurements and then expand the dielectric contribution investigation is detailed.

5.2.2 Numerical validation and modelling

In this subsection, the design of the numerical simulations reproducing the two experimental scenarios involving side-by-side and concentric tissue-mimicking and biological tissues is presented, in order to confirm the experimental findings and to obtain more quantitative information on the dielectric contribution of each tissue within the sensing radius. Then, the design of the numerical simulations is presented. These simulations model the contribution of individual tissues to the acquired dielectric data, as a function of the dielectric properties and geometrical distribution of each tissue within the radially heterogeneous samples.

5.2.2.1 Numerical design and settings

Numerical simulations were performed by following the methodology described in Section 4.2.2. For the slim form probe model, the probe features reported in Table 4.6 were used. According to the measurement scenario that the simulation was based on, either a 2D or 3D simulation environment was selected. In particular, two probe models were used:

- The 2D axially symmetric probe model (developed for the estimation of the sensing radius of the Keysight slim form probe), which was used for modelling concentrically heterogeneous samples (i.e., axially symmetric samples);
- A 3D probe model, which was used for modelling samples composed of side-by-side materials (i.e., non-axially symmetric samples).

Next, different sample geometries were created based on the measurement samples. In particular, all of the concentrically heterogeneous samples reported in Table 5.2 were simulated in the 2D axially symmetric environment. Conversely, due to the number of side-by-side materials constituting the samples with linear heterogeneity configuration, among the samples listed in Table 5.1, only Samples L1 and L4 were simulated in the 3D environment.

For the 2D simulations, the geometry of the slim form probe and samples modelled for the sensing radius investigation (detailed in Section 4.2.2), were used. For clarity, the 2D probe and sample geometry is also illustrated in Fig. 5.6. While the same probe model was used across all concentric scenarios, the size of the simulated samples was modified to reproduce each experimental scenario (reported in Table 5.2). For instance, for Samples C1 and C3, the inner material was modelled as a cylinder having a radius of 0.75 mm, while for Samples C2 and C4, the inner material was modelled as a cylinder having a radius of 1 mm. Furthermore, due to the difficulty of numerically reproducing the tissue irregularities of Samples C5 and C6, the measurements on those samples were not replicated numerically in exactly the same way (as was done for Samples C1, C2, C3 and C4). Specifically, Samples C5 and C6 were modelled with a geometry such that both fat and muscle tissues occupy 50% of the sensing volume, in order to facilitate comparison with the results from the fat-muscle interface of the simulated Sample L2. In fact, with the probe positioned at the fat-muscle interface, the side-by-side simulated fat and muscle tissues both occupy 50% of the sensing radius. For the simulated Samples C5 and C6, in order to ensure that each tissue occupies 50% of the sensing radius, the radius of the inner tissue, and consequently the size of the outer tissue, were calculated. The inner tissue radius was obtained from knowledge of the sensing radius (estimated from the simulations in Chapter 4), through:

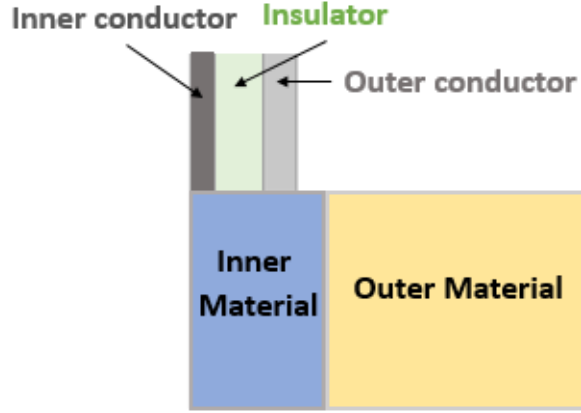


Figure 5.6: 2D axially symmetric model designed to evaluate the dielectric contribution of concentric materials to the acquired signal. Different values were used for the radius of the inner material and dielectric properties were assigned to the inner and outer materials of each simulated concentrically heterogeneous sample.

$$\frac{1}{2} \frac{\pi r_1^2}{\pi R^2} + \frac{1}{2} \frac{\pi (R - r_1)^2}{\pi R^2} = 1, \quad (5.3)$$

where r_1 and R were defined in Eq. (5.1). By solving Eq. (5.3), different values of inner tissue radius r_1 were obtained for the two samples, since two different values of sensing radius were found for the two samples consisting of the same tissue but with swapped locations in Section 4.3.2 (due to the fact that the permittivity of the inner material has a greater impact on the sensing radius). In fact, an r_1 of 0.71 mm was found for the sample having muscle as the inner tissue and fat as the outer tissue (since the sensing radius R found for such a sample in Section 4.3.2 is equal to 1 mm), while an r_1 of 0.64 mm was found for the sample having fat as the inner tissue and muscle as the outer tissue (since the sensing radius R found for such a sample in Section 4.3.2 is equal to 0.9 mm).

For the 3D simulations, the geometry of the slim form probe created for the 2D simulations was translated to the 3D environment, and the side-by-side materials from Samples L1 and L4 were modelled as two parallelepipeds adjacent to each other, with each size larger than the sensing volume (in order to allow for dielectric acquisition of an individual material without the influence of the adjacent material), as illustrated in Fig. 5.7. In the diagram of Fig. 5.7, the probe is positioned at the material interface, exactly in the middle of the sample, where both materials occupy 50% of the sensing volume. However, in the 3D simulations, different positions of the probe with distances between 0-10 mm from the interface (as for the experiments

CHAPTER 5. MATERIAL DIELECTRIC CONTRIBUTION

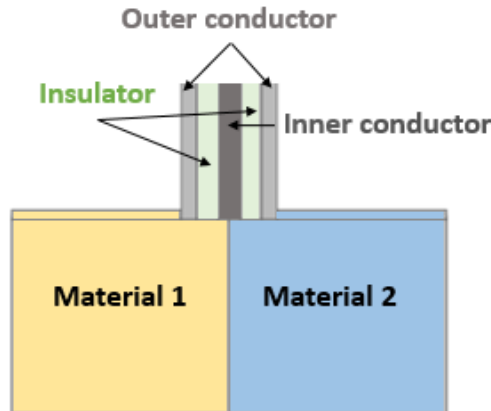


Figure 5.7: 3D simulation model designed to evaluate the dielectric contribution of side-by-side materials from the simulated Samples L1 and L4. In the diagram, the probe is positioned at the material interface (exactly in the middle of the sample). However, for each sample, different probe positions with distances between 0-10 mm from the interface were considered in order to estimate the radial distance at which only the dielectric properties of one material are detected (i.e., the radial distance at which the effect of the other material ceases).

presented in the previous subsection) were considered in order to estimate the radial distance at which only the dielectric properties of one material are detected (i.e., the radial distance at which the effect of the other material ceases).

After creating the probe and sample geometry, the dielectric properties of the two materials constituting each simulated sample were obtained by fitting one-pole or two-pole Debye/Cole-Cole models to the average measured data. Thus, the dielectric properties obtained from the measured data fitting were assigned to the materials of each simulation model. Either Debye or Cole-Cole models were selected based on the quality of the fit. Specifically, for Teflon and saline, the Cole-Cole parameters reported in Section 4.2.2 were used in the numerical simulations of concentric tissue-mimicking samples. In addition, the Debye parameters obtained for Phantom A, Phantom B, and the porcine muscle and fat tissues are reported in Table 5.3.

For both 2D and 3D models, the coaxial source and absorbing boundary settings presented in Section 4.2.2 were used. Furthermore, for the 2D environment, the mesh and solver settings as presented in Section 4.2.2 were used. For the 3D environment, a mesh with the minimum and maximum element sizes of 0.1 mm and 0.3 mm, respectively, was created and the iterative biconjugate gradient stabilised method (BICGSTAB) was used to solve the simulations [195]. The 3D simulations used a coarser mesh and a

CHAPTER 5. MATERIAL DIELECTRIC CONTRIBUTION

Table 5.3: Debye parameters to simulate radially heterogeneous samples, each consisting of two of the following materials: Phantom A, Phantom B, porcine muscle and fat.

Parameters	Phantom A	Phantom B	Muscle	Fat
ϵ_∞	7.03	39.17	9.99	5.14
ϵ_{s1}	8.56	55.22	51.04	6.87
τ_1 [s]	4.78e-9	6.44e-11	3.06e-10	9.22e-11
ϵ_{s2}	NA	NA	32.58	7.25
τ_2 [s]	NA	NA	8.87e-12	9.27e-12
σ_s [S/m]	0.01	0.99	0.99	0.40

different solver (BICGSTAB) compared to the 2D simulations, due to the higher complexity of the 3D environment and the limits of the computational memory. Although the mesh element sizes and the solvers differed between the 2D and 3D simulations, results obtained from the same scenarios run in both environments were compared and the results were confirmed to be consistent.

After the simulations were solved, the complex S_{11} parameters obtained from simulated samples were converted into complex permittivity values, using the open-ended coaxial probe antenna model [101], as specified in Section 4.2.2.

The experimental and numerical procedure followed for the estimation of the material/tissue contribution within radially heterogeneous samples (consisting of two side-by-side or concentric materials/tissues) is schematised in Fig. 5.8.

Besides the simulations performed to validate the experimental outcome, further simulations (the details of which are provided in the following subsection), were conducted for the two types of radially heterogeneous samples, in order to model, for each sample, the dielectric contribution of each tissue occupying the sensing radius.

5.2.2.2 Modelling the dielectric contribution of individual tissues occupying the sensing radius

Simulations involving further side-by-side and concentric biological tissues are detailed in this subsection. Such simulations were conducted in order to model individual tissue dielectric contribution and facilitate prediction of the acquired dielectric data from *a priori* information of the structure of the interrogated sample and the dielectric properties of the constituent tissues.

In order to model the dielectric contribution of two side-by-side tissues occupying the sensing radius, a 3D geometry like the one presented in the previous subsection (and illustrated in Fig. 5.7) was used. As such, the samples were modelled as two parallelepipeds, with each size larger than the

CHAPTER 5. MATERIAL DIELECTRIC CONTRIBUTION

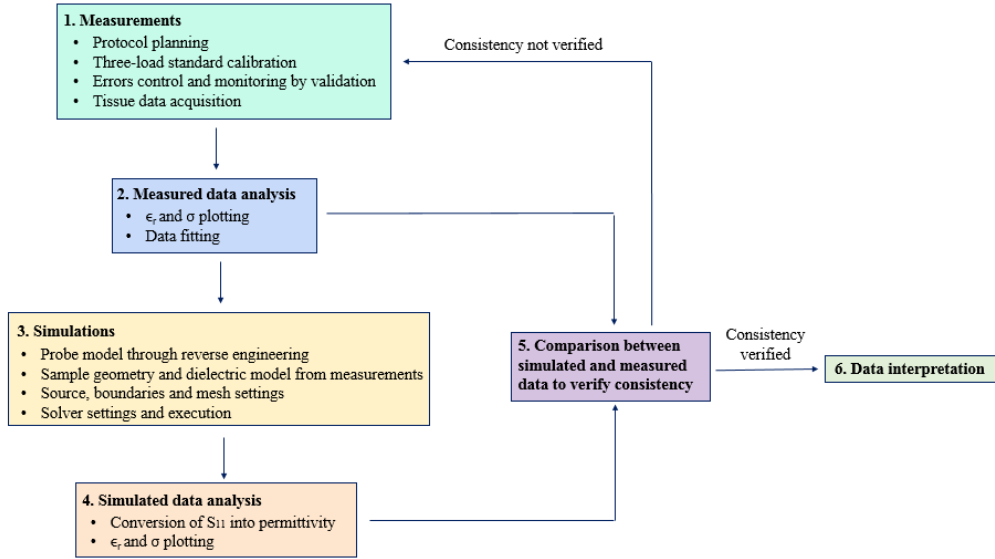


Figure 5.8: Flowchart summarising the experimental and numerical steps taken to estimate the material/tissue contribution within radially heterogeneous samples (consisting of two side-by-side or concentric materials/tissues). In case of mismatch between simulated and measured data, the measurements were repeated by monitoring all the confounders and by minimising the sources of error.

sensing volume, adjacent to each other. Next, simulations were conducted for different probe positions by moving the probe from Tissue 1 (on the left) to Tissue 2 (on the right) in discrete steps of 0.2 mm, in proximity of the tissue interface. By considering the distances from the centre of the probe to the tissue interface as negative when the probe was primarily in contact with Tissue 1 and the distances from the centre of the probe to the tissue interface as positive when the probe was primarily in contact with Tissue 2 (as with the experiments detailed in 5.2.1), numerical simulations were conducted at the following distances from the interface: -1.1 mm, -0.8 mm, -0.6 mm, -0.4 mm, -0.2 mm, 0 mm, 0.2 mm, 0.4 mm, 0.6 mm, 0.8 mm, 1.1 mm. The distance “0 mm” refers to the scenario when the probe is positioned at the tissue interface (where both tissues occupy 50% of the sensing radius). In addition, at the distance of -1.1 mm, the probe was solely in contact with Tissue 1, and, at the distance of 1.1 mm, the probe was solely in contact with Tissue 2. The maximum distance of 1.1 mm was selected, given that the sensing radius of the slim form probe does not exceed this value for the subset of tissues listed in Table 5.4 (as observed in Section 4.3.1).

On the other hand, in order to model the dielectric contribution of two concentric tissues occupying the sensing radius, a 2D geometry like the one

CHAPTER 5. MATERIAL DIELECTRIC CONTRIBUTION

presented in the previous subsection (and illustrated in Fig. 5.6) was used. Specifically, the concentric samples were modelled as a cylindrical inner tissue with variable radius ranging from 0.1 mm to 2.5 mm (that is larger than the maximum extent of the sensing radius observed in Section 4.3.1), surrounded by a concentric outer tissue that extends to a radius beyond that of the sensing radius.

For both types of radially heterogeneous samples, four different biological tissues were combined in six simulated samples, as listed in Table 5.4. Various tissue combinations were examined in order to span different permittivity magnitudes and contrasts in relative permittivity, ranging from 3:2 to 4:1. The tissue dielectric properties assigned to the simulation samples were obtained from the IT'IS database [190].

Once the simulation data was generated, the weight of each tissue contribution to the total acquired dielectric signal was calculated as in the study by Porter *et al.* [64]. Thus, considering that the measured dielectric data, for a fixed sample composition, is a combination of the dielectric properties of Tissue 1 and Tissue 2, the measured relative permittivity $\epsilon_{r,meas}$ can be expressed as follows:

$$\epsilon_{r,meas} = w_{m,T1} \epsilon_{r1} + w_{m,T2} \epsilon_{r2}, \quad (5.4)$$

where ϵ_{r1} is the relative permittivity of Tissue 1, ϵ_{r2} is the relative permittivity of Tissue 2, $w_{m,T1}$ is the dielectric weight of Tissue 1, and $w_{m,T2}$ is the weight of the properties of Tissue 2. In the case of samples in concentric configuration, Tissue 1 is the outer tissue and Tissue 2 is the inner tissue. Since the samples consist of only two tissues, the sum of the two dielectric contributions matches the total contribution; thus:

$$w_{m,T1} + w_{m,T2} = 1. \quad (5.5)$$

Combining equations Eq. (5.4) and Eq. (5.5), the weights can be calculated as follows:

$$w_{m,T1} = \frac{\epsilon_{r,meas} - \epsilon_{r2}}{\epsilon_{r1} - \epsilon_{r2}}, \quad (5.6)$$

$$w_{m,T2} = \frac{\epsilon_{r1} - \epsilon_{r,meas}}{\epsilon_{r1} - \epsilon_{r2}}. \quad (5.7)$$

When Tissue 1 (or the outer tissue) occupies the total sensing volume, Tissue 2 does not impact the measured dielectric data, then $w_{m,T2} = 0$, and $\epsilon_{r,meas} = \epsilon_{r1}$. Similarly, when the probe is only in contact with Tissue 2 (or the inner tissue), then $w_{m,T1} = 0$, and $\epsilon_{r,meas} = \epsilon_{r2}$.

CHAPTER 5. MATERIAL DIELECTRIC CONTRIBUTION

Table 5.4: Summary of simulated samples in linear and concentric heterogeneity configurations. The average relative permittivity values of the tissues across the range 2-6 GHz are specified in brackets.

Samples	Tissue 1/Outer Tissue	Tissue 2/Inner Tissue
S1	Muscle ($\epsilon_r=42.10$)	Fat ($\epsilon_r=9.20$)
S2	Fat ($\epsilon_r=9.20$)	Muscle ($\epsilon_r=42.10$)
S3	Bone ($\epsilon_r=17.00$)	Fat ($\epsilon_r=9.20$)
S4	Fat ($\epsilon_r=9.20$)	Bone ($\epsilon_r=17.00$)
S5	Blood ($\epsilon_r=55.60$)	Muscle ($\epsilon_r=42.10$)
S6	Muscle ($\epsilon_r=42.10$)	Blood ($\epsilon_r=55.60$)

Then, the calculated weights of the dielectric contribution of tissues were modelled using the generalised logistic function (also known as Richards curve [196]). The models for the weights of the two tissues constituting the radially heterogeneous sample were obtained with the following equations:

$$w_{m,T2} = \frac{1}{(a + be^{-cr})^{\frac{1}{d}}}, \quad (5.8)$$

$$w_{m,T1} = 1 - \frac{1}{(a + be^{-cr})^{\frac{1}{d}}}, \quad (5.9)$$

where r is the radial distance from the centre of the probe to the tissue interface for samples in linear configuration (or the radius of the inner tissue for samples in concentric configuration), and a , b , c and d are the four parameters of Richards curve.

The models above support prediction of the permittivity of a sample with radial heterogeneities based on knowledge of the structure and dielectric properties of the constituent tissues. In the following section, the developed models are presented, after discussing the results from the dielectric experiments and the corresponding numerical simulations.

5.3 Results and Discussion

This section examines the dielectric properties from the measurement and simulation scenarios described in Section 5.2 and reports the results in three subsections as follows. In the first subsection, the dielectric contribution of tissue-mimicking materials and biological tissues within radially heterogeneous structures in the linear configuration is examined from the acquired experimental and numerical data. In the second subsection, the same analysis was conducted for concentrically heterogeneous tissue-mimicking and biological samples. Lastly, in the third subsection, the numerical data obtained from simulations reproducing the interaction of the measurement probe with

biological tissues presenting the two types of radial heterogeneities, linear and concentric, are examined and modelled. The resulting models support prediction of the dielectric contribution of individual tissues from knowledge of the acquired dielectric signal and the interrogated sample structure.

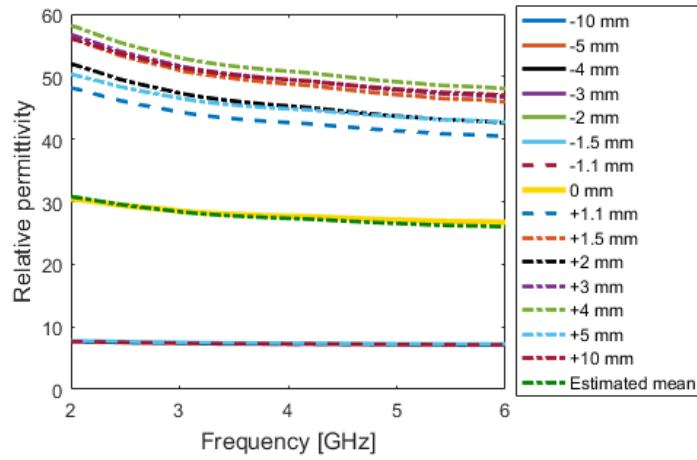
5.3.1 Dielectric contribution of materials in linear heterogeneity configuration

In Fig. 5.9, experimental and numerical results from Sample L1 (shown in Fig. 5.2), composed of Phantom A (Material 1, on the left side) and Phantom B (Material 2, on the right side), are illustrated over the range of 2-6 GHz. In particular, the numerical results illustrated in Fig. 5.9b were obtained from the 3D simulations that accurately reproduced the set of measurements conducted on Sample L1 and illustrated in Fig. 5.9a. Fig. 5.9 reports only the relative permittivity data obtained from the measurements and simulations, since Phantom A and Phantom B present conductivity values that follow a trend different from that of the conductivity of biological tissues [197]. However, both relative permittivity and conductivity values are then illustrated for the biological sample L4 in Fig. 5.10.

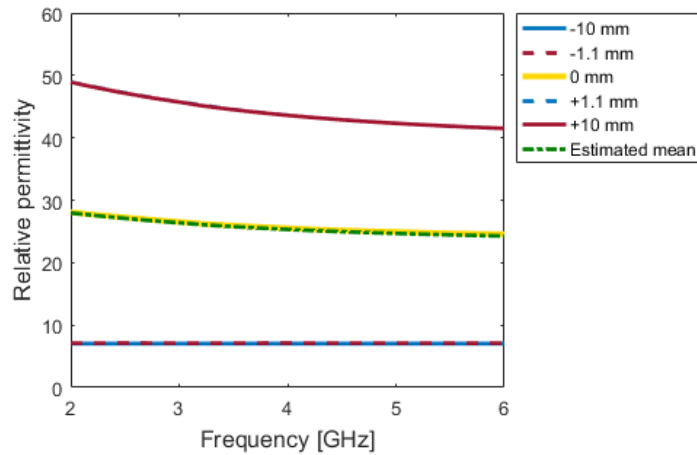
The values reported in the legend of each plot of Fig. 5.9 refer to the distances between the centre of the probe and the interface. As mentioned previously in Section 5.2.1, the distances are negative if the probe is positioned on the left material (Phantom A), and positive if the probe is positioned on the right material (Phantom B). Specifically, Fig. 5.9a illustrates the traces from the measurements taken on Phantom A at decreasing distances from the interface, the average trace from the three measurements taken at the interface, and the traces taken on Phantom B at increasing distances from the interface. On the other hand, besides the data from the simulation at the interface, Fig. 5.9b illustrates only the traces from the simulations performed on Phantom A and Phantom B at the distances of 1.1 mm and 10 mm. Specifically, the simulation data obtained at the intermediate distances between 1.1 mm and 10 mm are not illustrated in Fig. 5.9b, since such data overlaps with the plotted data from the distances of 1.1 mm and 10 mm, and thus does not provide additional information.

In both plots of Fig. 5.9, the measurements taken at the distances of -1.1 mm and +1.1 mm from Phantom A and Phantom B, respectively, are shown with dashed lines. These traces are highlighted since they correspond to measurements conducted with one side of the probe adjacent to the interface (since the total radius of the probe is equal to 1.1 mm). As is clear from both measurement and simulation plots of Fig. 5.9, at 1.1 mm

CHAPTER 5. MATERIAL DIELECTRIC CONTRIBUTION



(a)



(b)

Figure 5.9: Relative permittivity traces from (a) measurements and (b) simulations performed over the range of 2-6 GHz on Sample L1, composed of a linear configuration of Phantom A (left material) and Phantom B (right material). Both measurements and simulations were performed with the probe positioned over small increments in distance from the low permittivity (Phantom A) to the high permittivity phantom (Phantom B). The distances, reported in the legend, are negative if the probe is positioned on the left material (Phantom A), and positive if the probe is positioned on the right material (Phantom B). The traces from acquisitions performed at distances ± 1.1 mm between the probe centre and the interface are dashed. The thick yellow solid trace is from the measurement/simulation performed with the probe centre lined up with the phantom interface, and is overlapped by the relative permittivity trace obtained by averaging the relative permittivity values of Phantom A and Phantom B (indicated with a green dash-dotted line). While in (a) all the measurement traces are reported, in (b), the simulation data obtained at the intermediate distances between 1.1 mm and 10 mm are not illustrated, since this data overlaps with the 1.1 mm and 10 mm distance data, and thus does not provide additional information.

CHAPTER 5. MATERIAL DIELECTRIC CONTRIBUTION

the data is comparable with the data from larger distances, i.e., when the probe is further from the interface. Specifically, in Fig. 5.9b, the 1.1 mm distance data perfectly overlaps with the 10 mm data, and in Fig. 5.9a, the 1.1 mm data is within the measurement uncertainty of the phantoms. The uncertainty of Phantom B is higher than the uncertainty of Phantom A due to poor measurement repeatability, which can be attributed to the challenging fabrication procedure of high permittivity rubber-based phantoms. In fact, high permittivity phantoms require a large amount of carbon black and graphite that increase the viscosity of the compound making it hard to mix uniformly [194], [197]. Despite this, both the plots of Fig. 5.9 confirm that the sensing radius of the slim form probe is less than 1.5 mm, as estimated in Section 4.3.2.

Furthermore, in both measurement and simulation plots of Fig. 5.9, the relative permittivity data averaged across the interface measurements is illustrated with a thick yellow line. The average interface data is also compared to the estimated data (illustrated with a green dash-dotted line in both plots of Fig. 5.9), which is obtained by considering that the dielectric contribution of an individual material is proportional to the volume occupied within the sensing volume. Since, at the interface, both materials occupy 50% of the sensing volume, the estimated data is half way between the Phantom A and Phantom B traces. In both plots of Fig. 5.9, the relative permittivity data from interface acquisitions overlaps with the estimated relative permittivity data, thus confirming that Phantom A and Phantom B contribute equally to the dielectric data acquired at the interface. Specifically, in Fig. 5.9a, the difference between the measured and the estimated relative permittivity data at the interface is approximately 5%, which is within the standard deviation of the phantom measurements.

The results from the sets of experiments reported in Fig. 5.9 not only confirm the outcome of the sensing radius investigation presented in Section 4.3 (i.e., the sensing radius of the Keysight slim form probe is within 1.1 mm), but are also consistent with the experimental outcome in the study by Hagl *et al.* [65]. In fact, in the study by Hagl *et al.* [65], it was found that no error was introduced in the measurement when the probe was located at the edge of a region of homogeneous material (i.e., distance from probe centre to homogeneous material edge = 1.1 mm), indicating that the probe was not detecting the presence of the materials beyond the radius of the probe outer conductor. Furthermore, from the experiments illustrated in Fig. 5.9, it was also found that two side-by-side materials provide equal dielectric contribution to the acquired signal. These findings have been found across all of the heterogeneous samples in linear configuration, regardless of the permittivity contrast of the materials. As a demonstration, the results from

CHAPTER 5. MATERIAL DIELECTRIC CONTRIBUTION

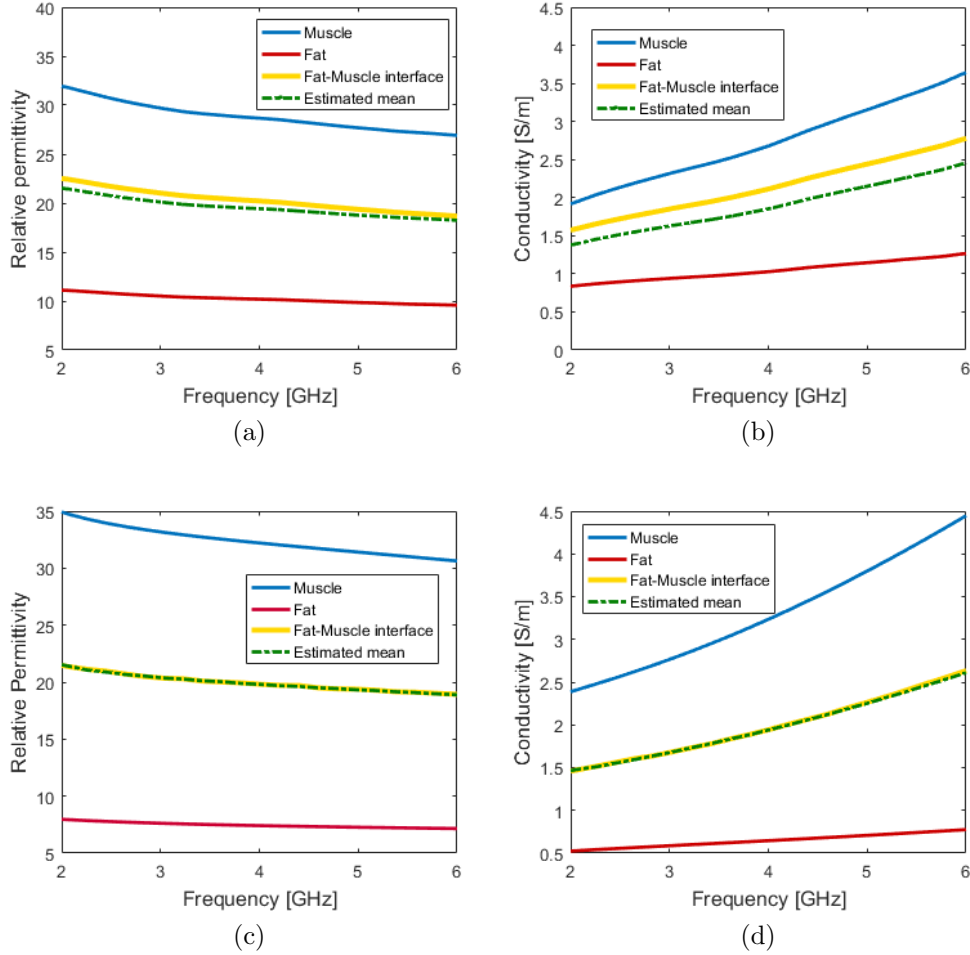


Figure 5.10: Relative permittivity and conductivity plots from the measurements (a-b) and simulations (c-d) performed on Sample L4. In all plots, the average data from muscle is reported with a blue solid line, the average data from fat with a red solid line, and the average data from the fat-muscle interface with a thick yellow line. Furthermore, across all the plots, the data acquired at the interface is compared with the data estimated by averaging the fat and muscle data (indicated with a green dash-dotted line). The permittivity values from the fat-muscle interface are halfway between the permittivity values of fat and muscle tissues and within 10% of the permittivity values calculated by averaging the fat and muscle permittivity.

the measurements and simulations performed on porcine tissue (Sample L4) are reported in Fig. 5.10.

In Fig. 5.10, measurements and simulation results from only three sites of Sample L4 (illustrated in Fig. 5.3) are reported due to the impossibility of performing measurements at controlled distances from the fat-muscle

interface of highly heterogeneous porcine samples, as mentioned in Section 5.2.1. Analysing both simulated and measured relative permittivity and conductivity data from side-by-side fat and muscle tissues across all plots of Fig. 5.10, it can be observed that the fat and muscle tissues contribute equally to the dielectric data acquired at the fat-muscle interface.

This experimental outcome is clear from the comparison between the average permittivity values from the fat-muscle tissue interface acquisitions and the estimated permittivity obtained by averaging the permittivity values from the acquired fat and muscle tissues. In Fig. 5.10c and Fig. 5.10d, the relative permittivity and conductivity acquired at the fat-muscle interface overlap perfectly with the estimated relative permittivity and conductivity. Conversely, in Fig. 5.10a and Fig. 5.10b, a small difference is found between measured and estimated values. Specifically, Fig. 5.10a shows that the difference between the mean measured relative permittivity at the fat-muscle tissue interface and the estimated relative permittivity is less than 5%. Similarly, Fig. 5.10b shows that the difference between the mean measured conductivity at the fat-muscle tissue interface and the estimated conductivity is less than 10%. However, such differences in relative permittivity and conductivity are within the measurement uncertainty of porcine samples.

Thus, from both measurements and simulations, it was observed that side-by-side tissue mimicking materials and biological tissues contribute equally to the acquired permittivity, regardless of material/tissue properties or contrast.

In order to verify how the dielectric tissue contribution depends on the spatial distribution of the tissues occupying the sensing volume, the results from concentric material compositions are reported in the following subsection.

5.3.2 Dielectric contribution of materials in concentric heterogeneity configuration

In this subsection, the data obtained from the dielectric measurements performed on concentrically heterogeneous samples is examined and discussed. While for heterogeneous samples in linear configuration the measured dielectric properties were consistent across all the samples (regardless of the permittivity contrast of the materials), from the measurements performed on concentric samples, it was observed that the measured dielectric properties changed based on the dielectric properties of the constituent materials within the sensing radius.

In order to examine how materials within the same sample structure have

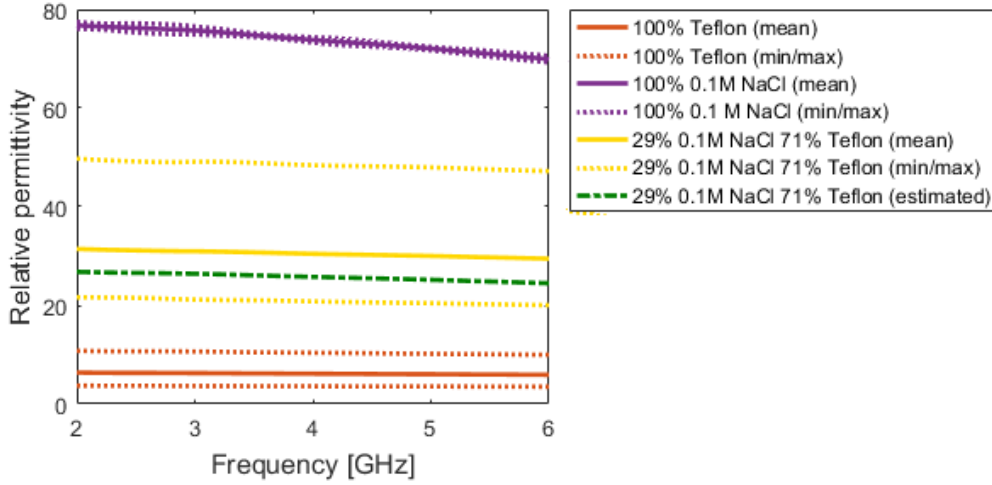


Figure 5.11: Plot of the relative permittivity mean, minimum and maximum values calculated across three measurements, each on 100% Teflon, 100% saline, and the concentrically heterogeneous sample consisting of 29% saline and 71% Teflon (Sample C1). The relative permittivity from Sample C1 is between that of Teflon and saline and overlaps with the permittivity estimated based on the material composition within the sensing radius.

a varying impact on the acquired dielectric signal based on the dielectric properties of the constituent materials, Fig. 5.11 and Fig. 5.12 report the results from the concentric samples C1 and C3, respectively. The results are reported only in terms of relative permittivity, since the same trend was found for conductivity. Both Samples C1 and C3 are composed of a 0.75 mm radius inner material. Although Samples C1 and C3 have the same structure, the inner material of Sample C1 occupies 29% of the sensing volume, while the inner material of Sample C3 occupies the 46% of the sensing volume. Such differences are due to the fact that the volume occupied by the inner material was calculated according to Eq. (5.1) based on the sensing radius values found in Section 4.3.1. In fact, in Section 4.3.1, for a concentric sample with saline as the inner material and Teflon as the outer material, such as Sample C1 (similar to the sample illustrated in Fig. 4.7), a sensing radius of 1.4 mm was found, while, for a concentric sample with Teflon (that has a permittivity approximately equivalent to that of PLA) as the inner material and saline as the outer material, such as Sample C3 (illustrated in Fig. 5.5), a sensing radius of 1.1 mm was found.

In particular, in Fig. 5.11 and Fig. 5.12, the measured relative permittivity is compared to that estimated based on the material composition within the sensing radius (which is 1.4 mm for C1 and 1.1 mm for C3). In each plot,

CHAPTER 5. MATERIAL DIELECTRIC CONTRIBUTION

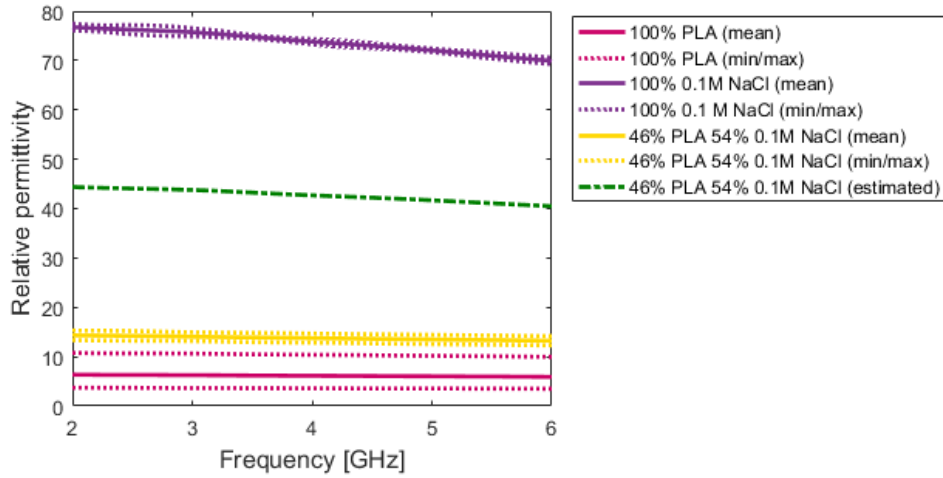


Figure 5.12: Plot of the relative permittivity mean, minimum and maximum values calculated across three measurements, each on 100% Teflon, 100% saline, and the concentrically heterogeneous sample consisting of 46% PLA and 54% saline (Sample C3). The relative permittivity from Sample C3 is close to that of PLA but 63% different from the relative permittivity estimated based on the material composition within the sensing radius.

the relative permittivity of the two individual materials constituting the concentric sample is also reported. In both Fig. 5.11 and Fig. 5.12, the average results from three different measurements (each after a different calibration) are summarised. Specifically, the mean, minimum, and maximum values are calculated across the three measurements. The measurements of PLA and Teflon (immersed in saline) have high variation and their average relative permittivity is higher than expected due to the difficulty of establishing a good contact between the probe and rigid materials. Also, the high variation in the measurements performed on Sample C1 (having 0.75 mm radius saline as the inner material and, thus, composed of 29% saline and 71% Teflon) is also due to the challenge of positioning the probe centre exactly in the centre of the Teflon aperture. In fact, during the measurement, we could not ensure that the Teflon aperture was perfectly equidistant from the probe sides.

However, in Fig. 5.11, the mean relative permittivity values obtained across the measurements on Sample C1 (yellow solid trace) overlap with the estimated relative permittivity values (green dash-dotted trace). On the other hand, in Fig. 5.12, the mean relative permittivity values obtained across the measurements on Sample C3 (yellow solid trace) are 63% different from the estimated relative permittivity values (green dash-dotted trace)

CHAPTER 5. MATERIAL DIELECTRIC CONTRIBUTION

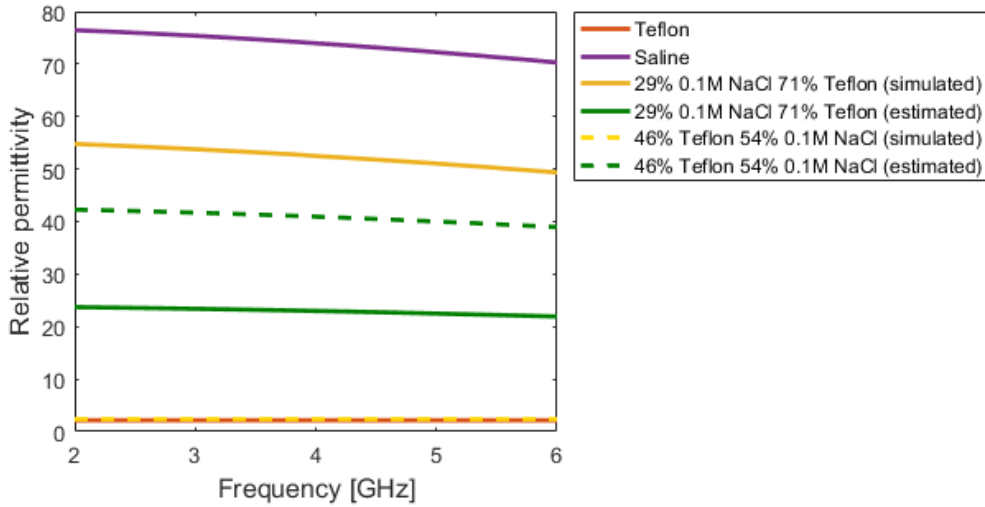


Figure 5.13: Plot of the relative permittivity values obtained from simulations performed with the following samples: 100% Teflon, 100% saline, 29% saline 71% Teflon (Sample C1), 46% Teflon 54% saline (Sample C3, with Teflon replacing PLA). The relative permittivity traces from Samples C1 and C3 (plotted with yellow solid and dashed lines, respectively) are compared with the relative permittivity traces estimated based on the material composition within the sensing radius of Sample C1 and C3 (plotted with green solid and dashed lines, respectively). While, for Sample C1, the estimated relative permittivity trace is about 40% different from the simulated relative permittivity, for Sample C3, the estimated relative permittivity trace is about 50% different from the simulated relative permittivity, which is approximately equal to the relative permittivity of Teflon.

and are very close to PLA relative permittivity values. Thus, while the dielectric properties of Sample C1 seem proportional to each individual material contribution, the dielectric properties of Sample C3 are dominantly impacted by the permittivity of the inner material. Even though Sample C1 and Sample C3 both have the same structure, the inner material of Sample C3 has significantly more impact on the measured dielectric properties than the inner material of Sample C1.

These results obtained for Samples C1 and C3 were validated through numerical simulations, and the results are summarised in Fig. 5.13. The simulations regarding Samples C1 and C3 were executed in the 2D axially-symmetric environment (as illustrated in Fig. 5.6) and reproduce accurately the dielectric measurements reported in Fig. 5.11 and Fig. 5.12, with the only difference being that PLA in C3 was replaced with Teflon (which has a permittivity very close to that of PLA). In this way, both simulated Samples C1 and C3 are composed of the same materials, Teflon and saline, but inversely arranged.

CHAPTER 5. MATERIAL DIELECTRIC CONTRIBUTION

As is clear from Fig. 5.13, the relative permittivity from the simulated sample with saline as the inner material (yellow solid line) is approximately 40% different from the relative permittivity estimated based on the material composition within the sensing radius (green solid line). On the other hand, the relative permittivity from the simulated sample with Teflon as the inner material (yellow dashed line) is almost equivalent to that of Teflon alone, and approximately 96% different from the relative permittivity estimated based on the material composition within the sensing radius (green dashed line).

Thus, this set of simulations confirms that the relative permittivity acquired from a concentric sample is not proportional to the percent volume occupied by the constituent materials. Specifically, the acquired dielectric signal is primarily dependent on the dielectric properties of the inner material, which has a much higher dielectric impact on the acquired signal than the outer material, particularly when the relative permittivity of the inner material is lower. This numerical outcome matches the experimental outcome, although the simulated relative permittivity of the 29% saline and 71% Teflon sample (plotted with a yellow solid line in Fig. 5.13) is approximately 25% different from the measured mean permittivity (plotted with a yellow solid line in Fig. 5.11). This relative permittivity difference between measurements and simulations can be attributed to the measurement challenge of positioning the probe centre exactly in the centre of the Teflon aperture.

Overall, the simulation results summarised in Fig. 5.13 are consistent with the experimental findings. Furthermore, the findings obtained from the measurements and simulations involving Samples C1 and C3 are consistent with the outcome of the sensing radius investigation reported in Section 4.3 and with the findings from the literature [181]. In fact, as observed by Anderson *et al.* [181] and confirmed in Section 4.3.1, the electric field intensity is higher in proximity of the inner conductor of the probe.

In addition, this outcome was confirmed by the measurements on Samples C2, C4, C5 and C6. Measurements performed on Samples C5 and C6 (an example of Sample C5 was provided in Fig. 5.4), permittivity data close to that of the inner tissue was obtained. To this extent, Fig. 5.14 reports the average relative permittivity measured from fat tissue, muscle tissue, and the two concentrically heterogeneous samples, Samples C5 with muscle as the inner tissue and fat as the outer tissue (indicated with a violet dashed line in Fig. 5.14) and Samples C6 with fat as the inner tissue and muscle as the outer tissue (indicated with a yellow dashed line in Fig. 5.14). In Fig. 5.14, it can be observed that the permittivity values obtained from Samples C5 are within 15% of the permittivity values obtained from muscle

CHAPTER 5. MATERIAL DIELECTRIC CONTRIBUTION

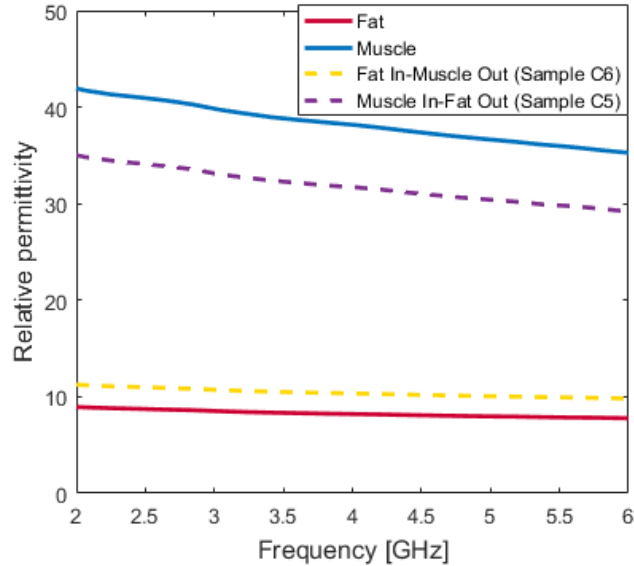


Figure 5.14: Average relative permittivity calculated across five measurements on muscle, fat, Samples C5, which consist of inner muscle tissue having radii ranging from 0.5 to 0.9 mm surrounded by fat tissue (indicated with a violet dashed line), and Samples C6, which consist of inner fat tissue having radii ranging from 0.5 to 0.9 mm surrounded by muscle tissue (indicated with a yellow dashed line). The permittivity values obtained from Samples C5 are within 15% of the permittivity values obtained from muscle tissue. On the other hand, the permittivity values obtained from Samples C6 are within 10% of the permittivity values obtained from fat tissue.

tissue. On the other hand, the permittivity values obtained from Samples C6 are within 10% of the permittivity values obtained from fat tissue. This comparison confirms that the inner tissue again has a dominant impact on the measured dielectric data.

Furthermore, for a more quantitative investigation, in Fig. 5.15, the simulation results from the two concentric samples consisting of 50% fat and 50% muscle described in Section 5.2.2 were compared with the simulation results from homogeneous fat and muscle samples. Fig. 5.15 reports the results from simulations with homogeneous fat, homogeneous muscle, a concentric sample consisting of 50% muscle and 50% fat, with muscle as the inner tissue and fat as the outer tissue (indicated with an orange dashed line), and a concentric sample consisting of 50% muscle and 50% fat, with fat as the inner tissue and muscle as the outer tissue (indicated with a light blue dashed line). The results are reported only in terms of relative permittivity, since the same trend was found for the S_{11} parameters and the conductivity.

CHAPTER 5. MATERIAL DIELECTRIC CONTRIBUTION

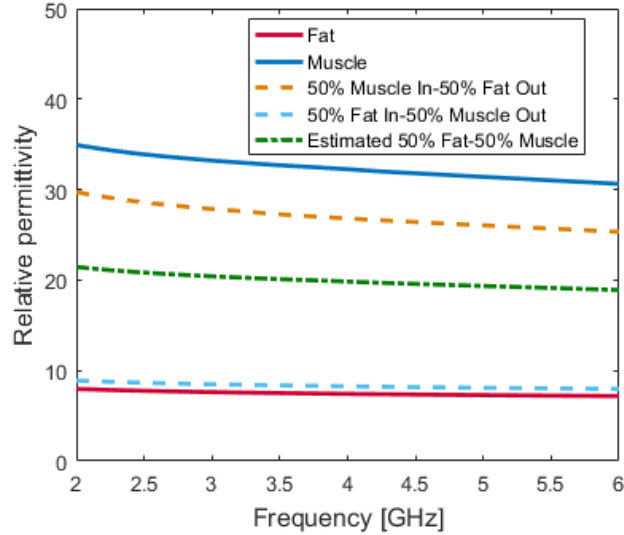


Figure 5.15: Relative permittivity obtained from 2D simulations of muscle, fat, and two 50% muscle and 50% fat tissue concentric samples, one with muscle as the inner tissue and fat as the outer tissue (indicated with an orange dashed line), and the other one with fat as the inner tissue and muscle as the outer tissue (indicated with a light blue dashed line). The relative permittivity from the simulated 50% fat and 50% muscle tissue concentric samples are significantly different from the relative permittivity values obtained by averaging the simulated fat and muscle permittivity.

As is clear in Fig. 5.15, the relative permittivity from the simulated 50% fat and 50% muscle tissue concentric samples are significantly different from the relative permittivity values obtained by averaging the simulated fat and muscle permittivity. Specifically, an average relative permittivity difference of 33% was found between the estimated relative permittivity and the acquired relative permittivity from the sample composed of 50% muscle and 50% fat, with muscle as the inner tissue and fat as the outer tissue. Furthermore, an average permittivity difference of 55% was found between the estimated relative permittivity and the relative permittivity from the sample composed of 50% muscle and 50% fat, with fat as the inner tissue and muscle as the outer tissue. These relative permittivity differences further confirm that the inner tissue has a higher impact than the outer tissue on the acquired permittivity, especially if the inner tissue has lower permittivity. Notably, the results for these concentric samples are substantially different from those obtained in the previous subsection with samples consisting of side-by-side 50% fat and 50% muscle tissues (and shown in Fig. 5.10), in which fat and muscle tissues contribute equally to the acquired permittivity.

To summarise, both the measurement and simulation results confirmed that in concentric heterogeneous samples the inner tissue has a larger impact on the acquired permittivity. Furthermore, the simulations demonstrated that the dielectric contribution of a tissue to the total permittivity is not only dependent on the spatial distribution of that tissue within the sensing volume, but also on the dielectric properties of the tissues.

While the findings presented in this subsection may seem obvious from an EM perspective [181], studies in the literature have regularly assumed equal dielectric contribution from all tissues within the sensing volume, when associating the acquired dielectric signal to the tissue composition of the interrogated sample [10]–[12], [15]. Therefore, this set of experiments demonstrate that the assumption of tissue dielectric contribution being proportional to the volume occupied by the tissue could be a significant source of error in the interpretation of dielectric data from heterogeneous biological samples.

5.3.3 Modelling of the individual tissue dielectric contribution within radially heterogeneous samples

In this subsection, the dielectric contribution of side-by-side and concentric samples is modelled for a subset of tissues, and then reported in terms of relative permittivity, as discussed at the end of Section 5.2.2.

Firstly, the data modelling the dielectric contribution of side-by-side tissues is reported. Then, the models regarding the dielectric contribution of concentric tissues are discussed.

5.3.3.1 Modelling of the dielectric contribution of tissues in linear heterogeneity configuration

The dielectric traces obtained from the simulations (described at the end of Section 5.2.2) performed on Sample S2 in linear configuration are illustrated in Fig. 5.16. In the legend of Fig. 5.16, the distances of the probe from the tissue interface are reported by considering the distances as negative when the probe was mostly in contact with the left tissue (fat), and positive when the probe was mostly in contact with the right tissue (muscle). As is clear from Fig. 5.16, as the probe location from the tissue interface becomes closer to +1.1 mm, the traces tend to the one of muscle. Furthermore, since, the traces reported in Fig. 5.16 are symmetric with respect to the trace of the fat-muscle interface, this trend indicates that the two tissues have equal contribution to the dielectric signal.

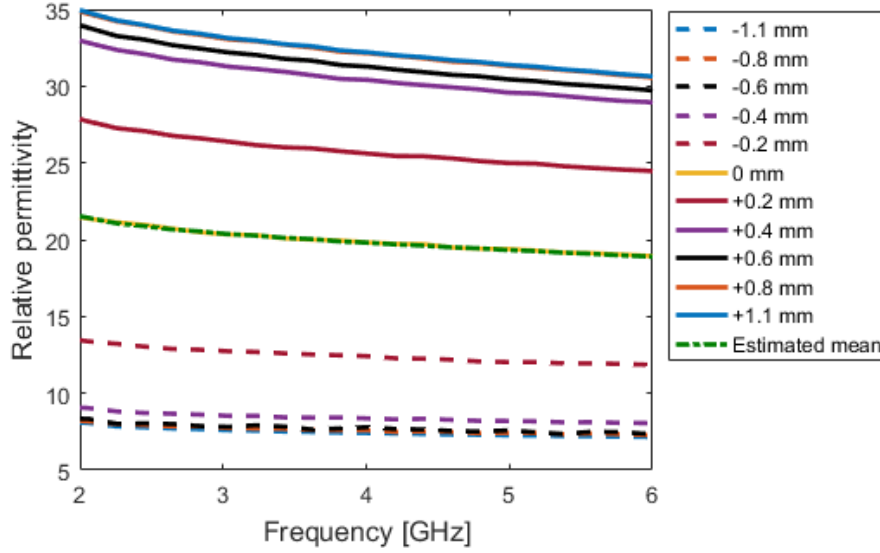


Figure 5.16: Relative permittivity traces obtained from simulations conducted on Sample S2 in linear configuration. Each trace corresponds to a specific location of the centre of the probe with respect to the tissue interface, which is indicated in the legend. Specifically, the distances are negative when the probe was mostly in contact with the left tissue (fat), and positive when the probe was mostly in contact with the right tissue (muscle). The reported traces are symmetric with respect to the trace of the fat-muscle interface, thus indicating that the two tissues have equal contribution to the dielectric signal.

In order to calculate the dielectric weights of the two tissues constituting Sample S2, Eq. (5.6) and Eq. (5.7) were applied to single frequency data obtained from the traces of Fig. 5.16. As a result, the dielectric weights of muscle (Tissue 2, on the right) of Sample S2 in linear configuration obtained at the single frequencies of 2 GHz and 6 GHz are illustrated in Fig. 5.17, in blue and in red, respectively, as a function of the probe distance from the tissue interface. The dielectric weights obtained at 2 GHz are approximately equivalent to the dielectric weights obtained at 6 GHz. Thus the two Richards functions fitting the two sets of data, at 2 GHz and 6 GHz, overlap. As a result, only one function was considered to fit the single frequency dielectric weights of muscle as follows:

$$w_{m,T2} = \frac{1}{(1 + 0.428e^{-5.646r})^{\frac{1}{0.515}}}, \quad (5.10)$$

where $w_{m,T2}$ is the dielectric weight of muscle for Sample S2 and r is the radial distance of the probe from the tissue interface.

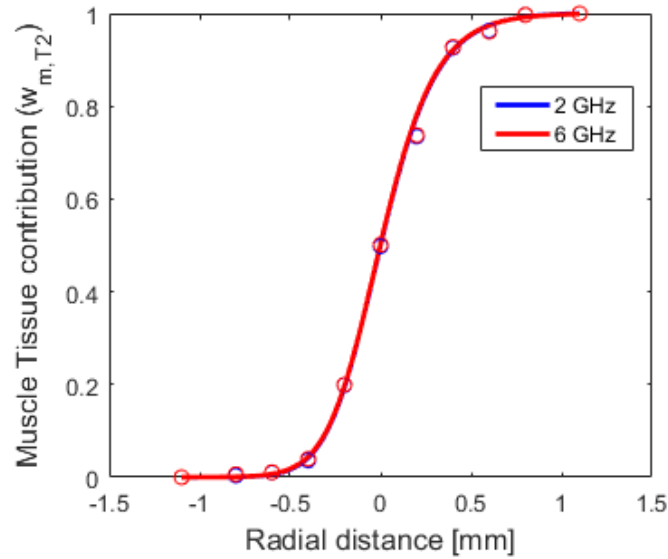


Figure 5.17: Dielectric weights of muscle (Tissue 2, on the right) for Sample S2 in linear configuration obtained at the single frequencies of 2 GHz and 6 GHz as a function of the probe distance from the tissue interface. The dielectric weights obtained at 2 GHz (indicated in blue) are approximately equivalent to the dielectric weights obtained at 6 GHz (indicated in red). Due to the fact that the two Richards functions fitting the two sets of data, at 2 GHz and 6 GHz, overlap, the dielectric weight can be generally represented by the function expressed in Eq. (5.10).

The above function ensured an accurate fitting with a RMSE of 0.011 and is valid for any single frequency between 2-6 GHz. Furthermore, such function can be used to model all of the tissues in linear configuration, since the same dielectric weights were obtained across all six simulated side-by-side samples. Thus, this set of numerical results confirm that the dielectric contribution of side-by-side tissues does not depend on the dielectric properties of the tissues constituting the interrogated sample.

5.3.3.2 Modelling of the dielectric contribution of tissues in concentric heterogeneity configuration

The dielectric traces obtained from the simulations performed on Samples S1 and S2 in concentric configuration (described at the end of Section 5.2.2) are illustrated in Fig. 5.18. Samples S1 and S2 consist of the same two tissues, muscle and fat, but with swapped location. The corresponding results are presented in Fig. 5.18, in order to highlight the importance of considering the location of the tissue while interpreting the dielectric data

CHAPTER 5. MATERIAL DIELECTRIC CONTRIBUTION

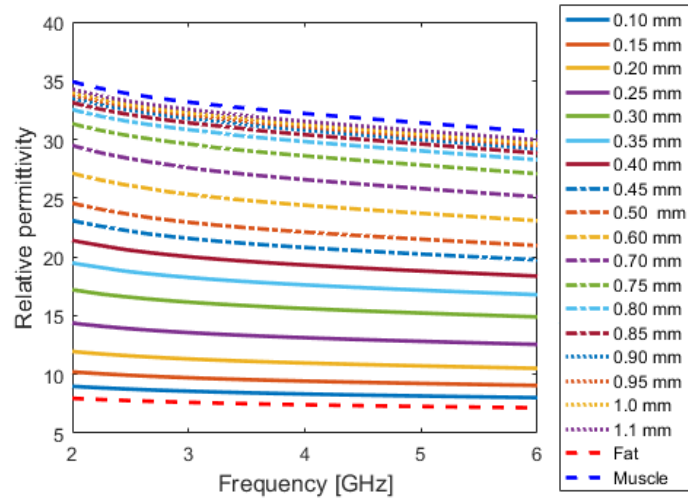
acquired from concentric tissues, as discussed in the previous subsection. In the legend of the two plots of Fig. 5.18, the radius of the inner tissue, to which each trace corresponds, are reported. In both plots of Fig. 5.18, as the radius of the inner tissue increases, the traces tend to that of the inner tissue. However, for both plots, most of the traces are closer to the trace of the inner tissue than that of the outer tissue, indicating that the inner tissue has greater dielectric impact on the acquired dielectric signal than the outer tissue. Furthermore, by comparing the relative permittivity traces from the two plots of Fig. 5.18, it can be observed that the traces of Fig. 5.18b tend to the trace of the inner tissue (fat, in this case) considerably faster than how the traces of Fig. 5.18a tend to the trace of the inner tissue (muscle, in this case). In fact, the dielectric trace corresponding to the inner tissue radius of 0.40 mm (reported with a dark red solid line) is half way between muscle and fat in Fig. 5.18a but is closer to fat in Fig. 5.18b.

The differences in trend between the two samples are better visualised in Fig. 5.19, in the plot of the dielectric weights of the inner tissue for the two samples S1 and S2, calculated according to Eq. (5.6) and Eq. (5.7), and reported as a function of the inner tissue radius. In particular, in Fig. 5.19, the two Richards curves fitted to the two sets of data from Sample S1 and Sample S2 highlight that the dielectric weights of the inner tissue of S2 (fat) increases faster than the weights of the inner tissue of S1 (muscle), thus confirming that tissues with a lower permittivity have a greater dielectric impact than tissues with a higher permittivity, as observed in the previous section. The parameters of the two Richards curves (illustrated in Fig. 5.19) are reported in Table 5.5, where the parameters of the models found for all tissues are summarised.

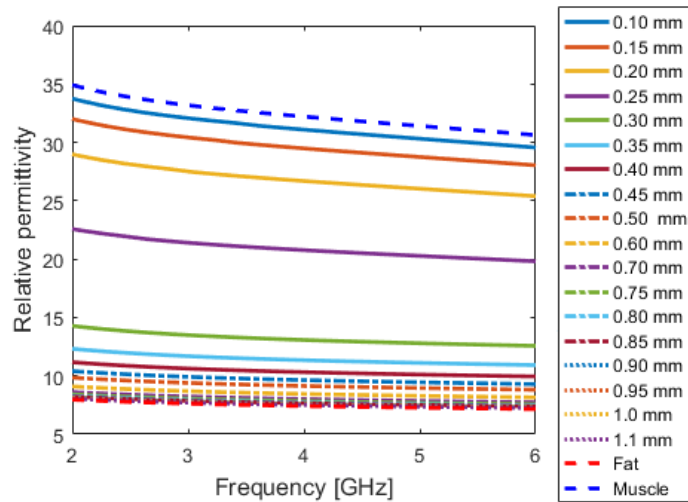
Furthermore, as for the samples in linear configuration, the dielectric weights calculated for the concentric samples are consistent across the range of 2-6 GHz. Thus the dielectric weights and the fitted curves reported in Fig. 5.19 can be considered for any single frequency between 2-6 GHz.

All fitted curves, each corresponding to a specific sample summarised in Table 5.5, are plotted in Fig. 5.20 for a general comparison. As is clear from Fig. 5.20, similarly to the concentric sample couplet S1 and S2, differences in trends were observed for other concentric sample couplets consisting of tissues inversely arranged (S3 and S4, and S5 and S6). However, the difference between the curves of two samples consisting of the same tissues but inversely arranged diminishes as the contrast in permittivity between the inner and outer tissues decreases. These findings are consistent with the outcome from the sensing radius investigation in Chapter 4, which demonstrated that the sensing radius is smaller for concentrically heterogeneous samples with a low permittivity inner tissue and with a low contrast in permittivity between the

CHAPTER 5. MATERIAL DIELECTRIC CONTRIBUTION



(a)



(b)

Figure 5.18: Relative permittivity traces obtained from simulations conducted on (a) Sample S1 and (b) Sample S2 in concentric configuration. Both samples consists of the same tissues, fat and muscle, but with swapped location. Specifically, Sample S1 has muscle as the inner tissue and fat as the outer tissue and Sample S2 has fat as the inner tissue and muscle as the outer tissue. In both plots, each trace corresponds to a specific radius of the inner tissue. By comparing the relative permittivity traces from (a) and (b), it can be observed that the traces of (b) tend to the trace of the inner tissue (fat, in this case) considerably faster than how the traces of (a) tend to the trace of the inner tissue (muscle, in this case). In fact, the dielectric trace corresponding to the inner tissue radius of 0.40 mm (reported with a dark red solid line) is half way between muscle and fat in (a) and closer to fat in (b).

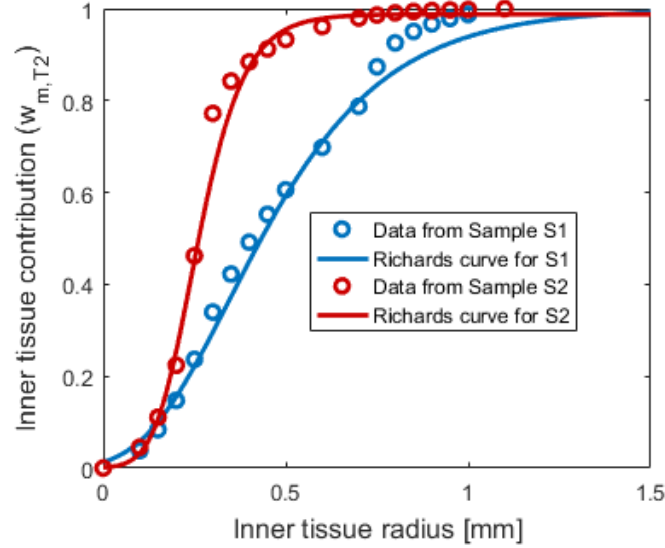


Figure 5.19: Dielectric weights of muscle (in blue) and fat (in red) for Sample S1 and Sample S2 in concentric configuration, respectively. The dielectric weights and the corresponding fitted Richards curves (parameters of which are reported in Table 5.5) are valid for any single frequency between 2-6 GHz. The two Richards curves fitted to the two sets of data from Sample S1 and Sample S2 highlight that the dielectric weights of fat increases faster than the weights of muscle, thus confirming that tissues with a lower permittivity has a greater dielectric impact than tissues with a higher permittivity.

Table 5.5: Best fit parameters and root mean square error for the dielectric weights of the inner tissue for all six concentric samples S1-S6.

S	a	b	c	d	RMSE
S1	1	5.130e-5	4.500	1.140e-5	0.023
S2	1	7.440	23.040	0.320	0.023
S3	1	-0.100	5.385	-0.021	0.023
S4	1	0.5293	9.791	0.052	0.023
S5	1	-0.100	6.912	-0.017	0.025
S6	1	0.757	9.721	0.075	0.025

inner and the outer tissues (compared to the concentrically heterogeneous samples with a high permittivity inner tissue and with a high contrast in permittivity between the inner and the outer tissues).

Notably, for all scenarios, the sensing radius was always within the probe radius. In fact, when the radius of the inner tissue is equivalent to the probe radius (1.1 mm), the contribution weight of the inner tissue is approximately equal to 1. This result further confirms the experimental and numerical outcome of the sensing radius investigation in Chapter 4.

In summary, the experimental and numerical investigation discussed in

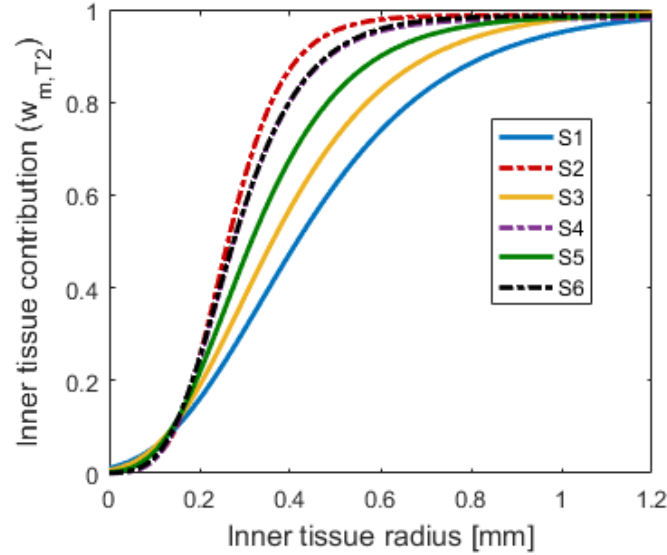


Figure 5.20: Model weights for the inner tissue obtained for all concentric samples, for frequencies between 2 and 6 GHz. The dielectric weights of the inner tissues are modelled with Richards curves, with corresponding parameters provided in Table 5.5.

this section demonstrated that the material distribution within the sensing volume greatly impacts how the materials contribute to the dielectric measurement. In fact, side-by-side material dielectric contribution is proportional to the volume occupied by the material within the sensing volume and does not depend on the material permittivity. Conversely, in concentrically arranged materials, the inner material contributes dominantly, especially if the material has low permittivity.

This outcome is particularly noteworthy, since in all known dielectric studies [10]–[12], [15], the contribution of a constituent tissue to the dielectric properties has always been assumed equivalent to the percent volume occupied by that tissue, regardless of the spatial distribution of the tissues. This outcome highlights the necessity of quantitatively estimating the dielectric contribution of each constituent tissue based on the tissue permittivity and spatial distribution within the sensing volume, when correlating the acquired dielectric data to the histology of the interrogated heterogeneous biological sample. To this extent, preliminary simulations similar to the those performed in this chapter are recommended to be performed before correlating the acquired dielectric data to the histology of the interrogated heterogeneous biological sample.

It is of note that the quantitative results obtained from this investigation

can be used only for radially heterogeneous tissues with the linear and concentric structures examined in this chapter. Hence, for an accurate dielectric characterisation of heterogeneous tissues with a more complex structure, further investigation is needed.

Lastly, although the general outcome of this investigation can be extended to any type of probe, the quantitative findings obtained for the slim form probe cannot be generalised to other probes. In fact, the sensing radius significantly depends on the probe design, e.g., the size of the inner conductor, the insulator, and the outer conductor, as demonstrated in Chapter 4.

5.4 Summary

For an accurate dielectric characterisation of highly heterogeneous biological tissues, which involves a rigorous correspondence between the acquired dielectric data and the histology of the sample, knowledge of the sensing volume needs to be accompanied by knowledge of the dielectric contribution of each tissue constituting the sensing volume. In past studies, the dielectric contribution of layered materials within the sensing depth has been thoroughly examined. Conversely, there are no quantitative studies in the literature investigating the dielectric contribution of radially heterogeneous materials within the sensing radius.

To this extent, this chapter presented both dielectric measurements and numerical simulations performed on several well-controlled radially heterogeneous samples. Specifically, in order to examine the dependence of the dielectric contribution on the material distribution and dielectric properties, two different radially heterogeneous samples were investigated in this chapter:

- Samples with linear heterogeneity configuration, consisting of two side-by-side tissue-mimicking materials and biological tissues spanning a wide range of permittivity;
- Samples with concentric heterogeneity configuration, consisting of two concentric tissue-mimicking materials and biological tissues spanning a wide range of permittivity.

Both measurements and simulations conducted on the above samples confirmed that the material dielectric contribution depends on the spatial distribution of the constituent materials. In particular, the following two findings were observed:

- Dielectric properties measured on two side-by-side materials are proportional to the volume occupied by each constituent material and do

CHAPTER 5. MATERIAL DIELECTRIC CONTRIBUTION

not depend on the individual dielectric properties of each constituent material;

- Dielectric properties measured on two concentric materials are not proportional to the volume occupied by each constituent material and depend on the individual dielectric properties of each constituent material.

For instance, within concentrically heterogeneous samples, the inner material has a significantly higher impact, up to 50% higher than the outer material, on the measured dielectric properties, especially if the inner material has lower permittivity.

From these results, it is clear that the weights for dielectric contribution do not always correspond to the volume occupied by the constituent materials. Therefore, for samples with concentric heterogeneities, making the assumption that the tissue dielectric contribution is proportional to the volume occupied by each tissue within the sensing volume can lead to significant errors.

Hence, in order to support the interpretation of dielectric data from side-by-side and concentrically heterogeneous biological samples, the dielectric data obtained numerically from a subset of biological tissues was modelled. These developed models enable prediction of the dielectric properties of a sample from *a priori* information regarding the radius occupied by each constituent tissue, and the dielectric properties of each individual tissue constituting the sample. While one general model was found to be capable of predicting the dielectric data of any sample consisting of side-by-side tissues, a specific model for each scenario was found to be necessary for concentric samples. Thus, the models developed for concentrically heterogeneous samples can be used to predict the dielectric data of only a subset of concentric samples, which have specific dielectric properties, already known from the literature.

Overall, this investigation enables prediction of the dielectric contribution of tissues within the sensing radius. Knowledge of the dielectric contribution of tissues within the interrogated sample supports the interpretation of the dielectric properties measured from heterogeneous tissues. The significance of this investigation, associated with the sensing radius estimation, is demonstrated in the following chapter, where the dielectric data acquired from a subset of biological samples are interpreted with the support of histological analysis.

Examination of post-measurement histology for heterogeneous biological tissues

Throughout the previous chapters of this thesis, the importance of conducting post-measurement histological analysis for an accurate dielectric characterisation of heterogeneous biological samples has been discussed. In particular, in Chapter 4 and Chapter 5, it was confirmed that errors in correlating the dielectric properties with the sample histology (i.e., the sample tissue content) can be attributed to erroneous estimation of the sensing radius or erroneous assumptions related to the dielectric contribution of individual tissues. Thus, in this chapter, the significance of the findings of the previous chapters (i.e., the impact of erroneous estimation of both the sensing radius and the tissue dielectric contribution) is investigated by conducting post-measurement histology on a set of radially heterogeneous tissue samples. As detailed in Chapter 3, histology can be affected by a number of confounders that can be only partially minimised. To this extent, this chapter also reports the challenges in the post-measurement histology process, and potential methods to address these challenges. In this chapter, the term “histology” is used, not only to define the study of the microscopic structure of cells and tissues, but also to define the process of differentiating the tissue types within a sample. In particular, in this chapter, two types of histology are presented: the microscope-based histology, or traditional histology, and the microCT-based histology.

In Section 6.1, the methodology of the study is described. Specifically, the choice of tissue samples is motivated in Section 6.1.1. The protocols for the dielectric measurement and traditional histology are detailed in Section 6.1.2 and Section 6.1.3, respectively. Finally, the methodology of microCT as an alternative histology technique to support the dielectric characterisation of biological tissues is described in Section 6.1.4.

In Section 6.2, the results from the dielectric measurements are discussed with the support of traditional histology and microCT. Firstly, Section 6.2.1

presents the challenges and limitations of traditional histology. Secondly, in Section 6.2.2, the results from traditional histology are reported and associated with the measured dielectric data. Specifically, the dielectric and histology data from key types of tissue samples is used to validate the sensing radius and dielectric contribution findings (from Chapter 4 and Chapter 5). Due to the invasive and time-consuming process of traditional histology, the feasibility of using microCT as an alternative to traditional histology is then evaluated in Section 6.2.3. Next, the applicability of the sensing radius and dielectric contribution findings for the dielectric characterisation of highly heterogeneous tissue samples is evaluated through both traditional histology and microCT-based histology in Section 6.2.4. Finally, the outcome of the analysis is summarised in Section 6.3.

6.1 Methodology

This section describes the methodology used to validate the significance of the sensing radius and dielectric contribution findings (from Chapter 4 and Chapter 5) for the dielectric characterisation of radially heterogeneous biological samples and to verify the generalisability of these findings to highly heterogeneous samples. Specifically, the methodology consists of dielectrically characterising a set of either radially or highly heterogeneous biological samples with the support of post-measurement traditional histology and/or microCT-based histology. To this extent, Section 6.1.1 motivates the choice of a set of heterogeneous tissue samples, Section 6.1.2 details the dielectric measurement protocol, and Section 6.1.3 details the traditional histology protocol. Furthermore, Section 6.1.4 presents the methodology used to evaluate the feasibility of using microCT as an alternative to traditional histology to support the dielectric characterisation of heterogeneous biological samples.

6.1.1 Choice of heterogeneous tissue samples

Biological samples presenting simple radial heterogeneities, such as kidney and muscle with fat inclusions, were selected to validate the significance of the sensing radius and dielectric contribution findings of Chapter 4 and Chapter 5. Most of these samples underwent post-measurement traditional histology and a subset of samples underwent microCT-based histology. The details of the various samples are provided in the next paragraphs.

In particular, ten samples were selected as representative radially heterogeneous samples to be analysed by post-measurement traditional histology.

CHAPTER 6. POST-MEASUREMENT HISTOLOGY

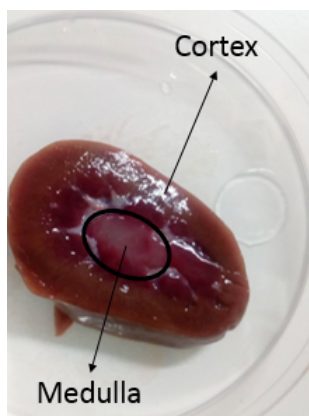


Figure 6.1: Example of ovine kidney sample, where the medulla region is easily distinguishable from the cortex region.

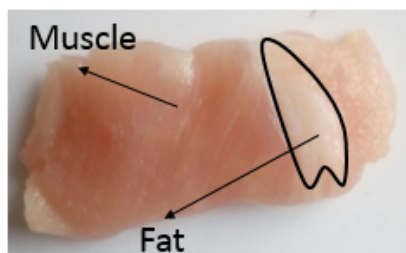


Figure 6.2: Example of porcine muscle sample, where the fat tissue is easily distinguishable from the muscle tissue.

The ten samples consisted of: three samples of ovine kidney, two samples of ovine muscle (with fat inclusions), and five samples of porcine muscle (with fat inclusions). All of the samples were obtained from a local butcher. Changes in the tissue morphology due to temperature variations and tissue dehydration were recorded during the measurement process and taken into account when interpreting the acquired dielectric data. While the three ovine kidney samples had consistent structures with defined cortex and medulla regions, like the sample illustrated in Fig. 6.1, the two ovine and the five porcine muscle samples showed varying structure. An example of the heterogeneity of ovine and porcine muscle samples is reported in Fig. 6.2.

Furthermore, two samples, i.e., rodent kidney and ovine muscle, were selected to perform preliminary experiments with microCT as a histology method. Specifically, the two samples were scanned to verify the applicability of microCT in distinguishing individual tissues within radially heterogeneous samples. The rodent kidney was from a laboratory mouse, while the ovine muscle was obtained from a local butcher.

CHAPTER 6. POST-MEASUREMENT HISTOLOGY

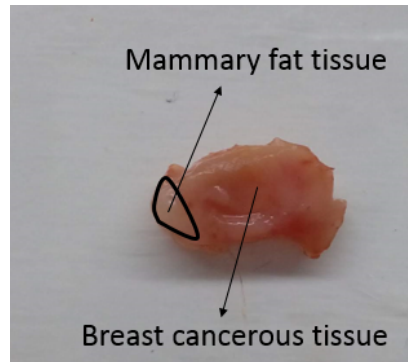


Figure 6.3: Mammary fat pad sample, where the fat tissue region is easily distinguishable from the cancerous region.

Lastly, a sample of mammary fat pad was selected to verify the applicability of the findings from Chapter 4 and Chapter 5 to highly heterogeneous samples (due to the fact that the mammary fat pad presents a highly complex structure). The mammary fat pad was excised from a rodent, in which human breast cancerous tissue had been injected into the mammary fat tissue and allowed to grow. A picture of the mammary fat pad is reported in Fig. 6.3.

In summary, three subsets of samples were analysed in three different studies, each having a different aim: validating the experimental findings in Chapter 4 and Chapter 5 (by post-measurement histological analysis of radially heterogeneous samples), evaluating microCT as a histology technique to overcome the challenges of traditional histology (by scanning a subset of radially heterogeneous samples), and validating the applicability of the experimental findings in Chapter 4 and Chapter 5 to highly heterogeneous samples (through both post-measurement traditional histology and microCT-based histology). The three studies and the corresponding investigated tissue samples are summarised in Table 6.1.

6.1.2 Dielectric measurement protocol

Dielectric experiments were performed with the Keysight slim form probe connected to the Agilent E8362B VNA across the MW range of 2-6 GHz. The slim form probe and the measurement frequency range of 2-6 GHz were selected for consistency with the experiments detailed in Chapter 4 and Chapter 5.

For each dielectric experiment, the measurement settings detailed in Chapter 4 were used. Thus, 21 frequency points were selected for consistency

CHAPTER 6. POST-MEASUREMENT HISTOLOGY

Table 6.1: Summary of the tissue samples analysed in three different studies, each having a different aim.

Study	Aim	Tissue samples
1st Study	Validating the experimental findings in Chapter 4 and Chapter 5 by post-measurement histological analysis of radially heterogeneous samples	<ul style="list-style-type: none"> ●3 samples of ovine kidney; ●2 samples of ovine muscle (with fat inclusions); ●5 samples of porcine muscle (with fat inclusions).
2nd Study	Evaluating microCT as a histology technique to overcome the challenges of traditional histology with radially heterogeneous samples	<ul style="list-style-type: none"> ●1 sample of rodent kidney; ●1 sample of ovine muscle.
3rd Study	Evaluating the applicability of the experimental findings in Chapter 4 and Chapter 5 to highly heterogeneous through both post-measurement traditional histology and microCT-based histology	<ul style="list-style-type: none"> ●1 sample of mammary fat pad

with the previous experiments and findings. Furthermore, the same measurement procedure was followed as used in the experiments of Chapter 4 and Chapter 5. Thus, before each measurement set, the system was calibrated and validated, and it was ensured that the measurement uncertainty was consistently within the values reported in Section 4.2.1 (i.e., 2.4% for relative permittivity and 4.6% for conductivity). Prior to measurements, tissue samples were kept in cling film. In this way, tissue dehydration was minimised by limiting the exposure of each sample to air. During tissue measurements, each sample was brought to the probe tip using a lift table, a firm contact between the probe and the tissue was kept, excess blood on the surface of the sample was removed using cotton swabs, and the tissue temperature was measured with an infrared thermometer. Furthermore, between each measurement, the probe was cleaned with an alcohol wipe in order to avoid contamination.

Dielectric experiments were conducted on the samples listed in the previous subsection. Specifically, measurements conducted on ovine/rodent kidney covered three regions of the sample: the homogeneous cortex region, the homogeneous medulla region and the radially heterogeneous region at the cortex/medulla interface. Measurements conducted on porcine and ovine muscle covered multiple regions of the sample, generally, consisting of: homogeneous muscle, homogeneous fat, radially heterogeneous regions with side-by-side or concentric muscle and fat. Finally, measurements of the mammary fat pad involved various heterogeneous regions mostly consisting of fat, mostly consisting of cancerous tissue, and consisting of a mixture of fat and cancerous tissue.

After conducting the measurements, the measurement sites were marked



Figure 6.4: Post-measurement marking on an ovine kidney sample for identifying the measurement sites during the histological analysis.

with a histology marker and then prepared for sample processing. Fig. 6.4 shows the marked measurement sites on an ovine kidney sample.

After marking the measurement sites, the samples underwent the histology steps summarised in Section 3.3.2 and detailed in the following subsection.

6.1.3 Traditional histology protocol

The protocol designed for post-measurement traditional histology consists of the following six steps:

1. Fixation;
2. Processing;
3. Embedding;
4. Slicing;
5. Staining;
6. Imaging.

Each step is discussed, in turn, below. Labelling was essential to ensuring that the samples and measurement sites could be uniquely identified throughout each step of the traditional histology protocol. Furthermore, due to the fact that parts of the histological process can cause shrinkage and deformation of the tissue samples [175], a subset of five samples were measured with a calliper before and after the steps of fixation and processing in order to monitor the change in size of the samples. Monitoring of the change in size of the sample supports identification of the measurement sites on the histology slides in order to find an accurate correspondence between measured dielectric data and histological content.

Fixation is the first step conducted to preserve the histology of the tissue sample. Fixation was performed by immersing the sample into a 10% w/v

CHAPTER 6. POST-MEASUREMENT HISTOLOGY



Figure 6.5: Sample illustrated in Fig. 6.4 after undergoing fixation in 10% w/v formalin solution. Two green stitches can be observed beside the measurement sites across the heterogeneous regions of the sample. The stitches were not inserted over the measurement sites in order to avoid tissue damage in the region of interest. Furthermore, the sample is placed into a cassette to be inserted into the tissue processor. The cassette was labelled with the unique identifier, i.e. LK7M 26-11, written in the pencil since graphite is resistant to all chemicals used by the tissue processor.

formalin solution. Specifically, in order to find the fixation time able to guarantee an adequate staining, samples were kept in formalin solution for different times ranging from 48 hours to 12 days. The fixation times were selected based on the results found in the literature [175]. In fact, histology studies found 48 hours to be an appropriate time for fixation, and over-fixation to provide better staining than under-fixation [175].

Either before or after fixation, the samples were cut in order to be fitted into the cassettes used by the Thermo Scientific Excelsior tissue processor. Furthermore, preliminary histology experiments showed that the marks on samples with a glossy texture (like kidney) were not resistant to sample processing. For this reason, in order to avoid exclusion of the samples (as in the study performed by Lazebnik *et al.* [10], [11]), the measurement sites across heterogeneous sample regions of the kidney samples were further marked with stitches. An example of the stitches being used for marking is reported in Fig. 6.5. The sample in Fig. 6.5 is the same sample reported in Fig. 6.4. Specifically, two green stitches can be observed beside the measurement sites across the heterogeneous regions of the sample. The stitches were not inserted over the measurement sites in order to avoid tissue damage. The distances between the stitches and the marked measurement sites were recorded at this stage and also after the tissue processing.

Once the fixed samples were placed into the cassettes, the tissue processor was operated. The tissue processor preserves the histological content of the samples, before the embedding in paraffin wax. Specifically, the tissue

CHAPTER 6. POST-MEASUREMENT HISTOLOGY

processor dehydrated the samples by immersing them in alcohol solutions having increasing concentration for specific time intervals. Lastly, the samples were washed out in xylene and then removed from the tissue processor.

Then, the samples were embedded in paraffin wax by taking into account the orientation of each sample, so that the measurement sites on each sample were easily identifiable.

Once the samples were embedded in paraffin blocks, the samples were sliced with a microtome and then placed on glass slides. The samples were generally cut in $5\ \mu\text{m}$ thick slices. This thickness allows for clear images of the slice (when it is being imaged by the microscope), since $5\ \mu\text{m}$ contains only a single layer of cells. However, for a few samples, thicknesses up to $30\ \mu\text{m}$ were used to obtain slices at specific depths of interest. In order to facilitate the slicing, the sample within the paraffin block was kept under 0°C . Furthermore, before performing the slicing, the angle of the blade of the microtome was set at 6° from the plane of the cassette containing the paraffin block. Then, the slicing was performed slowly and firmly. During the slicing process, the slices were taken with the support of tweezers and brushes and placed in a water bath of 35°C . Next, the slices were placed on glass slides that were appropriately labelled to keep track of the sequence of the slices, i.e., to facilitate the association of each slice to a specific depth of the sample. Further information about the challenges associated with sample slicing with the microtome are detailed in Section 6.2.1.

Next, the haematoxylin and eosin (H&E) staining was performed. This type of staining was selected since it is easy to perform and enables differentiating tissues based on the cell structure, since haematoxylin binds to the DNA (in the cell nuclei) and eosin to the proteins (in the cell cytoplasm) [175]. Since the H&E staining is effective only on hydrated samples, the slides were ordered in sequence in a rack, immersed in xylene to remove the paraffin, and re-hydrated in alcohol solutions with decreasing concentrations. Then, the rack was immersed in DI water and the H&E staining was performed. The H&E staining consisted of immersing the rack in haematoxylin for 20 seconds, tap water for 10 minutes, 95% ethanol solution for 2 minutes and then eosin Y for 2 minutes. However, before immersing the rack in eosin, the slides were checked quickly under the microscope to validate the haematoxylin staining (i.e., to verify that all of the cell nuclei were blue). In the case of unsuccessful haematoxylin staining, the procedure was repeated. In the same way, after performing the eosin staining, the slides were checked and, in case of unsuccessful eosin staining, the procedure was repeated. Lastly, the stained slices were dehydrated. The steps of the H&E staining protocol, from the re-hydration to the post-staining dehydration,

CHAPTER 6. POST-MEASUREMENT HISTOLOGY

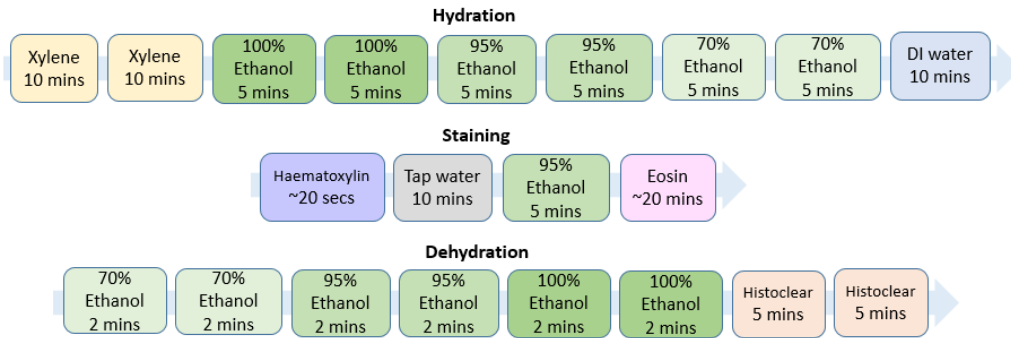


Figure 6.6: Summary of the H&E staining protocol, consisting of different steps, from the slice re-hydration to the staining and dehydration.

are summarised in Fig. 6.6.

After the staining, the slides were mounted using the DPX mounting medium (i.e., a mixture of distyrene, a plasticiser and xylene) between the slide and the coverslip. Each slide contained one sample slice. The DPX mounting medium has the same refractive index of glass and, thus, does not alter the imaging of the histological slices. Once the slides were mounted, they were left to dry for 24 hours at room temperature.

Finally, the slides were imaged with the Olympus VS120 digital slide scanner using from 50 to 100 focal points for each slice. Lastly, the slides were analysed with Olyvia (version 2.9.1) and Image J. The results of the histological analysis are discussed in Section 6.2.1 and Section 6.2.2.

6.1.4 MicroCT protocol

MicroCT is an imaging technique that uses X-rays to provide 2D or 3D cross-sectional views of the interior of a biological sample with a resolution higher than $5 \mu\text{m}$ in each spatial dimension [198]–[200]. MicroCT consists of an X-ray source, a filter, a sample holder containing the sample (making complete rotations of 360°), an array of detectors and a post-processing unit. Generally, the filtered X-ray beam hits the sample, which attenuates the signal. Then, the attenuated signal acquired by the detectors is processed to reconstruct the images.

MicroCT has been used in the literature for many applications, from the analysis of the trabecular structure of the bone to the visualisation of human coronary arteries [198], [200], [201]. In particular, there has been a growing interest in using microCT as an alternative to traditional histology in medical imaging and diagnostics, since microCT is non-invasive and less

CHAPTER 6. POST-MEASUREMENT HISTOLOGY

time-consuming than traditional histology [198]. In fact, microCT does not require slicing of the samples and, thus, allows 3D imaging of tissues in a configuration much closer to their natural condition.

For this reason, in this thesis, preliminary experiments were conducted to investigate the feasibility of using microCT imaging as a tool to support the dielectric characterisation of heterogeneous biological samples. Hence, microCT is investigated in this chapter as an alternative to traditional histology, in the context of interpreting the dielectric data from heterogeneous tissue samples.

MicroCT can be used for the analysis of varied tissues, from hard to soft tissues. No sample pre-processing is required for the imaging of hard tissue samples, such as bone, due to their high X-ray attenuation. However, the use of contrast agents is often necessary to enhance the contrast of soft tissues, due to their low X-ray attenuation [202], [203]. The most commonly used contrast agents are: Lugol's iodine, phosphomolybdic acid (PMA), phosphotungstic acid (PTA), osmium tetroxide (OsO_4) [199], [202]–[206]. Among these contrast agents, Lugol's iodine was selected for the microCT scans, since this contrast agent is inexpensive, simple, non-toxic and capable of penetrating rapidly and deeply through a large number of soft tissues [199], [202]. Furthermore, Lugol's iodine washes out naturally in 70% ethanol, thereby allowing the scanned sample to also undergo histological processing.

The staining with the Lugol's iodine consisted of the following three steps.

1. The samples were fixed for two days in 10% w/v formalin solution (this step is in common with the traditional histology procedure).
2. The samples were stored in 70% ethanol solution.
3. The samples were immersed in Lugol's iodine, consisting of a 2% potassium iodide (KI) and 1% iodine (I_2) aqueous solution, for five days. This staining time guarantees a complete perfusion of the agent across the tissues (which is not achieved in under-staining conditions) [203].

Either before or after fixation, the sample regions corresponding to the measurement sites were separated from the rest of the sample with a biopsy punch of 5 mm diameter (which is larger than the sensing radius of the slim form probe). In this way, each sample could fit into the sample holder of 9 mm diameter, which ensured a voxel resolution of 10 μm . In fact, the smaller the sample (and thus the sample holder), the better the resolution.

Then, after sample pre-processing, the samples immersed in Lugol's iodine (for 5 days) were imaged by Scanco $\mu\text{CT}100$. Before scanning the samples, the system source was set with a current of 100 μA and a voltage of 70 kVp, which resulted in the production of a spectrum of X-rays around the frequency of $1.7 \cdot 10^{19}$ Hz. Furthermore, the energy spectrum of the

X-ray beam was shaped by a 0.5 mm aluminium filter, which enhances the contrast produced by soft tissues [200].

Lastly, the samples were scanned and the acquired signals were processed to form a graphical representation of the attenuation distribution within the object. The image reconstruction was automatically performed by the built-in software of the microCT scanner. Lastly, the microCT images were analysed and processed with ImageJ and 3DSlicer. The preliminary results of the microCT scans are provided in Section 6.2.3. Furthermore, the microCT scan of the mammary fat pad that underwent traditional histology (after microCT) is discussed in Section 6.2.4.

6.2 Results and Discussion

This section discusses the correspondence between measured dielectric data and sample tissue content, both through traditional histology and microCT-based histology. Specifically, Section 6.2.1 reports the challenges of the traditional histology process and the methods to address these challenges. Then, Section 6.2.2 reports the analysis performed to associate the dielectric data with the sample histological content. This analysis has the aim of validating the sensing radius and dielectric contribution findings from Chapter 4 and Chapter 5, respectively. Furthermore, Section 6.2.3 discusses the advantages of performing microCT as an alternative to traditional histology by reporting the results from the preliminary experiments performed on a subset of samples. Lastly, Section 6.2.4 presents an analysis of interpreting the dielectric data acquired from a highly heterogeneous sample through traditional histology and microCT-based histology. Thus, Section 6.2.4 evaluates the applicability of the sensing radius and dielectric contribution findings for the dielectric characterisation of heterogeneous samples presenting complex tissue structures.

6.2.1 Traditional histology process and challenges

This subsection overviews each step of the traditional histology process conducted on the ten samples as part of the first study (as listed in Table 6.1). For each traditional histology step, the confounders and the corresponding methods to reduce the effect of these confounders are reported, with the aim of improving the accuracy in associating the acquired dielectric data with the sample histological content.

Firstly, fixation was performed. As is known from the literature, different fixation times can have different impacts on the quality of the staining and

CHAPTER 6. POST-MEASUREMENT HISTOLOGY

Table 6.2: Change in size for a subset of radially heterogeneous samples during traditional histology, from pre-fixation to post-processing. All samples were fixed for 3 days, except for Sample PM3 which was fixed for 2 days.

Sample	Shape	Pre-fixation size [mm]	Post-fixation size [mm]	Post-processing size [mm]
LK1	Triangular	Base: 15.12 Height: 16.75	Base: 15.21 Height: 16.05	Base: 15.62 Height: 12.68
LK2	Trapezoidal	Bottom base: 13.84 Top base: 9.85 Height: 24.44	Bottom base: 16.02 Top base: 9.50 Height: 26.37	Bottom base: 14.39 Top base: 8.65 Height: 19.54
PM1	Rectangular	Base: 9.68 Height: 8.66	Base: 11.64 Height: 7.62	Base: 10.17 Height: 6.52
PM2	Rectangular	Base: 18.43 Height: 13.42	Base: 19.17 Height: 14.44	Base: 15.19 Height: 13.34
PM3	Rectangular	Base: 16.87 Height: 13.24	Base: 15.76 Height: 15.37	Base: 13.12 Height: 11.35

therefore on the quality of the images at the microscope [175]. However, among the ten samples that underwent different fixation times (from 2 to 12 days), no notable difference in staining quality was seen for the purposes of tissue content assessment. Thus, all samples could be analysed in order to differentiate the different tissue content regions. However, it is important to note that the histological assessment here was done visually. For computer-automated methods, precision in the quality of staining may be more important.

Conversely, a considerable difference in sample size was found across the steps from fixation to sample processing (prior to embedding). The change in size was monitored for five samples, and is reported in Table 6.2. Among those five samples, two samples are ovine kidney and three samples are porcine muscle. As is clear from the table, the change in size for the ovine kidney is generally higher than for the porcine muscle. However, for both sample types, a general small increase in size was recorded between pre-fixation and post-fixation (for unclear reasons since previous histology studies recorded a tissue shrinkage in breast tissue samples [207]) and a general decrease in size was recorded between post-fixation and post-processing (due to dehydration). This phenomenon is illustrated for a porcine muscle sample (i.e., Sample PM1 in Table 6.2) in Fig. 6.7.

Furthermore, from Table 6.2, it can be noted that the change in size is not consistent across samples, but it depends on the sample constituent tissues and initial shape. Specifically, a higher change in size was observed for larger samples than for smaller ones, since larger samples tended to need to be compressed more when inserted into the cassettes. This trend was the case for Samples LK1, LK2 and PM2, which exhibited from 18% to 25% post-processing shrinkage in one direction as a result of the sample

CHAPTER 6. POST-MEASUREMENT HISTOLOGY

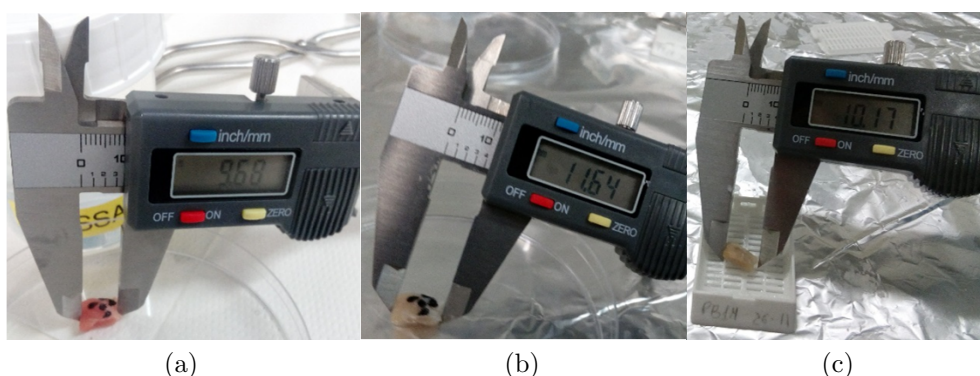


Figure 6.7: Photographs depicting the change in the size of a side of a porcine muscle sample (Sample PM1 in Table 6.2) through the traditional histology process, from (a) pre-fixation to (c) post-processing.

compression. Furthermore, a change in size of up to 22% was recorded for Sample PM3, due to the high fat content. In fact, it was noted that fat tissue tended to shrink and harden more than muscle tissue in the tissue processor.

After removing the samples from the tissue processor, it was found that four samples got damaged either entirely or only on the surface during the sample processing. This sample damage can be attributed to the fact that the samples were squeezed when inserted into the cassettes. An example of damaged sample after the sample processing is shown in Fig. 6.8. At this stage, only the sample in Fig. 6.8 was excluded, while the other three samples were further processed, since the damage of these samples involved only the surface.

No samples were excluded during the embedding. In fact, particular care was taken in putting the appropriate amount of paraffin wax so that the sample was moulded firmly into the cassette and the formation of air bubbles was prevented (in order to facilitate the sample slicing).

After the samples were embedded, the samples were sliced using the microtome. The slicing of the samples was challenging for fibrous tissue samples (e.g., muscle samples). In fact, the tissues from fibrous samples tended to tear and crumble during the slicing. An example of fibrous porcine muscle slices that were excluded is shown in Fig. 6.9. At this stage, three ovine and porcine muscle samples were excluded. Furthermore, two ovine kidney samples were fibrous only across the first 100-200 μm . However, the ovine kidney samples were not excluded from the analysis, since the samples were heterogeneous only radially and thus the surface histological content

CHAPTER 6. POST-MEASUREMENT HISTOLOGY



Figure 6.8: Ovine muscle sample that was excluded from histology after being damaged in the tissue processor.

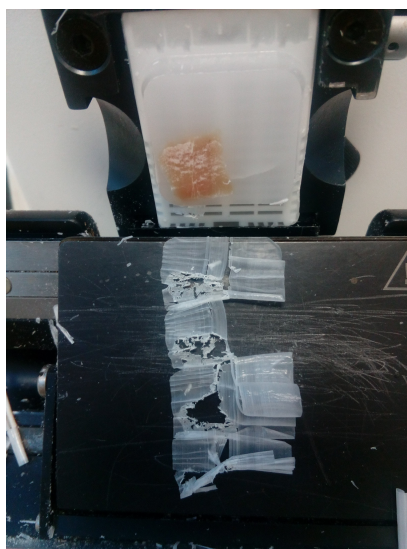


Figure 6.9: Porcine muscle sample that was excluded from histology, since the tissues constituting the sample were too fibrous and crumbled during slicing with the microtome.

did not contain additional information.

Up to this stage, four out of the ten samples had to be excluded (as discussed above), thus leaving six samples for further analysis. For each of the remaining six samples that underwent traditional histology, five to ten slides were analysed in order to verify that the samples were heterogeneous only across the radial extent (and not across the longitudinal extent). Hence, a subset of slices (for each sample that underwent all of the traditional histology process) were imaged by the digital scanner and analysed to

validate the sensing radius and dielectric contribution findings of Chapter 4 and Chapter 5, respectively.

Furthermore, the highly heterogeneous mammary fat pad was analysed histologically after the microCT scan. Despite the high heterogeneity of the mammary fat pad, fewer than ten slides of this sample were analysed due to the computational cost required to scan the entire sample. Both the microCT and traditional histology images of the mammary fat pad are presented in Section 6.2.4, after discussing the traditional histology results in combination with the measured dielectric data in Section 6.2.2 and after showing the feasibility of using microCT as an alternative to traditional histology in Section 6.2.3.

6.2.2 Dielectric characterisation of radially heterogeneous samples through traditional histology

This subsection presents the dielectric data obtained from a subset of samples that underwent post-measurement histological analysis, with the aim of validating the sensing radius and dielectric contribution findings of Chapter 4 and Chapter 5. Thus, in this subsection, the results from the first study (as detailed in Table 6.1) are discussed.

6.2.2.1 Validation of sensing radius findings

In order to validate the sensing radius findings of Chapter 4, the histological information and the corresponding dielectric data from a subset of radially heterogeneous biological samples are presented below. Specifically, Fig. 6.10 shows the histology of Sample PM1 previously reported in Table 6.2 and illustrated in Fig. 6.7. In order to facilitate the association of the dielectric data with the histological tissue content, post-fixation and post-processing sample pictures are reported together with a sample slice imaged with the microscope. Fig. 6.10a presents the five marked measurement sites, which are still visible (although faded) in Fig. 6.10b. Among the five measurement sites, one point was from muscle, two points from fat, and two points from two concentrically heterogeneous regions. The two fat measurement sites are from a smaller region (approximately as large as the probe) and a larger region (two-three times larger than the probe), which were considered for the validation of the sensing radius findings. Furthermore, Fig. 6.10c reports the 5 μm slice obtained at the depth of 0.3 mm, where fat tissue (which appears in white since the H&E staining cannot perfuse through hydrophobic tissues) can be distinguished from muscle tissue (which is represented in

CHAPTER 6. POST-MEASUREMENT HISTOLOGY

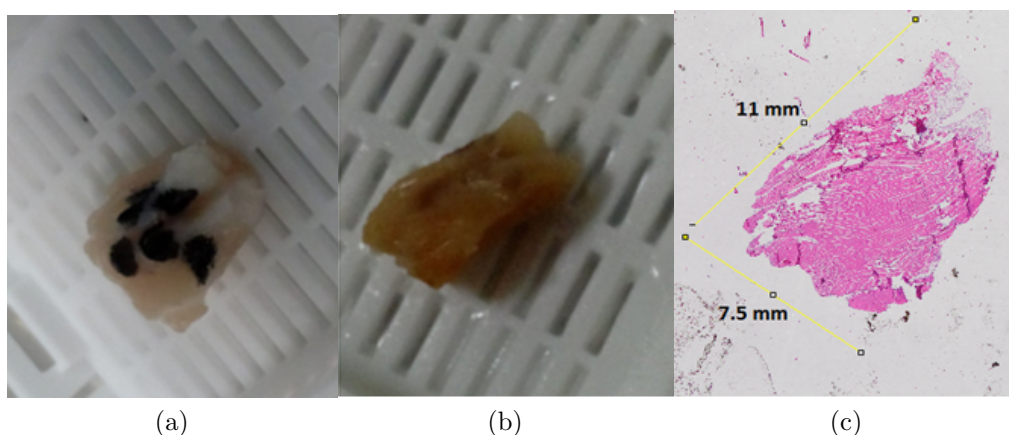


Figure 6.10: (a) Post-fixation picture, (b) post-processing picture and (c) $5\ \mu\text{m}$ thick histological slice of Sample PM1 (reported in Table 6.2) used to support the dielectric data acquired to validate the sensing radius findings of Chapter 4. The five marked measurement sites in (a) are faded in (b). Among the five measurement sites, one is from muscle, two from fat (from smaller and larger regions), and two from concentrically heterogeneous regions. The slice in (c) was obtained at the depth of 0.3 mm and is representative of the whole sample consisting of muscle tissue (which appears in pink due to the eosin staining) and fat tissue (which appears in white since the H&E staining cannot perfuse through hydrophobic tissues).

pink due to the eosin staining). The slice in Fig. 6.10c is representative of the whole sample, since slices at depths higher than 0.3 mm presented similar histological features (slices at depths lower than 0.3 mm were very fibrous and crumbly, thus not suitable for staining).

Fig. 6.10c also reports the size of the sample, which is 11 mm long and 7.5 mm wide. These dimensions are comparable with the dimensions reported in Table 6.2, thus suggesting that the sample was appropriately sliced (i.e., that the correct orientation was maintained through sample embedding and slicing). However, although a less than 8% difference in size was found for this sample between pre-fixation and post-processing (as reported in Table 6.2), a shrinkage above 50% was found for fat tissue. In fact, while the small fat region had a diameter of approximately 2.2 mm (which is the diameter of the probe) before fixation, a diameter of 1 mm was measured for the same region after sample processing. An imaged slice for the small fat region is highlighted and compared with the pre-fixation size in Fig. 6.11.

In addition, the dielectric traces from the muscle and fat regions of Sample PM1 are reported in Fig. 6.12 in terms of relative permittivity and conductivity. In Fig. 6.12, the muscle and fat reference data by Gabriel *et al.* [46] are also plotted.

CHAPTER 6. POST-MEASUREMENT HISTOLOGY

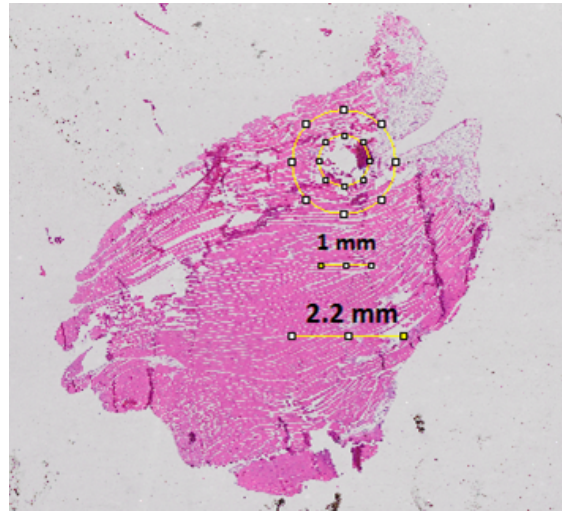


Figure 6.11: 5 μm thick histological slice of Sample PM1 used to support the dielectric data acquired to validate the sensing radius findings of Chapter 4. On the histological slice, the change in size of the small fat region is highlighted. Specifically, before fixation, the small fat region had a diameter of approximately 2.2 mm (which is the diameter of the probe). After processing, the diameter of the same region was 1 mm. This change in size suggests a fat tissue shrinkage of approximately 50%.

The difference between measured and reference relative permittivity data was approximately 20% for both muscle and fat. A smaller difference in conductivity was found between measured and reference data, which was approximately 5% for fat and 10% for muscle. Such differences in permittivity and conductivity, which were consistent across all the porcine samples, can be attributed to biological variability between and within animals, different tissue handling procedures and temperature variations. In fact, while the data by Gabriel *et al.* [46] is from freshly excised bovine muscle and fat samples, the data in this study is from porcine samples obtained from a butcher (not freshly excised).

Furthermore, the data from the smaller homogeneous fat region (within muscle) is comparable with the data from the larger homogeneous fat region. In fact, differences of less than 1% and 5% was found between the dielectric traces of the large and small regions, for relative permittivity and conductivity, respectively. Such differences are within the tissue measurement uncertainty. Therefore, the muscle surrounding the small fat region did not have any dielectric impact on the measurement. Hence, the measurements of Sample PM1 reported in Fig. 6.12 confirmed the sensing radius findings, demonstrating that, within regions larger than the sensing radius calculated numerically (which is 0.9 mm for fat), only the dielectric properties of the

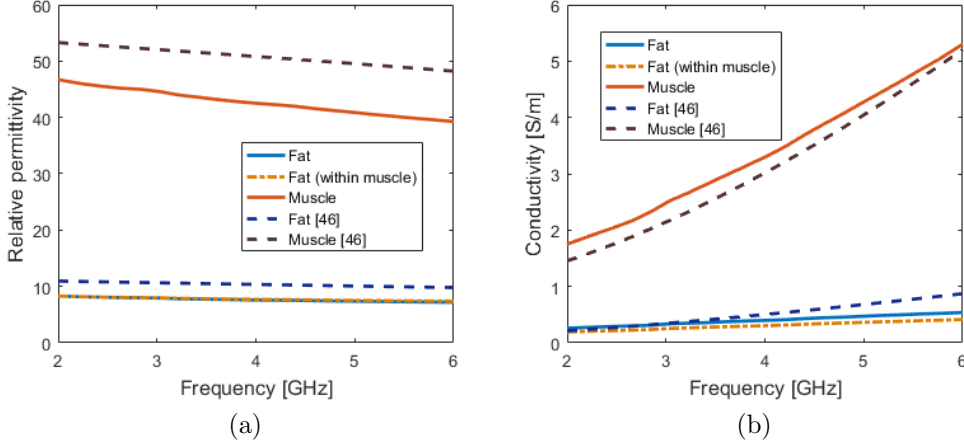


Figure 6.12: (a) Relative permittivity and (b) conductivity traces from three measurements performed on Sample PM1 to validate the sensing radius findings of Chapter 4. Among the three measurements, one measurement was performed on muscle, one measurement on a larger fat region (approximately two-three times larger than the probe) and one measurement on a smaller fat region (approximately as large as the probe). A difference of less than 5% was found between the measurements performed on the two fat regions, thus suggesting that the sensing radius for fat is within the size of the probe. In addition, in both (a) and (b), the bovine muscle and fat data by Gabriel *et al.* [46] is reported. Consistent differences of approximately 20% were found between measurement and reference relative permittivity data, which can be attributed to biological variability between and within animals, different tissue handling procedures and temperature variations.

tissue of interest are actually measured.

The sensing radius findings were then confirmed by the measurements on Sample PM1. However, if the histology alone was considered without taking into account the above 50% fat shrinkage, the results would have been inaccurate. In fact, if the fat tissue shrinkage was not monitored and taken into account, the slice in Fig. 6.11 would have led to the outcome that the sensing radius of the slim form probe for fat is 0.5 mm, half the diameter of the fat smaller region highlighted in Fig. 6.11, and just over half of the actual sensing radius.

Furthermore, the histological analysis supported the interpretation of the dielectric data from kidney samples, such as the sample reported in Fig. 6.13. A post-fixation sample picture is reported in Fig. 6.13, together with the corresponding 5 μm thick histological slice. Four marked measurement sites can be observed on the kidney sample in Fig. 6.13a: one faded measurement mark on the medulla and three measurement marks on the cortex. Among the three measurement sites on the cortex, the point that is less than 1

CHAPTER 6. POST-MEASUREMENT HISTOLOGY

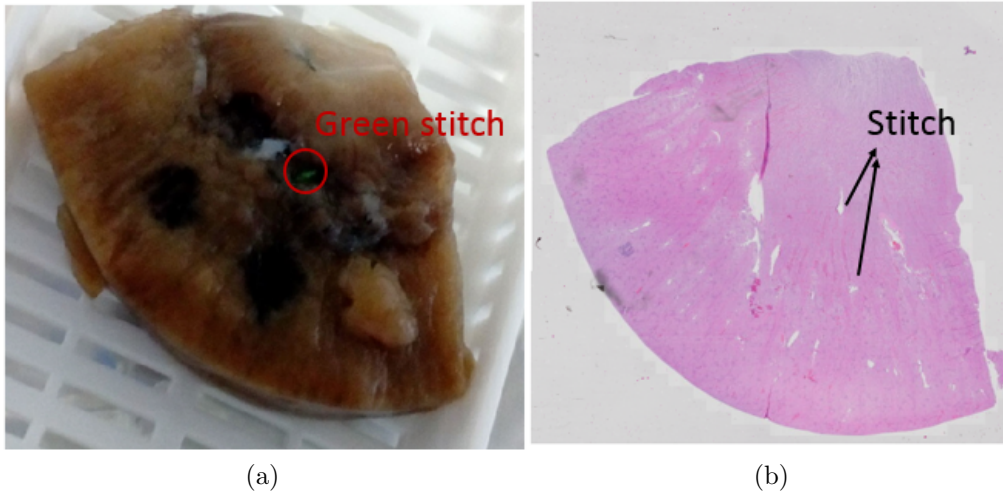


Figure 6.13: (a) Post-fixation picture and (b) 5 μm thick histological slice of a kidney sample used to support the dielectric data acquired to validate the sensing radius findings of Chapter 4. Four measurement sites are marked in (a): one faded on the medulla and three on the cortex. Among the three measurement sites on the cortex, the point that is less than 1 mm distant from the medulla was further marked with a green stitch, which is highlighted in (a). The extremities of the green stitch can be observed in (b) on the 5 μm histology slice that was obtained at the depth of 0.1 mm. This slice is representative of the whole sample, which was confirmed to have only radial heterogeneities. In (b), the medulla (which appears in the top right portion of the image) is not easily distinguishable from the cortex.

mm distant from the medulla was further marked with a green stitch. The extremities of the green stitch can be observed in Fig. 6.13b on the 5 μm histology slice. The illustrated slice is representative of the whole sample, which was found to have only radial heterogeneity. In Fig. 6.13b, the medulla and the cortex appear similar and are not easily distinguishable.

In order to facilitate the correspondence between dielectric data and histological information, the medulla and the measurement point marked with the stitch are further highlighted in Fig. 6.14. Specifically, the measurement point was identified by considering the location of the probe (which has a diameter of 2.2 mm) and the distance of the measurement point from the stitch.

The corresponding dielectric traces of the measurement sites illustrated in Fig. 6.13 are reported in Fig. 6.15 together with the reference data from Salahuddin *et al.* [133].

The measured data is comparable with the reference data. In fact, a difference of approximately 1% between the measured data and the reference data was found for medulla, for both relative permittivity and conductivity

CHAPTER 6. POST-MEASUREMENT HISTOLOGY

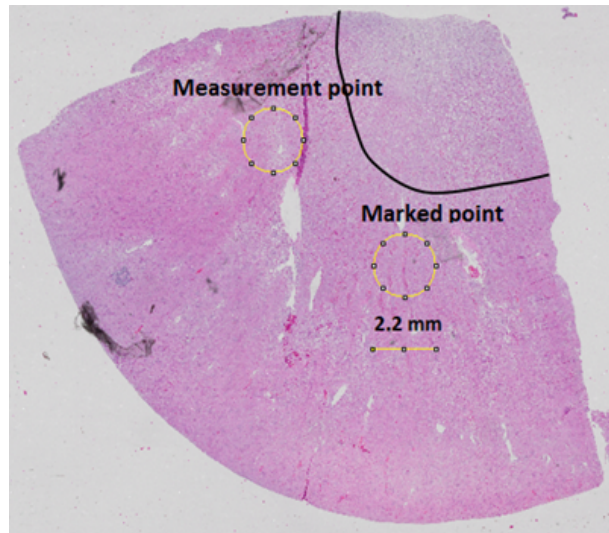


Figure 6.14: 5 μm histological slice of the kidney sample in Fig. 6.13 used to support the dielectric data acquired to validate the sensing radius findings of Chapter 4. On the histological slice, the medulla and the measurement point marked with the stitch are highlighted, in order to facilitate the correspondence between dielectric data and histological information. The measurement point was identified by considering the location of the probe (which has a diameter of 2.2 mm) and the distance of the measurement point from the stitch.

data. Differences of approximately 3% and 5% were found for cortex, in terms of relative permittivity and conductivity, respectively. These differences are all within the measurement uncertainty of biological tissues.

Furthermore, the data from the cortex measurement point close to the medulla overlaps with the average data from the cortex, which confirms that the sensing radius in cortex is less than 2.1 mm (i.e., the radius of the probe which is 1.1 mm + the distance of the measurement point from the medulla which is 1 mm), which is in agreement with the sensing radius findings from Chapter 4.

6.2.2.2 Validation of dielectric contribution findings

In order to validate the dielectric contribution findings of Chapter 5, the histological information and the corresponding dielectric data from a subset of radially heterogeneous biological samples are presented next. Specifically, Fig. 6.16 shows the histology of Sample LK2 (previously reported in Table 6.2). In order to facilitate the association of the dielectric data with the histological tissue content, post-fixation and post-processing sample pictures are reported together with a sample slice imaged with the microscope.

CHAPTER 6. POST-MEASUREMENT HISTOLOGY

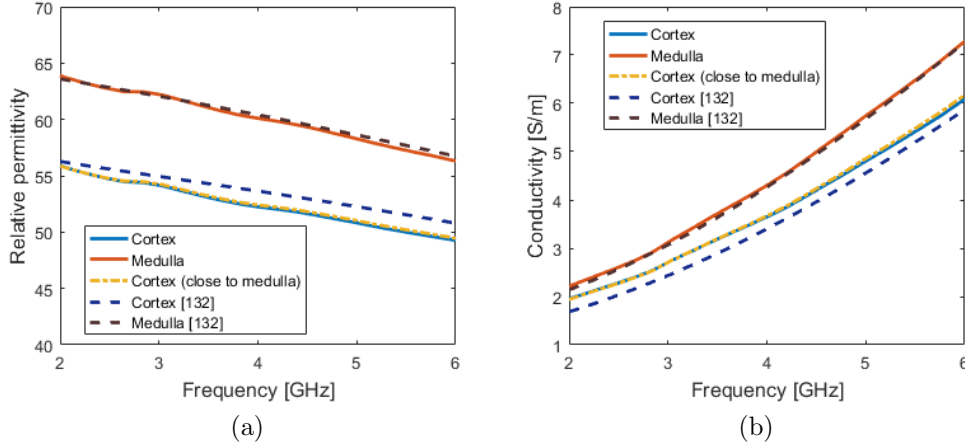


Figure 6.15: (a) Relative permittivity and (b) conductivity traces from three measurements performed on the kidney sample in Fig. 6.13 to validate the sensing radius findings of Chapter 4. Among the three measurements, one measurement was performed on the medulla, one measurement on the cortex far from the medulla and one measurement on the cortex close to the medulla. A difference of less than 1% was found between the measurements performed on the two cortex regions, thus suggesting that the sensing radius for cortex is within 2.1 mm (i.e., the radius of the probe which is 1.1 mm + the distance of the measurement point from the medulla which was 1 mm). In addition, in both (a) and (b), the porcine cortex and medulla data from Salahuddin *et al.* [133] is reported. The measurement data is in agreement with the reference data, since only differences within the tissue measurement uncertainty (less than 5%) were found between measurement and reference data.

Fig. 6.16a presents four marked measurement sites: one on the medulla, one at the interface between medulla and cortex, and two on the cortex (one close to and the other far from the interface). The measurement sites at and closer to the interface were further marked with green stitches, since the marks faded away during sample processing, as is clear from Fig. 6.16b. Furthermore, Fig. 6.16c reports the 10 μm slice obtained at the depth of 0.5 mm. A 10 μm instead of a 5 μm slice is reported, since it enables distinction between the medulla and cortex because of the additional cell layer present in the 10 μm slice compared to the 5 μm slice. The slice in Fig. 6.16c is representative of the whole sample, slices at depths higher than 0.5 mm presented the same histological features, thus suggesting that the sample was heterogeneous only radially (slices at depths lower than 0.5 mm were very fibrous and crumbly, thus not suitable for staining, and not analysed further).

On the histological slice in Fig. 6.16c, the extremities of the green stitch marking the measurement point at the interface between the cortex and

CHAPTER 6. POST-MEASUREMENT HISTOLOGY

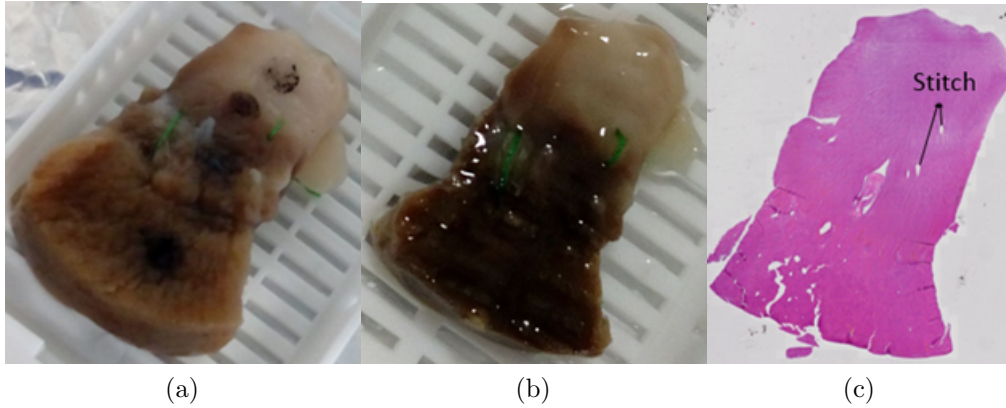


Figure 6.16: (a) Post-fixation picture, (b) post-processing picture and (c) 10 μm histological slice of Sample LK2 (reported in Table 6.2) used to support the dielectric data acquired to validate the dielectric contribution findings of Chapter 5. Among the four marked measurement sites in (a), two are from the medulla, two from the cortex (with one point closer to the medulla than the other) and one is at the cortex-medulla interface. The two measurement sites at/closer to the interface were further marked with green stitches, since the marks faded away during sample processing, as is clear in (b). In (c), the extremities of the green stitch marking the measurement point at the interface between the cortex and medulla are highlighted, since this point is used to validate the dielectric contribution findings of two side-by-side tissues. The slice in (c) is representative of the whole sample, which was found to have only radial heterogeneities. In (c), the 10 μm slice allows for the distinction of the medulla (which appears more blue than pink) from the cortex (which appears mostly pink).

medulla are highlighted, since this point is used to validate the dielectric contribution findings of two side-by-side tissues. In order to enhance the interpretation of the dielectric data from the cortex-medulla interface, the medulla and the measurement point at the interface (marked with the stitch) are highlighted on the 10 μm histology slice in Fig. 6.17. Specifically, the measurement point was identified by considering the location of the probe (which has a diameter of 2.2 mm) and the distance of the measurement point from the stitch. Furthermore, Fig. 6.17 reports the dimensions of the slice as a comparison with the dimensions of Sample LK2 reported in Table 6.2. The dimensions in Fig. 6.17 are the same as the dimensions in Table 6.2, thus suggesting that the sample was appropriately sliced in the desired orientation.

The dielectric traces of Sample LK2 corresponding to the measurements on the cortex, medulla and cortex-medulla interface are reported in Fig. 6.17. For an enhanced interpretation of the dielectric data, Fig. 6.17 reports the reference data from Salahuddin *et al.* [133] and the estimated signal at

CHAPTER 6. POST-MEASUREMENT HISTOLOGY

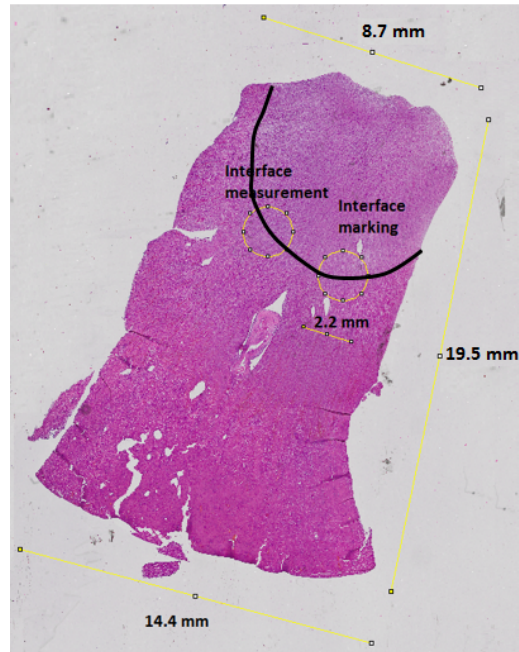


Figure 6.17: 10 μm histological slice of Sample LK2 used to support the dielectric data acquired to validate the dielectric contribution findings of Chapter 5. On the histological slice, the medulla and the measurement point at the cortex-medulla interface (marked with the stitch) are highlighted, in order to facilitate the correspondence between dielectric data and histological information. The measurement point was identified by considering the location of the probe (which has a diameter of 2.2 mm) and the distance of the measurement point from the stitch.

the interface obtained by averaging the cortex and medulla signals. The estimated signal from the average properties is the expected trace based on the finding that side-by-side tissues contribute equally to a dielectric measurement, when the probe is centered on the interface between the tissues, as discussed in Chapter 5.

The measured cortex and medulla data was consistently different from the reference data by Salahuddin *et al.* [133] and the data reported previously in Fig. 6.15, likely due to tissue dehydration, different tissue handling procedures and temperature variations. Specifically, differences of 9% and 10% were found for the cortex, in terms of relative permittivity and conductivity, respectively. In addition, differences of 5% and 6% were found for the cortex, in terms of relative permittivity and conductivity, respectively. The dielectric values for the medulla are closer to the reference data than for the cortex, due to the fact that the cortex regions dehydrate more rapidly than the medulla region. However, measuring the exact magnitude of the

CHAPTER 6. POST-MEASUREMENT HISTOLOGY

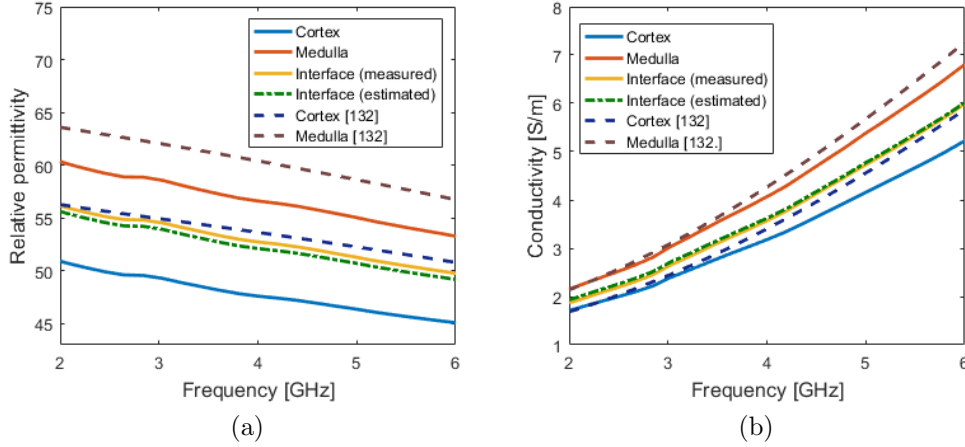


Figure 6.18: (a) Relative permittivity and (b) conductivity traces from three measurements performed on Sample LK2 to validate the findings (in Chapter 5) regarding the dielectric contribution of side-by-side tissues. Among the three measurements, one measurement was performed on the medulla, one measurement on the cortex (far from the medulla) and one measurement at the cortex-medulla interface. The data from the cortex-medulla interface is comparable with the estimated data obtained by averaging the data from the cortex and medulla, thus suggesting that the cortex and medulla had equal dielectric contribution to the dielectric signal acquired at the interface. In addition, in both (a) and (b), the porcine cortex and medulla data from Salahuddin *et al.* [133] is reported. The measured cortex and medulla data was consistently different from the reference data due to tissue dehydration, different tissue handling procedures and temperature variations.

properties is not the aim of this study, since the actual properties are not as important as comparing the tissue dielectric contributions.

Furthermore, in Fig. 6.18, the data from the cortex-medulla interface is comparable with the estimated data obtained by averaging the data from the cortex and medulla. In fact, less than 1% difference was found between the two dielectric traces, for both relative permittivity and conductivity, thus suggesting that the cortex and medulla had equal dielectric contribution to the dielectric signal acquired at the interface. Hence, with the support of the histological information summarised in Fig. 6.17, the measurements of Sample LK2 reported in Fig. 6.18 confirmed the dielectric contribution findings regarding side-by-side tissues.

In Chapter 5, concentric tissue arrangements were also examined along with the side-by-side arrangements. However, here, due to the irreversible shrinkage of fat tissue, the histological analysis was not able to support the validation of dielectric contribution findings regarding concentric tissues. For

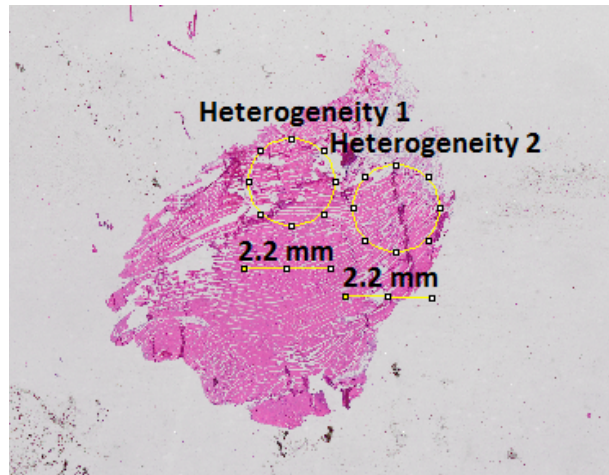


Figure 6.19: 5 μm histological slice of Sample PM1, where the two concentrically heterogeneous measurement points are highlighted with the aim of validating the findings (in Chapter 5) regarding the dielectric contribution of concentric tissues. However, the morphology of the two concentrically heterogeneous measurement sites changed during the traditional histology procedure, making the interpretation of the dielectric data in Fig. 6.20 difficult.

instance, Fig. 6.19 reports a histological slice of Sample PM1 by highlighting the two concentrically heterogeneous measurement sites. In the histology image, the fat tissue surrounding the muscle tissue is no longer visible, while it was clearly present before undergoing histological processing. Therefore, it was not possible to associate the dielectric traces reported in Fig. 6.20 with the histological information reported in Fig. 6.19. However, the results in terms of the measured dielectric data relative to the pre-processing dimensions of the tissue regions are consistent with the findings of Chapter 5.

Due to the limitations of traditional histology as a technique to support the dielectric characterisation of heterogeneous biological samples, the results of the preliminary experiments regarding microCT-based histology are provided in the following subsection.

6.2.3 MicroCT preliminary results

In this subsection, the results from the microCT preliminary experiments conducted in the second study are discussed, together with the advantages of microCT over traditional histology. In fact, compared to traditional histology, the sample pre-processing for microCT is less destructive and less time-consuming. As a result, the microCT-based histology presents less confounders than traditional histology. However, microCT has a few

CHAPTER 6. POST-MEASUREMENT HISTOLOGY

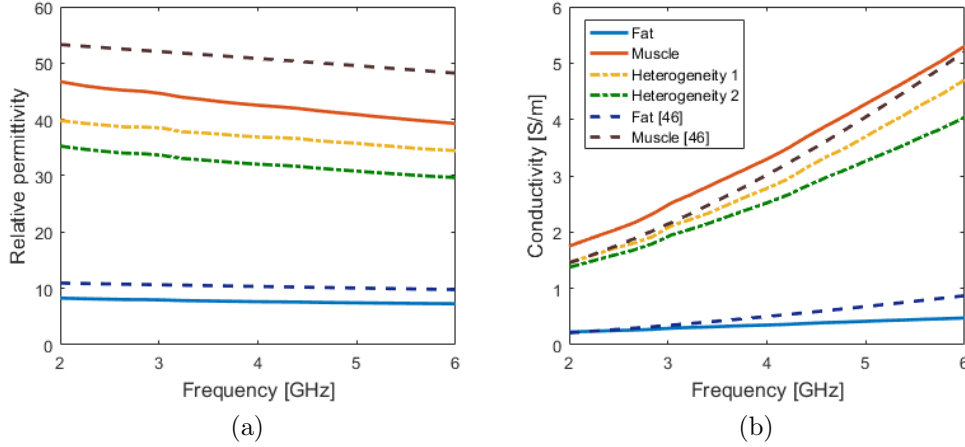


Figure 6.20: (a) Relative permittivity and (b) conductivity traces from four measurements performed on Sample PM1 to validate the findings (in Chapter 5) regarding the dielectric contribution of concentric tissues. Among the four measurements, one measurement was performed on muscle, one measurement on fat and two measurements on concentrically heterogeneous tissue consisting of muscle surrounded by concentric fat. Due to the morphology change of Sample PM1 during traditional histology, it was not possible to associate the dielectric traces from the concentrically heterogeneous points with the histological information reported in Fig. 6.19.

confounders in common with traditional histology, since fixation represents the first step in the sample pre-processing of both the techniques. Thus, the differences in size between the pre-fixation and post-fixation samples (which were discussed in Section 6.2.1) also need to be considered during the analysis of the images obtained by microCT.

The reconstructed images from the preliminary microCT scans (the second study in Table 6.1) performed on the two samples, ovine muscle and rodent kidney, are reported in Fig. 6.21 and Fig. 6.22, respectively. For each sample, only one slice along the z-axis is illustrated, due to the fact that the two scanned samples presented only radial heterogeneities, and therefore the other slices do not add further information. In both Fig. 6.21 and Fig. 6.22, the 1 mm scale is reported to support the interpretation of the images.

From the ovine sample in Fig. 6.21, it is easy to distinguish the muscle tissue, visualised in white, from the fat tissue, visualised in black, since Lugol's iodine is able to perfuse through muscle but not through fat [202].

On the other hand, Fig. 6.22 demonstrates that Lugol's iodine is able to perfuse through both the cortex and medulla tissues of the rodent kidney sample, but to different extents. In particular, the cortex region appears whiter than the medulla region. In Fig. 6.22, the medulla region is contoured

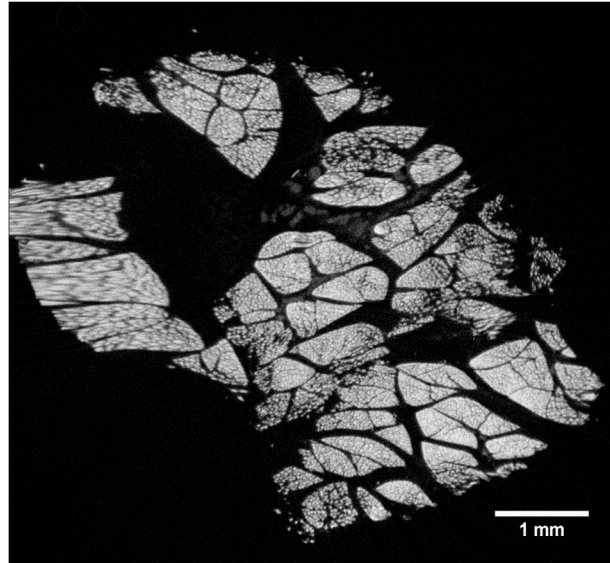


Figure 6.21: MicroCT scan obtained at $0.5 \mu\text{m}$ depth from the surface of an ovine muscle sample. From the image, it is easy to distinguish the muscle tissue, visualised in white, from the fat tissue, visualised in black, since the contrast agent (Lugol's iodine) is able to perfuse through muscle but not through fat.

by a red solid line for ease of visualisation.

In summary, these preliminary scans demonstrated that high quality images with a resolution of $10 \mu\text{m}$ can be obtained by using Lugol's iodine as contrast agent for microCT scans of ovine muscle and rodent kidney samples. Since previous studies found no staining differences among samples from different animal species [199], these preliminary results can be extended to muscle and kidney samples from other animal species.

Hence, these preliminary experiments demonstrated the feasibility of conducting microCT with Lugol's iodine as contrast agent as an alternative to traditional histology to support the dielectric characterisation of heterogeneous biological samples. For this reason, the microCT results are compared with the traditional histology results in the third study discussed in the following section.

6.2.4 Dielectric characterisation of a highly heterogeneous sample through microCT-based and traditional histology

In this subsection, both the results from microCT-based histology and traditional histology are used to interpret the dielectric data acquired from

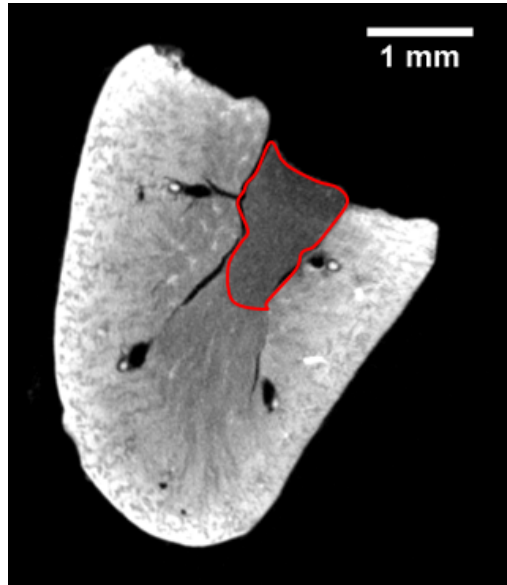


Figure 6.22: MicroCT scan obtained at 0.5 mm depth from the surface of a rodent kidney sample. From the image, it is easy to distinguish the cortex region from the medulla region, since the cortex region is brighter than the medulla region. For ease of visualisation, the medulla region is contoured by a red solid line.

a mammary fat pad, with the aim of validating the applicability of the findings of the previous experimental chapters on a highly heterogeneous biological sample.

As mentioned in Section 6.1.1, the mammary fat pad was dielectrically characterised by performing dielectric measurements across different points: three points on a mostly cancerous breast region, three points on a mostly fatty region and two points at the interface between the two regions. Each of the tissue regions were indicated by a surgeon specialising in breast cancer. The measured dielectric data is plotted in Fig. 6.23 together with the reference data from Lazebnik *et al.* [11].

In Fig. 6.23, while the average measured cancerous tissue data is close to the data by Lazebnik *et al.*, the average measured fatty tissue data is notably different. Specifically, differences within 10% and 6% were found for cancerous tissue relative permittivity and conductivity data, respectively. Conversely, differences above 80% were found for the fatty tissue dielectric data, thus suggesting that the mostly fatty tissue could present inclusions of cancerous tissue. Also the results from the interface between the cancerous and fat tissue regions suggest the presence of mostly cancerous tissue within these regions.

Furthermore, these results were confirmed by microCT and histological

CHAPTER 6. POST-MEASUREMENT HISTOLOGY

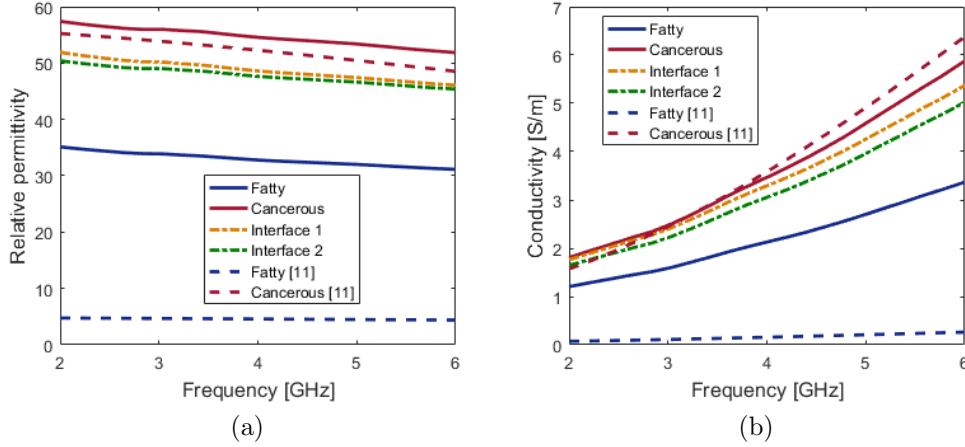


Figure 6.23: Relative permittivity and (b) conductivity traces from three measurement regions of the mammary fat pad, to validate the applicability of the findings of Chapter 4 and Chapter 5 to highly heterogeneous biological samples. The three measurement regions include a mostly cancerous breast region, a mostly fatty region and two points at the interface between the two regions. In addition, in both (a) and (b), the human breast cancerous and fat tissue data from Lazebnik *et al.* [11] is reported as reference. While the average measured cancerous tissue data is close to the reference data, the average measured fatty tissue data is notably different. The considerable differences (above 80%) between measurement and reference data for the fatty tissue region suggest that the mostly fatty tissue may have presented inclusions of cancerous tissue.

images obtained for the interface region of the mammary fat pad and reported in Fig. 6.24 and Fig. 6.25, respectively. In fact, the microCT image obtained at the depth of 0.3 mm and reported in Fig. 6.24 presents a highly heterogeneous structure. In the image, it is seen that homogeneous fat, which appears completely in black (as with the ovine muscle sample in Fig. 6.21), occupies less than the 1% of the entire volume. Most of the volume is occupied by a combination of tumour, fat and blood vessels (bright spots). Similar tissue content was found across all the scans obtained at different depths.

This outcome is further confirmed by the histology slice obtained at the depth of approximately 0.3 mm and reported in Fig. 6.25. The contours of the histological slice appears slightly different from the contours of the sample imaged by microCT. These changes are due to the orientation of the sample immersed in Lugol's iodine that was not parallel to the bottom of the sample holder during the microCT scan. However, the histological slice shows the same type of heterogeneity consisting of a combination of fat, tumour and blood vessels.

CHAPTER 6. POST-MEASUREMENT HISTOLOGY

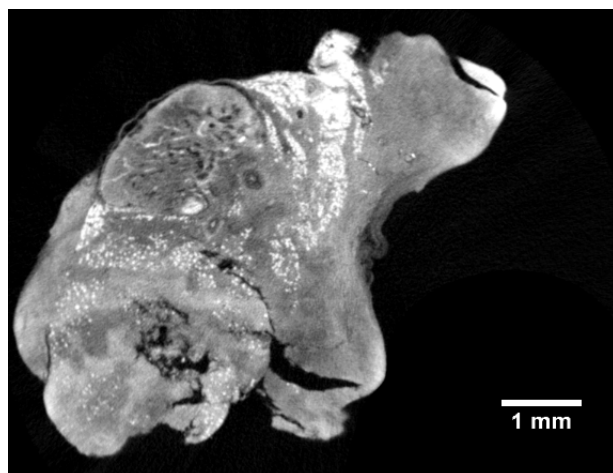


Figure 6.24: MicroCT scan obtained at 0.3 mm depth from the surface of the mammary fat pad. The heterogeneity visible in the image is representative of that of the whole sample, and illustrates the tissue structure of the mammary fat pad, which includes a heterogeneous mixture of tumour, fat and blood vessels (bright spots). The microCT scan supports the interpretation of the dielectric traces in Fig. 6.23.

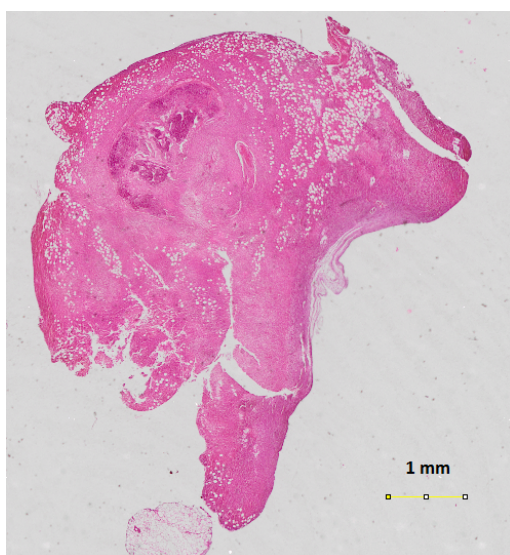


Figure 6.25: 5 μm histological slice obtained at 0.3 mm depth from the surface from the mammary fat pad. Together with the microCT scan in Fig. 6.24, the histological slice including a heterogeneous mixture of tumour, fat and blood vessels (bright spots), supports the interpretation of the dielectric traces in Fig. 6.23. The contours of the histological slice appear slightly different from the contours of the sample imaged by microCT. These changes are due to the orientation of the sample immersed in Lugol's iodine that was not parallel to the bottom of the sample holder during the microCT scan.

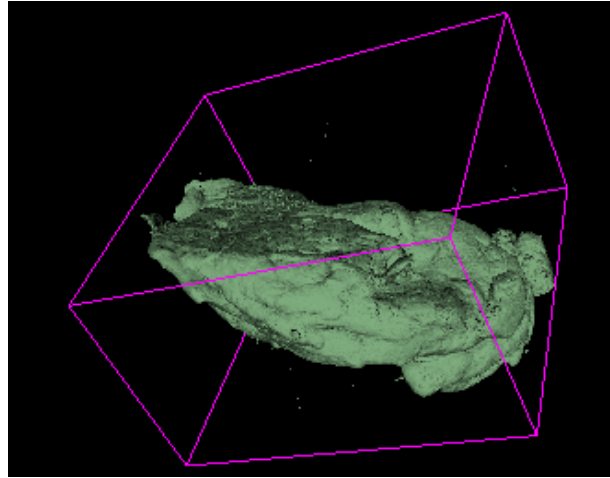


Figure 6.26: 3D reconstruction of the mammary fat pad from the microCT scans (a 2D slice of which is reported in Fig. 6.24). The reconstruction shows that the sample immersed in Lugol’s iodine during the scan was not parallel to the bottom of the sample holder. This suggests that the orientation of the scanned sample needs to be taken into account when associating the measured dielectric data with the tissue structure reconstructed from the microCT scans.

Thus, both microCT-based histology and traditional histology were able to provide an extent of the heterogeneity of the sample. However, due to the highly heterogeneous nature of the sample, it is not possible to accurately associate the measured dielectric data with the histological content of the sample. Although microCT allows for the calculation of the percentage of volume occupied by each tissue, the dielectric contribution of each tissue cannot be calculated because the relationship between volume occupied by each tissue and dielectric contribution is not directly proportional (as was observed in Chapter 5) and, thus, unknown for samples showing complex structures.

To conclude, although microCT-based histology and traditional histology were able to provide an extent of the sample heterogeneity, these tools alone are not sufficient to find an accurate correspondence between dielectric data and tissue content of highly heterogeneous samples. To this extent, further studies need to be conducted. These studies may involve 3D reconstruction of the measured samples, which can be simplified and used to simulate the EM interaction of the sample with the dielectric probe. These EM simulations could be used to identify the sensing radius and sensing depth and to model the dielectric contribution of each tissue within the sensing volume for accurate dielectric profiling of the measured heterogeneous samples. As an example, the microCT scans of the mammary fat pad were processed in

CHAPTER 6. POST-MEASUREMENT HISTOLOGY

Slicer (version 4.10.1) to reconstruct the 3D structure of the sample, which is reported in Fig. 6.26. The 3D reconstruction of the mammary fat pad in Fig. 6.26 shows that the sample immersed in Lugol's iodine during the scan was not parallel to the bottom of the sample holder. Samples that are not parallel to the bottom of the holder can lead to inaccurate association of the dielectric data with the sample constituent tissues when single slice analysis is conducted and the different distances of each image corner from the sample surface is not taken into account. Thus, the 3D reconstructed structure in Fig. 6.26 suggests that the orientation of the scanned sample needs to be taken into account when associating the measured dielectric data with the tissue structure reconstructed from the microCT scans. Further suggestions regarding future work to be conducted with the aim of improving the dielectric characterisation of biological tissues are reported in the next and final chapter of this thesis.

In summary, the results of this section suggest that a customised traditional histology protocol would be needed for different biological samples depending on their level of heterogeneity and their constituent tissue types. For example, for an accurate histological characterisation, different types of marking need to be considered based on the texture of each sample constituent tissue. Also, the shrinkage of each sample constituent tissue needs to be monitored during the traditional histology process and taken into account when associating the acquired dielectric data with the sample tissue content. Furthermore, a higher number of slices need to be considered for an accurate histological profile of highly heterogeneous samples. However, a high number of histology slices requires a notable burden of time, computational memory and resources. Furthermore, due to the destructive nature of traditional histology (e.g., slices tearing and crumbling), a subset of slices may unavoidably get damaged and the histological information of a portion of sample can get lost. For these reasons, the use of microCT to reconstruct the full histological sample profile is strongly recommended as a tool to improve the dielectric characterisation of highly heterogeneous biological samples.

6.3 Summary

In this chapter, the significance of the experimental findings summarised in Chapter 4 and Chapter 5 (i.e., the sensing radius and dielectric contribution findings) has been demonstrated in the dielectric characterisation of radially heterogeneous biological samples. In particular, a subset of biological tissue samples was analysed histologically after the acquisition of the dielectric

CHAPTER 6. POST-MEASUREMENT HISTOLOGY

properties.

During the post-measurement histological process, the challenges in associating the dielectric data with the sample histological information were identified. For instance, it was found that sample fixation and processing modify the sample morphology and that the sample processing and slicing can irreversibly damage the tissues. However, despite the limited histological information obtained for each sample, three radially heterogeneous samples were analysed histologically in combination with the acquired dielectric properties. This analysis partly validated the significance of the sensing radius and dielectric contribution findings in the dielectric characterisation of radially heterogeneous tissue samples. The significance of the experimental findings was not fully validated, because of the histology confounders compromising the interpretation of the dielectric data. For instance, the sample processing step caused a tissue shrinkage of above 50% within a subset of biological samples, which thus compromised the determination of the sensing radius and the dielectric contribution of the tissues constituting the sample.

Thus, due to the time-consuming, invasive and destructive process of traditional histology, microCT was evaluated as a novel histology technique to support the correspondence between the acquired dielectric data and the tissue content of a heterogeneous sample. Specifically, a subset of samples were scanned with microCT, and preliminary results were examined. The technique was found to be non-destructive, less invasive and less time-consuming than traditional histology. The only limitation of the technique involves the sample staining with a contrast agent, which can alter the morphology of the tissue sample on the basis of the staining time.

Finally, both microCT-based histology and traditional histology were conducted on a highly heterogeneous tissue sample (the mammary fat pad) to evaluate the applicability of the sensing radius and dielectric contribution findings to highly heterogeneous tissue samples. This final analysis highlighted the applicability of these findings to radially heterogeneous samples with simple structures. However, further investigation is needed for accurate dielectric characterisation of highly heterogeneous samples. To this extent, Chapter 7 summarises the findings of this thesis and suggests potential dielectric studies to be conducted with the support of microCT.

Conclusions and future work

This chapter summarises the research objectives and results of this thesis. The motivation and main findings of this thesis are summarised in Section 7.1. Appropriate future work to develop and extend the findings of this thesis are presented in Section 7.2, which concludes this thesis.

7.1 Summary and Conclusions

Accurate knowledge of the dielectric properties of biological tissues is crucial for dosimetry studies and the design and optimisation of new EM diagnostic and therapeutic systems. In fact, accurate dielectric measurement of biological tissues is crucial in achieving high-quality tissue dielectric data, which can be used for reliable dosimetry calculations and the implementation of effective EM medical devices. Dielectric measurements of biological tissues in the MW range may be performed using the transmission line, cavity, and open-ended coaxial probe techniques. The open-ended coaxial probe is the most common technique since it is non-destructive and applicable for both *in vivo* and *ex vivo* tissue measurements over a broad frequency range. Although the dielectric measurement with the open-ended coaxial probe technique appears straightforward, a number of equipment-related and tissue-related confounders can affect the measurement procedure, thus compromising the reliability of the measured dielectric data. To this extent, numerous studies have been conducted with the aim of developing standard techniques to compensate for or reduce the effect of equipment-related confounders on the measured data. Also, a number of studies have investigated the effect of tissue-related confounders on the measured dielectric data. However, standard techniques to address tissue-related confounders have not been developed, and the impact of many tissue-related confounders remains unclear. For this reason, tissue-related confounders and sources of error are often the cause of tissue dielectric data inconsistencies.

This general overview of the state-of-the-art of the dielectric measurement of biological tissues is presented in Chapter 1, which introduces the motivation for this thesis. Firstly, this thesis reviews all of the measurement

CHAPTER 7. CONCLUSIONS AND FUTURE WORK

confounders, with specific focus on tissue-related confounders. Then, since inconsistencies in dielectric data mostly involve heterogeneous biological tissues, the confounders associated with tissue heterogeneity are investigated. Quantitative analyses of various confounders impacting dielectric data from heterogeneous tissues are the primary contribution of this thesis.

Chapter 2 discusses fundamental background information regarding the dielectric properties of biological tissues and provides a detailed overview of the state-of-the-art in the acquisition of dielectric properties of biological tissues, both in terms of measurement techniques and seminal dielectric studies. In this chapter, tissue-related confounders such as temperature variations, unsteady probe-sample contact, sample handling procedures, *in vivo* versus *ex vivo* differences, and sample tissue heterogeneity are identified. Among these confounders, tissue heterogeneity is the confounder that most affects the measurement repeatability, and thus leads to inconsistencies in dielectric data.

Open-ended coaxial probe measurement confounders and common practices

Chapter 3 discusses tissue-related confounders, focussing on the confounders related to tissue heterogeneity. Specifically, Chapter 3 discusses each step of the open-ended coaxial probe measurement protocol, highlighting common practices, challenges, and techniques for controlling and/or compensating for confounders. Initially, Chapter 3 discusses the calibration and validation steps, with the corresponding equipment-related confounders. Subsequently, the focus is on the sample handling, the actual measurement procedure and the sample post-processing, with the corresponding tissue-related confounders. In particular, the last part of the chapter differentiates the dielectric characterisation of homogeneous biological tissues from the dielectric characterisation of heterogeneous biological tissues. In fact, while homogeneous biological samples do not require sample post-processing, post-measurement histological analysis is generally conducted for heterogeneous biological samples. Histological analysis of a heterogeneous biological sample enables identification of the constituent tissue types in the sample that may have contributed to the acquired dielectric properties, thus facilitating the association of the acquired dielectric data with the tissue content of the sample. However, different confounders can affect the histological procedure and the selection of the portion of the sample (i.e., the histology region) to examine with the microscope. General confounders (i.e., not tissue-specific) that can affect the histology procedure include poor fixation, uneven levels of staining, different procedures of slide digitation, and inconsistent histo-

CHAPTER 7. CONCLUSIONS AND FUTURE WORK

logical interpretation and tissue categorisation. Moreover, when selecting the histology region, factors related to the calculation of the sensing volume of the probe and the calculation of the dielectric contribution of each tissue within the sensing volume need to be taken into account for an accurate interpretation of the acquired dielectric data. The sensing volume and the tissue dielectric contributions are generally determined by preliminary experiments and numerical simulations. The calculation of the sensing volume and the dielectric contribution of each tissue occupying the sensing volume are not straightforward, since both sensing volume and dielectric contribution can be sample-specific, i.e., dependent on the characteristics of the tissue sample. However, in order to simplify the calculation of the sensing volume and the tissue dielectric contribution within the sensing volume, it is recommended to consider the maximum sensing volume as the starting point for the tissue sample dielectric characterisation. Then, the sensing volume estimation can be refined based on the results of preliminary simulations or experiments, which take into account the dielectric properties of each sample constituent. To this extent, Chapter 4 includes estimations of both maximum sensing radius and sensing radius depending on the dielectric properties of the constituent tissues within the sensing volume.

Sensing radius analysis and modelling

Chapter 4 highlights the importance of an accurate calculation of the sensing volume, not only to define the histology region within highly heterogeneous biological samples, but also to define the minimum size of the homogeneous tissue region that ensures accurate tissue dielectric measurements, without the influence of surrounding tissues within biological samples with simple heterogeneities. This chapter also presents the state-of-the-art in sensing volume studies and provides the motivation for investigating the sensing radius. While the sensing depth had been previously examined in a range of scenarios, the sensing radius had only been analysed in select scenarios with limited number of probes and tissue-mimicking materials. Therefore, Chapter 4 examines the sensing radius both numerically and experimentally with a range of probes of different dimensions and a wide variety of materials including biological tissues, with the aim of modelling the dependence of the sensing radius on the probe dimensions and the interrogated tissue properties. Firstly, the dependence of the maximum sensing radius on the dimensions of the coaxial probe, i.e. the inner conductor radius, insulator width, outer conductor inner radius and outer conductor width, is analysed. This analysis leads to the conclusions that the sensing radius: i) is not affected by the width of the outer conductor, ii) increases

CHAPTER 7. CONCLUSIONS AND FUTURE WORK

approximately linearly with the inner radius of the outer conductor (and thus with the radius of the inner conductor and the width of the insulator), and iii) is primarily affected by the radius of the inner conductor. Secondly, the dependence of the sensing radius on the dielectric properties of concentric biological samples, consisting of an inner tissue surrounded by a concentric outer tissue, is analysed. This analysis suggests that the sensing radius increases with the contrast in relative permittivity between the two concentric constituent tissues, and that the relative permittivity of the inner tissue greatly impacts the value of the sensing radius. Specifically, the lower the impedance mismatch between the probe and the inner tissue (i.e., the higher the permittivity of the inner issue), the higher the estimated sensing radius. Lastly, the sensing radius values obtained numerically are used for the development of two sets of regression line and neural network models. The first set of models are able to predict the sensing radius from knowledge of the probe dimensions and sample dielectric properties, while the second set of models are able to predict the sensing radius of the Keysight slim form probe, the most commonly used probe in recent tissue dielectric studies, from knowledge of the sample dielectric properties. For both sets of models, the neural network is found to generally outperform the regression line and is able to predict the sensing radius with an average accuracy to within approximately 5%.

The outcomes of the study in Chapter 4 confirm that the sensing radius depends on the dielectric properties of the individual tissues occupying the sensing volume, which, in turn, enables the interpretation of the dielectric properties of the interrogated sample. This interdependence between sensing volume and tissue dielectric properties represents a challenge for the dielectric characterisation of heterogeneous biological tissues. In order to address this challenge, it is recommended to use the maximum sensing radius estimation for an initial interpretation of the dielectric properties measured from a heterogeneous sample, which can then be refined if the dielectric properties of the individual tissues constituting the sample are known. This methodology represents the foundation for a rigorous estimation of the sensing radius, which supports accurate and consistent dielectric measurement of biological tissues. However, even with a rigorous estimation of the sensing radius, inaccuracies in the dielectric characterisation of highly heterogeneous tissue samples can occur, due to the lack of knowledge about the dielectric contribution of the tissues within the sensing radius to the acquired dielectric data.

CHAPTER 7. CONCLUSIONS AND FUTURE WORK

Sample tissue dielectric contribution analysis and modelling

Chapter 5 examines the dielectric contribution of the sample constituents (within the sensing radius) to the acquired dielectric data. This analysis is conducted through both dielectric measurements and numerical simulations performed on several well-controlled radially heterogeneous samples. Specifically, in order to examine the dependence of the dielectric contribution on the material distribution and dielectric properties, two different radially heterogeneous samples are investigated: samples with linear heterogeneity configuration, consisting of two side-by-side tissue-mimicking materials or biological tissues spanning a wide range of permittivities, and samples with concentric heterogeneity configuration, consisting of two concentric tissue-mimicking materials or biological tissues spanning a wide range of permittivities. Both measurements and simulations conducted on these samples confirm that the material dielectric contribution depends on the spatial distribution of the constituent materials within the sensing volume. In particular, the measurements and simulations conducted on the samples with the linear heterogeneity configuration suggest that the dielectric properties measured at the interface of two side-by-side materials are proportional to the volume occupied by each constituent material and do not depend on the individual dielectric properties of each constituent material. Conversely, the measurements and simulations conducted on the samples with the concentric heterogeneity configuration suggest that the measured dielectric properties are not proportional to the volume occupied by each constituent material and depend on the individual dielectric properties of each constituent material. Overall, this investigation provides the foundation for more accurate dielectric measurements of heterogeneous tissues.

Sample tissue dielectric characterisation through histology

The significance of the sensing radius and dielectric contribution findings of Chapter 4 and Chapter 5, respectively, is demonstrated in Chapter 6, where heterogeneous biological samples are analysed dielectrically with the support of post-measurement histological analysis. In particular, the results of Chapter 6 are consistent with the sensing radius values obtained for specific tissue types in Chapter 4, and the outcome regarding the dielectric contribution of side-by-side tissues, which suggests that the dielectric properties measured at the interface of two side-by-side tissues are proportional to the volume occupied by each constituent tissue. However, in Chapter 6, the significance of all the findings of Chapter 4 and Chapter 5 is not fully demonstrated, because of the traditional histology challenges compromising the interpretation of the dielectric data, when the acquired data is associ-

CHAPTER 7. CONCLUSIONS AND FUTURE WORK

ated with the sample histological information. The sources of error of the traditional histology process are mostly related to sample fixation and processing, which irreversibly change the sample morphology and compromise the histological analysis of subsets of histological slices. Hence, due to the invasive and often destructive nature of traditional histology, Chapter 6 also evaluates microCT as a novel histology technique to support the correspondence between the acquired dielectric data and the tissue content of a heterogeneous sample. Lastly, both microCT-based histology and traditional histology are conducted on a highly heterogeneous tissue sample to evaluate the applicability of the sensing radius and dielectric contribution findings to highly heterogeneous tissue samples. This final analysis suggests that knowledge of the sensing radius and the dielectric contribution of each tissue within the sensing radius is fundamental for the dielectric characterisation of radially heterogeneous biological samples. However, further investigation is needed for accurate dielectric characterisation of highly heterogeneous biological samples.

7.2 Future Work

Conclusions from the review of the state-of-the-art in tissue dielectric studies, provided in Chapter 2, suggest that future work should involve standardising the dielectric measurement protocol for biological tissues.

Standard methods to compensate for measurement confounders

As standard techniques have been developed in the past to compensate for equipment-related confounders, standard methods to compensate for tissue-related confounders could be developed in the future in order to reduce uncertainty in tissue data, which causes inconsistencies across studies. To this extent, the effect of each tissue-related confounder could be quantified, and the possible compensation procedures for each confounder compared. In this way, the techniques that guarantee the highest accuracy and repeatability in the measurement could be standardised. In particular, since the tissue-related confounders that introduce the highest uncertainty in the dielectric measurement of homogeneous biological tissues include probe-tissue contact and sample moisture content, extensive studies could be conducted to find standard methods to reduce these confounders. For instance, along with a close visual inspection of the probe tip and the tissue surface, the probe-sample contact could be improved by using appropriate force and position sensors, which could considerably increase the stability of the measurement system. In addition, along with minimising the time between surgical

CHAPTER 7. CONCLUSIONS AND FUTURE WORK

removal of the sample and dielectric data acquisition, the sample moisture content could be monitored with the use of a weigh scale. However, due to the large number of tissue-related confounders, it is not possible to deal with all of confounders with the same level of accuracy. In particular, if new sensors are used in dielectric measurements to control or monitor some parameters, the system complexity increases and other experimental errors may need to be considered. To this extent, the introduction of any new sensor in the standard measurement procedure needs to be supported by a number of experiments capable of demonstrating a significant increase in measurement accuracy and repeatability, although such a sensor would come at the cost of increasing the complexity of the system.

This thesis also suggests additional standardised steps in the dielectric measurement protocol in order to improve the dielectric characterisation of heterogeneous biological tissues, since measurements of heterogeneous tissues generally show a lower repeatability compared to those of homogeneous tissues. The low repeatability of heterogeneous biological tissues measurements could be increased by firstly characterising dielectrically every small homogeneous tissue region of the investigated heterogeneous sample, wherever possible. In fact, performing dielectric measurements on every small homogeneous tissue region enables accurate single tissue dielectric characterisation, which provides a complete dielectric profiling of the heterogeneous tissue sample. Single tissue dielectric characterisation can also provide an extent of the dielectric contribution of each single tissue within a heterogeneous measurement region.

Standard definition of sensing volume

In order to enhance the correspondence between dielectric data acquired from a heterogeneous sample and the histological content of the sample, a standardised definition of sensing volume and a standardised methodology for the calculation of the sensing radius and sensing depth are needed. A standard definition of sensing volume would result in equivalent values of sensing radius and sensing depth for specific probes and samples, calculated uniformly across different studies. Also, a standard methodology to calculate the standardly defined sensing volume would allow for the development of tools able to predict the sensing volume from knowledge of the physical dimensions of the probe and the dielectric properties of the tissues constituting the sample. Such tools could be used on a large scale across different research groups for the evaluation of the sensing volume of a specific probe for a specific sample.

Besides a standard calculation of the sensing volume, for the dielec-

CHAPTER 7. CONCLUSIONS AND FUTURE WORK

tric characterisation of highly heterogeneous biological sample, a standard methodology to associate the acquired dielectric data with the histological content of the sample is needed. Currently, such methodology is supported by the histological analysis of the sample previously characterised dielectrically. The histological process presents important limitations, which involve the change in morphology and the irreversible damage of the analysed sample. The irreversible damage of a sample can result in the loss of histological information, which can compromise the interpretation of the acquired dielectric data. For this reason, the histological analysis can be used only for samples with limited radial heterogeneities, within which the loss of histological slices does not compromise the reconstruction of the sample histological content. However, for an accurate histological analysis of these samples, future work needs to be conducted to monitor and compensate for the changes in morphology of each tissue constituting the analysed sample.

Standard techniques to support post-measurement processing

For an accurate analysis of highly heterogeneous biological samples, traditional histology is not recommended and novel non-invasive techniques need to be investigated. For instance, the histological analysis can be replaced by microCT, which is able to reconstruct the sample constituent tissue structure while minimising the change in sample morphology. However, in order to adopt microCT as standard technique to support the dielectric characterisation of heterogeneous biological tissues, extensive studies need to be conducted. For instance, a standard sample marking technique needs to be adopted to keep track of the sample orientation during the microCT scan. The sample marking would be vital since the microCT scan is generally performed with the sample immersed in a staining solution, where the sample can move. Therefore, the microCT images will not be in the same orientation as the original position in which the dielectric measurement was performed. As such, registration between the orientation of the sample in the microCT images and the orientation of the sample during the dielectric measurement will be needed. Furthermore, a standard staining protocol for soft tissues, for this application, needs to be developed. The staining of soft tissues with contrast agents is fundamental to increasing the tissue X-ray attenuation and thus enhancing the contrast between the different tissue types. Besides enhancing the soft tissue visualisation, the use of contrast agents can significantly shrink the tissues. Thus, a standard staining technique capable of enhancing the contrast of soft tissues and minimising the tissue shrinkage needs to be found. Furthermore, standard techniques that take into account the tissue shrinkage need to be developed to accurately

CHAPTER 7. CONCLUSIONS AND FUTURE WORK

reconstruct the sample 3D structure from the microCT scans. In this way, each tissue constituting the measurement sample can be segmented and imported as a computer aided-design (CAD) model to an EM simulation software. These EM simulations would then reproduce and validate the dielectric measurements of heterogeneous biological samples.

Lastly, all of the system settings and measurement meta-data could be accurately recorded to promote the reproducibility of the dielectric experiments. Hence, the introduction of standard measurement techniques, together with standard reporting of the measured data and recorded meta-data, will improve the accuracy and repeatability of tissue dielectric measurements, which will then result in more accurate dosimetry calculations and more reliable designs of EM-based medical technologies. Over the long-term, the resulting improvements in dielectric data will promote safer EM-based devices and will support more effective and efficient patient care.

Bibliography

- [1] D. Formica and S. Silvestri, “Biological effects of exposure to magnetic resonance imaging: an overview,” *Biomedical engineering online*, vol. 3, p. 11, 2004.
- [2] A. Martellosio, M. Pasian, M. Bozzi, *et al.*, “Exposure Limits and Dielectric Contrast for Breast Cancer Tissues : Experimental Results up to 50 GHz,” in *11th European Conference on Antennas and Propagation (EUCAP)*, 2017, pp. 667–671.
- [3] N. K. Nikolova, “Microwave imaging for breast cancer,” *IEEE Microwave Magazine*, vol. 12, no. 7, pp. 78–94, 2011.
- [4] M. Pastorino, *Microwave imaging*. John Wiley & Sons, 2010.
- [5] S. Noghianian, *Introduction to Microwave Imaging*. Springer New York, 2014.
- [6] Y. Zou and Z. Guo, “A review of electrical impedance techniques for breast cancer detection,” *Medical Engineering and Physics*, vol. 25, no. 2, pp. 79–90, 2003.
- [7] B. Brown, “Electrical impedance tomography (EIT): a review,” *Journal of Medical Engineering & Technology*, vol. 27, no. 3, pp. 97–108, 2003.
- [8] A. D. Waldmann, C. F. Ortola, M. M. Martinez, *et al.*, “Position-dependent distribution of lung ventilation - A feasibility study,” *SAS 2015 - 2015 IEEE Sensors Applications Symposium, Proceedings*, 2015.
- [9] J. Avery, T. Dowrick, M. Faulkner, *et al.*, “A versatile and reproducible multi-frequency electrical impedance tomography system,” *Sensors*, vol. 17, no. 2, 2017.
- [10] M. Lazebnik, L. McCartney, D. Popovic, *et al.*, “A large-scale study of the ultrawideband microwave dielectric properties of normal breast tissue obtained from reduction surgeries,” *Physics in medicine and biology*, vol. 52, no. 10, pp. 2637–2656, 2007.

BIBLIOGRAPHY

- [11] M. Lazebnik, D. Popovic, L. McCartney, *et al.*, “A large-scale study of the ultrawideband microwave dielectric properties of normal, benign and malignant breast tissues obtained from cancer surgeries,” *Physics in medicine and biology*, vol. 52, no. 20, pp. 6093–6115, 2007.
- [12] R. J. Halter, T. Zhou, P. M. Meaney, *et al.*, “The correlation of in vivo and ex vivo tissue dielectric properties to validate electromagnetic breast imaging: initial clinical experience,” *Physiological measurement*, vol. 30, no. 6, S121–S136, 2009.
- [13] E. Porter, E. Kirshin, A. Santorelli, *et al.*, “Time-domain multistatic radar system for microwave breast screening,” *IEEE Antennas and Wireless Propagation Letters*, vol. 12, pp. 229–232, 2013.
- [14] R. Scapatucci, G. Bellizzi, I. Catapano, *et al.*, “An effective procedure for MNP-enhanced breast cancer microwave imaging,” *IEEE Transactions on Biomedical Engineering*, vol. 61, no. 4, pp. 1071–1079, 2014.
- [15] T. Sugitani, S. Kubota, S. Kuroki, *et al.*, “Complex permittivities of breast tumor tissues obtained from cancer surgeries,” *Applied Physics Letters*, vol. 104, no. 25, (253702)1–5, 2014.
- [16] M. O’Halloran, F. Morgan, D. Flores-Tapia, *et al.*, “Prototype Ultra Wideband Radar System for Bladder Monitoring Applications,” *Progress In Electromagnetics Research C*, vol. 33, pp. 17–28, 2012.
- [17] K. Arunachalam, P. MacCarini, V. De Luca, *et al.*, “Detection of vesicoureteral reflux using microwave radiometry system characterization with tissue phantoms,” *IEEE Transactions on Biomedical Engineering*, vol. 58, no. 6, pp. 1629–1636, 2011.
- [18] D. Ireland and M. E. Bialkowski, “Microwave Head Imaging for Stroke Detection,” *Progress In Electromagnetics Research M*, vol. 21, pp. 163–175, 2011.
- [19] M. Persson, A. Fhager, H. D. Trefna, *et al.*, “Microwave-based stroke diagnosis making global prehospital thrombolytic treatment possible,” *IEEE Transactions on Biomedical Engineering*, vol. 61, no. 11, pp. 2806–2817, 2014.
- [20] T. Dowrick, C. Blochet, and D. Holder, “In vivo bioimpedance measurement of healthy and ischaemic rat brain: implications for stroke imaging using electrical impedance tomography,” *Physiological Measurement*, vol. 36, no. 6, pp. 1273–1282, 2015.

BIBLIOGRAPHY

- [21] R. Scapaticci, O. M. Bucci, I. Catapano, *et al.*, “Differential microwave imaging for brain stroke followup,” *International Journal of Antennas and Propagation*, 2014.
- [22] N. R. Datta, S. G. Ordóñez, U. S. Gaipl, *et al.*, “Local hyperthermia combined with radiotherapy and-/or chemotherapy: Recent advances and promises for the future,” *Cancer Treatment Reviews*, vol. 41, no. 9, pp. 742–753, 2015.
- [23] R. Issels, L. Lindner, P. Ghadjar, *et al.*, “Improved overall survival by adding regional hyperthermia to neo-adjuvant chemotherapy in patients with localized high-risk soft tissue sarcoma (HR-STs): Long-term outcomes of the EORTC 62961/ESHO randomized phase III study,” *European Journal of Cancer*, vol. 51, S716, Sep. 2015.
- [24] R. Wessalowski, D. T. Schneider, O. Mils, *et al.*, “Regional deep hyperthermia for salvage treatment of children and adolescents with refractory or recurrent non-testicular malignant germ-cell tumours: An open-label, non-randomised, single-institution, phase 2 study,” *The Lancet Oncology*, vol. 14, no. 9, pp. 843–852, 2013.
- [25] V. Ekstrand, H. Wiksell, I. Schultz, *et al.*, “Influence of electrical and thermal properties on RF ablation of breast cancer: is the tumour preferentially heated?” *Biomedical Engineering Online*, vol. 4, no. 41, 2005.
- [26] I. Bargellini, E. Bozzi, R. Cioni, *et al.*, “Radiofrequency ablation of lung tumours,” *Insights into imaging*, vol. 2, no. 5, pp. 567–576, 2011.
- [27] S. A. Curley, P. Marra, K. Beatty, *et al.*, “Early and late complications after radiofrequency ablation of malignant liver tumors in 608 patients,” *Annals of surgery*, vol. 239, no. 4, pp. 450–8, 2004.
- [28] P. R. Stauffer, F. Rossetto, M. Prakash, *et al.*, “Phantom and animal tissues for modelling the electrical properties of human liver,” *International Journal of Hyperthermia*, vol. 19, no. 910867416, pp. 89–101, 2003.
- [29] D. Yang, M. Converse, D. Mahvi, *et al.*, “Measurement and analysis of tissue temperature during microwave liver ablation,” *IEEE Transactions on Biomedical Engineering*, vol. 54, no. 1, pp. 150–155, 2007.
- [30] V. Lopresto, R. Pinto, G. Lovisolò, *et al.*, “Changes in the dielectric properties of ex vivo bovine liver during microwave thermal ablation at 2.45 GHz,” *Physics in Medicine and Biology*, vol. 57, no. 8, pp. 2309–2327, 2012.

BIBLIOGRAPHY

- [31] M. Lazebnik, M. Converse, J. H. Booske, *et al.*, “Ultrawideband temperature-dependent dielectric properties of animal liver tissue in the microwave frequency range,” *Physics in medicine and biology*, vol. 51, no. 7, pp. 1941–1955, 2006.
- [32] C. L. Brace, “Temperature-dependent dielectric properties of liver tissue measured during thermal ablation: toward an improved numerical model,” in *IEEE Engineering in Medicine and Biology Society*, 2008, pp. 230–233.
- [33] P. Wust, B. Hildebrandt, G. Sreenivasa, *et al.*, “Hyperthermia in combined treatment of cancer,” *The lancet oncology*, vol. 3, no. 8, pp. 487–497, 2002.
- [34] M. Ahmed, C. L. Brace, F. T. Lee, *et al.*, “Principles of and advances in percutaneous ablation,” *Radiology*, vol. 258, no. 2, pp. 351–369, 2011.
- [35] D. E. Dupuy, “Image-guided Thermal Ablation of Lung Malignancies,” *Radiology*, vol. 260, no. 3, pp. 633–655, 2011.
- [36] Z. Ji and C. L. Brace, “Expanded modeling of temperature-dependent dielectric properties for microwave thermal ablation,” *Physics in medicine and biology*, vol. 56, no. 16, pp. 5249–64, 2011.
- [37] M. Cavagnaro, R. Pinto, and V. Lopresto, “Numerical models to evaluate the temperature increase induced by ex vivo microwave thermal ablation,” *Physics in Medicine and Biology*, vol. 60, no. 8, pp. 3287–3311, 2015.
- [38] T. England and N. Sharples, “Dielectric Properties of the Human Body in the Microwave Region of the Spectrum,” *Nature*, vol. 163, pp. 487–488, 1949.
- [39] H. F. Cook, B. Rajewsky, K. H. Osswald, *et al.*, “The dielectric behaviour of some types of human tissues at microwave frequencies,” *British Journal of Applied Physics*, vol. 2, no. 10, pp. 295–300, 1951.
- [40] H. P. Schwan and K. Li, “Capacity and Conductivity of Body Tissues at Ultrahigh Frequencies,” *Proceedings of the IRE*, vol. 41, no. 12, pp. 1735–1740, 1953.
- [41] H. P. Schwan, “Electrical Properties of Tissue and Cell Suspensions,” *Advances in Biological and Medical Physics*, vol. 5, pp. 147–209, 1957.
- [42] E. Burdette, F. Cain, and J. Seals, “In vivo probe measurement technique for determining dielectric properties at VHF through microwave frequencies,” *IEEE Transactions on Microwave Theory and Techniques*, vol. 28, no. 4, pp. 414–427, 1980.

BIBLIOGRAPHY

- [43] M. A. Stuchly and S. S. Stuchly, “Dielectric properties of biological substances - tabulated,” *Journal of Microwave Power*, vol. 15, no. 1, pp. 19–25, 1980.
- [44] A. Kraszewski, M. A. Stuchly, S. S. Stuchly, *et al.*, “In vivo and in vitro dielectric properties of animal tissues at radio frequencies,” *Bioelectromagnetics*, vol. 3, no. 4, pp. 421–432, 1982.
- [45] K. Foster and H. Schwan, “Dielectric properties of tissues and biological materials: a critical review,” *Critical reviews in biomedical engineering*, vol. 17, pp. 25–104, 1989.
- [46] S. Gabriel, R. W. Lau, and C. Gabriel, “The dielectric properties of biological tissues: II. Measurements in the frequency range 10 Hz to 20 GHz,” *Physics in medicine and biology*, vol. 41, no. 11, pp. 2251–2269, 1996.
- [47] A. Peyman, S. Holden, and C. Gabriel, “Mobile Telecommunications and Health Research Programme: Dielectric Properties of Tissues at Microwave Frequencies,” Tech. Rep., 2005.
- [48] A. Peyman, B. Kos, M. Djokić, *et al.*, “Variation in dielectric properties due to pathological changes in human liver,” *Bioelectromagnetics*, vol. 36, no. 8, pp. 603–612, 2015.
- [49] A. Martellosio, M. Pasian, M. Bozzi, *et al.*, “Dielectric properties characterization from 0.5 to 50 GHz of breast cancer tissues,” *IEEE Transactions on Microwave Theory and Techniques*, vol. 65, no. 3, pp. 998–1011, 2017.
- [50] A. Gregory and R. Clarke, “A review of RF and microwave techniques for dielectric measurements on polar liquids,” *IEEE Transactions on Dielectrics and Electrical Insulation*, vol. 13, no. 4, pp. 727–743, 2006.
- [51] M. Stuchly, T. Athey, G. Samaras, *et al.*, “Measurement of Radio Frequency Permittivity of Biological Tissues with an Open-Ended Coaxial Line: Part II - Experimental Results,” *IEEE Transactions on Microwave Theory and Techniques*, vol. 30, no. 1, pp. 87–92, 1982.
- [52] J. L. Schwartz and G. A. Mealing, “Dielectric properties of frog tissues in vivo and in vitro,” *Physics in medicine and biology*, vol. 30, no. 2, pp. 117–124, 1985.

BIBLIOGRAPHY

- [53] A. P. O'Rourke, M. Lazebnik, J. M. Bertram, *et al.*, "Dielectric properties of human normal, malignant and cirrhotic liver tissue: in vivo and ex vivo measurements from 0.5 to 20 GHz using a precision open-ended coaxial probe," *Physics in medicine and biology*, vol. 52, no. 15, pp. 4707–19, 2007.
- [54] L. Abdilla, C. Sammut, and L. Z. Mangion, "Dielectric properties of muscle and liver from 500 MHz–40 GHz," *Electromagnetic Biology and Medicine*, vol. 32, no. 2, pp. 244–252, 2013.
- [55] C. Gabriel and A. Peyman, "Dielectric measurement: error analysis and assessment of uncertainty," *Physics in medicine and biology*, vol. 51, no. 23, pp. 6033–6046, 2006.
- [56] A. Peyman, S. J. Holden, S. Watts, *et al.*, "Dielectric properties of porcine cerebrospinal tissues at microwave frequencies: in vivo, in vitro and systematic variation with age," *Physics in medicine and biology*, vol. 52, no. 8, pp. 2229–45, 2007.
- [57] A. Peyman, A. Rezazadeh, and C. Gabriel, "Changes in the dielectric properties of rat tissue as a function of age at microwave frequencies," *Physics in medicine and biology*, vol. 46, no. 6, pp. 1617–1629, 2001.
- [58] A. Peyman, C. Gabriel, E. H. Grant, *et al.*, "Variation of the dielectric properties of tissues with age: the effect on the values of SAR in children when exposed to walkie-talkie devices," *Physics in medicine and biology*, vol. 54, pp. 227–241, 2009.
- [59] A. Peyman, "Dielectric properties of tissues; variation with structure and composition," in *2009 International Conference on Electromagnetics in Advanced Applications*, 2009, pp. 863–864.
- [60] S. Chaudhary, R. Mishra, A. Swarup, *et al.*, "Dielectric properties of normal & malignant human breast tissues at radiowave & microwave frequencies," *Indian J Biochem Biophys*, vol. 21, no. 1, pp. 76–9, 1984.
- [61] W. T. Joines, Y. Zhang, C. Li, *et al.*, "The measured electrical properties of normal and malignant human tissues from 50 to 900 MHz," *Medical physics*, vol. 21, no. 4, pp. 547–550, 1994.
- [62] D. O'Loughlin, M. J. O'Halloran, B. M. Moloney, *et al.*, "Microwave Breast Imaging: Clinical Advances and Remaining Challenges," *IEEE Transactions on Biomedical Engineering*, vol. 65, no. 11, pp. 2580–2590, 2018.

BIBLIOGRAPHY

- [63] E. Porter and M. O'Halloran, "Investigation of Histology Region in Dielectric Measurements of Heterogeneous Tissues," *IEEE Transactions on Antennas and Propagation*, vol. 65, no. 10, pp. 5541–5552, 2017.
- [64] E. Porter, A. La Gioia, A. Santorelli, *et al.*, "Modeling of the Dielectric Properties of Biological Tissues within the Histology Region," *IEEE Transactions on Dielectrics and Electrical Insulation*, vol. 24, no. 5, pp. 3290–3301, 2017.
- [65] D. Hagl, D. Popovic, S. C. Hagness, *et al.*, "Sensing volume of open-ended coaxial probes for dielectric characterization of breast tissue at microwave frequencies," *IEEE Transactions on Microwave Theory and Techniques*, vol. 51, no. 4, pp. 1194–1206, 2003.
- [66] P. M. Meaney, A. P. Gregory, N. R. Epstein, *et al.*, "Microwave open-ended coaxial dielectric probe: interpretation of the sensing volume re-visited," *BMC Medical Physics*, vol. 14, no. 1, p. 3, 2014.
- [67] H. P. Schwan and K. R. Foster, "RF Field Interactions with Biological Systems: Electrical Properties and Biophysical Mechanisms," *Proceedings of the IEEE*, vol. 68, no. 1, pp. 104–113, 1980.
- [68] A. Bakshi and U. Bakshi, *Electromagnetic Waves and Transmission Lines*. Technical Publications Pune, 2008, p. 846.
- [69] J. L. Schepps and K. R. Foster, "The UHF and microwave dielectric properties of normal and tumour tissues: variation in dielectric properties with tissue water content," *Physics in medicine and biology*, vol. 25, no. 6, pp. 1149–1159, 1980.
- [70] A. M. Campbell, "Measurements and analysis of the microwave dielectric properties of tissues," PhD thesis, University of Glasgow, 1990, pp. 1–143.
- [71] S. Gabriel, R. W. Lau, and C. Gabriel, "The dielectric properties of biological tissues: III. Parametric models for the dielectric spectrum of tissues," *Physics in medicine and biology*, vol. 41, no. 11, pp. 2271–2293, 1996.
- [72] A. Gregory, R. Clarke, T. Hodgetts, *et al.*, "RF and microwave dielectric measurements upon layered materials using coaxial sensors," Tech. Rep., 2008, pp. 1–88.
- [73] R. Gulich, M. Köhler, P. Lunkenheimer, *et al.*, "Dielectric spectroscopy on aqueous electrolytic solutions," *Radiation and Environmental Biophysics*, vol. 48, no. 1, pp. 107–114, 2009.

BIBLIOGRAPHY

- [74] E. D. Eastman, "Conductivity and frequency," *Journal of the American Chemical Society*, vol. 42, no. 8, pp. 1648–1655, 1920.
- [75] Agilent, "Basics of Measuring the Dielectric Properties of Materials," Tech. Rep., 2005, pp. 1–33.
- [76] K. R. Foster, J. L. Schepps, R. D. Stoy, *et al.*, "Dielectric properties of brain tissue between 0.01 and 10 GHz," *Physics in medicine and biology*, vol. 24, no. 6, pp. 1177–1187, 1979.
- [77] T. Reinecke, L. Hagemeyer, V. Schulte, *et al.*, "Quantification of Edema in Human Brain Tissue by Determination of Electromagnetic Parameters," in *IEEE Sensors 2013*, Baltimore, MD, 2013, pp. 1–4.
- [78] A. Nicolson and G. F. Ross, "Measurement of the Intrinsic Properties of Materials by Time-Domain Techniques," *IEEE Transactions on Instrumentation and Measurement*, vol. 19, no. 4, pp. 377–382, 1970.
- [79] W. B. Weir, "Automatic Measurement of Complex Dielectric Constant and Permeability," *Proceedings of the IEEE*, vol. 62, no. 1, pp. 33–36, 1974.
- [80] J. Baker-Jarvis, E. J. Vanzura, and W. A. Kissick, "Improved technique for determining complex permittivity with the transmission/reflection method," *IEEE Transactions on Microwave Theory and Techniques*, vol. 38, no. 8, pp. 1096–1103, 1990.
- [81] J. Baker-Jarvis, M. Janezic, P. Domich, *et al.*, "Analysis of an Open-Ended Coaxial Probe with Lift-off for Non destructive Testing," *IEEE Transactions on Instrumentation and Measurement*, vol. 43, no. 5, pp. 1–8, 1994.
- [82] S. Kim and J. Baker-Jarvis, "An Approximate Approach To Determining the Permittivity and Permeability near $\lambda/2$ Resonances in Transmission/Reflection Measurements," *Progress In Electromagnetics Research B*, vol. 58, pp. 95–109, 2014.
- [83] A. H. Boughriet, C. Legrand, and A. Chapoton, "Noniterative stable transmission/reflection method for low-loss material complex permittivity determination," *IEEE Transactions on Microwave Theory and Techniques*, vol. 45, no. 1, pp. 52–57, 1997.
- [84] M. R. Tofighi and A. Daryoush, "Comparison of two post-calibration correction methods for complex permittivity measurement of biological tissues up to 50 GHz," *IEEE Transactions on Instrumentation and Measurement*, vol. 51, no. 6, pp. 1170–1175, 2002.

BIBLIOGRAPHY

- [85] M. R. Tofghi and A. S. Daryoush, "Characterization of the complex permittivity of brain tissues up to 50 GHz utilizing a two-port microstrip test fixture," *IEEE Transactions on Microwave Theory and Techniques*, vol. 50, no. 10, pp. 2217–2225, 2002.
- [86] G. R. Facer, D. A. Notterman, and L. L. Sohn, "Dielectric spectroscopy for bioanalysis: From 40 Hz to 26.5 GHz in a microfabricated wave guide," *Applied Physics Letters*, vol. 78, no. 7, pp. 996–998, 2001.
- [87] K. Shibata, K. Tani, O. Hashimoto, *et al.*, "Measurement of Complex Permittivity for Liquid Phantom by Transmission Line Method Using Coaxial Line," *IEICE Transactions on Electronics*, vol. 87-C, no. 5, pp. 689–693, 2004.
- [88] D. V. Land and A. M. Campbell, "A quick accurate method for measuring the microwave dielectric properties of small tissue samples," *Physics in medicine and biology*, vol. 37, no. 1, pp. 183–192, 1992.
- [89] A. Campbell and D. V. Land, "Dielectric properties of female human breast tissue measured in vitro at 3.2 GHz," *Physics in medicine and biology*, vol. 37, no. 1, pp. 193–210, 1992.
- [90] Z. Peng, J. Y. Hwang, and M. Andriese, "Maximum sample volume for permittivity measurements by cavity perturbation technique," *IEEE Transactions on Instrumentation and Measurement*, vol. 63, no. 2, pp. 450–455, 2014.
- [91] D. K. Misra, "A quasi-static analysis of open-ended coaxial lines," *IEEE Transactions on Microwave Theory and Techniques*, vol. 35, no. 10, pp. 925–928, 1987.
- [92] J. P. Grant, R. N. Clarke, G. T. Symm, *et al.*, "A critical study of the open-ended coaxial-line sensor technique for RF and microwave complex permittivity measurements," *J. Phys. E: Sci. Instrum.*, vol. 22, pp. 757–770, 1989.
- [93] T. W. Athey, M. A. Stuchly, and S. S. Stuchly, "Measurement of radio frequency permittivity of biological tissues with an open-ended coaxial line: Part I," *IEEE Transactions on Microwave Theory and Techniques*, vol. 30, no. 1, pp. 82–86, 1982.
- [94] S. Jenkins, A. W. Preece, T. E. Hodgetts, *et al.*, "Comparison of three numerical treatments for the open-ended coaxial line sensor," *Electronics Letters*, vol. 26, no. 4, pp. 234–236, 1990.

BIBLIOGRAPHY

- [95] D. Misra, "On the Measurement of the Complex Permittivity of Materials by an Open-Ended Coaxial Probe," *IEEE Microwave and Guided Wave Letters*, vol. 5, no. 5, pp. 161–163, 1995.
- [96] D. Popovic, M. Okoniewski, D. Hagl, *et al.*, "Volume Sensing Properties of Open Ended Coaxial Probes for dielectric spectroscopy of breast tissue," in *IEEE Antennas and Propagation Society*, Boston, MA, 2001, pp. 254–257.
- [97] H. P. Schwan and K. R. Foster, "Microwave dielectric properties of tissue. Some comments on the rotational mobility of tissue water," *Biophysical journal*, vol. 17, no. 2, pp. 193–197, 1977.
- [98] P. De Langhe, K. Blomme, L. Martens, *et al.*, "Measurement of low-permittivity materials based on a spectral-domain analysis for the open-ended coaxial probe," *IEEE Transactions on Instrumentation and Measurement*, vol. 42, no. 5, pp. 879–886, 1993.
- [99] H. Levine and C. H. Papas, "Theory of the circular diffraction antenna," *Journal of Applied Physics*, vol. 22, no. 1, pp. 29–43, 1951.
- [100] C. Gabriel, E. H. Grant, and I. R. Young, "Use of time domain spectroscopy for measuring dielectric properties with a coaxial probe," *Journal of Physics E: Scientific Instruments*, vol. 19, no. 10, pp. 843–846, 1986.
- [101] D. Berube, F. M. Ghannouchi, and P. Savard, "A Comparative Study of Four Open-Ended Coaxial Probe Models for Permittivity Measurements of Lossy Dielectric/Biological Materials at Microwave Frequencies," *IEEE Transactions on Microwave Theory and Techniques*, vol. 44, no. 10, pp. 1928–1934, 1996.
- [102] D. V. Blackham and R. D. Pollard, "An Improved Technique for Permittivity Measurements Using a Coaxial Probe," *IEEE Transactions on Instrumentation and Measurement*, vol. 46, no. 5, pp. 1093–1099, 1997.
- [103] M. A. Rzepecka and S. S. Stuchly, "A Lumped Capacitance Method for the Measurement of the Permittivity and Conductivity in the Frequency and Time Domain—A Further Analysis," *IEEE Transactions on Instrumentation and Measurement*, vol. 24, no. 1, pp. 27–32, 1975.
- [104] M. A. Stuchly and S. S. Stuchly, "Coaxial Line Reflection Methods for Measuring Dielectric Properties of Biological Substances at Radio and Microwave Frequencies—A Review," *IEEE Transactions on Instrumentation and Measurement*, vol. 29, no. 3, pp. 176–183, 1980.

BIBLIOGRAPHY

- [105] R. Zajíček, L. Oppl, and J. Vrba, “Broadband measurement of complex permittivity using reflection method and coaxial probes,” *Radio-engineering*, vol. 17, no. 1, pp. 14–19, 2008.
- [106] F. M. Ghannouchi and R. G. Bosisio, “Measurement of microwave permittivity using a six-port reflectometer with an open-ended coaxial line,” *IEEE Transactions on Instrumentation and Measurement*, vol. 38, no. 2, pp. 505–508, 1989.
- [107] E. Silavwe, “Development of Novel Microwave and Millimetre-wave Sensors for Liquid Characterisation,” PhD thesis, University of Leeds, 2017, pp. 1–154.
- [108] G. Deschamps, “Impedance of an antenna in a conducting medium,” *IRE Transactions on Antennas and Propagation*, vol. 10, no. 5, pp. 648–650, 1962.
- [109] D. Popovic, L. McCartney, C. Beasley, *et al.*, “Precision open-ended coaxial probes for in vivo and ex vivo dielectric spectroscopy of biological tissues at microwave frequencies,” *IEEE Transactions on Microwave Theory and Techniques*, vol. 53, no. 5, pp. 1713–1721, 2005.
- [110] C. Gabriel, T. Y. Chan, and E. H. Grant, “Admittance models for open ended coaxial probes and their place in dielectric spectroscopy,” *Physics in medicine and biology*, vol. 39, no. 12, pp. 2183–2200, 1994.
- [111] D. Popovic and M. Okoniewski, “Effects of mechanical flaws in open-ended coaxial probes for dielectric spectroscopy,” *IEEE Microwave and Wireless Components Letters*, vol. 12, no. 10, pp. 401–403, 2002.
- [112] A. Sabouni, C. Hahn, S. Noghianian, *et al.*, “Study of the Effects of Changing Physiological Conditions on Dielectric Properties of Breast Tissues,” *ISRN Biomedical Imaging*, vol. 2013, no. Article ID 894153, pp. 1–5, 2013.
- [113] Keysight, “N1501A Dielectric Probe Kit 10 MHz to 50 GHz: Technical Overview. Available at: <http://www.keysight.com/en/pd-2492144-pn-N1501A/dielectric-probe-kit>. [Accessed 30 October 2017].,” Tech. Rep., 2015.
- [114] T. Karacolak, R. Cooper, E. S. Unlu, *et al.*, “Dielectric properties of porcine skin tissue and in vivo testing of implantable antennas using pigs as model animals,” *IEEE Antennas and Wireless Propagation Letters*, vol. 11, pp. 1686–1689, 2012.

BIBLIOGRAPHY

- [115] E. C. Burdette, P. G. Friederich, R. L. Seaman, *et al.*, “In Situ Permittivity of Canine Brain : Regional Variations and Postmortem Changes,” *IEEE Transactions on Microwave Theory and Techniques*, vol. 34, no. 1, pp. 38–50, 1986.
- [116] A. Kraszewski, M. A. Stuchly, and S. S. Stuchly, “ANA Calibration Method for Measurements of Dielectric Properties,” *IEEE Transactions on Instrumentation and Measurement*, vol. IM-32, no. 2, pp. 385–387, 1983.
- [117] S. R. Smith and K. R. Foster, “Dielectric properties of low-water-content tissues,” *Physics in medicine and biology*, vol. 30, no. 9, pp. 965–973, 1985.
- [118] M. Zhadobov, R. Augustine, R. Sauleau, *et al.*, “Complex permittivity of representative biological solutions in the 2-67GHz range,” *Bioelectromagnetics*, vol. 33, no. 4, pp. 346–355, 2012.
- [119] S. Di Meo, A. Martellosio, M. Pasian, *et al.*, “Experimental Validation of the Dielectric Permittivity of Breast Cancer Tissues up to 50 GHz,” in *IEEE MTT-S (IMWS-AMP)*, 2017, pp. 20–22.
- [120] A. Nyshadham, C. Sibbald, and S. Stuchly, “Permittivity measurements using open-ended sensors and reference liquid calibration - an uncertainty analysis,” *IEEE Trans. Microwave Theory and Techniques*, vol. 40, no. 2, pp. 305–314, 1992.
- [121] J. Anderson, C. L. Sibbald, and S. S. Stuchly, “Dielectric measurements using a rational function model,” *IEEE Transactions on Microwave Theory and Techniques*, vol. 42, no. 2, pp. 199–204, 1994.
- [122] T. Sugitani, K. Arihiro, and T. Kikkawa, “Comparative study on dielectric constants and conductivities of invasive ductal carcinoma tissues,” *Annual International Conference of the IEEE Engineering in Medicine and Biology Society*, vol. 2015, pp. 4387–4390, 2015.
- [123] A. Surowiec, S. S. Stuchly, L. Eidus, *et al.*, “In vitro dielectric properties of human tissues at radiofrequencies,” *Physics in medicine and biology*, vol. 32, no. 5, p. 615, 1987.
- [124] R. Pethig, “Dielectric Properties of Biological Materials: Biophysical and Medical Applications,” *IEEE Transactions on Electrical Insulation*, vol. EI-19, no. 5, pp. 453–474, 1984.
- [125] C. Gabriel, S. Gabriel, and E. Corthout, “The dielectric properties of biological tissues: I. Literature survey,” *Physics in Medicine and Biology*, vol. 41, no. 11, pp. 2231–2249, 1996.

BIBLIOGRAPHY

- [126] C. Gabriel, *Tissue dielectric properties*, Federal Communication Commission, Washington, DC (USA), 2008. Available online at: <https://www.fcc.gov/general/body-tissue-dielectric-parameters> [Accessed on 19/02/2018].
- [127] D. Andreuccetti, R. Fossi, and C. Petrucci, *An Internet resource for the calculation of the dielectric properties of body tissues in the frequency range 10 Hz - 100 GHz*. IFAC-CNR, Florence (Italy), 1997. Based on data published by C. Gabriel et al. in 1996. Available online at: <http://niremf.ifac.c>.
- [128] E. Alanen, T. Lahtinen, and J. Nuutinen, "Variational formulation of open-ended coaxial line in contact with layered biological medium," *IEEE Transactions on Biomedical Engineering*, vol. 45, no. 10, pp. 1241–1248, 1998.
- [129] E. C. Burdette, J. Seals, S. P. Auda, et al., "Review of the Dielectric Properties of Animal and Human Tumours Determined from In Vivo Measurements," *Critical Reviews in Biomedical Engineering*, vol. 44, no. 4, pp. 293–318, 2016.
- [130] A. Shahzad, K. Sonja, M. Jones, et al., "Investigation of the effect of dehydration on tissue dielectric properties in ex vivo measurements," *Biomedical Physics & Engineering Express*, vol. 3, no. 4, pp. 1–9, 2017.
- [131] B. N. Taylor and C. E. Kuyatt, "Guidelines for Evaluating and Expressing the Uncertainty of NIST Measurement Results, NIST Technical Note 1297," Tech. Rep., 1994.
- [132] A. Peyman and C. Gabriel, "Dielectric properties of porcine glands, gonads and body fluids," *Physics in Medicine and Biology*, vol. 57, no. 19, 2012.
- [133] S. Salahuddin, A. La Gioia, A. Shahzad, et al., "An anatomically accurate dielectric profile of the porcine kidney," *Biomedical Physics and Engineering Express*, vol. 4, no. 2, 2018.
- [134] A. Shahzad, D. Clausing, P. Prakash, et al., "Broadband dielectric properties of adrenal gland for accurate anatomical modelling in medical applications," *Proceedings of the 2017 19th International Conference on Electromagnetics in Advanced Applications, ICEAA 2017*, pp. 1465–1468, 2017.

BIBLIOGRAPHY

- [135] P. M. Meaney, A. P. Gregory, J. Seppälä, *et al.*, “Open-Ended Coaxial Dielectric Probe Effective Penetration Depth Determination,” *IEEE Transactions on Microwave Theory and Techniques*, vol. 64, no. 3, pp. 915–923, 2016.
- [136] T. Marsland and S. Evans, “Dielectric measurements with an open-ended coaxial probe,” *IEE Proceedings H Microwaves, Antennas and Propagation*, vol. 134, no. 4, pp. 341–349, 1987.
- [137] E. Piuzzi, C. Merla, G. Cannazza, *et al.*, “A comparative analysis between customized and commercial systems for complex permittivity measurements on liquid samples at microwave frequencies,” *IEEE Transactions on Instrumentation and Measurement*, vol. 62, no. 5, pp. 1034–1046, 2013.
- [138] Hewlett-Packard, *Automating the HP 8410B Microwave Network Analyzer*, 1980.
- [139] J. Bobowski and T. Johnson, “Permittivity measurements of biological samples by an open-ended coaxial line,” *Progress In Electromagnetics Research*, vol. 40, no. February, pp. 159–183, 2012.
- [140] P. H. Smith, *Transmission Line Calculator*, 1939.
- [141] U. Kaatze, “Complex Permittivity of Water as a Function of Frequency and Temperature,” *Journal of Chemical Engineering Data*, vol. 34, no. 4, pp. 371–374, 1989.
- [142] S. Salahuddin, E. Porter, P. M. Meaney, *et al.*, “Effect of logarithmic and linear frequency scales on parametric modelling of tissue dielectric data,” *Biomedical Physics & Engineering Express*, vol. 3, pp. 1–11, 2017.
- [143] R. Buchner, G. T. Hefter, and M. P. May, “Dielectric relaxation of aqueous NaCl solutions,” *The Journal of Physical Chemistry*, vol. 103, no. 1, pp. 1–9, 1999.
- [144] Y. Z. Wei and S. Sridhar, “Radiation-Corrected Open-Ended Coax Line Technique for Dielectric Measurements of Liquids up to 20 GHz,” *IEEE Transactions on Microwave Theory and Techniques*, vol. 39, no. 3, pp. 526–531, 1991.
- [145] A. P. Gregory and R. N. Clarke, “Tables of the Complex Permittivity of Dielectric Reference Liquids at Frequencies up to 5 GHz, NPL Report MAT 23,” Tech. Rep., 2012, pp. 1–87.
- [146] A. Peyman, C. Gabriel, and E. H. Grant, “Complex permittivity of sodium chloride solutions at microwave frequencies,” *Bioelectromagnetics*, vol. 28, no. 4, pp. 264–274, 2007.

BIBLIOGRAPHY

- [147] B. P. Jordan, R. J. Sheppard, and S. Szwarnowski, "The dielectric properties of formamide, ethanediol and methanol," *Journal of Physics D: Applied Physics*, vol. 11, no. 5, p. 695, 1978.
- [148] J. Barthel and R. Buchner, "High frequency permittivity and its use in the investigation of solution properties," *Pure and Applied Chemistry*, vol. 63, no. 10, pp. 1473–1482, 1991.
- [149] A. Stogryn, "Equations for Calculating the Dielectric Constant of Saline Water," *IEEE Transactions on Microwave Theory and Techniques*, vol. 19, no. 8, pp. 733–736, 1971.
- [150] K. Nortemann, J. Hilland, and U. Kaatze, "Dielectric Properties of Aqueous NaCl Solutions at Microwave Frequencies," *Journal of Physical Chemistry A*, vol. 101, no. 1, pp. 6864–6869, 1997.
- [151] K. Lamkaouchi, A. Balana, G. Delbos, *et al.*, "Permittivity measurements of lossy liquids in the range 26–110 GHz," *Measurement Science and Technology*, vol. 14, no. 4, pp. 444–450, 2003.
- [152] J. K. Vij, T. Grochulski, A. Kocot, *et al.*, "Complex permittivity measurements of acetone in the frequency region 50–310 GHz," *Molecular Physics*, vol. 72, no. 2, pp. 353–361, 1991.
- [153] U. Kaatze, R. Pottel, and M. Schaefer, "Dielectric spectrum of dimethyl sulfoxide / water mixtures as a function of composition," vol. 93, no. 14, pp. 5623–5627, 1989.
- [154] A. P. Gregory and R. N. Clarke, "Dielectric metrology with coaxial sensors," *Measurement Science and Technology*, vol. 18, no. 5, pp. 1372–1386, 2007.
- [155] P. M. Meaney, A. Golnabi, M. W. Fanning, *et al.*, "Dielectric volume measurements for biomedical applications," in *2009 13th International Symposium on Antenna Technology and Applied Electromagnetics and the Canadian Radio Sciences Meeting*, vol. M, 2009, pp. –3.
- [156] C. Johnson and A. Guy, "Nonionizing electromagnetic wave effects in biological materials and systems," *Proceedings of the IEEE*, vol. 60, no. 6, pp. 692–718, 1972.
- [157] L. Farrugia, P. S. Wismayer, L. Z. Mangion, *et al.*, "Accurate in vivo dielectric properties of liver from 500 MHz to 40 GHz and their correlation to ex vivo measurements," *Electromagnetic Biology and Medicine*, vol. 8378, no. August, pp. 1–9, 2016.

BIBLIOGRAPHY

- [158] P. Nopp, E. Rapp, H. Pfützner, *et al.*, “Dielectric properties of lung tissue as a function of air content,” *Physics in medicine and biology*, vol. 38, no. 6, pp. 699–716, 1993.
- [159] C. Gabriel, A. Peyman, and E. H. Grant, “Electrical conductivity of tissue at frequencies below 1 MHz,” *Physics in medicine and biology*, vol. 54, no. 16, pp. 4863–4878, 2009.
- [160] D. Haemmerich, R. Ozkan, S. Tungjitkusolmun, *et al.*, “Changes in electrical resistivity of swine liver after occlusion and postmortem,” *Medical & biological engineering & computing*, vol. 40, no. 1, pp. 29–33, 2002.
- [161] J. B. Ranck and S. L. Bement, “The Specific Impedance of the Dorsal Columns of Cat: an Inisotropic Medium,” *Experimental neurology*, vol. 11, pp. 451–463, 1965.
- [162] F. X. Hart and W. R. Dunfee, “In vivo measurement of the low-frequency dielectric spectra of frog skeletal muscle,” *Physics in medicine and biology*, vol. 38, no. 8, pp. 1099–112, 1993.
- [163] S. Huclova, D. Baumann, M. Talary, *et al.*, “Sensitivity and specificity analysis of fringing-field dielectric spectroscopy applied to a multi-layer system modelling the human skin,” *Physics in Medicine and Biology*, vol. 56, no. 24, pp. 7777–7793, 2011.
- [164] E. Alanen, T. Lahtinen, and J. Nuutinen, “Measurement of dielectric properties of subcutaneous fat with open-ended coaxial sensors,” *Physics in medicine and biology*, vol. 43, no. 3, pp. 475–85, 1998.
- [165] M. Cavagnaro, F. Frezza, R. Laurita, *et al.*, “A model to evaluate dielectric properties of human tissues based on water content,” in *8th International Symposium on Medical Information and Communication Technology (ISMICT)*, 2014, pp. 1–5.
- [166] M. Fujii, “Maximum frequency range limit of multi-pole debye models of human body tissues,” *IEEE Microwave and Wireless Components Letters*, vol. 22, no. 2, pp. 73–75, 2012.
- [167] J. Clegg and M. P. Robinson, “A genetic algorithm for optimizing multi-pole Debye models of tissue dielectric properties,” *Physics in Medicine and Biology*, vol. 57, pp. 6227–6243, 2012.
- [168] F. Krewer, F. Morgan, and M. O’Halloran, “Development of accurate multi-pole Debye functions for electromagnetic tissue modelling using a genetic algorithm,” *Progress In Electromagnetics Research Letters*, vol. 43, pp. 137–147, 2013.

BIBLIOGRAPHY

- [169] S. Salahuddin, E. Porter, F. Krewer, *et al.*, “Optimised analytical models of the dielectric properties of biological tissue,” *Medical Engineering & Physics*, vol. 43, pp. 103–111, 2017.
- [170] A. Modiri and K. Kiasaleh, “Permittivity estimation for breast cancer detection using particle swarm optimization algorithm,” in *Annual International Conference of the IEEE Engineering in Medicine and Biology Society*, 2011, pp. 1359–62.
- [171] D. F. Kelley, T. J. Destan, and R. J. Luebbers, “Debye function expansions of complex permittivity using a hybrid particle swarm-least squares optimization approach,” *IEEE Transactions on Antennas and Propagation*, vol. 55, no. 7, pp. 1999–2005, 2007.
- [172] W. D. Hurt, “Multiterm Debye dispersion relations for permittivity of muscle,” *IEEE Transactions on Biomedical Engineering*, vol. 32, no. 1, pp. 60–64, 1985.
- [173] B. Young, P. Woodford, and G. O’Dowd, *Wheater’s Functional Histology: A Text and Colour Atlas*. 2013, vol. 6th ed.
- [174] S. S. Cross, “Grading and scoring in histopathology,” *Histopathology*, vol. 33, no. 2, pp. 99–106, 1998.
- [175] M. Veta, J. P. W. Pluim, P. J. Van Diest, *et al.*, “Breast cancer histopathology image analysis: A review,” *IEEE Transactions on Biomedical Engineering*, vol. 61, no. 5, pp. 1400–1411, 2014.
- [176] H. M. Verkooijen, J. L. Peterse, M. E. I. Schipper, *et al.*, “Interobserver variability between general and expert pathologists during the histopathological assessment of large-core needle and open biopsies of non-palpable breast lesions,” *European Journal of Cancer*, vol. 39, no. 15, pp. 2187–2191, 2003.
- [177] D. S. Gomes, S. S. Porto, D. Balabram, *et al.*, “Inter-observer variability between general pathologists and a specialist in breast pathology in the diagnosis of lobular neoplasia, columnar cell lesions, atypical ductal hyperplasia and ductal carcinoma in situ of the breast,” *Diagnostic Pathology*, vol. 9, no. 1, p. 121, 2014.
- [178] J. C. Gage, M. Schiffman, W. C. Hunt, *et al.*, “Cervical histopathology variability among laboratories: A population-based statewide investigation,” *American Journal of Clinical Pathology*, vol. 139, no. 3, pp. 330–335, 2013.

BIBLIOGRAPHY

- [179] M. Lazebnik, “Ultrawideband Spectroscopy and Dielectric Properties Contrast Enhancement for Microwave Breast Cancer Detection and Treatment,” PhD thesis, University of Wisconsin - Madison, 2008, p. 245.
- [180] D. A. G. Bruggeman, “Berechnung verschiedener physikalischer konstanten von heterogenen substanzen. 1. Dielektizitätskonstanten und leitfähigkeiten der mischkörper aus isotropen substanzen,” *Ann. Phys. (Leipzig)*, vol. 24, pp. 636–679, 1935.
- [181] L. S. Anderson, G. B. Gajda, and S. S. Stuchly, “Analysis of an Open-Ended Coaxial Line Sensor in Layered Dielectrics,” *IEEE Transactions on Instrumentation and Measurement*, vol. IM-35, no. 1, pp. 13–18, 1986.
- [182] K. Folgerø and T. Tjomsland, “Permittivity measurement of thin liquid layers using open-ended coaxial probes,” *Measurement Science and Technology*, vol. 7, no. 8, pp. 1164–1173, 1996.
- [183] P. De Langhe, L. Martens, and D. De Zutter, “Design Rules for an Experimental Setup Using an Open-Ended Coaxial Probe Based on Theoretical Modelling,” *IEEE Transactions on Instrumentation and Measurement*, vol. 43, no. 6, pp. 810–817, 1994.
- [184] J. Daffe and R. G. Olsen, “An integral equation technique for solving rotationally symmetric electrostatic problems in conducting and dielectric material,” *IEEE Transactions on Power Apparatus and Systems*, vol. PAS-98, no. 5, pp. 1609–1616, 1979.
- [185] G. Chen, K. Li, and Z. Ji, “Bilayered Dielectric Measurement With an Open-Ended Coaxial Probe,” *IEEE Transactions on Microwave Theory and Techniques*, vol. 42, no. 6, pp. 966–971, 1994.
- [186] S. Bakhtiari, S. I. Ganchev, and R. Zoughi, “Analysis of Radiation from an Open-Ended Coaxial Line into Stratified Dielectrics,” *IEEE Transactions on Microwave Theory and Techniques*, vol. 42, no. 7, pp. 1261–1267, 1994.
- [187] S. Hoshina, Y. Kanai, and M. Miyakawa, “A numerical study on the measurement region of an open-ended coaxial probe used for complex permittivity measurement,” *IEEE Transactions on Magnetics*, vol. 37, no. 5, pp. 3311–3314, 2001.
- [188] Keysight Technologies, “Agilent PNA Microwave Network Analyzers,” Tech. Rep., 2009, pp. 1–64.
- [189] J. P. Dunsmore, *Handbook of Microwave Component Measurements: with Advanced VNA Techniques*, Wiley, Ed. 2012, pp. 102–107.

BIBLIOGRAPHY

- [190] P. Hasgall, F. Di Gennaro, C. Baumgartner, *et al.*, *IT'IS Database for thermal and electromagnetic parameters of biological tissues*.
- [191] K. Levenberg, "A method for the solution of certain non-linear problems in least squares," *Quart. Appl. Math.*, vol. 2, pp. 164–168, 1944.
- [192] D. W. Marquardt, "An Algorithm for Least-Squares Estimation of Nonlinear Parameters," *Journal of the Society for Industrial and Applied Mathematics*, vol. 11, no. 2, pp. 431–441, 1963.
- [193] A. Ozalp, "Revisiting the Wisconsin-Calgary Dielectric Spectroscopy Study of Breast Tissue Specimens," Tech. Rep., 2015.
- [194] A. Santorelli, O. Laforest, E. Porter, *et al.*, "Image Classification for a Time-Domain Microwave Radar System : Experiments with Stable Modular Breast Phantoms," *European Conference on Antennas and Propagation (EuCAP)*, 2015.
- [195] H. A. Van der Vorst, "Bi-CGSTAB: A Fast and Smoothly Converging Variant of Bi-CG for the Solution of Nonsymmetric Linear Systems," *SIAM Journal on Scientific and Statistical Computing*, vol. 13, no. 2, pp. 631–644, 1992.
- [196] F. J. Richards, "A Flexible Growth Function for Empirical Use," *Journal of Experimental Botany*, vol. 10, no. 29, pp. 290–300, 1959.
- [197] J. D. Garrett and E. C. Fear, "Average Dielectric Property Analysis of Complex Breast Tissue with Microwave Transmission Measurements," *Sensors*, vol. 15, no. 1, pp. 1199–1216, 2015.
- [198] W. Vågberg, J. Persson, L. Szekely, *et al.*, "Cellular-resolution 3D virtual histology of human coronary arteries using x-ray phase tomography," *Scientific Reports*, vol. 8, no. 1, pp. 1–7, 2018.
- [199] B. D. Metscher, "MicroCT for developmental biology: A versatile tool for high-contrast 3D imaging at histological resolutions," *Developmental Dynamics*, vol. 238, no. 3, pp. 632–640, 2009.
- [200] A. du Plessis, C. Broeckhoven, A. Guelpa, *et al.*, "Laboratory x-ray micro-computed tomography: A user guideline for biological samples," *GigaScience*, vol. 6, no. 6, pp. 1–11, 2017.
- [201] A. Laib, J. L. Kumer, S. Majumdar, *et al.*, "The temporal changes of trabecular architecture in ovariectomized rats assessed by microCT," *Osteoporosis International*, vol. 12, no. 11, pp. 936–941, 2001.

BIBLIOGRAPHY

- [202] P. Heimel, N. V. Swiadek, P. Slezak, *et al.*, “Iodine-Enhanced Micro-CT Imaging of Soft Tissue on the Example of Peripheral Nerve Regeneration,” *Contrast Media and Molecular Imaging*, vol. 2019, 2019.
- [203] R. Balint, T. Lowe, and T. Shearer, “Optimal contrast agent staining of ligaments and tendons for X-ray computed tomography,” *PLoS ONE*, vol. 11, no. 4, 2016.
- [204] E. Descamps, A. Sochacka, B. de Kegel, *et al.*, “Soft tissue discrimination with contrast agents using micro-ct scanning,” *Belgian Journal of Zoology*, vol. 144, no. 1, pp. 20–40, 2014.
- [205] J. M. Juliana, I. Zanette, P. B. Noël, *et al.*, “Three-dimensional non-destructive soft-tissue visualization with X-ray staining micro-tomography,” *Scientific Reports*, vol. 5, pp. 1–7, 2015.
- [206] K. A. Faraj, V. M. Cuijpers, R. G. Wismans, *et al.*, “Micro-Computed Tomographical Imaging of Soft Biological Materials Using Contrast Techniques,” *Tissue Engineering Part C: Methods*, vol. 15, no. 3, pp. 493–499, 2009.
- [207] C. Horn and C. Naugler, “Breast specimen shrinkage following formalin fixation,” *Pathology and Laboratory Medicine International*, vol. 6, pp. 11–14, 2014.